

**BIOCOMPOSITES OF POLY(LACTIC ACID) AND
CELLULOSE NANOFIBERS FROM CASSAVA PULP**



**A Thesis Submitted in Partial Fulfillment of the Requirements for the
Degree of Doctor of Philosophy in Polymer Engineering**

Suranaree University of Technology

Academic Year 2016

คอมพอสิตชีวภาพของพอลิแลคติกแอซิดและเส้นใยนาโนเซลลูโลสจากกากมัน
ตำปะหลัง



วิทยานิพนธ์นี้เป็นส่วนหนึ่งของการศึกษาตามหลักสูตรปริญญาวิศวกรรมศาสตรดุษฎีบัณฑิต
สาขาวิชาวิศวกรรมพอลิเมอร์
มหาวิทยาลัยเทคโนโลยีสุรนารี
ปีการศึกษา 2559

BIOCOMPOSITES OF POLY(LACTIC ACID) AND CELLULOSE NANOFIBERS FROM CASSAVA PULP

Suranaree University of Technology has approved this thesis submitted in partial fulfillment of the requirements for the Degree of Doctor of Philosophy.

Thesis Examining Committee

Nitinat Suppakarn
(Asst. Prof. Dr. Nitinat Suppakarn)

Chairperson

Yupaporn Chyt
(Assoc. Prof. Dr. Yupaporn Ruksakulpiwat)

Member (Thesis Advisor)

Chaiwat Ruksakulpiwat
(Assoc. Prof. Dr. Chaiwat Ruksakulpiwat)

Member

Wimonlak Sutapun
(Asst. Prof. Dr. Wimonlak Sutapun)

Member

Kasama Jarukumjorn
(Assoc. Prof. Dr. Kasama Jarukumjorn)

Member

Pranee Chumsamrong
(Asst. Prof. Dr. Pranee Chumsamrong)

Member

Ittipol Jangchud
(Assoc. Prof. Dr. Ittipol Jangchud)

Member

Kontorn Chamniprasart
(Assoc. Prof. Flt. Lt. Dr. Kontorn Chamniprasart)

Sukit Limpijumngong
(Prof. Dr. Sukit Limpijumngong)

Vice Rector for Academic Affairs
and Innovation

Dean of Institute of Engineering

ทันน์ ชิ เหงียน : คอมโพสิตชีวภาพของพอลิแลคติกแอซิดและเส้นใยนาโนเซลลูโลสจากกาก
มันสำปะหลัง (BIOCOMPOSITES OF POLY(LACTIC ACID) AND CELLULOSE
NANOFIBERS FROM CASSAVA PULP) อาจารย์ที่ปรึกษา : รองศาสตราจารย์
ดร.ยุพาพร รักสกุลพิวัฒน์, 281 หน้า.

ในการศึกษานี้ เส้นใยนาโนเซลลูโลสใช้เป็นสารตัวเติมในคอมพอสิตของพอลิแลคติกแอซิดและเส้นใยนาโนเซลลูโลส เส้นใยนาโนเซลลูโลสที่มีเส้นผ่านศูนย์กลางในช่วง 12-24 นาโนเมตรแต่ความยาวไม่สามารถวัดได้ สกัดได้จากกากมันสำปะหลังโดยกระบวนการอัลคาไลน์ การฟอก และกระบวนการไฮโดรไลซิสด้วยกรด กระบวนการไฮโดรไลซิสด้วยกรดทำโดยใช้กรดไฮโดรคลอริกและกรดซัลฟูริกในอัตราส่วน 1:2 โดยปริมาตร พบว่าปริมาณผลึกของเส้นใยนาโนเซลลูโลสเพิ่มขึ้นอย่างมีนัยสำคัญ โดยไม่สูญเสียความเสถียรทางความร้อน ความเข้มข้นของกรด อัตราส่วนระหว่างกรดต่อกากมันสำปะหลัง และเวลาในการไฮโดรไลซิสมีค่าเท่ากับ 6.5 โมลต่อลิตร 150 มิลลิเมตรต่อ 2 กรัม และ 60 นาที ตามลำดับ

เทคนิคการวัดการกระเจิงของรังสีเอ็กซ์ที่มุมเล็กโดยแสงซินโครตรอน ใช้ในการศึกษาผลของปริมาณเส้นใยนาโนเซลลูโลสต่อพฤติกรรมการเกิดผลึกของคอมพอสิตระหว่างพอลิแลคติกแอซิดและเส้นใยนาโนเซลลูโลส นอกจากนี้ยังศึกษาผลของปริมาณเส้นใยนาโนเซลลูโลสต่อสมบัติเชิงกล สัมฐานวิทยาและสมบัติเชิงความร้อนของพอลิเมอร์คอมพอสิต ผลจากการวัดการกระเจิงของรังสีเอ็กซ์ที่มุมเล็กโดยแสงซินโครตรอน พบว่าการเติมเส้นใยนาโนเซลลูโลสจะทำให้อัตราเร็วในการเกิดผลึกเพิ่มขึ้น แต่อย่างไรก็ตาม เมื่อเพิ่มปริมาณเส้นใยนาโนเซลลูโลสจาก 0.1 ไป 0.5 เปอร์เซ็นต์โดยน้ำหนัก ไม่ได้มีผลต่อการเปลี่ยนแปลงอัตราเร็วในการเกิดผลึกของคอมพอสิต ค่าความต้านทานแรงกระทำของคอมพอสิตระหว่างพอลิแลคติกแอซิดและเส้นใยนาโนเซลลูโลสสูงกว่าพอลิแลคติกแอซิดอย่างเห็นได้ชัด แต่ค่าความต้านทานการดึงยึด ค่าความยืดสูงสุด ณ จุดขาดและความเสถียรต่อความร้อนของคอมพอสิตระหว่างพอลิแลคติกแอซิดและเส้นใยนาโนเซลลูโลส ไม่เปลี่ยนแปลงอย่างมีนัยสำคัญเมื่อเทียบกับพอลิแลคติกแอซิด ค่าความต้านทานแรงกระทำของคอมพอสิตระหว่างพอลิแลคติกแอซิดและเส้นใยนาโนเซลลูโลสลดลงเมื่อปริมาณเส้นใยนาโนเซลลูโลสสูงขึ้นในขณะที่ความเสถียรทางความร้อน ไม่เปลี่ยนแปลง

ในงานวิจัยนี้ประสบความสำเร็จในการกราฟท์ไกลซิซิลเมทาคริเลทบนพอลิแลคติกแอซิดโดยการหลอมผสมในเครื่องบดผสมภายใน ปริมาณของไกลซิซิลเมทาคริเลท 10% โดยน้ำหนักและเวลาในการผสม 10 นาทีเป็นสภาวะที่เหมาะสมในการเตรียมพอลิแลคติกแอซิดกราฟท์ด้วยไกลซิซิลเมทาคริเลท พบว่าค่าความยืดสูงสุด ณ จุดขาดและค่าความต้านทานแรงกระทำของพอลิแลคติกแอซิดกราฟท์ด้วยไกลซิซิลเมทาคริเลทมีค่าสูงกว่าพอลิแลคติกแอซิด

พอลิแลคติกแอซิดกราฟท์ด้วยไกลซิซิลเมทาคริเลทใช้เป็นตัวเชื่อมประสานที่มีประสิทธิภาพสำหรับคอมพอลิทีระหว่างพอลิแลคติกแอซิดและเส้นใยนาโนเซลลูโลส การใส่พอลิแลคติกแอซิดกราฟท์ด้วยไกลซิซิลเมทาคริเลทช่วยปรับปรุงการกระจายตัวของเส้นใยนาโนเซลลูโลส และการเพิ่มการยึดติระหว่างผิวหนังของพอลิแลคติกแอซิดและเส้นใยนาโนเซลลูโลส อัตราเร็วของการเกิดผลึกของคอมพอลิทีระหว่างพอลิแลคติกแอซิดและเส้นใยนาโนเซลลูโลสที่ใส่พอลิแลคติกแอซิดกราฟท์ด้วยไกลซิซิลเมทาคริเลท ยังสูงขึ้นเมื่อเทียบกับที่ไม่ใส่ตัวเชื่อมประสาน นอกจากนี้ การใส่พอลิแลคติกแอซิดกราฟท์ด้วยไกลซิซิลเมทาคริเลทในคอมพอลิทีส่งผลให้มีการเพิ่มขึ้นของค่าความต้านทานแรงกระแทก และค่าความต้านทานการดึงยืดและค่าความยืดสูงสุด ณ จุดขาดมีค่าเพิ่มขึ้นเล็กน้อย



มหาวิทยาลัยเทคโนโลยีสุรนารี

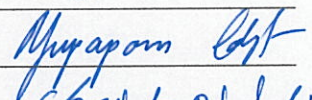
สาขาวิชา วิศวกรรมพอลิเมอร์

ปีการศึกษา 2559

ลายมือชื่อนักศึกษา

ลายมือชื่ออาจารย์ที่ปรึกษา

ลายมือชื่ออาจารย์ที่ปรึกษาร่วม



THANH CHI NGUYEN : BIOCOMPOSITES OF POLY(LACTIC ACID) AND
CELLULOSE NANOFIBERS FROM CASSAVA PULP.

THESIS ADVISOR : ASSOC. PROF. YUPAPORN RUKSAKULPIWAT, Ph.D.,
281 PP.

POLYLACTIC ACID/CASSAVA PULP/CELLULOSE NANOFIBERS/PLA-g-
GMA/COMPOSITES

In this study, cellulose nanofibers (CNFs) were used as fillers in PLA/CNFs composites. CNFs with a diameter in the range of 12-24 nm and immeasurable length were extracted successfully from cassava pulp (CP) by submitting to alkali, bleaching, and acid hydrolysis treatments. In the acid hydrolysis treatment, by using a mixture of HCl/H₂SO₄ (1:2 v/v) as the hydrolysis reagent, a significant enhancement in degree of crystallinity without considerable loss in thermal stability of cellulose nanofibers was obtained. With the same acid type (HCl/H₂SO₄ (1:2 v/v)), the appropriate acid concentration, acid/pulp ratio, and hydrolysis time for the acid hydrolysis treatment of cassava pulp was 6.5 M, 150ml/2g, and 60 min, respectively.

Effects of CNFs content on the crystallization behavior of PLA/CNFs composites were studied by synchrotron small angle X-ray scattering (SAXS) technique. In addition, mechanical, morphological, and thermal properties of composites were also investigated. The SAXS results showed that with the addition of CNFs, the crystallization rate of composites slightly increased. However, increasing fiber content from 0.1 to 0.5 wt% did not result in a considerable change in the crystallization rate of PLA/CNFs composites. A notable improvement in impact strength of PLA/CNFs composites in relation to that of neat

PLA was observed. Nevertheless, the tensile strength, elongation at break, and thermal stability of PLA/CNFs composites did not change significantly compared to those of PLA. The impact strength of PLA/CNFs composites decreased with increasing CNFs content while the thermal stability of composites was not influenced significantly by CNFs content.

Glycidyl methacrylate (GMA) was successfully grafted onto poly (lactic acid) (PLA) by melt mixing method in an internal mixer. The GMA content of 10 wt% and the mixing time of 10 min were suitable for preparation of the graft copolymer. The elongation at break and impact strength of glycidyl methacrylate grafted poly (lactic acid) (PLA-g-GMA) were significantly higher than those of neat PLA.

PLA-g-GMA was used as an effective compatibilizer for PLA/CNFs composites. With the addition of PLA-g-GMA, the better dispersion of CNFs, as well as the enhanced interfacial adhesion between CNFs and PLA could be observed. The crystallization rate of PLA in PLA/PLA-g-GMA/CNFs composites was enhanced considerably compared to that of neat PLA and PLA/CNFs composites. Moreover, PLA/PLA-g-GMA/CNFs composites revealed the improved impact strength. Meanwhile, the tensile strength and elongation at break of composites were slightly improved with the addition of PLA-g-GMA.

School of Polymer Engineering

Academic Year 2016

Student's Signature _____

Advisor's Signature _____

Co-Advisor's Signature _____

ACKNOWLEDGEMENTS

I am grateful to the SUT-PhD Scholarship for Asian Countries Program of the Suranaree University of Technology, Thailand for the financial support and Siam Synchrotron Light Research Institute for the SAXS instrument.

I would like to express my sincere gratitude to my thesis advisor, Assoc. Prof. Dr. Yupaporn Ruksakulpiwat, for her valuable advice, support, encouragement, and kindness throughout my study at the Suranaree University of Technology. Moreover, the grateful appreciation is given to Assoc. Prof. Dr. Chaiwat Ruksakulpiwat, my co-advisor for his advice and support during my research work. Also, I would like to thank my academic advisor Asst. Prof. Dr. Nitinat Suppakarn, for her guidance during my 1st year study. In addition, my gratitude is expressed to Asst. Prof. Dr. Wimonlak Sutapun, Assoc. Prof. Dr. Kasama Jarukumjorn, Asst. Prof. Dr. Pranee Chumsamrong, and Assoc. Prof. Dr. Ittipol Jangchud, for their valuable suggestions and guidance as committee members.

Many thanks go to lecturers and staff members of the School of Polymer Engineering and the Center for Scientific and Technological Equipment of the Suranaree University of Technology for their help throughout the period of my study.

Finally, I would deeply like to thank my parents, siblings, and friends, for their support and encouragement during my Ph.D. course at the Suranaree University of Technology, Thailand.

Thanh Chi Nguyen

TABLE OF CONTENTS

	Page
ABSTRACT (THAI)	I
ABSTRACT (ENGLISH).....	III
ACKNOWLEDGEMENTS	V
TABLE OF CONTENTS.....	VI
LIST OF TABLES	XIII
LIST OF FIGURES	XV
SYMBOLS AND ABBREVIATIONS.....	XXVII
CHAPTER	
I INTRODUCTION	1
1.1 General background	1
1.2 Research objectives.....	5
1.3 Scopes and limitations of the Study.....	5
1.4 References	7
II LITERATURE REVIEWS	10
2.1 Cassava pulp (CP).....	10
2.2 Cellulose nanofibers (CNFs).....	11
2.3 Challenges in the production of cellulose nanofibers	17
2.4 Potential applications of crystalline cellulose nanofibers	19

TABLE OF CONTENTS (Continued)

	Page
2.5 Preparation of crystalline cellulose nanofibers	21
2.6 Chemical modification of crystalline cellulose nanofibers	28
2.7 Poly(lactic acid) (PLA)	30
2.8 Crystallization behavior of PLA	35
2.9 Graft copolymer	37
2.10 Cellulose nanofibers (CNFs) reinforced PLA-based composites	44
2.11 Effect of cellulose nanofibers on physical properties of PLA-based composites	47
2.12 References	50
III EXTRACTION OF CRYSTALLINE CELLULOSE FIBERS FROM CASSAVA PULP	60
3.1 Abstract	60
3.2 Introduction	61
3.3 Experimental	63
3.3.1 Materials	63
3.3.2 Preparation of crystalline cellulose fibers from cassava pulp	63
3.3.3 Characterization of crystalline cellulose fibers	64
3.4 Results and discussion	66
3.4.1 Morphological characterization of crystalline cellulose fibers	66
3.4.2 Chemical composition	67

TABLE OF CONTENTS (Continued)

	Page
3.4.3 X-ray diffraction analysis	69
3.4.4 FTIR spectroscopy analysis	70
3.4.5 Thermal stability	72
3.4.6 Effect of hydrolysis temperature on the crystallinity and thermal stability of obtained crystalline cellulose fibers	73
3.4.7 Effect of hydrolysis time on the crystallinity and thermal stability of obtained crystalline cellulose fibers	75
3.5 Conclusions	78
3.6 References	79
IV EXTRACTION OF CELLULOSE MICROFIBERS FROM CASSAVA PULP	83
4.1 Abstract	83
4.2 Introduction	84
4.3 Experimental	86
4.3.1 Materials	86
4.3.2 Preparation of cellulose microfibrils from cassava pulp	86
4.3.3 Characterization of cellulose microfibrils	87
4.4 Results and discussion	89
4.4.1 Morphological analysis of the fibers	89
4.4.2 Chemical composition of fibers	94

TABLE OF CONTENTS (Continued)

	Page
4.4.3 X-ray diffraction analysis	96
4.4.4 FTIR spectroscopy analysis	99
4.4.5 Thermal stability	100
4.5 Conclusions	102
4.6 References	104
 V EXTRACTION OF CELLULOSE NANOFIBERS	
FROM CASSAVA PULP	107
5.1 Abstract	107
5.2 Introduction	108
5.3 Materials and methods	111
5.3.1 Materials	111
5.3.2 Preparation of cellulose nanofibers	111
5.3.3 Characterization	113
5.4 Results and discussion	115
5.4.1 Chemical composition of fibers	115
5.4.2 Morphological investigation of the fibers	116
5.4.3 X-ray diffraction (XRD)	117
5.4.4 Spectroscopic analysis (FTIR)	121
5.4.5 Thermal stability	124

TABLE OF CONTENTS (Continued)

	Page
5.4.6 Effect of acid types on crystallinity and thermal stability of obtained cellulose nanofibers	126
5.4.7 Effect of acid/pulp ratio on crystallinity and thermal stability of obtained cellulose nanofibers	130
5.4.8 Effect of hydrolysis time on crystallinity and thermal stability of obtained cellulose nanofibers	133
5.4.9 Effect of acid concentration on crystallinity and thermal stability of obtained cellulose nanofibers	136
5.5 Conclusions	139
5.6 References	140
VI GLYCIDYL METHACRYLATE GRAFTED POLY(LACTIC ACID)	145
6.1 Abstract	145
6.2 Introduction	146
6.3 Materials and methods	150
6.3.1 Materials	150
6.3.2 Preparation of PLA-g-GMA	150
6.3.3 Purification of prepared PLA-g-GMA	151
6.3.4 Characterization of PLA-g-GMA	151
6.4 Results and discussion	154

TABLE OF CONTENTS (Continued)

	Page
6.4.1 Characterization of glycidyl methacrylate grafted poly (lactic acid)	154
6.4.2 Effect of GMA content on GMA grafting and physical properties of PLA-g-GMA	163
6.4.3 Effect of mixing time on GMA grafting and physical properties of PLA-g-GMA	173
6.5 Conclusions	181
6.6 References	182
VII BIOCOMPOSITES OF POLY(LACTIC ACID) AND CELLULOSE	
NANOFIBERS FROM CASSAVA PULP	186
7.1 Abstract	186
7.2 Introduction	187
7.3 Materials and methods	191
7.3.1 Materials	191
7.3.2 Preparation of PLA composites	191
7.3.3 Characterization	192
7.4 Results and discussion	198
7.4.1 Morphological properties	198
7.4.2 Isothermal crystallization behavior by SAXS	201

TABLE OF CONTENTS (Continued)

	Page
7.4.3 Effect of PLA-g-GMA and fiber content on the crystallization behavior of PLA/CNFs composites	211
7.4.4 Thermal properties	218
7.4.5 Mechanical properties	225
7.5 Conclusions	231
7.6 References	232
VIII CONCLUSIONS	239
APPENDICES	
APPENDIX A. Chemical composition, crystallinity index of cassava pulp and treated fibers, and full-range ¹³ C-NMR spectra of GMA and PLA-g-GMA	243
APPENDIX B. Publications	254
BIOGRAPHY	281

LIST OF TABLES

Table	Page
2.1 Composition of cassava pulp	11
3.1 The chemical composition of untreated cassava pulp and acid treated fibers ...	68
3.2 Crystallinity index of untreated cassava pulp and acid treated fibers	69
3.3 Crystallinity index of acid treated fibers at different hydrolysis temperatures ..	74
3.4 Crystallinity index of acid treated fibers at different hydrolysis times	77
4.1 The chemical composition of untreated cassava pulp and treated fibers at various stages of treatment	96
4.2 Crystallinity index of untreated cassava pulp and treated fibers at various stages of treatment	97
5.1 The chemical composition of untreated cassava pulp and treated fibers at each stage of treatment	116
5.2 Crystallinity index (CI) of cassava pulp fibers at different stages of treatment	121
5.3 Crystallinity index (CI) of cellulose nanofibers extracted using three different types of acid	127
5.4 Crystallinity index (CI) of cellulose nanofibers at various acid/pulp ratios	131
5.5 Crystallinity index (CI) of cellulose nanofibers at various hydrolysis times ...	135
5.6 Crystallinity index (CI) of cellulose nanofibers at various acid concentrations	137

LIST OF TABLES (Continued)

Table	Page
6.1	The weight-average molecular weights (\bar{M}_w), the number-average molecular weights (\bar{M}_n), and the polydispersity index (PDI) of PLA and PLA-g-GMA. [GMA]=10 wt%, mixing time = 10 min.....
	158
6.2	MFI of pure PLA and PLA-g-GMA, [GMA] =10 wt%, mixing time = 10 min
	160
6.3	The relative area of characteristic peaks of PLA and GMA calculated from $^1\text{H-NMR}$ spectra of PLA-g-GMA at various GMA contents, mixing time = 10 min
	164
6.4	Thermal properties of pure PLA and PLA-g-GMA at different GMA contents, mixing time = 10 min
	173
6.5	The relative area of characteristic peaks of GMA and PLA calculated from $^1\text{H-NMR}$ spectra of PLA-g-GMA at various mixing times
	174
6.6	Thermal properties of PLA and PLA-g-GMA at different mixing times, [GMA] = 10 wt%
	181
7.1	Composition of composites
	192
7.2	Thermal properties of the pure PLA, PLA-g-GMA, and composites with different fiber contents.....
	225

LIST OF FIGURES

Figure	Page
2.1 Basic chemical structure of cellulose showing the cellobiose repeating unit	12
2.2 Polymorphs of cellulose and the main steps to obtain them	14
2.3 Acid hydrolysis breaks down disordered (amorphous) regions and isolates nanocrystals	21
2.4 Red circles demonstrate potential sites of hydrolysis. Regions of high crystallinity possess fewer sites and therefore take longer to be broken down	22
2.5 Scheme of main steps needed to prepare CCNFs from lignocellulosic biomass	24
2.6 Schematic diagram illustrating the various types of chemical modifications on cellulose nanofibers surface	29
2.7 Single step process for cellulose hydrolysis and esterification of hydroxyl groups using a mixture of acetic and hydrochloric acid	30
2.8 Two enantiomeric forms of lactic acid: (<i>S</i>)- and (<i>R</i>)-2-hydroxypropionic acid	31
2.9 The three diastereomeric structures of lactide (3,6-dimethyl-1,4-dioxane-2,5-dione)	32
2.10 Synthesis methods for high-molecular-weight PLA	34
2.11 The represent structure of graft copolymer	37

LIST OF FIGURES (Continued)

Figure	Page
2.12 Proposed reaction pathway for the grafting reaction of GMA to PCL	40
2.13 Mechanism of the grafting of GMA onto the PLA chain	43
3.1 SEM micrographs of untreated cassava pulp (a) and acid treated fibers (b)	67
3.2 Transmission electron micrograph from diluted suspension of acid treated fibers	68
3.3 X-ray diffraction patterns of untreated cassava pulp (a) and acid treated fibers (b)	70
3.4 FTIR spectra of untreated cassava pulp (a) and acid treated fibers (b)	71
3.5 TGA curves of untreated cassava pulp and acid treated fibers	72
3.6 X-ray diffraction patterns of (a) untreated cassava pulp, (b) CCFs-50, (c) CCFs-70, and (d) CCFs-60	74
3.7 TGA curves of untreated cassava pulp and acid treated fibers at different hydrolysis temperatures	75
3.8 X-ray diffraction patterns of (a) untreated cassava pulp, (b) CCFs-30min, (c) CCFs-45min, and (d) CCFs-60min	76
3.9 TGA curves of untreated cassava pulp and acid treated fibers at different hydrolysis times	78
4.1 SEM micrographs of untreated cassava pulp (a) and acid treated fibers at 50 °C (b), 60 °C (c), and 70 °C (d)	91
4.2 SEM images of alkali treated fibers for 2 h (a), 3 h (b), and 4 h (c)	92

LIST OF FIGURES (Continued)

Figure	Page
4.3 SEM images of alkali-acid treated fibers (a) and acid-alkali treated fibers (b)	94
4.4 3D AFM image of obtained cellulose microfibrils	94
4.5 X-ray diffraction patterns of untreated cassava pulp (a), alkali treated fibers (b), acid treated fibers (c), acid-alkali treated fibers (d), and alkali-acid treated fibers (e)	98
4.6 FTIR spectra of cassava pulp (a), alkali treated fibers (b), and acid treated fibers (c)	98
4.7 FTIR spectra of cassava pulp (a), acid-alkali treated fibers (b), and alkali-acid treated fibers (c)	99
4.8 TGA curves of raw cassava pulp and treated fibers at various stages of treatment	102
5.1 Scanning electron micrographs of (a) cassava pulp, (b) alkali-treated fibers, and (c) bleached-treated fibers	119
5.2 (a) Transmission electron micrograph from diluted suspension of cellulose nanofibers, (b) diameter distribution of obtained cellulose nanofibers	120
5.3 X-ray diffraction patterns of (a) raw, (b) alkali treated, (c) bleached, and (d) acid hydrolyzed cassava pulp	121
5.4 FTIR spectra of (a) raw, (b) alkali treated, (c) bleached, and (d) acid hydrolyzed cassava pulp	124

LIST OF FIGURES (Continued)

Figure	Page
5.5 TGA and DTG curves of raw, alkali treated, bleached, and acid hydrolyzed cassava pulp	126
5.6 X-ray diffraction patterns of (a) raw cassava pulp, (b) CNFs-H, (c) CNFs-HS, and (d) CNFs-S	128
5.7 TGA and DTG curves of raw cassava pulp and cellulose nanofibers extracted using three different types of acid	129
5.8 X-ray diffraction patterns of (a) raw cassava pulp, (b) CNFs-100ml/2g, (c) CNFs-150ml/2g, and (d) CNFs-200ml/2g	131
5.9 TGA and DTG curves of raw cassava pulp and cellulose nanofibers at various acid/fiber ratios	132
5.10 X-ray diffraction patterns of (a) raw cassava pulp, (b) CNFs-30min, (c) CNFs-90min, and (d) CNFs-60min	135
5.11 TGA and DTG curves of raw cassava pulp and cellulose nanofibers at various hydrolysis times	136
5.12 X-ray diffraction patterns of (a) raw cassava pulp, (b) CNFs-5.5M, (c) CNFs-6.5M, and (d) CNFs-7.5M	137
5.13 TGA and DTG curves of raw cassava pulp and cellulose nanofibers at various acid concentrations	139
6.1 Mechanism of the grafting of GMA onto the PLA chain	149

LIST OF FIGURES (Continued)

Figure	Page
6.2 FTIR spectra of pure PLA and PLA-g-GMA, [GMA] = 10 wt%, mixing time = 10 min.....	155
6.3 ¹ H-NMR spectra of PLA, GMA and PLA-g-GMA, [GMA] = 10 wt%, mixing time = 10 min.....	156
6.4 ¹³ C-NMR spectra of pure PLA, GMA and PLA-g-GMA, [GMA] = 10 wt%, mixing time = 10 min.....	157
6.5 Gel permeation chromatogram of PLA and PLA-g-GMA, [GMA] = 10 wt%, mixing time = 10 min	159
6.6 Shear viscosity of pure PLA and PLA-g-GMA at various shear rates. [GMA] = 10 wt%, mixing time = 10 min	160
6.7 XRD patterns of PLA and PLA-g-GMA before and after the tensile test, [GMA] = 10 wt%, mixing time = 10 min	162
6.8 SEM images of tensile fractured surface of pure PLA (a) and PLA-g-GMA (b), [GMA] =10 wt%, mixing time = 10 min	162
6.9 Effect of GMA monomer content on GMA grafting yield, mixing time = 10 min	163
6.10 Effect of GMA monomer content on GMA grafting efficiency, mixing time = 10 min	165
6.11 Stress-strain curves of pure PLA and PLA-g-GMA at different GMA contents, mixing time = 10 min	166

LIST OF FIGURES (Continued)

Figure	Page
6.12 Effect of GMA content on tensile strength of PLA-g-GMA, mixing time = 10 min	167
6.13 Effect of GMA content on elongation at break of PLA-g-GMA, mixing time = 10 min	168
6.14 Effect of GMA content on impact strength of PLA-g-GMA, mixing time = 10 min	169
6.15 DSC thermograms of PLA and PLA-g-GMA at different GMA contents (cooling scan), mixing time = 10 min	170
6.16 DSC thermograms of PLA and PLA-g-GMA at various GMA contents (second heating scan), mixing time = 10 min	172
6.17 Effect of mixing time on GMA grafting yield, [GMA] = 10 wt%	175
6.18 Stress-strain curves of pure PLA and PLA-g-GMA at various mixing times, [GMA] = 10 wt%	176
6.19 Effect of mixing time on tensile strength of PLA-g-GMA, [GMA] = 10 wt%	176
6.20 Effect of mixing time on elongation at break of PLA-g-GMA, [GMA] = 10 wt%	177
6.21 Effect of mixing time on impact strength of PLA-g-GMA, [GMA] = 10 wt%	178

LIST OF FIGURES (Continued)

Figure	Page
6.22 DSC thermograms of PLA and PLA-g-GMA at various mixing times (cooling scan), [GMA] = 10 wt%	180
6.23 DSC thermograms of PLA and PLA-g-GMA at various mixing times (second heating scan), [GMA] = 10 wt%	180
7.1 Schematic diagram of the SAXS BL1.3W beamline	193
7.2 SEM micrographs of the tensile fractured surfaces of pure PLA (a), PLA/CNFs0.1 (b), PLA/CNFs0.3 (c), PLA/CNFs0.5 (d), PLA/PLA-g-GMA/CNFs0.1 (e), PLA/PLA-g-GMA/CNFs0.3 (f), and PLA/PLA-g-GMA/CNFs0.5 (g)	200
7.3 Detailed view of the tensile fractured surfaces of PLA/CNFs0.5 (a) and PLA/PLA-g-GMA/CNFs0.5 (b) composites showing the interfacial adhesion between fibers and PLA matrix	201
7.4 Lorentz-corrected SAXS profiles of pure PLA, PLA-g-GMA, and PLA/PLA-g-GMA/CNFs0.1 composite obtained at 200 °C. The insets show the 2D-SAXS patterns of these samples	202
7.5 Lorentz-corrected SAXS profiles of pure PLA, PLA-g-GMA, and PLA/PLA-g-GMA/CNFs0.1 composite obtained at 120 °C after 5 min of crystallization time. The insets show the 2D-SAXS patterns of these samples	203

LIST OF FIGURES (Continued)

Figure	Page
7.6 Lorentz-corrected SAXS profiles of pure PLA, PLA-g-GMA, and PLA/PLA-g-GMA/CNFs0.1 composite obtained at 120 °C after 10 min of crystallization time. The insets show the 2D-SAXS patterns of these samples	204
7.7 Lorentz-corrected SAXS profiles of pure PLA, PLA-g-GMA, and PLA/PLA-g-GMA/CNFs0.1 composite obtained at 120 °C after 20 min of crystallization time. The insets show the 2D-SAXS patterns of these samples	205
7.8 Lorentz-corrected SAXS profiles of pure PLA, PLA-g-GMA, and PLA/PLA-g-GMA/CNFs0.1 composite obtained at 120 °C after 30 min of crystallization time. The insets show the 2D-SAXS patterns of these samples	206
7.9 Lorentz-corrected SAXS profiles of pure PLA, PLA-g-GMA, and PLA/PLA-g-GMA/CNFs0.1 composite obtained at 120 °C after 40 min of crystallization time. The insets show the 2D-SAXS patterns of these samples	207
7.10 Lorentz-corrected SAXS profiles of pure PLA, PLA-g-GMA, and PLA/PLA-g-GMA/CNFs0.1 composite obtained at 120 °C after 50 min of crystallization time. The insets show the 2D-SAXS patterns of these samples	208

LIST OF FIGURES (Continued)

Figure	Page
7.11 Lorentz-corrected SAXS profiles of pure PLA, PLA-g-GMA, and PLA/PLA-g-GMA/CNFs0.1 composite obtained at 120 °C after 60 min of crystallization time. The insets show the 2D-SAXS patterns of these samples	208
7.12 The plot of the changes of maximum Iq^2 versus <i>crystallization time</i> of PLA, PLA-g-GMA, and PLA/PLA-g-GMA/CNFs0.1 composite	209
7.13 The SAXS curves from the experimental data and fitting results using the paracrystalline model of PLA, PLA-g-GMA, and PLA/PLA-g-GMA/CNFs0.1 composites at 120 °C after 20 min of crystallization time.....	210
7.14 Crystallization time dependence of the average long period (L) and lamellar thickness (L_c) of PLA, PLA-g-GMA, and PLA/PLA-g- GMA/CNFs0.1 composites crystallized at 120 °C	211
7.15 Lorentz-corrected SAXS profiles of PLA/CNFs composites with various fiber contents obtained at 120 °C at 0 min of crystallization time. The insets show the 2D-SAXS patterns of the respective samples	212

LIST OF FIGURES (Continued)

Figure	Page
7.16 Lorentz-corrected SAXS profiles of PLA/CNFs composites with various fiber contents obtained at 120 °C after 5 min of crystallization time. The insets show the 2D-SAXS patterns of the respective samples	213
7.17 Lorentz-corrected SAXS profiles of PLA/CNFs composites with various fiber contents obtained at 120 °C after 10 min of crystallization time. The insets show the 2D-SAXS patterns of the respective samples	214
7.18 Lorentz-corrected SAXS profiles of PLA/PLA-g-GMA/CNFs composites with various fiber contents obtained at 120 °C at 0 min of crystallization time. The insets show the 2D-SAXS patterns of the respective samples	214
7.19 Lorentz-corrected SAXS profiles of PLA/PLA-g-GMA/CNFs composites with various fiber contents obtained at 120 °C after 5 min of crystallization time. The insets show the 2D-SAXS patterns of the respective samples	215
7.20 Lorentz-corrected SAXS profiles of PLA/PLA-g-GMA/CNFs composites with various fiber contents obtained at 120 °C after 10 min of crystallization time. The insets show the 2D-SAXS patterns of the respective samples	217

LIST OF FIGURES (Continued)

Figure	Page
7.21 The plot of the changes of maximum Iq^2 versus <i>crystallization time</i> of PLA/CNFs and PLA/PLA-g-GMA/CNFs composites with various fiber loadings	218
7.22 TGA and DTG curves of pure PLA and PLA/CNFs composites with different fiber loadings	220
7.23 TGA and DTG curves of pure PLA, PLA/CNFs0.5, and PLA/PLA-g-GMA/CNFs0.5 composites	220
7.24 TGA and DTG curves of pure PLA and PLA/PLA-g-GMA/CNFs composites with different fiber loadings	221
7.25 DSC thermograms of PLA and composites with various fiber loadings (cooling cycle)	222
7.26 DSC thermograms of PLA and composites with various fiber loadings (second heating cycle)	224
7.27 Tensile modulus of PLA, PLA-g-GMA, and composites with different fiber loadings	226
7.28 Tensile strength of PLA, PLA-g-GMA, and composites with different fiber loadings	228
7.29 Elongation at break of PLA, PLA-g-GMA, and composites with different fiber loadings	229

LIST OF FIGURES (Continued)

Figure	Page
7.30 Impact strength of PLA, PLA-g-GMA, and composites with different fiber loadings	230



SYMBOLS AND ABBREVIATIONS

°C	=	Degree Celsius
T	=	Temperature
%	=	Percent
wt	=	Weight
v	=	Volume
μm	=	Micrometer
nm	=	Nanometer
MPa	=	Megapascal
GPa	=	Gigapascal
cal	=	Calorie
kJ	=	Kilojoule
J	=	Joule
L	=	Liter
mL	=	Milliliter
mg	=	Milligram
g	=	Gram
kg	=	Kilogram
m ²	=	Square meter
cm ²	=	Square centimeter
cm ³	=	Cubic centimeter

SYMBOLS AND ABBREVIATIONS (Continued)

cm^{-1}	=	Per centimeter
s	=	Second
min	=	Minute
h	=	Hour
ΔH	=	Heat of fusion
M	=	Mole per liter
rpm	=	Revolutions per minute
CI	=	Crystallinity index
$\% X_c$	=	Degree of crystallinity
Eq.	=	Equation
L	=	Long period
L_c	=	Lamellar thickness

CHAPTER I

INTRODUCTION

1.1 General background

It is known that there has been a surge of interest in the industrial applications of composites containing biofibers. So far, biopolymers have been tremendously used as a matrix for biofiber reinforced composites. One of the most important biodegradable polymers is poly(lactic acid) (PLA), whose monomer unit is derived from renewable natural resources such as starch, sugar, and cellulose. Besides its renewability, biodegradability, and greenhouse gas neutrality, PLA also possesses good mechanical properties and can be easily processed (Garlotta, Doane, Shogren, Lawton, and Willett, 2003). However, PLA is still more expensive than many petroleum-derived commodity plastics. It has some poor physical properties such as slow crystallization rate, high brittleness, and low thermal stability which hinder PLA to be used for various end-use applications (Rudnik, 2010). Hence, incorporation of nano-sized reinforcements within PLA matrix has been considered a promising method to overcome obstacles for the use of PLA (Hong and Kim, 2013).

In order to improve tensile strength and thermal stability of PLA, many studies have been carried out to investigate the addition of natural fibers such as jute fiber (Plackett, Andersen, Pedersen, and Nielsen, 2003), kenaf fibers (Ochi, 2008) and ramie fibers (Tao, Yan, and Jie, 2009) as the reinforcing agents. The results showed that the tensile strength and thermal stability of natural fibers reinforced PLA were

greatly improved. The crystallinity of PLA-based composites was found to be improved with the addition of cellulose nanofibers. It is ascribed to a nucleating agent action of the nanofillers. The cellulose nanofiber-induced crystallization effect is strongly dependent on the composite processing technique, thermal history of the material, as well as shape, surface area and rigidity of the fibers (Lin, Chen, Huang, Dufresne, and Chang, 2009); (Sanchez-Garcia and Lagaron, 2010); (Fortunati et al., 2012). Moreover, the enhancement in the crystallization rate of cellulose nanofibers reinforced PLA composites was also reported (Pei, Zhou, and Berglund, 2010). This improvement is attributed to the heterogeneous nucleating action of the nanofibers, which results in an increase of the overall crystallization rate, reduction of the nucleation induction period and an increase in the number of primary nucleation sites.

Cassava (*Manihot esculenta*) is a root crop largely grown in tropical countries such as Thailand and Brazil. It is a starch-rich material, also containing proteins, lipids, lignocellulosic fibers and sugars. The industrial exploitation of cassava starch involves the elimination of soluble sugars and the separation of fibers resulting in a purified starch and a solid residue called cassava pulp (CP). In addition to residual starch, this material contains 15-50 % cellulose fibers (dry weight basis) (Teixeira et al., 2012). These characteristics suggest the possibility of using the CP as a source for the extraction of CNFs. This not only produces the high-value product but also contributes to solving environmental issues.

In order to produce fully renewable and biodegradable composites, which are the next generation of materials, both the polymer matrix and the reinforcements should be derived from renewable resources (Pandey et al., 2005). The use of cellulose fibers as a reinforcing phase in composites has had numerous well-known

advantages, e.g., low density; renewable nature; high specific properties; modest abrasivity during processing; biodegradability; relatively reactive surface, which can be used for grafting specific groups, and also their useful physical and chemical properties. However, for reinforcement applications, cellulose fibers present some disadvantages, for instance, high moisture absorption, poor wettability, incompatibility with most of the polymer matrices and limitation of processing temperature (Siqueira, Bras, and Dufresne, 2010).

So far, acid hydrolysis process has been considered to be an effective method for the extraction of CNFs from lignocellulosic materials. This method requires the purification treatment for the isolation of cellulose by removing non-cellulosic materials – hemicellulose, lignin, etc. A purification treatment consisting of an alkali treatment with sodium hydroxide (NaOH) or potassium hydroxide (KOH) followed by a bleaching step using acetate buffer (solution of NaOH and glacial acetate acid) and sodium chlorite (NaClO₂). This preliminary step to obtain pure cellulose fibers is crucial and must be done carefully. The alkali extraction is carried out to solubilize most of the hemicelluloses while the bleaching treatment is performed to remove lignin, as well as whiten the materials.

Cellulose fibers are semicrystalline. This means that apart from crystalline domains, cellulose also occurs in an amorphous state. The cellulose amorphous regions are randomly oriented in a spaghetti-like arrangement leading to a lower density compared to crystalline regions (Saxena and Brown, 2005); (de Souza Lima and Borsali, 2004). The amorphous regions act as structural defects which are susceptible to acid attack, and under controlled conditions, they may be removed leaving crystalline regions intact. (de Souza Lima and Borsali, 2004); (Thielemans, Warbey,

and Walsh, 2009). During the acid hydrolysis process, the hydronium ions can penetrate the cellulose chains in the amorphous domains promoting the hydrolytic cleavage of the glycosidic bonds and releasing individual crystallites. It is ascribed to the faster hydrolysis kinetics of amorphous domains compared to crystalline ones. From this process, cellulose nanofibers can be released and extracted from the lignocellulosic materials.

One of the main drawbacks of PLA-based composites reinforced with cellulose fibers is the incompatibility between hydrophilic cellulose fibers and hydrophobic non-polar PLA matrix. This leads to the poor dispersion of CNFs in PLA matrix, as well as the poor adhesion at fiber-matrix interface, which results in low mechanical properties of cellulose fibers reinforced PLA-based composites (Lu, Askeland, and Drzal, 2008).

Up to now, there have been many methods used to overcome the problem above such as using a compatibilizer, modifying the surface of fibers to make them less hydrophilic and modifying hydrophobic PLA matrix to make it more hydrophilic, thus adhering better with cellulose fibers. So far, various cellulose surface modification techniques including silylation, TEMPO oxidation, acetylation and the use of surfactants have been researched to create possibilities for combining cellulose nanofibers with PLA. However, the mechanical properties of the resulting composites are not high as expected and the process is time consuming and very expensive. In addition, surface modification of CNFs can negatively affect biodegradation of the final composites (Qu, Gao, Wu, and Zhang, 2010).

With its dual functionality consisting of epoxy and acrylic groups, glycidyl methacrylate (GMA) has been increasingly used as a grafting monomer. GMA grafted polymers have been used as reactive compatibilizers in cellulose fibers reinforced

polyester composites (Fortunati, Puglia, Kenny, Haque, and Pracella, 2013). It is usually believed that epoxy groups of GMA can react with the hydroxyl groups of cellulose fibers. Therefore, it is expected that the PLA-CNFs adhesion and the dispersion of cellulose nanofibers in PLA matrix can be improved by using glycidyl methacrylate grafted poly(lactic acid) (PLA-g-GMA) as a compatibilizer.

1.2 Research objectives

The main objectives of this research can be classified as follows:

- (i) To study the extraction of cellulose nanofibers from cassava pulp.
- (ii) To study the effects of reaction conditions on properties of obtained cellulose nanofibers.
- (iii) To study the preparation of glycidyl methacrylate grafted poly(lactic acid) (PLA-g-GMA).
- (iv) To study the effects of cellulose nanofibers (CNFs) on properties of PLA/CNFs composites.
- (v) To study the effects of PLA-g-GMA on properties of PLA/CNFs composites.

1.3 Scopes and limitations of the study

Crystalline cellulose fibers were directly extracted from cassava pulp without any purification by using sulfuric acid hydrolysis treatment. The influences of hydrolysis temperature and time on the crystallinity and thermal stability of obtained fibers were studied. Cellulose microfibers were prepared from cassava pulp by submitting to alkali and acid treatment. The alkali and acid treatments of cassava pulp

were carried out by using NaOH and HCl solutions, respectively. The effects of reaction sequence for these chemical treatments on physical properties of obtained cellulose microfibers were investigated. Cellulose nanofibers were extracted from cassava pulp by acid hydrolysis method. With this method, cassava pulp was treated by alkali treatment, bleaching treatment and acid hydrolysis treatment. The alkali treatment of cassava pulp was performed by using NaOH solution. The bleaching treatment was carried out by using acetate buffer (NaOH and glacial acetic acid) and aqueous chlorite (NaClO_2). Meanwhile, three different types of acid (HCl, a mixture of HCl/ H_2SO_4 (1:2 v/v) and H_2SO_4) were used in the acid hydrolysis process. The effects of acid concentration, acid/pulp ratio, and hydrolysis time on the crystallinity and thermal stability of fibers were studied. The morphological structures of the ensuing fibers were investigated by scanning electron microscopy (SEM), transmission electron microscopy (TEM) and atomic force microscopy (AFM). The chemical composition of fibers was determined by NDF, ADF and ADL methods. Chemical structure, degree of crystallinity and thermal stability of fibers were investigated by Fourier transform infrared (FTIR) spectroscopy, X-ray diffraction (XRD) and thermogravimetric analysis (TGA), respectively. Glycidyl methacrylate grafted poly(lactic acid) (PLA-g-GMA) was prepared by melt mixing in an internal mixer using dicumyl peroxide (DCP) as an initiator. The influences of GMA content and mixing time on physical properties of PLA-g-GMA were investigated. The chemical structures of PLA-g-GMA were characterized by ^1H nuclear magnetic resonance spectroscopy ($^1\text{H-NMR}$), ^{13}C nuclear magnetic resonance spectroscopy ($^{13}\text{C-NMR}$) and FTIR. Molecular weights and polydispersity index (PDI) of PLA-g-GMA were determined by gel permeable chromatography (GPC). The rheological

properties of PLA-g-GMA were studied using capillary rheometer and melt flow indexer. The PLA/CNFs composites were melt blended using an internal mixer. The effects of CNFs and CNFs content on the crystallization behavior and mechanical, morphological and thermal properties of PLA/CNFs composites were elucidated. The influences of PLA-g-GMA on the crystallization behavior and mechanical, morphological and thermal properties of PLA/CNFs composites were investigated. The morphologies of the composites were observed by scanning electron microscopy (SEM). The crystallization rate of PLA in PLA/CNFs composites was studied by synchrotron small angle X-ray scattering (SAXS) technique. The mechanical properties of all composites were compared. Thermal properties of PLA/CNFs composites were investigated by differential scanning calorimetry (DSC) and thermogravimetric analysis (TGA).

1.4 References

- De Souza Lima, M. M., and Borsali, R. (2004). Rodlike cellulose microcrystals: structure, properties, and applications. **Macromolecular Rapid Communications**. 25: 771-787.
- Fortunati, E., et al. (2012). Multifunctional bionanocomposite films of poly (lactic acid), cellulose nanocrystals and silver nanoparticles. **Carbohydrate Polymers**. 87: 1596-1605.
- Fortunati, E., Puglia, D., Kenny, J. M., Haque, M. M.-U., and Pracella, M. (2013). Effect of ethylene-co-vinyl acetate-glycidyl methacrylate and cellulose microfibrils on the thermal, rheological and biodegradation properties of poly

- (lactic acid) based systems. **Polymer Degradation and Stability**. 98: 2742-2751.
- Garlotta, D., Doane, W., Shogren, R., Lawton, J., and Willett, J. (2003). Mechanical and thermal properties of starch-filled poly (D, L-lactic acid)/poly (hydroxy ester ether) biodegradable blends. **Journal of Applied Polymer Science**. 88: 1775-1786.
- Hong, J., and Kim, D. S. (2013). Preparation and physical properties of polylactide/cellulose nanowhisker/nanoclay composites. **Polymer Composites**. 34: 293-298.
- Lin, N., Chen, G., Huang, J., Dufresne, A., and Chang, P. R. (2009). Effects of polymer-grafted natural nanocrystals on the structure and mechanical properties of poly (lactic acid): A case of cellulose whisker-graft-polycaprolactone. **Journal of Applied Polymer Science**. 113: 3417-3425.
- Lu, J., Askeland, P., and Drzal, L. T. (2008). Surface modification of microfibrillated cellulose for epoxy composite applications. **Polymer**. 49: 1285-1296.
- Ochi, S. (2008). Mechanical properties of kenaf fibers and kenaf/PLA composites. **Mechanics of Materials**. 40: 446-452.
- Pandey, J. K., et al. (2005). Recent advances in biodegradable nanocomposites. **Journal of Nanoscience and Nanotechnology**. 5: 497-526.
- Pei, A., Zhou, Q., and Berglund, L. A. (2010). Functionalized cellulose nanocrystals as biobased nucleation agents in poly (l-lactide)(PLLA)-crystallization and mechanical property effects. **Composites Science and Technology**. 70: 815-821.

- Plackett, D., Andersen, T. L., Pedersen, W. B., and Nielsen, L. (2003). Biodegradable composites based on L-poly lactide and jute fibres. **Composites Science and Technology**. 63: 1287-1296.
- Qu, P., Gao, Y., Wu, G., and Zhang, L. (2010). Nanocomposites of poly (lactic acid) reinforced with cellulose nanofibrils. **BioResources**. 5: 1811-1823.
- Rudnik, E. (2010). **Compostable polymer materials**. Amsterdam: Elsevier.
- Sanchez-Garcia, M. D., and Lagaron, J. M. (2010). On the use of plant cellulose nanowhiskers to enhance the barrier properties of polylactic acid. **Cellulose**. 17: 987-1004.
- Saxena, I. M., and Brown, R. M. (2005). Cellulose biosynthesis: current views and evolving concepts. **Annals of Botany**. 96: 9-21.
- Siqueira, G., Bras, J., and Dufresne, A. (2010). Cellulosic bionanocomposites: a review of preparation, properties and applications. **Polymers**. 2: 728-765.
- Tao, Y., Yan, L., and Jie, R. (2009). Preparation and properties of short natural fiber reinforced poly (lactic acid) composites. **Transactions of Nonferrous Metals Society of China**. 19: s651-s655.
- Teixeira, E. d. M., et al. (2012). Properties of thermoplastic starch from cassava bagasse and cassava starch and their blends with poly (lactic acid). **Industrial Crops and Products**. 37: 61-68.
- Thielemans, W., Warbey, C. R., and Walsh, D. A. (2009). Permselective nanostructured membranes based on cellulose nanowhiskers. **Green Chemistry**. 11: 531-537.

CHAPTER II

LITERATURE REVIEW

2.1 Cassava pulp (CP)

Cassava (*Manihot esculenta* Crantz) pulp is the solid waste produced as a consequence of starch production. This pulp contains high starch content (50-60 % dry basis) (Sriroth, Chollakup, Chotineeranat, Piyachomkwan, and Oates, 2000). In addition to residual starch, this material contains 15-50 % cellulose fibers (dry weight basis) (Teixeira et al., 2012). In Thailand, cassava starch is a large and growing industry with about 10 million tons of fresh cassava roots used for the production of starch, generating at least 1 million tons of pulp annually (Sriroth et al., 1999). The main application for the large quantities of waste material produced each year, after drying, is as a low value animal feed or fertilizer. Table 2.1 shows the composition of cassava pulp produced after starch extraction at a starch factory in Thailand. Significant amounts of starch (60.6 %) and non-starch polysaccharide (29 % as fiber) were detected in the pulp. Monosaccharide analysis of the nonstarch polysaccharides indicated that glucans, such as cellulose, were the major polysaccharide. The analyzed compounds accounted for 94.7 % of the weight of the total dry pulp (Kosugi et al., 2009).

Table 2.1 Composition of cassava pulp (Kosugi et al., 2009).

Components	g/100 g Dry pulp
Starch	60.6
Reducing sugars (glucose) ^a	4.7 (0.09) ^a
Nitrogen	0.4
<i>Non-starch polysaccharides</i>	
Glucan	19.1
Xylan	4.2
Arabinan	1.4
Galactan	0.5
Mannan	0.7
Others	0.9
Klason lignin	2.2
Total	94.7

2.2 Cellulose nanofibers (CNFs)

2.2.1 Structure and morphology of cellulose

Cellulose is considered to be the most abundant renewable polymer on the Earth. This structural material is naturally organized as microfibrils linked together to form cellulose fibers. It is biosynthesized by a number of living organisms ranging from higher to lower plants, some amoebae, sea animals, bacteria and fungi.

Regardless of its source, cellulose consists of a linear homopolysaccharide composed of β -D-glucopyranose units linked together by β -1-4-linkages (Abdul Khalil et al., 2014). The basic chemical structure of cellulose is presented in Figure 2.1. The repeating unit is a dimer of glucose, known as cellobiose. Each monomer has three hydroxyl groups, and it is therefore obvious that these hydroxyl groups and their ability to form hydrogen bonds play a major role in directing the crystalline packing and also governing the physical properties of cellulose. The

number of glucose units or the degree of polymerization (DP) is up to 20,000, but its value can vary among a wide range.

In nature, cellulose does not occur as an isolated individual molecule, but it is found as assemblies of individual cellulose chain-forming fibers. The morphological hierarchy is defined by elementary fibrils, which pack into larger units called microfibrils. The latter are in turn assembled into familiar cellulose fibers, which are presented schematically in Figure 2.1.

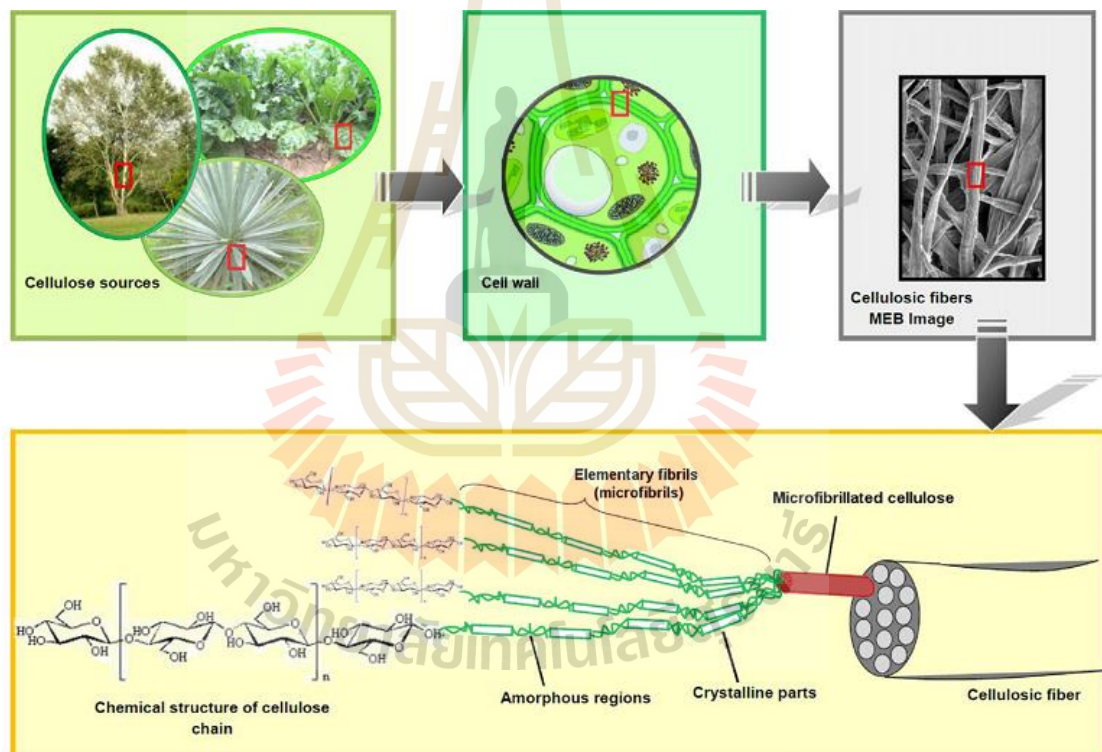


Figure 2.1 Basic chemical structure of cellulose showing the cellobiose repeating unit (Lavoine, Desloges, Dufresne, and Bras, 2012).

Within the cellulose fibrils there are crystalline regions where the cellulose chains are arranged in a highly ordered structure. It is these crystalline regions that are extracted, resulting in nanocrystalline cellulose. Besides that, there are also amorphous regions where the cellulose chains are arranged in a disordered structure. In the crystalline regions the inter- and intra-molecular interactions networks and the molecular orientations can vary, giving rise to cellulose polymorphs or allomorphs. So far, there are six interchangeable polymorphs have been identified, I, II, III_I, III_{II}, IV_I, IV_{II}. They are shown in Figure 2.2.

Native cellulose, namely cellulose I, is the crystalline cellulose. The term regenerated cellulose, also called cellulose II, is used to refer to cellulose precipitated out of solutions, generally alkali solutions. These represent the two main polymorphs of cellulose. The current knowledge on the crystallography and biosynthesis of cellulose strongly suggests that the structure of cellulose is made up of parallel chains (Dinand, Vignon, Chanzy, and Heux, 2002), whereas the crystalline structure of cellulose II is described as antiparallel (Sugiyama, Persson, and Chanzy, 1991). Cellulose I is not the most stable form of cellulose. An additional hydrogen bond per glucose residue in cellulose II makes this allomorph the most thermodynamically stable form (Saxena and Brown, 2005).

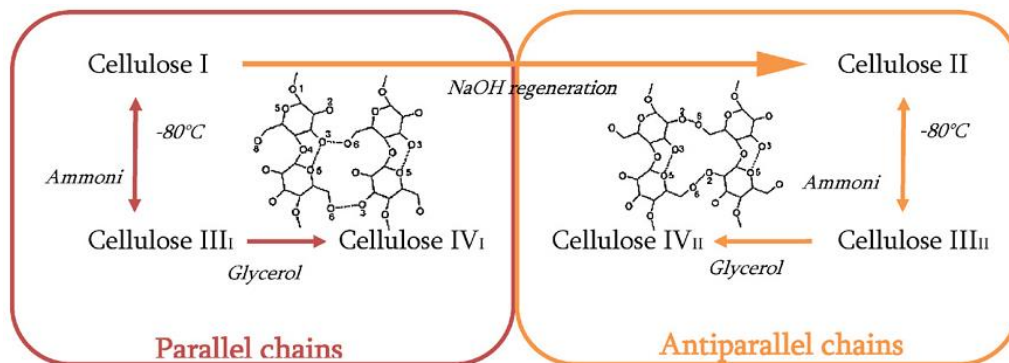


Figure 2.2 Polymorphs of cellulose and the main steps to obtain them (Lavoine et al., 2012).

The transformation of cellulose I to cellulose II is a subject of interest of many studies despite the fact that Mercer discovered this transformation in 1850, when submitting native cellulose to a treatment with strong alkali. The mechanism of this transformation was a topic of intense debate that still continues. The existence of two different crystalline forms in native cellulose, I_{α} and I_{β} , was first demonstrated by Atalla and Vander Hart (Atalla and Vanderhart, 1984) from nuclear magnetic resonance (NMR) experiments with cross polarization/magic angle spinning (CP-MAS). Atalla and Vanderhart (1984) proposed that most native celluloses are mixtures of cellulose I_{α} and I_{β} , solving a long time problem in the scientific community. The triclinic I_{α} allomorph is predominant in algal-bacterial celluloses, while the monoclinic I_{β} form is the allomorph present in the cellulose typical from annual plants (ramie and cotton). Some physical properties of cellulose fibers depend on the ratio of these two allomorphs (Saxena and Brown, 2005). It was discovered that the structural forms I_{α} and I_{β} can be found not only within the same cellulose sample, but also along a given microfibril

(Sugiyama, Okano, Yamamoto, and Horii, 1990). Cellulose I_{α} is a metastable form and can be converted into the I_{β} form by an annealing treatment (Saxena and Brown, 2005). The material used for cellulose nanofiller is native cellulose (cellulose I) which is responsible for mechanical properties due to its high modulus and crystallinity.

In higher plants, cellulose plays an essential role like reinforcing element in the cell wall, generally together with lignin and hemicelluloses. These three polymers are closely associated making up lignocellulosic biomass. Actually, the lignocellulosic structure can be regarded as a bionanocomposite, which results from a unique interplay between nano-scale domains of cellulose, hemicelluloses and lignin. The relative content of cellulose and lignin in lignocellulosic biomass varies among species. From a technological point of view, lignin content evaluation in the biomass is important to optimize the chemical and mechanical pre-treatment parameters necessary to produce a pure cellulose pulp. Indeed lignin is the hardest chemical component to take away from lignocellulosic biomass.

2.2.2 Cellulose nanofibers

Cellulose nanofibers (CNFs) are formed by web-like structure with widths and lengths of 5–70 nm and between 100 nm and several micrometres respectively. The fibers are highly crystalline, between 54 and 88 % (Moon, Martini, Nairn, Simonsen, and Youngblood, 2011). The aspect ratio, defined as the length to diameter ratio, spans a broad range. The variety of dimensions, morphologies and degree of crystallinity depend on the source of cellulosic materials and conditions under which preparation is carried out as well as on the experimental technique used. Moreover, as the cleaving of cellulose chains occurred randomly during the acid hydrolysis process, the dimensions of CNFs are not uniform. CNFs derived from

tunicate and bacterial cellulose is generally larger in dimensions compared to those obtained from wood and cotton. This is because tunicate and bacterial cellulose are highly crystalline hence there are lower fractions of amorphous domains that need to be cleaved resulting in the production of larger nanofibers.

Cellulose fibers and microfibrils do not display a regular surface. This means that apart from crystalline domains, cellulose also occurs in a non-crystalline state (amorphous). The cellulose amorphous regions are randomly oriented in a spaghetti-like arrangement leading to a lower density compared to nanocrystalline regions. The equatorial positions of the glucopyranose residues stabilize the structure of cellulose, increasing its rigidity and resulting in extensive intra and intermolecular hydrogen bonding that also causes insolubility in water. On the other hand, the amorphous regions are susceptible to acid attack and, under controlled conditions, they may be removed leaving crystalline regions intact. De Souza Lima and Borsali (2004) described the principle of the disruption of the amorphous regions of cellulose in order to produce nanocrystalline cellulose. The hydronium ions can penetrate the material in these amorphous domains promoting the hydrolytic cleavage of the glycosidic bonds releasing individual crystallites.

The precise morphological characteristics of CNFs are usually studied by microscopy (transmission electron microscopy, TEM; scanning electron microscopy, SEM; atomic force microscopy, AFM) or light scattering techniques, including small angle neutron scattering (SANS) and polarized or depolarized dynamic light scattering (DLS and DDLS respectively). The most conventional and common one is TEM, which can directly provide high-resolution images, but this technique typically shows aggregation of the fibers, mainly due to the drying step for the preparation of the

specimen. Usually, the very dilute suspension of cellulose nanofibers is prepared in order to overcome this problem. AFM has been widely used to provide valuable and rapid indication of surface topography of CNFs under ambient conditions, at scale length down to Ångström level. However, this technique has the drawback of tip-broadening resulting in overestimation of crystallite dimensions (Holt, Stoyanov, Pelan, and Paunov, 2010). Light scattering techniques have recently been brought forward as an important tool in determining CNFs dimensions, through the development of models. Braun, Dorgan, and Chandler (2008) used low angle laser light scattering at reduced particle concentration and obtained values of CNFs from cotton linter of 13 nm wide and 272 nm long.

2.3 Challenges in the production of cellulose nanofibers

Extraction is central to further developing and processing cellulose nanofibers (CNFs) into functional, high-value added materials, and, as such, attempts to face the drawbacks in the conventional methodology, to reduce the cost and enlarge the production are continuously investigated. In particular, the reduction in the cost of CNFs production is often addressed, because it could increase the number of markets appropriate for CNFs applications. Some problems and attempts to face them are discussed in the following sections.

2.3.1 Use of residual biomass to produce cellulose nanofibers

Because plant-based cellulose fibers have the potential to be extracted into nanofibers thinner than bacterial cellulose, many researchers have been extensively studying the extraction of cellulose nanofibers from wood and other plant fibers. However, due to the complicated multilayered structure of plant fibers and the

interfibrillar hydrogen bonds, the fibrils obtained by common methods (high pressure homogenizer, a grinder, cryocrushing) are aggregated nanofibers with a wide distribution in width. Abraham et al. (2011) have recently developed a simple and low cost process to obtain an aqueous stable colloid suspension of cellulose nanofibrils from various lignocellulosic fibers. They considered three different start fibers: banana (pseudo stem), jute (stem) and pineapple leaf fiber. The authors concluded that pineapple leaf fiber is the best one for the preparation of cellulose nanofibers; however, jute fiber is cheaply and abundantly available and the raw jute fiber has about 60–70 % cellulose content. Hence for the cost effective production of cellulose nanofibers, jute fiber is the potential candidate.

2.3.2 Increase of crystalline cellulose nanofibers yield from sulfuric acid hydrolysis

Efforts in increasing the yield in CCNFs extraction have important impact on final cost. Hamad and Hu (2010) carried out a systematic investigation of the structure–process–yield interrelations in the CCNFs extraction from a commercial softwood Kraft pulp. CCNFs with high crystallinity (>80 %) was obtained using 64 % sulfuric acid, with yields between 21 and 38 %. The highest yield was obtained using a temperature of 65 °C when shortening the reaction time down to 5 min. Moreover, Bondeson, Mathew, and Oksman (2006) investigated optimizing the hydrolysis conditions by an experimental factorial design matrix and demonstrated that CCNFs are obtained with a yield of 30 % (based on initial weight) with sulfuric acid 63.5 % (w/w) for 2 h.

2.3.3 Drying of obtained crystalline cellulose nanofibers

In most cases CCNF was processed as aqueous suspension because of its hydrophilic nature and propensity to agglomerate during drying. In fact, during drying, forces resulting from the removal of water and high temperature may drive the molecular contact of CCNF and cause agglomeration. There is a well perceived need to develop robust processes to dry CCNF which will maintain nanoscale dimensions for material applications (where a dry form is necessary) and to mitigate the higher transportation costs of aqueous suspensions. Furthermore, not only drying but also understanding the drying process is necessary for the use of CCNF in developing industrial applications in polymer composites. The well-established method of oven drying causes increase in dimensions to hundreds of microns or even to millimetres, so the nanoscale dimensions of obtained cellulose fibers are lost. Peng, Gardner, and Han (2012) showed a comparative investigation between different methods such as freeze drying, supercritical drying, and spray drying. The obtained results indicated that freeze drying and supercritical drying create highly networked structures of agglomerates with multi-scalar dimensions including nanoscale. The spray drying was proposed by the authors as a technically suitable manufacturing process to dry CCNF suspensions: the particle sizes range from nano to micron scale and are controllable, the cost is low and the method is scalable.

2.4 Potential applications of crystalline cellulose nanofibers

Crystalline cellulose nanofibers have been used as reinforcing materials in polymeric nanocomposites displaying enhanced properties when compared to conventional fillers. Several studies have demonstrated the utility of CCNF enhancing

the mechanical properties of polyoxyethylene based polymer electrolyte systems. However, the high hydrophilicity of cellulose has set limitations to its applications in non-polar composites. To overcome this deficiency, a variety of methods have been proposed for the surface modification of crystalline cellulose nanofibers. These modifications include the use of surfactants possessing polar heads and long hydrophobic tails, as well as the grafting of various hydrophobic moieties on the surface of CCNF.

The surface modifications produced CCNF dispersible in non-polar solvents but their utility toward aqueous media was diminished. Therefore, modification of the crystalline cellulose nanofibers with hydrophobic blocks while retaining their hydrophilic character can greatly expand their application areas toward both polar and nonpolar environments. Moreover, selective grafting of the hydrophobic polymer chains at specific locations on the CCNF should further promote their utility. The weak boundary layers between the individual components are often responsible for the composite failures that are typically occurring between polar and non-polar materials. However, strong boundary adhesion can be achieved by surface modification and crosslinking reactions. Therefore, a site-specific and uniform grafting of crystalline cellulose nanofibers with hydrophobic polymer chains, should offer strong interactions with both polar and non-polar components, and thus provide strong boundary binding.

Furthermore, the high melting temperature of the crystalline cellulose nanofibers may further benefit the thermal transition properties of any covalently attached functional polymers on them. It is therefore likely that the increase in the overall thermal stability of the composites will expand the application temperature ranges of such composites.

2.5 Preparation of crystalline cellulose nanofibers

The main process for the isolation of CCNF from cellulose fibers is based on acid hydrolysis. Disordered or paracrystalline regions of cellulose are preferentially hydrolyzed, as shown in Figure 2.3, whereas crystalline regions that have a higher resistance to acid attack remain intact. Thus, following an acid treatment that hydrolyzes the cellulose (leading to removal of the microfibrils at the defects), crystalline cellulose nanofibers are produced. The obtained CCNFs have a morphology similar to the original cellulose fibers.

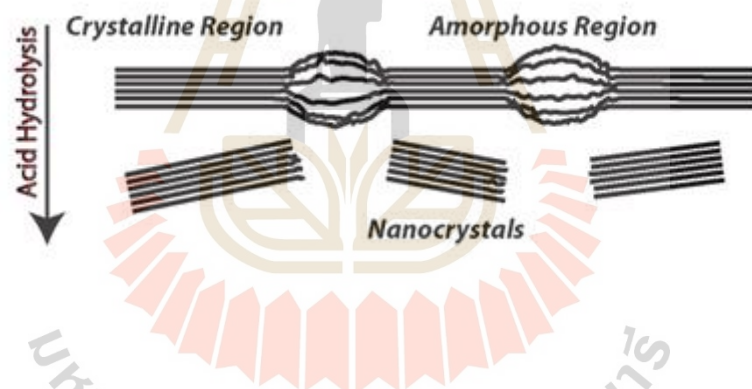


Figure 2.3 Acid hydrolysis breaks down disordered (amorphous) regions and isolates nanocrystals (Oke, 2010).

The overall efficiency of the hydrolysis process is affected by several factors such as acid type, hydrolysis temperature, and acid concentration. It is believed that acid interacts mainly with the amorphous regions of cellulose, as they are the most easily accessible and have the greatest surface area. Therefore, the amorphous regions are the first to be targeted by the strong acid, followed by regions of increased

crystallinity (Figure 2.4). The reaction continues until all the amorphous region is hydrolyzed to glucose and then slows down significantly as the remaining acid attacks to the surface of the residual crystalline regions as well as the reducing end groups of cellulose. The selection of hydrolysis conditions plays an important role in the production of crystalline cellulose nanofibers. On the other hand, the amorphous region needs to be hydrolyzed but the conditions should be mild enough to avoid complete hydrolysis of cellulose to glucose or even carbonization.

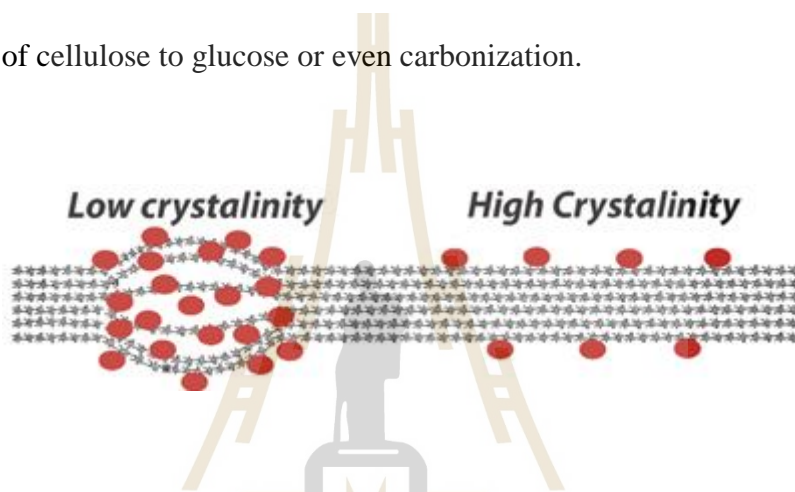


Figure 2.4 Red circles demonstrate potential sites of hydrolysis. Regions of high crystallinity possess fewer sites and therefore take longer to be broken down (Oke, 2010).

The actual occurrence of the acid cleavage event is attributed to differences in the kinetics of hydrolysis between amorphous and crystalline domains. In general, acid hydrolysis of native cellulose induces a rapid decrease in its degree of polymerization (DP), to the so-called level-off DP (LODP). The DP subsequently decreases much more slowly, even during prolonged hydrolysis times. LODP has been thought to correlate with crystal sizes along the longitudinal direction of cellulose chains present in the original cellulose before the acid hydrolysis. This hypothesis was based on the reasonable assumption that disordered or para-crystalline domains are regularly

distributed along the microfibrils and therefore they are more susceptible to acid attack (in contrast to crystalline regions that are more impervious to attack).

Typical procedures currently employed for the production of CCNF consist of subjecting pure cellulosic material to strong acid hydrolysis under strictly controlled conditions of temperature, agitation, and time. The nature of the acid and the acid-to-cellulosic fibers ratio are also important parameters that affect the preparation of CCNF. A resulting suspension is subsequently diluted with water and washed with successive centrifugations. Dialysis against distilled water is then performed to remove any free acid molecules from the dispersion. Additional steps such as filtration, differential centrifugation, or ultracentrifugation (using a saccharose gradient) have been also used; an example of the main steps needed to prepare CCNF from lignocellulosic biomass is shown in Figure 2.5.

Sulfuric and hydrochloric acids have been extensively used for CCNF preparation, but phosphoric and hydrobromic acids have also been used for such purposes. If the CCNFs are prepared by hydrolysis in hydrochloric acid, their ability to disperse is limited and their aqueous suspensions tend to flocculate.

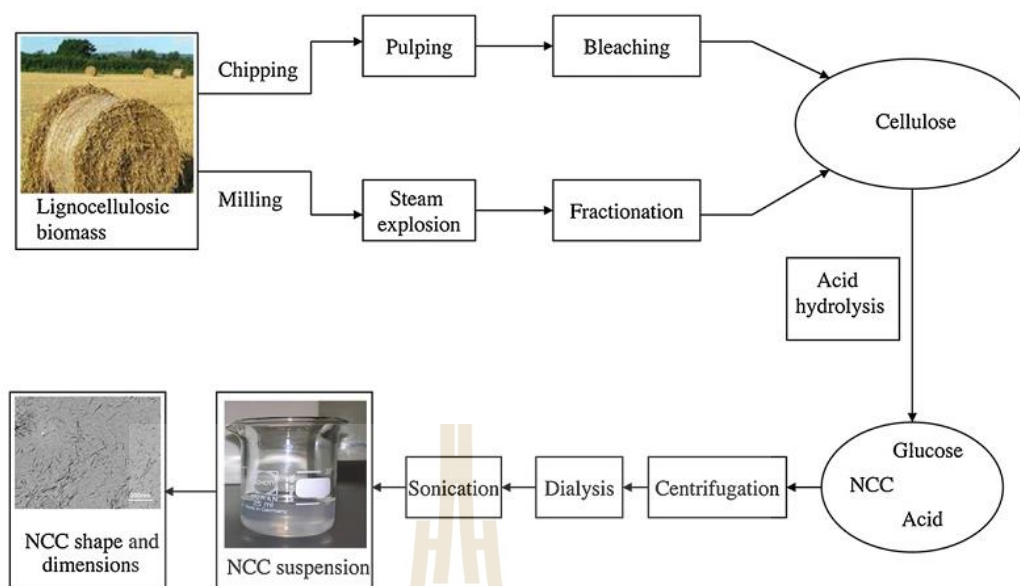


Figure 2.5 Scheme of main steps needed to prepare CCNFs from lignocellulosic biomass (Lavoine et al., 2012).

On the other hand, when sulfuric acid is used as a hydrolyzing agent, it reacts with the surface hydroxyl groups of cellulose to yield charged surface sulfate esters that promote dispersion of the CCNF in water. However, the introduction of charged sulfate groups compromises the thermal stability of the nanofibers. Also, differences in the rheological behavior have been shown between suspensions obtained from sulfuric acid hydrolysis and those obtained from hydrochloric acid.

2.5.1 Preparation of crystalline cellulose nanofibers by acid hydrolysis

Silvério, Flauzino Neto, Dantas, and Pasquini (2013) investigated the preparation of crystalline cellulose nanofibers from corncobs by sulfuric acid hydrolysis process. Pre-treatment steps including alkali treatment and bleaching process were carried out before cellulose nanofibers were obtained by hydrolysis

process using sulfuric acid (H_2SO_4) as a hydrolyzing agent. The results of chemical composition of the samples indicated that the pre-treatment steps removed effectively hemicelluloses and lignin. Moreover, the needle-like cellulose nanofibers were observed by using AFM technique. It confirms that the extraction of crystalline cellulose nanofibers from corncob was successful. The results from XRD analysis also showed that after acid treatment, the crystallinity of samples increased significantly and structure of cellulose was maintained.

Mandal and Chakrabarty (2011) investigated the extraction of nanocellulose from sugarcane by acid hydrolysis. Sulfuric acid was used as a hydrolyzing agent. Alkaline treatment was carried out before acid treatment in order to remove hemicelluloses and lignin. The result from AFM indicated that the nanocellulose was obtained in the range of 70-90 nano.

Sadeghifar, Filpponen, Clarke, Brougham, and Argyropoulos (2011) studied the extraction of crystalline cellulose nanofibers from cotton fibers. Hydrobromic acid (HBr) was used as a hydrolyzing agent. Before acid treatment, alkaline treatment was also carried out to remove hemicelluloses and lignin. The results showed that the 7-8 nm in diameter and 100-200 nm in lengths cellulose nanofibers were extracted successfully with high crystallinity. This indicated that besides sulfuric acid and hydrochloric acid, hydrobromic acid was also an effective hydrolyzing agent for the preparation of crystalline cellulose nanofibers.

Liu, Zhong, Chang, Li, and Wu (2010) studied on preparation of cellulose nanofibers from bamboo fibers. Nitric acid (HNO_3) was used as a hydrolyzing agent. The acid hydrolysis treatment of bamboo fibers was carried out at 50 °C for 24 h. The results showed that the obtained cellulose nanofibers had typical cellulose I

structure, and the morphology was dependent on concentration in the suspension. At low concentration (0.1 wt% solids of bamboo cellulose nanofibers), nanofibers of 50–100 nm assembled into leaf nervations; at high concentration (10.0 wt% solids of bamboo cellulose nanofibers), nanofibers congregated into a micro-sized “flower” geometry. The different geometries resulting from aggregation intensity of bamboo cellulose nanofibers were due to high surface electrostatic energy and large surface area.

Braun and Dorgan (2008) investigated the isolation of cellulose nanofibers from cotton linter using hydrochloric acid (HCl) as a hydrolyzing agent. The acid hydrolysis treatment of cotton linter was performed at 105 °C for 20 min. Multiangle laser-light scattering (MALLS) results showed that the diameter polydispersity and the length polydispersity of obtained cellulose nanofibers was 3.0 and 2.3, respectively. The thermal stability of cellulose nanofibers was found to be higher than that of cotton linter.

2.5.2 Preparation of crystalline cellulose nanofibers by other methods

In addition to acid hydrolysis process, oxidation process and using ionic liquids were also the effective methods for the preparation of crystalline cellulose nanofibers. These methods does not require pre-treatment steps. Leung et al. (2011) investigated the preparation of carboxylated cellulose nanofibers from many different cellulosic materials by using a versatile one-step oxidation process. Ammonium persulfate (APS), an oxidant with low long-term toxicity, high water solubility, was used as oxidizing agent. The biomass materials used as starting materials includes flax, flax shives, hemp, triticale, microcrystalline cellulose (MCC), wood pulp, whatman CF1, and bacterial cellulose. The result from AFM micrographs confirmed the

production of highly uniform cellulose nanofibers with significantly smaller diameters compared to those obtained by acid treatment (Cao, Chen, Chang, Stumborg, and Huneault, 2008). Cellulose nanofibers prepared from different celluloses also showed a similar mean particle length and length polydispersity. The results from XRD analysis also presented the higher crystallinity of cellulose nanofibers compared to starting materials. Qin, Tong, Chin, and Zhou (2011) investigated the production of carboxylated cellulose nanofibers (c-CNFS) from cotton linter pulp by using TEMPO (2,2,6,6-Tetramethyl-piperidine-1-oxyl)-NaBr-NaClO as oxidation system. In this research, Cotton linter pulp was oxidized in the TEMPO-NaBr-NaClO system with ultrasonic treatment. With this method, the cellulose nanofibers having high carboxylate content were produced directly. The results from TEM indicated that the cellulose nanofibers were obtained with 5-10 nm in width and 200-400 nm in length. It demonstrated that the simple oxidation process by using TEMPO-NaBr-NaClO with ultrasonic treatment was an effective method to prepare cellulose nanofibers from cotton linter pulp.

Man et al. (2011) investigated the preparation of cellulose nanofibers by treating microcrystalline cellulose (MCC) with 1-butyl-3-methylimidazolium hydrogen sulfate (bmimHSO₄) ionic liquid. The hydrolysis of microcrystalline cellulose by bmimHSO₄ ionic liquid was found to be quite similar to acid hydrolysis. In this reaction, ionic liquid reacted with microcrystalline cellulose in a similar manner as acids in acid hydrolysis. Ionic liquid caused hydrolytic cleavage of glycosidic bonds between two anhydroglucose units that resulted in rearrangement of the interlinking chain ends, which eased in the release of internal strain (Klemm, Heublein, Fink, and Bohn, 2005). The ionic liquid dissolved the amorphous portion and left behind the crystalline regions.

Ionic liquid treatment, along with mechanical stirring resulted in disintegration of the microcrystalline cellulose structure into cellulose nanofibers. The result from TEM showed that the cellulose nanofibers have a needle like shape with a diameter of 21.42 nm at the center and tapers off to 13.38 nm at the end. The thermal stability of obtained cellulose nanofibers was found to be lower than that of starting material. It is most likely due to adhesion of the sulfate group from the ionic liquid onto the surface of nanocrystalline cellulose.

2.6 Chemical modification of crystalline cellulose nanofibers

Taking advantage of the large number of hydroxyl groups at the surface of nanocellulose substrates, different chemical modifications have been attempted, including esterification, etherification, oxidation, silylation, amidation, and polymer grafting (Figure 2.6). In an attempt to avoid complex surface functionalization routes, many researchers have recently combined the synthesis and functionalization of CCNF in a single step. By utilizing a mixture of acetic acid, hydrochloric acid and organic acids, CCNFs were synthesized and functionalized using the Fischer esterification process (Figure 2.7). Non-covalent surface modification, including the use of adsorbing surfactants and coupling agents, has been also studied.

All chemical functionalization have been mainly conducted (1) to tune the surface characteristics of nanocelluloses to promote their dispersion in nonpolar organic media and/or to improve their compatibility with hydrophobic matrices in nanocomposites; (2) to introduce stable negative or positive charges on the surface of nanocellulose, mainly CCNF, to obtain better electrostatic repulsion induced dispersion, especially when exploring their self-assembly properties.

The main challenge for the chemical functionalization of the different nanocellulose substrates is to conduct it in such a way that it only changes their surface while preserving their original morphology, avoiding any polymorphic conversion, and maintaining the integrity of their native crystalline structure.

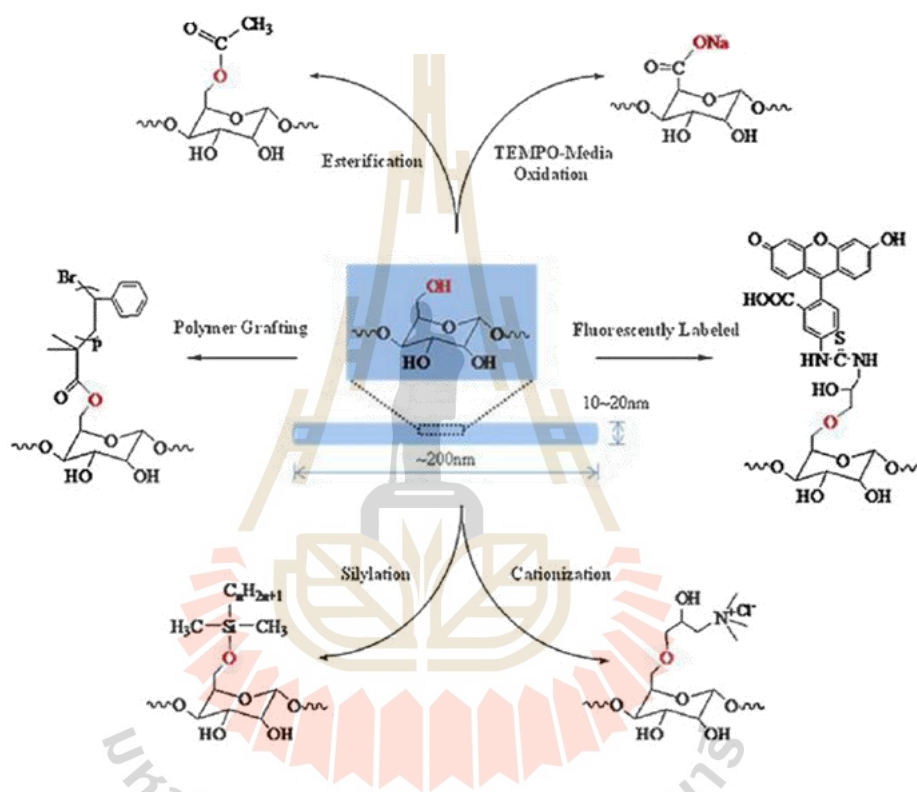


Figure 2.6 Schematic diagram illustrating the various types of chemical modifications on cellulose nanofibers surface (Peng, Dhar, Liu, and Tam, 2011).

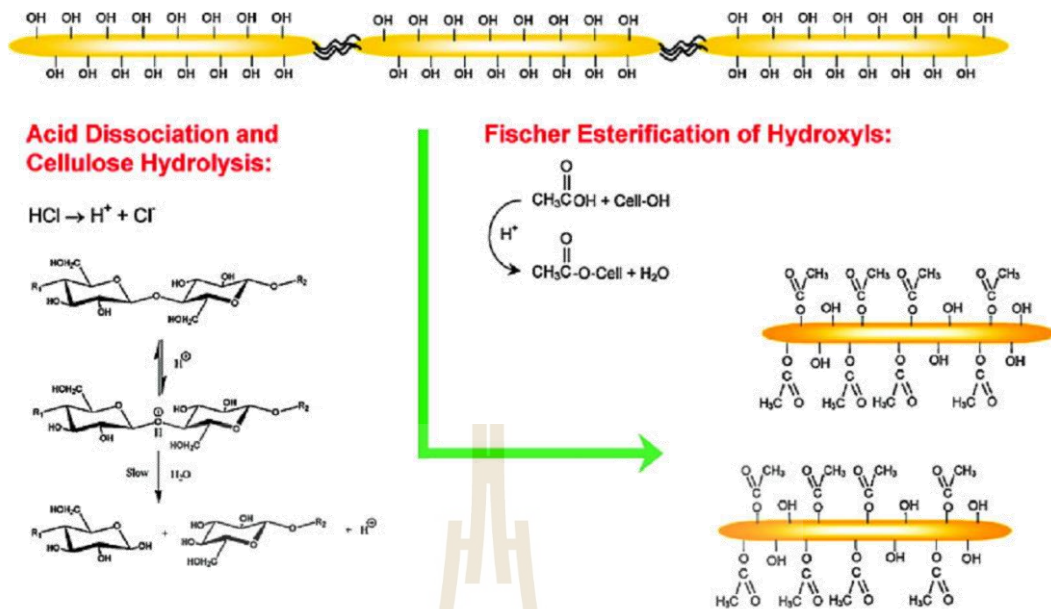


Figure 2.7 Single step process for cellulose hydrolysis and esterification of hydroxyl groups using a mixture of acetic and hydrochloric acid (Peng et al., 2011).

2.7 Poly(lactic acid) (PLA)

Poly(lactic acid) belongs to the family of aliphatic polyesters commonly made from α -hydroxy acids, which include polyglycolic acid or polymandelic acid, and are considered biodegradable and compostable. PLA is a thermoplastic, high-strength, high-modulus polymer that can be made from annually renewable resources to yield articles for use in either the industrial packaging field or the biocompatible/bioabsorbable medical device market. It is easily processed on standard plastics equipment to yield molded parts, film, or fibers (Hartmann and Kaplan, 1998). It is one of the few polymers in which the stereochemical structure can easily be modified by polymerizing a controlled mixture of the L- or D-isomers to yield high

molecular-weight amorphous or crystalline polymers that can be used for food contact and are generally recognized as safe (GRAS) (Conn et al., 1995).

PLA is most commonly synthesized either through polycondensation of lactic acid (2-hydroxy propionic acid) or ring-opening polymerization of lactide (LA) (the dimer of lactic acids). Lactic acid is the simplest 2-hydroxycarboxylic acid (or α -hydroxy acid) with a chiral carbon atom and exists in two enantiomeric forms (Figure 2.8).

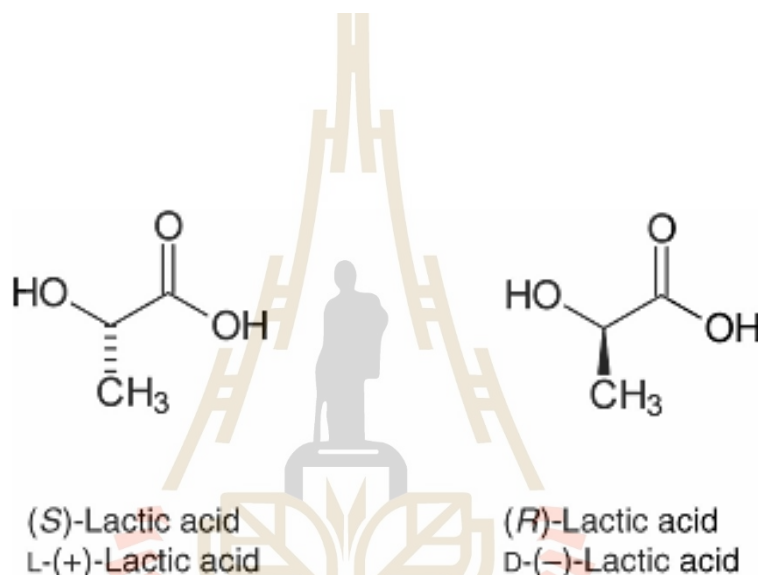


Figure 2.8 Two enantiomeric forms of lactic acid: (*S*)- and (*R*)-2-hydroxypropionic acid (Auras, Lim, Selke, and Tsuji, 2011).

The chirality of lactic acid often results in confusion regarding nomenclature. A number of different names are used in the literature. This confusion is the result of mixing the molecular structure and a physical property (optical rotation). (*S*)-Lactic acid (or L-lactic acid) has a slightly positive specific optical rotation and is frequently named L-(+)-lactic acid (Holten, Muller, and Reh binder, 1971). However, a concentrated solution of (*S*)-lactic acid at equilibrium contains lactic acid oligomers,

which results in an overall negative optical rotation. Therefore, it is advised to use the structural R/S notation or the older notation of L and D and avoid the + and - of the optical rotation.

The dehydrated, cyclic dimer of lactic acid is commonly called lactide (3,6-dimethyl-1,4-dioxane-2,5-dione). Due to the two asymmetric carbon atoms in the molecule, lactide exists in three different forms (Figure 2.9). In addition to the three diastereomeric structures mentioned above, also a racemate of D-lactide and L-lactide exists: *rac*-lactide or DL-lactide.

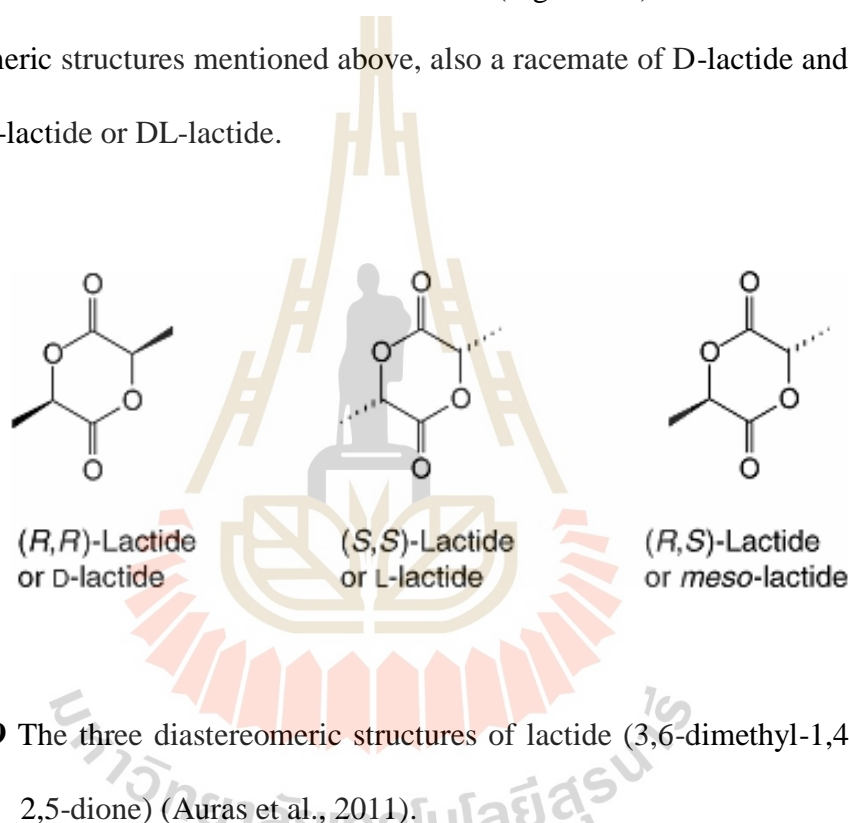
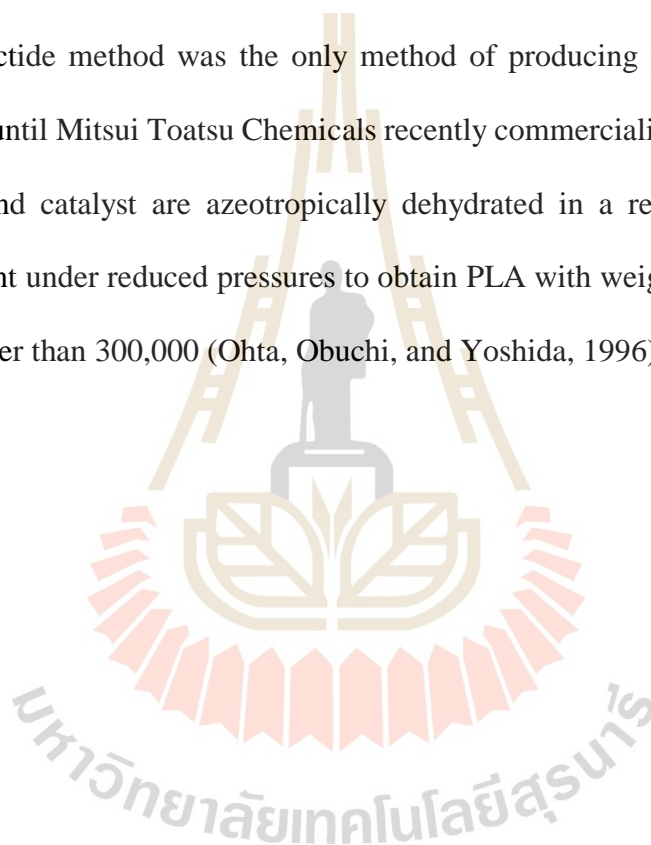


Figure 2.9 The three diastereomeric structures of lactide (3,6-dimethyl-1,4-dioxane-2,5-dione) (Auras et al., 2011).

Commercial PLA is usually prepared from L-lactide (LLA), because the resulting polymer poly(L-lactic acid) (PLLA) is semicrystalline with a relatively high melting and glass transition temperature (T_g). The synthesis of lactic acid into high-molecular weight PLA can follow two different routes of polymerization, as shown in Figure 2.10. Lactic acid is condensation polymerized to yield a low-molecular-weight, brittle, glassy polymer, which, for the most part, is unusable for any applications unless

external coupling agents are used to increase the molecular weight of the polymer. The molecular weight of this condensation polymer is low due to the viscous polymer melt, the presence of water, impurities, the statistical absence (low concentration) of reactive end-groups, and the “back-biting” equilibrium reaction that forms the six-member lactide ring. The second route of producing PLA is to collect, purify, and ring-open polymerize lactide to yield high-weight- average molecular weight ($M_w > 100,000$) PLA. The lactide method was the only method of producing pure, high-molecular-weight PLA until Mitsui Toatsu Chemicals recently commercialized a process wherein lactic acid and catalyst are azeotropically dehydrated in a refluxing, high-boiling, aprotic solvent under reduced pressures to obtain PLA with weight-average molecular weights greater than 300,000 (Ohta, Obuchi, and Yoshida, 1996).



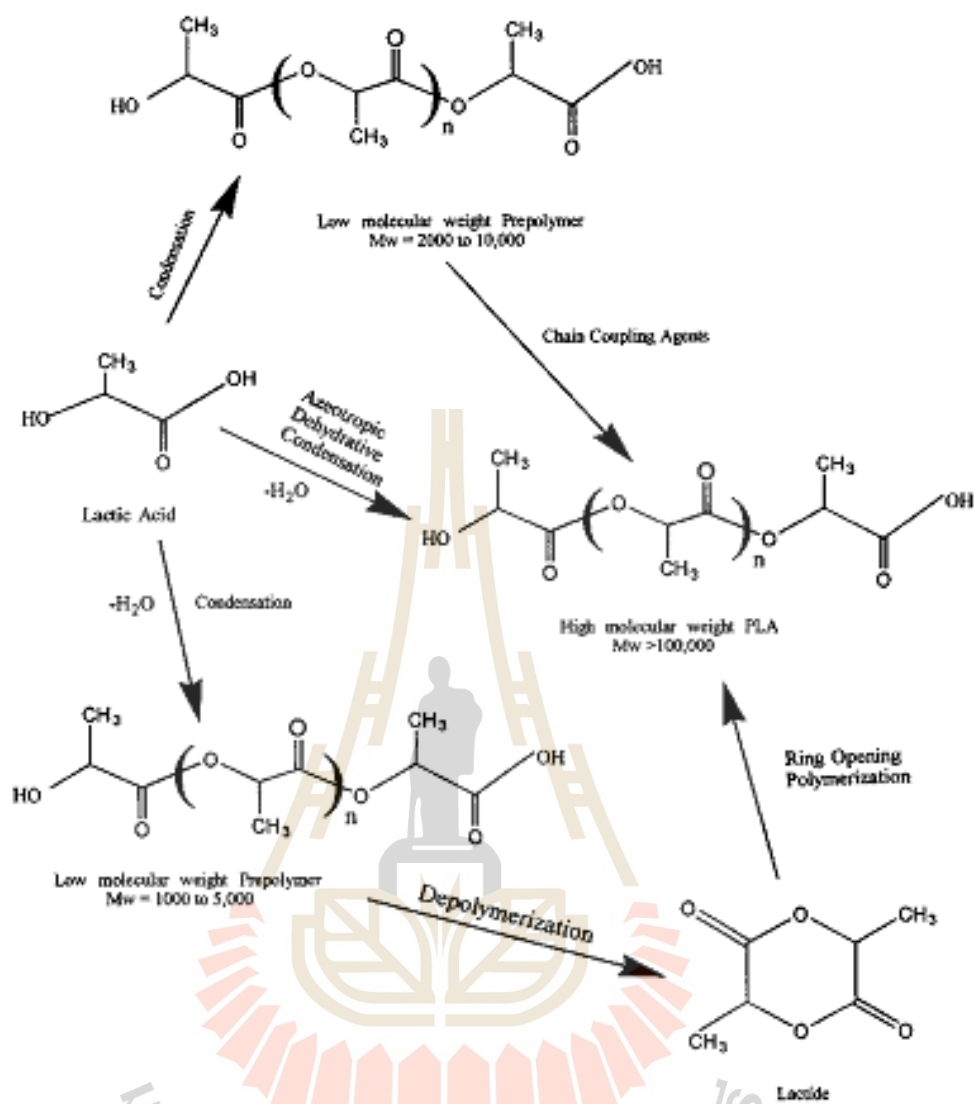


Figure 2.10 Synthesis methods for high-molecular-weight PLA (Garlotta, 2001).

Poly(lactic acid) homopolymers have a glass-transition and melt temperature of about 55 °C and 175 °C, respectively. They require processing temperatures in excess of 185-190 °C (Spinu, Jackson, Keating, and Gardner, 1996). PLA is degraded by simple hydrolysis of the ester bond and does not require the presence of enzymes to catalyze this hydrolysis. The rate of degradation is dependent on the size and shape of

the article, the isomer ratio, and the temperature of hydrolysis. In order for PLA to be processed on large-scale production lines in applications such as injection molding, blow molding, thermoforming, and extrusion, the polymer must possess adequate thermal stability to prevent degradation and maintain molecular weight and properties (Garlotta, 2001).

2.8 Crystallization behavior of PLA

2.8.1 Crystal structure

Different crystal structures have been reported for PLA, the formation of which depends on the crystallization conditions. The most common α -form occurring in conventional melt and solution crystallization conditions was first reported by De Santis and Kovacs (De Santis and Kovacs, 1968). Based on WAXD and IR data, Zhang et al. (2005) reported the slightly different α' -form for PLA crystallized below 120 °C. The chain conformation and crystal system of α' -form is similar to α structure, but with a looser and less ordered chain packing. As a consequence of its looser chain packing and disordered structure, the α' crystal leads to a lower modulus and barrier properties and to higher elongation at break compared to α crystal (Cocca, Di Lorenzo, Malinconico, and Frezza, 2011). Stretching, solution spinning, or high hot draw ratios induce the formation of β -crystal structures, a unit cell with $a = 1.031$ nm, $b = 1.821$ nm, and $c = 0.900$ nm, and a chain conformation with left-handed 3_1 helices (Hoogsteen, Postema, Pennings, Ten Brinke, and Zugenmaier, 1990). The melting temperature of the β structure is about 10 °C lower compared to α crystal, implying that β form is thermally less stable. A more ordered crystal modification called γ was also reported (Cartier et al., 2000). In the γ -form which was obtained by epitaxial crystallization of

PLA on hexamethylbenzene, two chains are oriented antiparallel in the crystal cell. Besides the homo-crystallization of PLLA and PDLA, these two enantiomeric chains can co-crystallize together and form a stereocomplex.

2.8.2 Kinetics of crystallization

Kinetics through visual observation

The overall crystallization kinetics is typically examined in terms of two independent phenomena: initial crystal nucleation and of subsequent crystal growth. In practice, optical microscopy on thin polymer films is used to determine the nucleation density and spherulite growth rates in isothermal conditions. The polymer film is usually first melted and rapidly cooled to the desired temperature. The size and number of spherulites can then be monitored over time. The spherulite density decreased with temperature and the decreasing rate gradually accelerated with temperature. The growth phenomenon is evaluated by measuring spherulite radius with time. The crystal growth rate (G) is equal to the slope of the spherulite radius vs. time curve, while extrapolation of this data to zero-radius can be used to determine the induction time (related to nucleation kinetics). Usually G is constant for a specific crystallization temperature.

Kinetics through calorimetry

Calorimetry is another technique used to study the crystallization kinetics. In particular, calorimetry enables quantification of transition temperatures and enthalpies in isothermal and non-isothermal modes. For isothermal characterizations, after initial quenching below the glass transition temperature or directly from the melt state, the amorphous polymer is rapidly brought to the selected crystallization temperature T_c . Heat flow is then measured as a function of time until crystallization is completed. The heat flow data is converted into an absolute crystallinity level or more

commonly, to a fraction relative to the final crystallinity level. When such crystallinity growth curves is obtained, they can be curve-fitted with the Avrami model:

$$X_t = 1 - \exp[-(kt)^n]$$

Where k is a kinetic rate constant and n is the Avrami exponent. The Avrami exponent is typically between 2 and 4 for polymer crystallization and is associated to the nucleation mechanism (homogeneous vs. heterogeneous and simultaneous vs. sporadic), dimensionality of crystal growth and growth mechanism.

To rapidly compare the crystallization rates of materials, it is convenient to report the crystallization half-time ($t_{1/2}$) defined as the time required to attain half of the final crystallinity ($X_t = 0.5$). The half-time is typically reported as a function of temperature enabling the determination of the optimal temperature window.

2.9 Graft copolymer

Graft copolymers are a special type of branched copolymer in which the side chains are structurally distinct from the main chain. The illustration in Figure 2.11 depicts a special case where the main chain and side chains are composed of distinct homopolymers. However, the individual chains of a graft copolymer may be homopolymers or copolymers.

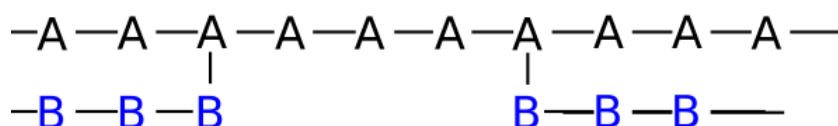


Figure 2.11 The represent structure of graft copolymer.

Where A units refer to the main chain or backbone and B units is the side chain of graft copolymer. It is well known that graft copolymers of vinyl monomers such as styrene, acrylonitrile, methylmethacrylate can be directly used to improve compatibility, impact, and low temperature properties of thermoplastics. Moreover, it can be employed as the compatibilizers for promoting the interaction between immiscible phases in the blends.

Free radical grafting of polyolefin with monomers containing potentially reactive group is one of the attracting methods to modify basic properties of the pristine polymer (Russell, 2002). Especially, it is powerful method to produce compatibilizer for the blends of polar and nonpolar polymer pair. It is because that chemical reaction between functional groups in the modified nonpolar and polar polymer during mixing procedure gives good miscibility of the blend. Vinyl monomers such as, maleic anhydride, dibutyl maleate, maleic acid, dimethyl aminoethyl methacrylate, and glycidyl methacrylate (GMA) are widely adopted as grafting monomer using various grafting method, which is radical reaction using chemical initiator (Pesneau, Champagne, and Huneault, 2004), high energy irradiation (Choi and Nho, 2000), plasma (Petasch, Räuchle, Walker, and Elsner, 1995), UV photografting (Abdel-Razik, Ali, Abdelaal, and Sarhan, 1996), and solvothermal process (Qi, Yu, Shen, Liu, and Zhou, 2006).

2.9.1 Graft copolymerization of GMA by melt grafting

Glycidyl methacrylate (GMA) is a well-known bifunctional monomer, which consists of acrylic and epoxy groups. The epoxy group of GMA can react with many other groups, such as hydroxyl and carboxyl groups, whereas acrylic groups show

the capability of free-radical grafting of GMA onto the polymer chain. The GMA-grafted copolymer is a potential compatibilizing agent for reducing the interfacial tension in polymer blends or a coupling agent in polymer-based composites. In recent years, studies of the grafting GMA onto various polymer species such as polycaprolactone (PCL), polypropylene (PP), low and high density polyethylene (LDPE, HDPE), and poly(lactic acid) have been reported.

Cho, Eom, Kim, and Park (2008) investigated the melt grafting of GMA onto high-density polyethylene (HDPE) in the presence of free radical initiators in the batch mixer. The results showed that the crystallinity of HDPE decreased monotonically with the increase in GMA content.

Kim, Cho, and Park (2001) investigated the melt grafting of GMA onto PCL in a batch mixer using benzoyl peroxide as an initiator. The result from $^1\text{H-NMR}$ spectra indicated that the graft content increased with the increase of GMA concentration. Moreover, the tensile strength and elongation at break of PCL-g-GMA were comparable to those of the unmodified PCL. It indicated that there was probably no reduction in the molecular weight and thus no change in the tensile properties. It was also found that the tensile strength at yield decreased with increase of the GMA content. This decrease of tensile strength at yield was attributed to the decrease of crystallinity with the GMA content. The grafting mechanism of PCL-g-GMA is shown in Figure 2.12.

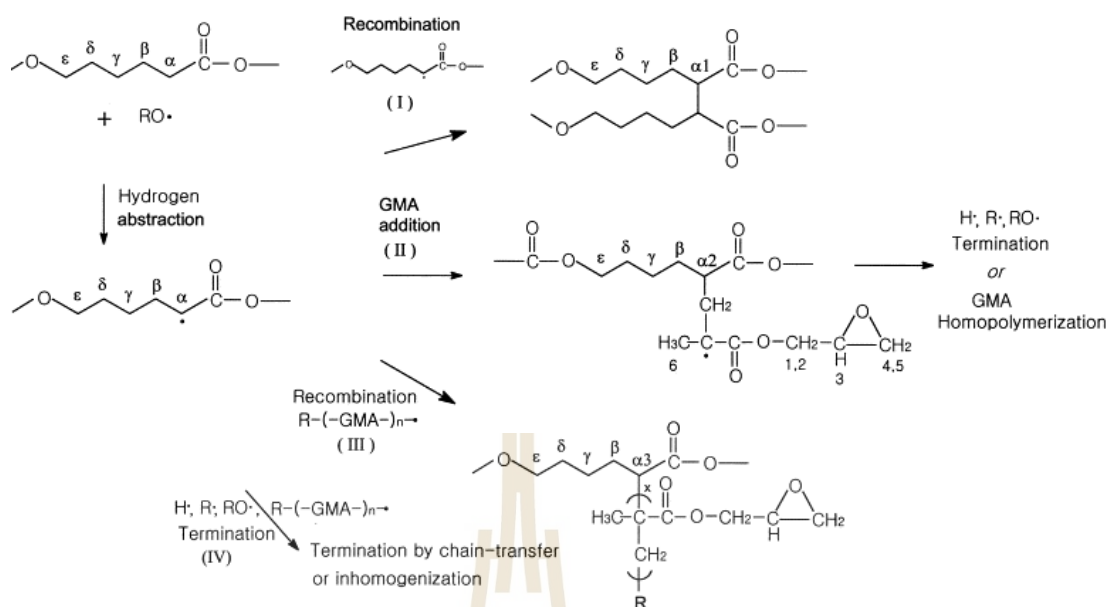


Figure 2.12 Proposed reaction pathway for the grafting reaction of GMA to PCL (Kim et al., 2001).

Burton, Woodhead, Coates, and Gough (2010) studied the melt-phase grafting of glycidyl methacrylate (GMA) onto polypropylene on a closely intermeshing corotating twin-screw extruder. The modification of the base polypropylene to produce GMA-grafted polypropylene was achieved via peroxide-induced hydrogen abstraction from the polypropylene followed by the grafting of the GMA monomer. In this study, the order of the reactant addition was investigated as a route to improving graft yields and reducing side reactions (degradation). The results showed that the order of injection of the reactants played an important role in achieving an increase in the degree of grafting. When the GMA was injected before the peroxide, the grafting degree increased and the chain scission decreased considerably.

Xu et al. (2015) investigated the grafting of GMA onto PP chains by melt grafting using a homemade reactive corotating twin-screw extruder. The degree of grafting was determined by a chemical titration method. The thermal behaviors of glycidyl methacrylate (GMA)-grafted polypropylene (PP) (PP-g-GMA) were investigated by differential scanning calorimetry (DSC), polarized optical microscopy (POM), wide-angle X-ray diffraction (WAXD), dynamic mechanical analysis (DMA), and thermogravimetric analysis (TGA). DSC results suggested that the GMA grafted PP exhibited higher crystallization temperature, higher melting temperature, and higher crystallinity compared with the neat PP. The isothermal crystallization kinetics was analyzed with the Avrami equation and the total crystallization activation energy was calculated. It was concluded that the crystallization processes of PP and the grafted PP were controlled by nucleation and the values of the crystallization activation energy of PP and the grafted PP were almost identical. POM results suggested that the GMA grafted PP exhibited smaller spherulites size compared with the neat PP. WAXD patterns indicated that the neat PP encouraged the formation of γ phase, compared with the grafted PP, during the crystallization process. DMA results showed that melt grafting did not induce a clear effect on the γ -transition and β -transition of the amorphous phase but resulted in a decrease in mobility of the PP chains in the crystals. TGA curves suggested that the melt grafting slightly improved the thermal stability of PP.

2.9.2 GMA-grafted poly(lactic acid) (PLA-g-GMA) as a compatibilizing agent for PLA-based composites

Xu, Tang, and Zhu (2012) studied the grafting of GMA onto PLA chain via free-radical polymerization under nitrogen in toluene solution. The results of FTIR

and $^1\text{H-NMR}$ spectra with the appearance of new peaks, which are attributed to epoxy group, confirmed that the GMA was successfully grafted onto the PLA chain. The result from GPC analysis also showed that the molecular weight and polydispersity of glycidyl methacrylate grafted poly(lactic acid) (PLA-g-GMA) increased compared to that of pure PLA. Moreover, using PLA-g-GMA as a coupling agent for PLA/bamboo fiber biocomposites helped to improve the mechanical properties of composites. The flexural modulus and flexural strength of the PLA/bamboo fiber biocomposites increased obviously as the content of PLA-g-GMA increased. The improvements were due to the improved interfacial adhesion between the bamboo fibers and the PLA matrix. The addition of PLA-g-GMA also enhanced the crystallization of the PLA.

Liu, Jiang, and Chen (2012) investigated the grafting of GMA onto PLA in a batch mixer using benzoyl peroxide as an initiator. The result showed that the graft content increased from 1.8 to 11.0 % as the GMA concentration in the feed was varied from 5 to 20 wt%. Compared with the pure PLA, tensile strength at break of PLA-g-GMA was slightly decreased. This decrease of tensile strength at break was attributed to the decrease of crystallinity of the PLA. This was due to the hindrance of PLA crystallization by the increase of chain structural irregularity caused by grafting reaction. The grafting mechanism of GMA onto PLA is presented in Figure 2.13. As can be seen from Figure 2.13 that the GMA grafting can take place on the PLA macroradical through step (2) and step (3). Furthermore, the crosslinking reaction through step (1) can occur during the grafting reaction. Besides that, it is reported that the epoxy group of GMA can react with hydroxyl groups and carboxyl end groups of PLA in the melt mixing (Jeong and Xanthos, 2007). Moreover, the physical properties of PLA/starch blend was improved significantly when using PLA-g-GMA as a

compatibilizer for the blend. It was due to the better interfacial adhesion between PLA and starch.

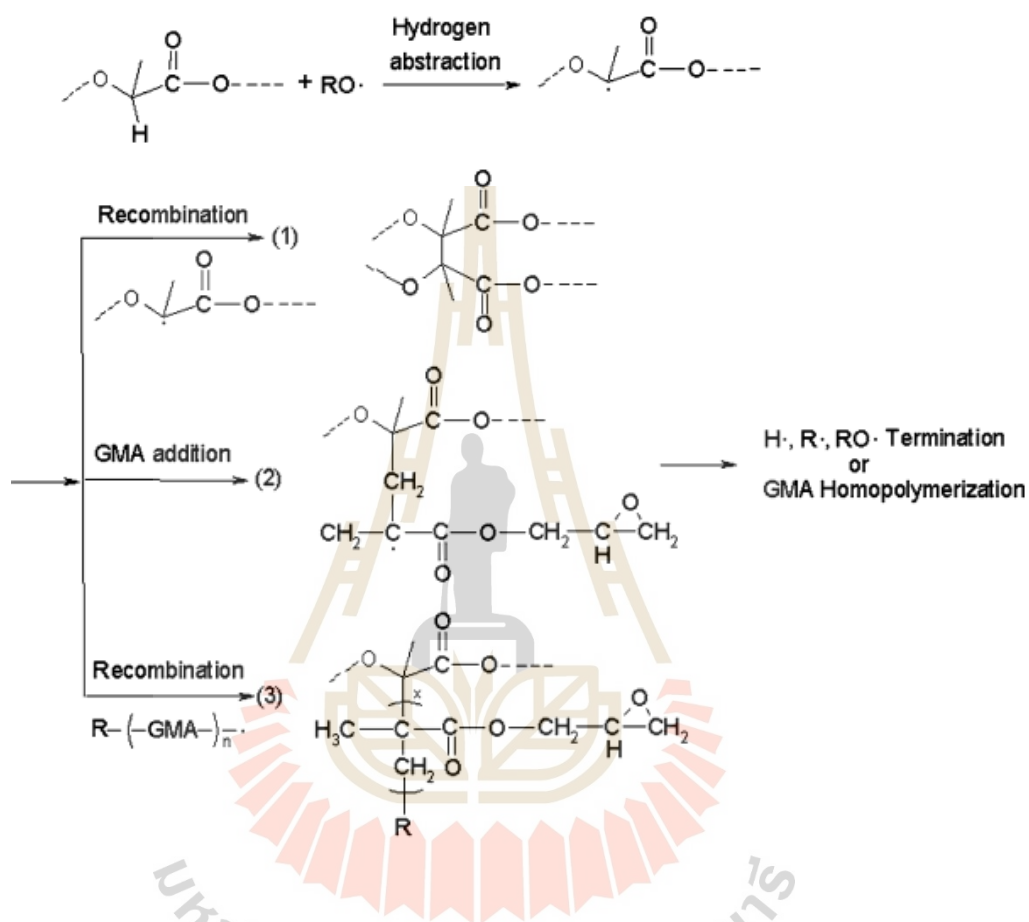


Figure 2.13 Mechanism of the grafting of GMA onto the PLA chain (Liu et al., 2012).

Mohanty and Nayak (2015) studied on the synthesis of poly (lactic acid) (PLA)-graft-glycidyl methacrylate (GMA) as well as its influence on the properties of PLA/banana fiber biocomposites. PLA-g-GMA was synthesized by melt blending PLA with GMA using benzoyl peroxide (BPO) and dicumyl peroxide (DCP) as initiators. Graft copolymerization was confirmed by FTIR and ¹H-NMR spectroscopic studies. Moreover, elemental analysis showed that the graft copolymerization using BPO

obtained higher % of grafting as compared with DCP. The influence of PLA-g-GMA content on the mechanical, thermal and moisture resistance properties of the composite was investigated. The results showed that the addition of 15 wt% PLA-g-GMA content in the biocomposite provided optimum tensile and flexural strength, which is attributed to the greater compatibility between fiber and PLA matrix. Furthermore, impact strength of PLA-g-GMA compatibilized biocomposites increasing gradually with increasing PLA-g-GMA content. The thermal stability and moisture absorption resistance of biocomposites were improved with the addition of PLA-g-GMA.

Li, Zhou, and Pei (2010) prepared a novel copolymer of PLA and glycidyl methacrylate (PLA-co-PGMA) by free radical polymerization and used it to modify the cellulose surface. The characterization of the PLA-co-PGMA copolymers was conducted by FTIR and gel permeation chromatography (GPC). FTIR analysis proved the reactions of bacterial cellulose and PLA-co-PGMA and ensured efficient chemical bonding of them. Moreover, contact angle measurements revealed that the hydrophilic character of the cellulose nanofibers can be strongly decreased after the treatment. Interfacial thermodynamic properties were studied and the results suggested that PLA-co-PGMA was efficient in the modification of bacterial cellulose nanofibers surface and in improvement of compatibility of PLA/cellulose nanofibers composites. In addition, after being modified with PLA-co-PGMA), the dispersability of the cellulose nanofibers in PLA matrix was found to be improved.

2.10 Cellulose nanofibers (CNFs) reinforced PLA-based composites

Incorporation of cellulose nanofibers into a polymer matrix may have several positive consequences. For example, well-dispersed cellulose nanonocrystals are

expected to improve mechanical performance through stress transfer from the matrix to the cellulose nanofibers. Changes in polymer chain mobility as well as crystalline nucleation effect may also affect thermomechanical behavior and barrier properties. There are however two major challenges in the dispersion of cellulose nanofibers into a polymer matrix. The first one is that the CNFs are produced in an aqueous media. The elimination of the suspending media through freeze-drying or spray-drying may therefore cause CNF agglomeration. The second challenge is related to the highly hydrophilic character of cellulose nanofibers, which may also cause their dispersion to be more difficult in non-polar polymer matrices. So far, melt blending and solvent casting have been the main processing routes used in the majority of studies on polymer–CNF composites. However, during melt processing, agglomeration of CNF is prone to occur due to poor polymer wetting on the hydrophilic CNF surface and to strong particle–particle interactions. Moreover, because of the high temperature and intensive mixing involved in melt-processing, degradation of the CNF is also possible. To avoid these problems, solvent mixing followed by solvent casting has been used. Nevertheless, solution blending is not a viable mixing route for industrial production of reinforced thermoplastics.

Ahmad and Luyt (2012) studied CNF reinforced PLA composites with various CNF contents by using an internal mixer. The results from TEM images showed that the poor dispersion of freeze-dried pristine CNF in PLA matrix was observed. However, with the presence of CNF the stiffness of the nanocomposites was improved, but the intensity of the glass transition relaxation was reduced. Moreover, the incorporation of CNF altered the crystallization and the melting behavior of PLA.

Raquez et al. (2012) prepared modified CNF reinforced PLA composites by using melt-extrusion technique in a twin-screw microextruder. CNF was modified by the functional trialkoxysilanes bearing various organic moieties (alkyl, amino, and (meth)acryloxy). The results from thermal and morphological characterization showed that the dispersion of silanized CNF in PLA matrix was improved. However, the presence of aggregates was still evidenced, which indicated that nanolevel dispersion was not generalized. Besides that, the thermomechanical and thermal analyses also showed that silanized CNF acted as reinforcing agent for PLA matrix, enhancing the crystallinity degree and reinforcing the thermomechanical properties of PLA matrix.

In order to improve the melt-mixing procedure, the use of a surfactant has been investigated. Surfactant was solution blended to the CNF suspension, water was eliminated by freeze-drying of the surfactant/CNF system prior to melt-mixing in the PLA matrix. Bondeson and Oksman (2007) investigated the preparation of biodegradable nanocomposites based on 5 wt% CNF and PLA by using an extrusion process. An anionic surfactant (5, 10 and 20 wt%) was used to improve the dispersion of the CNF in the PLA matrix. The results showed that increased surfactant content resulted in improved dispersion of CNF but at the same time degraded the PLA matrix. The tensile strength and elongation at break of composites were improved.

A hybrid approach was also considered: a master batch of PLA/CNF was first prepared by solution-blending in chloroform and then casted for solvent evaporation. PLA/CNF films were cut into small pieces and extruded with the PLA matrix. Pristine and chemically modified CNF were used in the same study. With the combination of both processing methods (solution-blending and melt extrusion) the prevention of CNF degradation and excellent improvement in the nanocrystals dispersion were observed

(Bitinis et al., 2013). A similar approach was also used by Jonoobi, Harun, Mathew, and Oksman (2010) for preparing cellulose nanofibers reinforced PLA-based composites.

Another technique where ring-opening polymerized PLA branches on the surface of CNF was carried out could also improve the properties of PLA/CNF composites (Braun, Dorgan, and Hollingsworth, 2012). The covalent bonding of PLA on the surface of the CNF resulted in improved compatibility between grafted-CNF and the PLA matrix. As a result, the better dispersion of CNF in PLA matrix was obtained, leading to the improvement of the physical properties of composites.

2.11 Effect of cellulose nanofibers on physical properties of PLA-based composites

Frone, Berlioz, Chailan, and Panaitescu (2013) investigated the morphology and thermal properties of PLA-cellulose nanofibers composites. The composites were prepared by using a fully automated laboratory two roll mill from Brabender (Polymix 110L). Two blends containing 2.5 wt% of silanized and unsilanized cellulose nanofibers were investigated in this research. DSC measurements revealed higher degree of crystallinity for the composites containing untreated nanofibers and demonstrated the role of cellulose nanofibers as nucleating agents. With the addition of cellulose nanofibers, the cold crystallization peak became broader and was shifted to lower temperatures as compared to the cold crystallization of neat PLA. It was an indication of faster crystallization induced by cellulose nanofillers which acted as nucleating agents for PLA. In the case of PLA/silanized cellulose nanofibers, the peak was sharper and shifted to higher values than that of the neat PLA. This behavior was

a result of the silane treatment which improved the adhesion to the matrix. It led to the decrease of the mobility of the PLA chains which are close to the nanofibers. As a result, the crystallization rate was slower.

Pei, Zhou, and Berglund (2010) prepared PLLA/silylated cellulose nanofibers (SCNF) nanocomposites with low nanofiber content (1-2 %) by solvent casting method. In this study, CNFs were silylated by using n-dodecyldimethylchlorosilane (DDMSiCl). The results indicated that after modification, the dispersion of CNFs in PLA matrix was improved significantly. The result of mechanical properties of obtained nanocomposites also presented that the composites reinforced with unmodified cellulose nanofibers did not show any improvements in tensile modulus and tensile strength compared to pure PLLA. Meanwhile, the addition of only 1 wt% of SCNF in PLLA resulted in a 27 % increase in tensile modulus and a 21 % increase in the tensile strength compared to pure PLLA. However, the elongation at break was reduced in both PLLA/CNF and PLLA/SCNF composite samples. It was because the stiff reinforcements of cellulose nanofibers caused substantial local stress concentrations and failure at reduced strain. The influence of CNFs and SCNFs on crystallization rate of PLLA was investigated by polarized optical microscopy (POM) technique. The results showed that with the addition of CNF, the nucleus density of PLLA crystallites increased at 5 min and 10 min as compared to the pure PLLA. Furthermore, the nucleus density increased significantly with the addition of SCNF. It was due to improved dispersion of cellulose nanofibers in the PLLA matrix. As a result, more crystals were able to nucleate and grow on the increased surface area of the interfaces because of increasing numbers of nucleating particles. Therefore, obviously,

the crystallization rate of PLLA was improved dramatically by addition of bio-based nucleating agents of CNF and SCNF.

Espino-Pérez et al. (2013) studied the preparation of PLA/urethanized cellulose nanofibers nanocomposites with filler contents ranging from 2.5 to 15 wt% using solvent casting method. Cellulose nanofibers were modified by *n*-octadecyl isocyanate. The results showed that unmodified nanofibers did not affect significantly on crystallization behavior of PLA. However, the modified nanofibers had a clear evidence of nucleating effect, which increased with its concentration. Moreover, the results from mechanical properties of nanocomposites indicated that both tensile strength and elongation at break of composites reinforced with unmodified nanofibers decreased with increasing content of nanofibers. It was due to the poor dispersion of unmodified nanofibers in PLA matrix. Conversely, the mechanical properties of biocomposites were improved when modified nanofibers were incorporated. Improvement was higher at lower concentrations. In addition, the results of barrier properties of obtained nanocomposites showed that the oxygen permeability did not show any significant differences between the neat polymer and PLA/unmodified nanofibers and PLA/modified nanofibers composites.

Lin, Huang, Chang, Feng, and Yu (2011) investigated the preparation of PLA/acetylated cellulose nanofibers nanocomposite with nanofiber content ranging from 1 to 10 % by solution casting. The results from mechanical properties of nanocomposites presented that when the nanofibers were introduced at 6 wt% into the PLA-based polymeric matrix, the tensile strength of the PLA/acetylated nanofibers nanocomposite was enhanced by 61.3 % and the Young's modulus was 1.5-fold greater than those of the neat PLA. This was mainly attributed to the endurance of higher stress

of the rigid nanofibers and the improved interfacial adhesion between filler and matrix. Moreover, the thermal property of the nanocomposites was also improved by the addition of cellulose nanofibers. Additionally, because of nucleation of the cellulose nanofibers, the crystalline properties of all nanocomposites were enhanced.

Sanchez-Garcia and Lagaron (2010) investigated the effect of cellulose nanofibers on the barrier properties of PLA-based nanocomposites. In this study, the cellulose nanofibers reinforced PLA nanocomposites were prepared by incorporating 1, 2, 3 and 5 wt% of the cellulose nanofibers into the PLA matrix by a chloroform solution casting method. The results indicated that the water permeability of nanocomposites decreased with the addition of cellulose nanofibers by up to 82 % and the oxygen permeability by up to 90 %. Optimum barrier enhancement was found for composites containing loadings of cellulose nanofibers below 3 wt%. From these results, cellulose nanofibers exhibited novel significant potential in coatings, membranes and food agrobased packaging applications.

2.12 References

- Abdel-Razik, E., Ali, M., Abdelaal, M., and Sarhan, A. (1996). Homogeneous Photoinouced Graft Copolymerization of Acrylamide onto Abs Copolymers in the Presence of 4-Acetyldiphenyl as Photosensitizer.: 1. Influence of Butadiene Content in Abs Copolymers. **Polymer—Plastics Technology and Engineering**. 35: 865-876.
- Abdul Khalil, H. P. S., et al. (2014). Production and modification of nanofibrillated cellulose using various mechanical processes: A review. **Carbohydrate Polymers**. 99: 649-665.

- Abraham, E., et al. (2011). Extraction of nanocellulose fibrils from lignocellulosic fibres: A novel approach. **Carbohydrate Polymers**. 86: 1468-1475.
- Ahmad, E., and Luyt, A. (2012). Morphology, thermal, and dynamic mechanical properties of poly (lactic acid)/sisal whisker nanocomposites. **Polymer Composites**. 33: 1025-1032.
- Atalla, R. H., and Vanderhart, D. L. (1984). Native Cellulose: A Composite of Two Distinct Crystalline Forms. **Science**. 223: 283-285.
- Auras, R. A., Lim, L.-T., Selke, S. E., and Tsuji, H. (2011). **Poly (lactic acid): synthesis, structures, properties, processing, and applications**. New York: John Wiley & Sons.
- Bitinis, N., et al. (2013). Poly (lactic acid)/natural rubber/cellulose nanocrystal bionanocomposites Part I. Processing and morphology. **Carbohydrate Polymers**. 96: 611-620.
- Bondeson, D., Mathew, A., and Oksman, K. (2006). Optimization of the isolation of nanocrystals from microcrystalline cellulose by acid hydrolysis. **Cellulose**. 13: 171-180.
- Bondeson, D., and Oksman, K. (2007). Dispersion and characteristics of surfactant modified cellulose whiskers nanocomposites. **Composite Interfaces**. 14: 617-630.
- Braun, B., and Dorgan, J. R. (2008). Single-step method for the isolation and surface functionalization of cellulosic nanowhiskers. **Biomacromolecules**. 10: 334-341.

- Braun, B., Dorgan, J. R., and Chandler, J. P. (2008). Cellulosic Nanowhiskers. Theory and Application of Light Scattering from Polydisperse Spheroids in the Rayleigh–Gans–Debye Regime. **Biomacromolecules**. 9: 1255-1263.
- Braun, B., Dorgan, J. R., and Hollingsworth, L. O. (2012). Supra-molecular ecobionanocomposites based on polylactide and cellulosic nanowhiskers: synthesis and properties. **Biomacromolecules**. 13: 2013-2019.
- Burton, E. L., Woodhead, M., Coates, P., and Gough, T. (2010). Reactive grafting of glycidyl methacrylate onto polypropylene. **Journal of Applied Polymer Science**. 117: 2707-2714.
- Cao, X., Chen, Y., Chang, P. R., Stumborg, M., and Huneault, M. A. (2008). Green composites reinforced with hemp nanocrystals in plasticized starch. **Journal of Applied Polymer Science**. 109: 3804-3810.
- Cartier, L., et al. (2000). Epitaxial crystallization and crystalline polymorphism of polylactides. **Polymer**. 41: 8909-8919.
- Cho, K. Y., Eom, J. Y., Kim, C. H., and Park, J. K. (2008). Grafting of glycidyl methacrylate onto high-density polyethylene with reaction time in the batch mixer. **Journal of Applied Polymer Science**. 108: 1093-1099.
- Choi, S.-H., and Nho, Y. C. (2000). Radiation-induced graft copolymerization of binary monomer mixture containing acrylonitrile onto polyethylene films. **Radiation Physics and Chemistry**. 58: 157-168.
- Cocca, M., Di Lorenzo, M. L., Malinconico, M., and Frezza, V. (2011). Influence of crystal polymorphism on mechanical and barrier properties of poly (l-lactic acid). **European Polymer Journal**. 47: 1073-1080.

- Conn, R., et al. (1995). Safety assessment of polylactide (PLA) for use as a food-contact polymer. **Food and Chemical Toxicology**. 33: 273-283.
- De Santis, P., and Kovacs, A. J. (1968). Molecular conformation of poly(S-lactic acid). **Biopolymers**. 6: 299-306.
- De Souza Lima, M. M., and Borsali, R. (2004). Rodlike Cellulose Microcrystals: Structure, Properties, and Applications. **Macromolecular Rapid Communications**. 25: 771-787.
- Dinand, E., Vignon, M., Chanzy, H., and Heux, L. (2002). Mercerization of primary wall cellulose and its implication for the conversion of cellulose I→cellulose II. **Cellulose**. 9: 7-18.
- Espino-Pérez, E., et al. (2013). Influence of chemical surface modification of cellulose nanowhiskers on thermal, mechanical, and barrier properties of poly (lactide) based bionanocomposites. **European Polymer Journal**. 49: 3144-3154.
- Frone, A. N., S. Berlioz, J.-F. Chailan and D. M. Panaitescu (2013). Morphology and thermal properties of PLA–cellulose nanofibers composites. **Carbohydrate Polymers**. 91: 377-384.
- Garlotta, D. (2001). A literature review of poly (lactic acid). **Journal of Polymers and the Environment**. 9: 63-84.
- Hamad, W. Y., and Hu, T. Q. (2010). Structure–process–yield interrelations in nanocrystalline cellulose extraction. **The Canadian Journal of Chemical Engineering**. 88: 392-402.
- Hartmann, M., and Kaplan, D. (1998). **Biopolymers from renewable resources**. Berlin: Springer-Verlag.

- Holt, B. L., Stoyanov, S. D., Pelan, E., and Paunov, V. N. (2010). Novel anisotropic materials from functionalised colloidal cellulose and cellulose derivatives. **Journal of Materials Chemistry**. 20: 10058-10070.
- Holten, C., Muller, A., and Reh binder, D. (1971). **Properties and chemistry of lactic acid and derivatives**. Weinheim: Verlag Chemie Gmbh.
- Hoogsteen, W., Postema, A., Pennings, A., Ten Brinke, G., and Zugenmaier, P. (1990). Crystal structure, conformation and morphology of solution-spun poly (L-lactide) fibers. **Macromolecules**. 23: 634-642.
- Jeong, B. J., and Xanthos, M. (2007). Reactive modification of PBT with applications in low density extrusion foaming. **Polymer Engineering & Science**. 47: 244-253.
- Jonoobi, M., Harun, J., Mathew, A. P., and Oksman, K. (2010). Mechanical properties of cellulose nanofiber (CNF) reinforced polylactic acid (PLA) prepared by twin screw extrusion. **Composites Science and Technology**. 70: 1742-1747.
- Kim, C.-H., Cho, K., and Park, J.-K. (2001). Grafting of glycidyl methacrylate onto polycaprolactone: preparation and characterization. **Polymer**. 42: 5135-5142.
- Klemm, D., Heublein, B., Fink, H. P., and Bohn, A. (2005). Cellulose: fascinating biopolymer and sustainable raw material. **Angewandte Chemie (International ed. in English)**. 44: 3358-3393.
- Kosugi, A., et al. (2009). Production of ethanol from cassava pulp via fermentation with a surface-engineered yeast strain displaying glucoamylase. **Renewable Energy**. 34: 1354-1358.

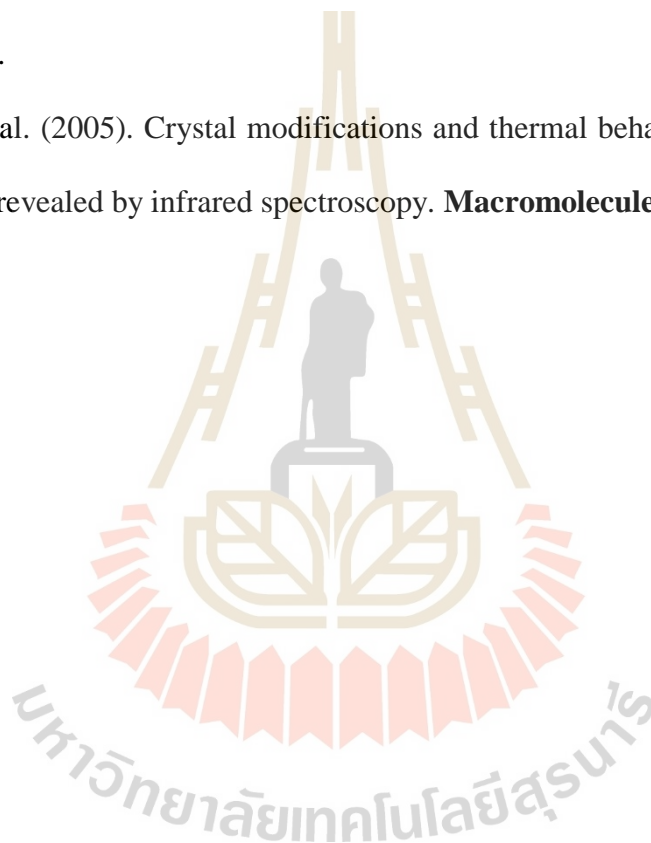
- Lavoine, N., Desloges, I., Dufresne, A., and Bras, J. (2012). Microfibrillated cellulose – Its barrier properties and applications in cellulosic materials: A review. **Carbohydrate Polymers**. 90: 735-764.
- Leung, A. C., et al. (2011). Characteristics and Properties of Carboxylated Cellulose Nanocrystals Prepared from a Novel One-Step Procedure. **Small**. 7: 302-305.
- Li, Z. Q., Zhou, X. D., and Pei, C. H. (2010). Synthesis of PLA-co-PGMA copolymer and its application in the surface modification of bacterial cellulose. **International Journal of Polymeric Materials**. 59: 725-737.
- Lin, N., Huang, J., Chang, P. R., Feng, J., and Yu, J. (2011). Surface acetylation of cellulose nanocrystal and its reinforcing function in poly (lactic acid). **Carbohydrate Polymers**. 83: 1834-1842.
- Liu, D., Zhong, T., Chang, P. R., Li, K., and Wu, Q. (2010). Starch composites reinforced by bamboo cellulosic crystals. **Bioresource Technology**. 101: 2529-2536.
- Liu, J., Jiang, H., and Chen, L. (2012). Grafting of glycidyl methacrylate onto poly (lactide) and properties of PLA/starch blends compatibilized by the grafted copolymer. **Journal of Polymers and the Environment**. 20: 810-816.
- Man, Z., et al. (2011). Preparation of cellulose nanocrystals using an ionic liquid. **Journal of Polymers and the Environment**. 19: 726-731.
- Mandal, A., and Chakrabarty, D. (2011). Isolation of nanocellulose from waste sugarcane bagasse (SCB) and its characterization. **Carbohydrate Polymers**. 86: 1291-1299.

- Mohanty, S., and Nayak, S. K. (2015). Effect of poly (lactic acid)-graft-glycidyl methacrylate as a compatibilizer on properties of poly (lactic acid)/banana fiber biocomposites. **Polymers for Advanced Technologies**. 27: 515-524.
- Moon, R. J., Martini, A., Nairn, J., Simonsen, J., and Youngblood, J. (2011). Cellulose nanomaterials review: structure, properties and nanocomposites. **Chemical Society Reviews**. 40: 3941-3994.
- Ohta, M., Obuchi, S., and Yoshida, Y., **US Patent** 5,512,653 (to Misui Tuatsu), 1996.
- Oke, I. (2010). Nanoscience in nature: cellulose nanocrystals. **Studies by Undergraduate Researchers at Guelph**. 3: 77-80.
- Pei, A., Zhou, Q., and Berglund, L. A. (2010). Functionalized cellulose nanocrystals as biobased nucleation agents in poly (l-lactide)(PLLA)-crystallization and mechanical property effects. **Composites Science and Technology**. 70: 815-821.
- Peng, B. L., Dhar, N., Liu, H. L., and Tam, K. C. (2011). Chemistry and applications of nanocrystalline cellulose and its derivatives: A nanotechnology perspective. **The Canadian Journal of Chemical Engineering**. 89: 1191-1206.
- Peng, Y., Gardner, D., and Han, Y. (2012). Drying cellulose nanofibrils: in search of a suitable method. **Cellulose**. 19: 91-102.
- Pesneau, I., Champagne, M. F., and Huneault, M. A. (2004). Glycidyl methacrylate-grafted linear low-density polyethylene fabrication and application for polyester/polyethylene bonding. **Journal of Applied Polymer Science**. 91: 3180-3191.

- Petasch, W., Räuchle, E., Walker, M., and Elsner, P. (1995). Improvement of the adhesion of low-energy polymers by a short-time plasma treatment. **Surface and Coatings Technology**. 74: 682-688.
- Qi, R., Yu, Q., Shen, Y., Liu, Q., and Zhou, C. (2006). Grafting copolymerization of maleic anhydride onto styrene-butadiene-styrene block copolymer through solvothermal process. **Journal of Applied Polymer Science**. 102: 5274-5279.
- Qin, Z.-Y., Tong, G., Chin, Y. F., and Zhou, J.-C. (2011). Preparation of ultrasonic-assisted high carboxylate content cellulose nanocrystals by TEMPO oxidation. **BioResources**. 6: 1136-1146.
- Raquez, J.-M., et al. (2012). Surface-modification of cellulose nanowhiskers and their use as nanoreinforcers into polylactide: a sustainably-integrated approach. **Composites Science and Technology**. 72: 544-549.
- Russell, K. (2002). Free radical graft polymerization and copolymerization at higher temperatures. **Progress in Polymer Science**. 27: 1007-1038.
- Sadeghifar, H., Filpponen, I., Clarke, S. P., Brougham, D. F., and Argyropoulos, D. S. (2011). Production of cellulose nanocrystals using hydrobromic acid and click reactions on their surface. **Journal of Materials Science**. 46: 7344-7355.
- Sanchez-Garcia, M. D., and Lagaron, J. M. (2010). On the use of plant cellulose nanowhiskers to enhance the barrier properties of polylactic acid. **Cellulose**. 17: 987-1004.
- Saxena, I., and Brown, M. (2005). Cellulose Biosynthesis: Current Views and Evolving Concepts. **Annals of Botany**. 96: 9-21.

- Silvério, H. A., Flauzino Neto, W. P., Dantas, N. O., and Pasquini, D. (2013). Extraction and characterization of cellulose nanocrystals from corncob for application as reinforcing agent in nanocomposites. **Industrial Crops and Products**. 44: 427-436.
- Spinu, M., Jackson, C., Keating, M., and Gardner, K. (1996). Material design in poly (lactic acid) systems: block copolymers, star homo-and copolymers, and stereocomplexes. **Journal of Macromolecular Science, Part A: Pure and Applied Chemistry**. 33: 1497-1530.
- Sriroth, K., Chollakup, R., Chotineeranat, S., Piyachomkwan, K., and Oates, C. G. (2000). Processing of cassava waste for improved biomass utilization. **Bioresource Technology**. 71: 63-69.
- Sriroth, K., et al. (1999). Cassava starch granule structure–function properties: influence of time and conditions at harvest on four cultivars of cassava starch. **Carbohydrate Polymers**. 38: 161-170.
- Sugiyama, J., Okano, T., Yamamoto, H., and Horii, F. (1990). Transformation of Valonia cellulose crystals by an alkaline hydrothermal treatment. **Macromolecules**. 23: 3196-3198.
- Sugiyama, J., Persson, J., and Chanzy, H. (1991). Combined infrared and electron diffraction study of the polymorphism of native celluloses. **Macromolecules**. 24: 2461-2466.
- Teixeira, E. d. M., et al. (2012). Properties of thermoplastic starch from cassava bagasse and cassava starch and their blends with poly (lactic acid). **Industrial Crops and Products**. 37: 61-68.

- Xu, T., Tang, Z., and Zhu, J. (2012). Synthesis of polylactide-graft-glycidyl methacrylate graft copolymer and its application as a coupling agent in polylactide/bamboo flour biocomposites. **Journal of Applied Polymer Science**. 125: E622-E627.
- Xu, X., et al. (2015). Thermal Behavior of Polypropylene-g-glycidyl Methacrylate Prepared by Melt Grafting. **Journal of Macromolecular Science, Part B**. 54: 32-44.
- Zhang, J., et al. (2005). Crystal modifications and thermal behavior of poly (L-lactic acid) revealed by infrared spectroscopy. **Macromolecules**. 38: 8012-8021.



CHAPTER III

EXTRACTION OF CRYSTALLINE CELLULOSE FIBERS FROM CASSAVA PULP

3.1 Abstract

In this research, crystalline cellulose fibers (CCFs) were directly extracted from a by-product of the cassava starch industry, viz. the cassava pulp (CP). Fibers were obtained by submitting the cassava pulp to acid hydrolysis treatment using sulfuric acid (H_2SO_4) as a hydrolyzing reagent. The hydrolysis was performed at different temperatures and times in order to investigate the effect of hydrolysis conditions on physical properties of obtained cellulose fibers. The material obtained after chemical treatment of CP was carefully characterized and its chemical composition was determined. The cellulose content of acid treated fibers was found to increase significantly compared to that of untreated cassava pulp. The morphological structure of the ensuing fibers was investigated by scanning electron microscopy (SEM) and transmission electron microscopy (TEM). X-ray diffraction (XRD) analysis revealed that the crystallinity increased after acid hydrolysis treatment. However, the crystallinity degree of fibers did not change considerably with the increase of temperature and hydrolysis time. The thermal stability of cassava pulp and cellulose fibers was also investigated using thermogravimetric analysis (TGA). It was found that the thermal stability of sulfuric acid treated fibers was lower than that of cassava pulp,

and the increase of hydrolysis time and temperature led to lowering the thermal stability of obtained cellulose fibers.

3.2 Introduction

Natural fibers can generally be classified based on their origin. The chemical composition of plant fibers depends on the type, age, and origin of the fiber, as well as the extraction method. The properties of natural fibers depend on their composition (Bledzki and Gassan, 1999). The major component of plant fibers is cellulose, which is a natural hydrophilic polymer composed of poly(1,4- β -D-anhydroglucopyranose) units. These units contain hydroxyl groups that enable cellulose to establish strong hydrogen bonds. The other major components of natural fibers are hemicelluloses and lignin. Hemicellulose is a branched multiple polysaccharide polymer composed of different types of sugars including glucose, xylose, galactose, arabinose, and mannose. Lignin is a highly crosslinked phenolic polymer. Both hemicellulose and lignin are amorphous polymers, whereas cellulose is a semicrystalline polymer.

Cassava is a starch-rich material, also containing proteins, lipids, lignocellulosic fibers, and sugars. The industrial exploitation of cassava starch involves the removal of soluble sugars and the separation of fibers resulting in a purified starch and a solid residue called cassava pulp. The cassava pulp is mainly composed of water (70–80 wt%), residual starch, and lignocellulosic fibers. The lignocellulosic fibers content ranges between 15 and 50 wt% of the total solid residue (dry weight basis), the remainder being residual starch (Matsui et al., 2004); (De Morais Teixeira, Róz, Luzia, de Carvalho, and da Silva Curvelo, 2005); (Pandey et al., 2000). These characteristics

suggest the possibility of using the cassava pulp as a source of lignocellulosic fibers for the extraction of new cellulose fiber structures.

Cellulose fibers attain tremendous attraction due to their unique characteristics such as very large surface to volume ratio, high surface area, good mechanical properties including a high Young's modulus, high tensile strength (Takagi and Asano, 2007); (Šturcová, Davies, and Eichhorn, 2005); (Dufresne, 2003) and a very low coefficient of thermal expansion (Takashi, Ikuyo, and Koichi, 2004), and formation of highly porous mesh as compared to other commercial fibers. These fibrous materials have recently attracted considerable interest in their role as reinforcing agents in composite materials.

Among several methods for preparing crystalline cellulose fibers, the acid hydrolysis is the most well-known and widely used. Under controlled conditions, acid hydrolysis allows removal of the amorphous regions of cellulose fiber whilst keeping the crystalline domains intact in the form of crystalline cellulose fibers (Habibi, Lucia, and Rojas, 2010); (Peng, Dhar, Liu, and Tam, 2011); (De Morais Teixeira et al., 2011). Removing the amorphous region influences the structure and crystallinity of the fibers. Furthermore, the thermal stability and surface morphology of the fibers are affected by the removal of the amorphous parts. During the cellulose fibers extraction process, the crystallinity of fibers was enhanced while the decrease in the thermal stability was observed in the case of using sulfuric acid as a hydrolysis reagent (Kargarzadeh et al., 2012); (Li et al., 2009). So far, many different resources have been used to prepare crystalline cellulose fibers, such as wood fibers (Beck-Candanedo, Roman, and Gray, 2005), coconut husk fibers (Rosa et al., 2010), bananas (Deepa et al., 2011), sisal (De

Rodriguez, Thielemans, and Dufresne, 2006), and pineapple leaves (Cherian et al., 2010).

In this study, crystalline cellulose fibers obtained from cassava pulp fibers without any purification have been prepared using sulfuric acid as a hydrolysis reagent. The effects of hydrolysis temperature and time on the crystallinity and thermal stability of the fibers were also explored.

3.3 Experimental

3.3.1 Materials

Cassava pulp was obtained from Ratchasima Boonpa Co., Ltd. Sulfuric acid (95.0–98.0 wt%) was purchased from Carlo. Cellulose membrane (D9402) was supplied from Sigma–Aldrich.

3.3.2 Preparation of crystalline cellulose fibers from cassava pulp

Before submitted to acid hydrolysis treatment, cassava pulp was ground, separated by a sieve with the mesh size of 250–425 μm , and dried in an oven at 130 $^{\circ}\text{C}$ for 25 h in order to remove excess moisture. About 10 g of cassava pulp were dispersed in 200 mL of 6.5 M sulfuric acid into a flask under mechanical stirring. Hydrolysis was conducted at different temperatures (50, 60, and 70 $^{\circ}\text{C}$) and times (30, 45, and 60 min) under vigorous stirring. The excess of sulfuric acid was removed from the ensuing suspension by centrifugation at 9000 rpm for 10 min. After that, the suspension was submitted to dialysis against distilled water using a cellulose membrane until the pH reached 6–7. The resulting suspension was submitted to an ultrasonic treatment for 10 min and stored in a refrigerator.

3.3.3 Characterization of crystalline cellulose fibers

3.3.3.1 Transmission electron microscopy (TEM)

TEM (Phillips model Tecnai G2 F30 S/TEM S-Twin) was used to examine the morphology of crystalline cellulose fibers extracted from cassava pulp. A drop of a diluted suspension (1 wt%) was deposited on the surface of a clean copper grid. The grid was negatively stained with 3 % (w/w) solution of uranyl acetate for 10s and dried at room temperature. The TEM analysis was carried out with an accelerating voltage of 80 kV.

3.3.3.2 Scanning electron microscopy (SEM)

The surface morphology of obtained crystalline cellulose fibers was observed by scanning electron microscopy (SEM) (model JSM6400). Before SEM observation, the specimens were coated with a thin gold film using a vacuum sputtering apparatus. The accelerating voltage was 20 kV.

3.3.3.3 Chemical composition

The chemical composition (dry weight basis) of untreated cassava pulp and acid treated fibers was determined according to a standard method of Animal Feed (EN ISO 13906:2008 and AOAC 973.18). The lignin content was measured according to acid detergent lignin (ADL) method. The (cellulose + lignin) content was determined by acid detergent fibers (ADF) method while the lignocellulose (cellulose + hemicellulose +lignin) content was estimated by neutral detergent fibers (NDF) method. The hemicellulose content was determined by subtracting ADF from NDF. Meanwhile, the cellulose content was found by subtracting ADL from ADF.

3.3.3.4 X-ray diffraction (XRD)

The crystallinity of cassava pulp and acid treated fibers was determined by X-ray diffraction analysis using a D8 advanced Bruker AXS diffractometer. The diffracted intensity of CuK α radiation (wavelength of 0.1542 nm) was recorded between 5° and 40° (2θ angle range) with a scan rate of 2° min⁻¹ at 40 kV and 40 mA. Samples were analyzed in transmission mode. Before performing XRD analysis, all specimens were dried at 50 °C for 12 h in an air-circulating oven. The crystallinity index (CI) was evaluated by using empirical method (Segal, Creely, Martin, and Conrad, 1959) as follows:

$$CI\% = \frac{(I_{002} - I_{am})}{I_{002}} \times 100 \quad (3.1)$$

In which I_{002} is the maximum intensity of diffraction of the (0 0 2) lattice peak at a 2θ angle between 21° and 23°, which represents both crystalline and amorphous materials. I_{am} is the intensity of diffraction of the amorphous material, which is taken at a 2θ angle between 18° and 20° where the intensity is at a minimum (Dai, Fan, and Collins, 2013).

3.3.3.5 Fourier transform infrared spectroscopy (FTIR)

The infrared spectrum of cassava pulp and acid treated fibers was obtained by a Bruker/Tensor27 II FT-IR spectrometer using attenuated total reflectance (ATR) equipped with platinum diamond crystal (TYPE A225/QL). The experiments were conducted in the range of 4000-400 cm⁻¹ with a resolution of 4 cm⁻¹ and total scans of 64 for each sample.

3.3.3.6 Thermogravimetric analysis (TGA)

Thermal stability of cassava pulp and crystalline cellulose fibers was determined using a Mettler Toledo thermogravimetric instrument (TGA/DSC1). All measurements were carried out under a nitrogen atmosphere with a gas flow of 100 mL · min⁻¹ by heating the samples from 50 to 800 °C at a heating rate of 10 °C · min⁻¹. The sample with a weight between 5 and 10 mg was used for each run.

3.4 Results and discussion

3.4.1 Morphological characterization of crystalline cellulose fibers

Figure 3.1 shows the SEM micrograph of untreated cassava pulp and acid treated fibers. For cassava pulp, granular and partially disrupted starch can be observed besides cellulose fibers. After acid hydrolysis of cassava pulp, a continuous and paper-like fibrous network film was observed. This dense web-like structure consists of crystalline cellulose fibers.

Figure 3.2 shows the TEM image of the diluted suspension obtained after acid hydrolysis. As shown in Figure 3.2, the separation of individual crystalline cellulose fibers was not observed. This indicates that the hydrolysis of cellulose fibers was not complete. It is thought due to the fact that the hydrolysis of cassava pulp was carried out without any purification, a large amount of low molecular weight sugars and cementing components such as hemicellulose and lignin exists in the cassava pulp fibers. This led to lowering the efficiency of acid hydrolysis process. As a consequence, the separation of individual crystalline cellulose fibers did not take place efficiently.

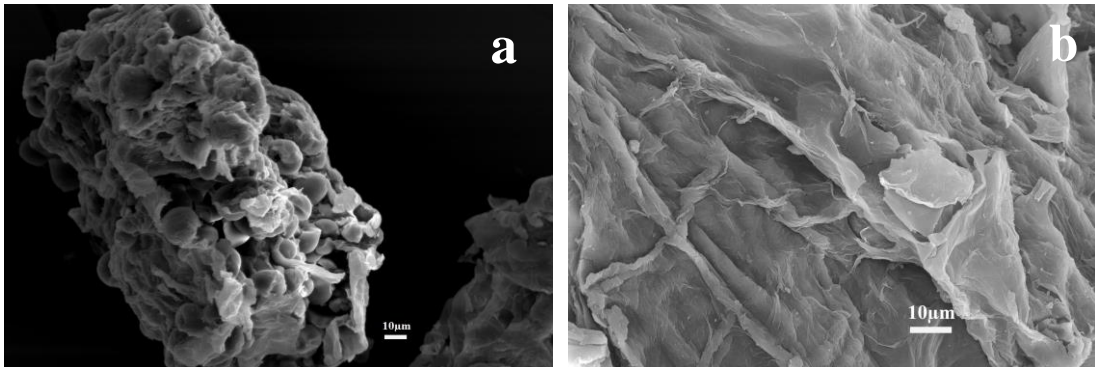


Figure 3.1 SEM micrographs of untreated cassava pulp (a) and acid treated fibers (b).

3.4.2 Chemical composition

Table 3.1 shows the chemical composition of the untreated cassava pulp and acid treated fibers. Upon acid treatment without any purification, the cellulose content of acid treated fibers was significantly higher than that of untreated one. The hemicellulose and lignin contents were found to slightly decrease after hydrolysis. However, as shown in Table 3.1, a relatively large amount of non-lignocellulose compounds still exists in the acid treated fibers. The presence of these impurities in the treated fibers could explain the aspect of the crystalline cellulose fibers films observed by SEM (Figure 3.1b). The expected porosity of the film could be filled with these impurities (Teixeira et al., 2009).



Figure 3.2 Transmission electron micrograph from diluted suspension of acid treated fibers.

Table 3.1 The chemical composition of untreated cassava pulp and acid treated fibers.

Sample	Lignocellulose			Non-lignocellulose (%)
	Cellulose (%)	Lignin (%)	Hemicellulose (%)	
Cassava pulp	21.12	3.53	8.64	66.71
Acid treated fibers	64.81	3.28	7.10	24.81

3.4.3 X-ray diffraction analysis

Both intra- and intermolecular hydrogen bonding occur in cellulose via hydroxyl groups, which results in various ordered crystalline arrangements. Figure 3.3 shows the XRD patterns for cassava pulp and acid treated fibers. The corresponding crystallinity index values are listed in Table 3.2. As shown in Figure 3.3, both diffractograms display three well-defined peaks around $2\theta = 15^\circ$, 22.7° , and 34.5° . These diffraction peaks were assigned to the typical reflection planes of cellulose I, 101, 002, and 040, respectively (Klemm, Heublein, Fink, and Bohn, 2005). It was observed that the acid treatment resulted in a narrowing and an increase of the magnitude of those three peaks most probably because of the higher crystallinity level of the hydrolyzed cellulose fibers compared to that of the untreated fibers present in cassava pulp. The peaks observed around $2\theta = 26.5^\circ$ and 30.0° are attributed to the use of small divergence slit, not from the structure of material. From Table 3.2 it can be seen that the crystallinity was enhanced after hydrolysis. However, the apparent relatively low degree of crystallinity of the hydrolyzed cellulose fibers confirms the presence of other compounds than crystalline cellulose fibers and also suggests that amorphous cellulosic domains remain. This result is in good agreement with TEM observations and indicates that not really crystalline cellulose fibers but rather partially hydrolyzed fibrillated cellulose was obtained after the acid hydrolysis treatment.

Table 3.2 Crystallinity index of untreated cassava pulp and acid treated fibers.

Sample	Crystallinity index (%)
Cassava pulp	21.59
Acid treated fibers	44.71

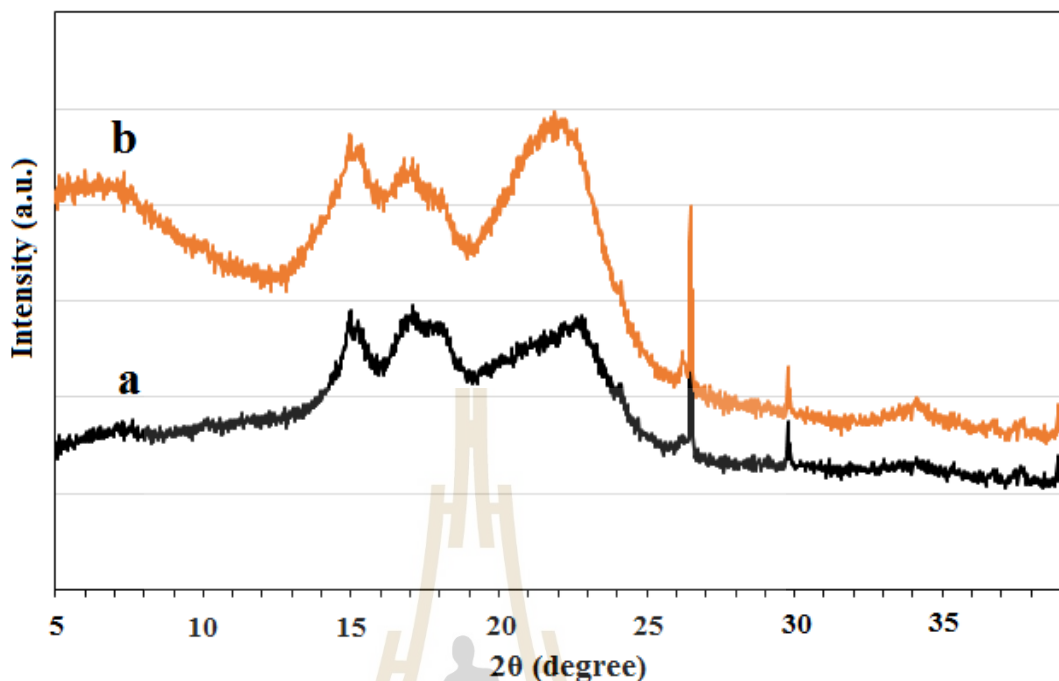


Figure 3.3 X-ray diffraction patterns of untreated cassava pulp (a) and acid treated fibers (b).

3.4.4 FTIR spectroscopy analysis

Figure 3.4 shows infrared spectra of untreated cassava pulp and acid treated fibers. In the spectrum of cassava pulp, the band near 1740 cm^{-1} is assigned mainly to the C=O stretching vibration of the carbonyl and acetyl groups in the xylan component of hemicelluloses and in the lignin (Siqueira, Bras, and Dufresne, 2010). After acid hydrolysis treatment, this peak became stronger as observed in the spectrum of acid treated fibers. This is attributed to carboxyl or aldehyde absorption arising from oxidation of the hydroxyl groups that could occur during acid hydrolysis treatment (Morán, Alvarez, Cyras, and Vázquez, 2008). The bands located around 1260 cm^{-1} ,

1060 cm^{-1} , and 898 cm^{-1} observed in both spectra were associated with the C–O and C–H stretching vibrations of the cellulose component (Alemdar and Sain, 2008). The higher intensity of these peaks observed in the spectrum of acid treated fibers indicates that the treated fibers have a higher cellulose content. This result is consistent with the chemical composition data shown in Table 3.1. It is worth noting that after acid treatment, the apparent peak located around 810 cm^{-1} was observed. This band is ascribed to C–O–S vibration indicating the presence of the sulfate groups at the outer surface of cellulose (Chen, Zhang, Zhao, and Chen, 2013).

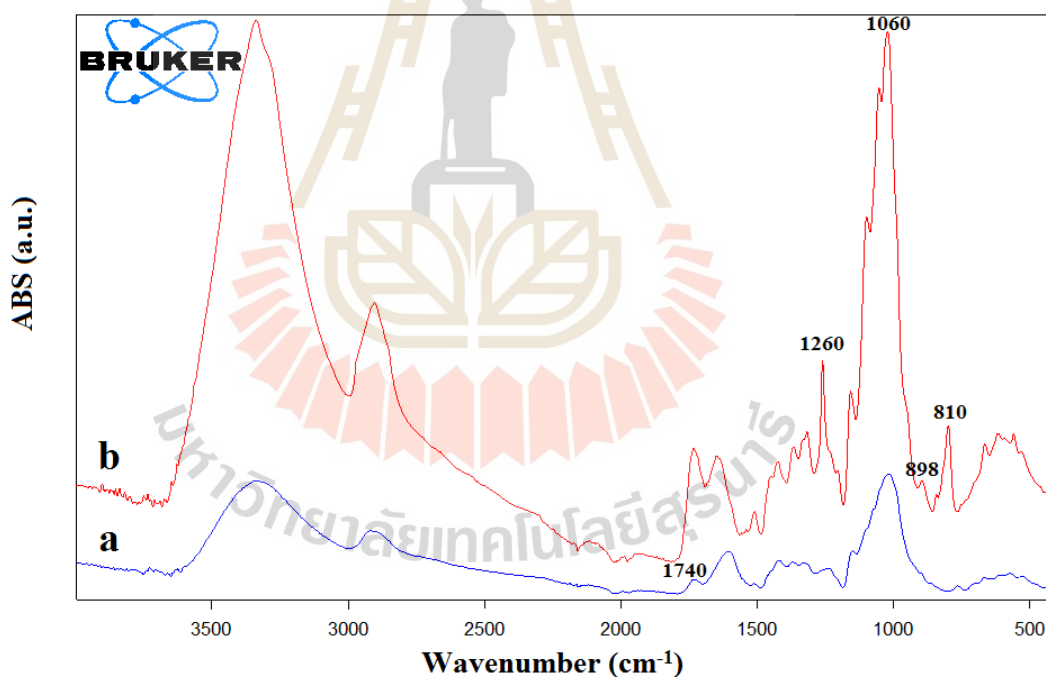


Figure 3.4 FTIR spectra of untreated cassava pulp (a) and acid treated fibers (b).

3.4.5 Thermal stability

The thermal stability of both cassava pulp and acid treated fibers was characterized using thermogravimetric analysis. It was observed from Figure 3.5 that the TGA curves of both untreated cassava pulp and acid treated fibers show an initial drop between 50 and 150 °C which corresponds to a mass loss of absorbed moisture. The initial decomposition temperature was 260 and 210 °C for cassava pulp and acid treated fibers, respectively, and it can be attributed to starch and cellulose depolymerization in both cases. The lower decomposition temperature of acid treated fibers compared to that of untreated one is due to the dehydration reaction caused by the sulfate groups introduced at the outer surface of cellulose during the acid hydrolysis treatment (Roman and Winter, 2004).

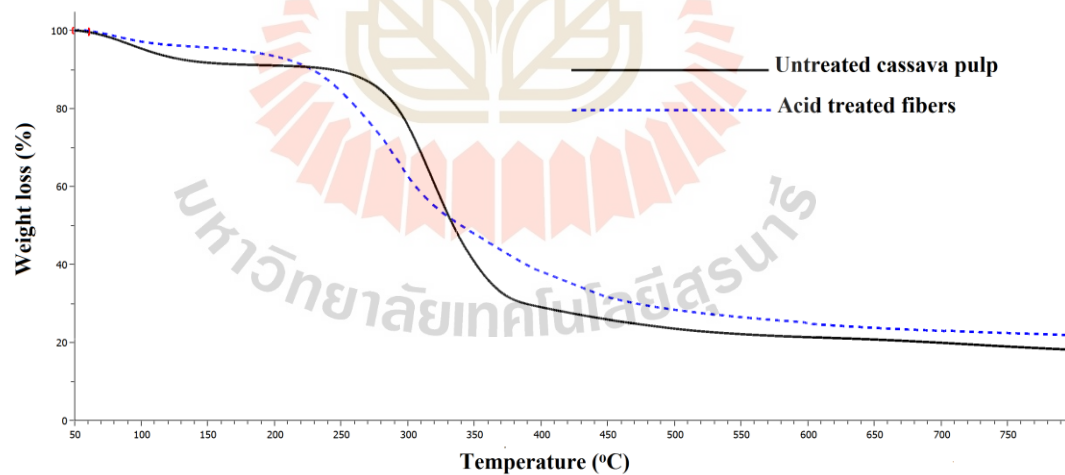


Figure 3.5 TGA curves of untreated cassava pulp and acid treated fibers.

3.4.6 Effect of hydrolysis temperature on the crystallinity and thermal stability of obtained crystalline cellulose fibers

3.4.6.1 Crystallinity by XRD analysis

Figure 3.6 shows the XRD patterns of untreated cassava pulp and obtained CCFs at various temperatures. The crystallinity index values are shown in Table 3.3. It was expected that increasing hydrolysis temperature could lead to enhancing the crystallinity of fibers due to more extensive hydrolysis of the amorphous regions of cellulose. As shown in Table 3.3, an increase in the crystallinity of fibers was observed as the temperature of hydrolysis was increased from 50 to 60 °C. However, with further increase of hydrolysis temperature up to 70 °C, the crystallinity of fibers was found to slightly lower. This can be attributed to some degradation of crystalline cellulose occurring during the hydrolysis under a high temperature. This result indicates that with the acid concentration of 6.5 M and the hydrolysis time of 45 min, the hydrolysis temperature of 60 °C was optimal for the crystallinity degree of obtained CCFs.

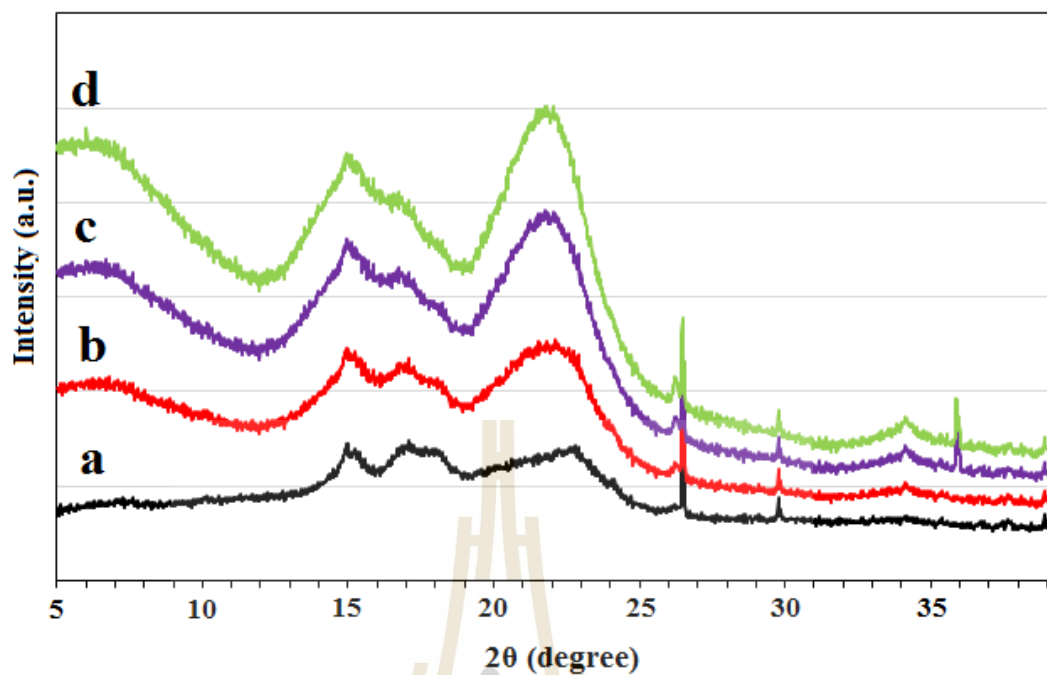


Figure 3.6 X-ray diffraction patterns of (a) untreated cassava pulp, (b) CCFs-50, (c) CCFs-70, and (d) CCFs-60.

Table 3.3 Crystallinity index of acid treated fibers at different hydrolysis temperatures.

Sample	Crystallinity index (%)
CCFs-50	41.21
CCFs-60	44.71
CCFs-70	44.01

3.4.6.2 Thermal stability

The TG curves of untreated cassava pulp and acid treated fibers at various hydrolysis temperatures are presented in Figure 3.7. It was observed that the thermal stability of obtained crystalline cellulose fibers was lower than that of untreated cassava pulp fibers and slightly decreased with the increase of hydrolysis

temperature from 50 to 70 °C. It is thought that the higher degree of sulfation of surface of the CCFs and the degradation of crystalline cellulose could occur during the hydrolysis under a high temperature. As a consequence, the thermal stability of fibers lowered with increasing temperature of hydrolysis.

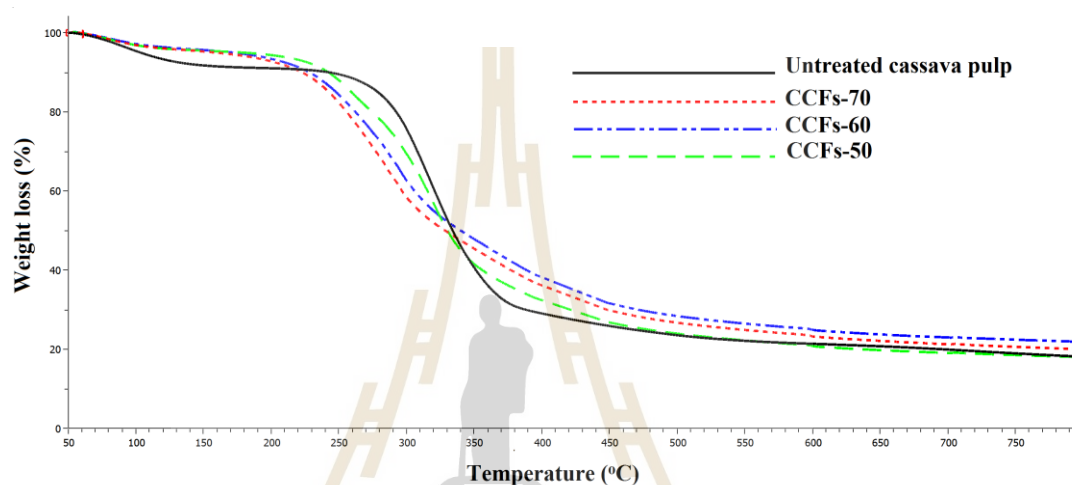


Figure 3.7 TGA curves of untreated cassava pulp and acid treated fibers at different hydrolysis temperatures.

3.4.7 Effect of hydrolysis time on the crystallinity and thermal stability of obtained crystalline cellulose fibers

3.4.7.1 Crystallinity by XRD analysis

Hydrolysis time is one of the most important parameters to consider in the extraction of crystalline cellulose fibers by acid hydrolysis method. Too long a reaction will digest the cellulose completely; too short a reaction will yield only large undispersable fibers and aggregates (Beck-Candanedo, Roman, and Gray, 2005).

Figure 3.8 and Table 3.4 show the XRD patterns and crystallinity index values of CCFs at various hydrolysis times. As shown in Table 3.4, the crystallinity of acid treated fibers did not change significantly with the increase of hydrolysis time from 30 to 60 min. Just a slight increase in the crystallinity can be observed as the hydrolysis time was increased from 30 to 60 min. This result indicates that with the acid concentration and hydrolysis temperature of 6.5 M and 60 °C, respectively, the hydrolysis time of 60 min did not cause the destruction of cellulose crystalline regions in the CCFs.

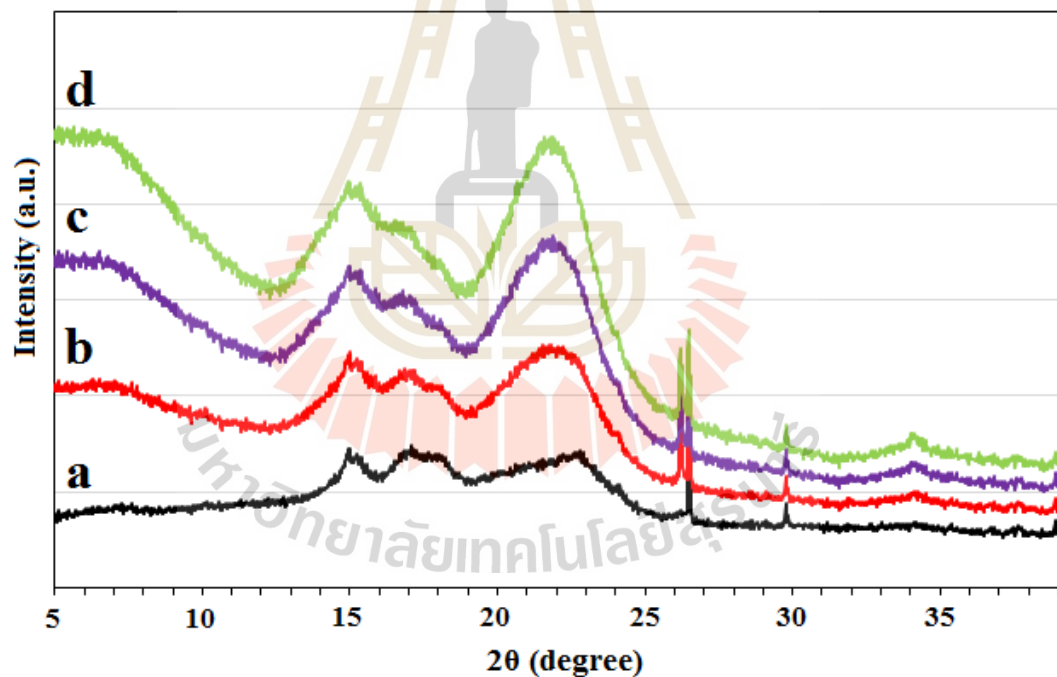


Figure 3.8 X-ray diffraction patterns of (a) untreated cassava pulp, (b) CCFs-30min, (c) CCFs-45min, and (d) CCFs-60min.

Table 3.4 Crystallinity index of acid treated fibers at different hydrolysis times.

Sample	Crystallinity index (%)
CCFs-30min	44.41
CCFs-45min	44.71
CCFs-60min	45.02

3.4.7.2 Thermal stability

Figure 3.9 shows the TG curves of untreated cassava pulp and acid treated fibers at various hydrolysis times. As observed from Figure 3.9, the temperature at which the decomposition occurs slightly decreased with an increase in the hydrolysis time. This is because the longer the hydrolysis time, the greater will be the sulfation of surface of the obtained CCFs. This leads to more sulfate groups at the outer surface of cellulose. These groups caused the dehydration reaction to occur (Roman and Winter, 2004). Furthermore, it is worth noting that even though the crystallinity of CCFs slightly increased with the increase of hydrolysis time (Table 3.4), the negative effect caused by sulfate groups dominated the positive effect resulting from a slight increase in crystallinity on the thermal stability of CCFs. As a consequence, the thermal stability of obtained CCFs decreased.

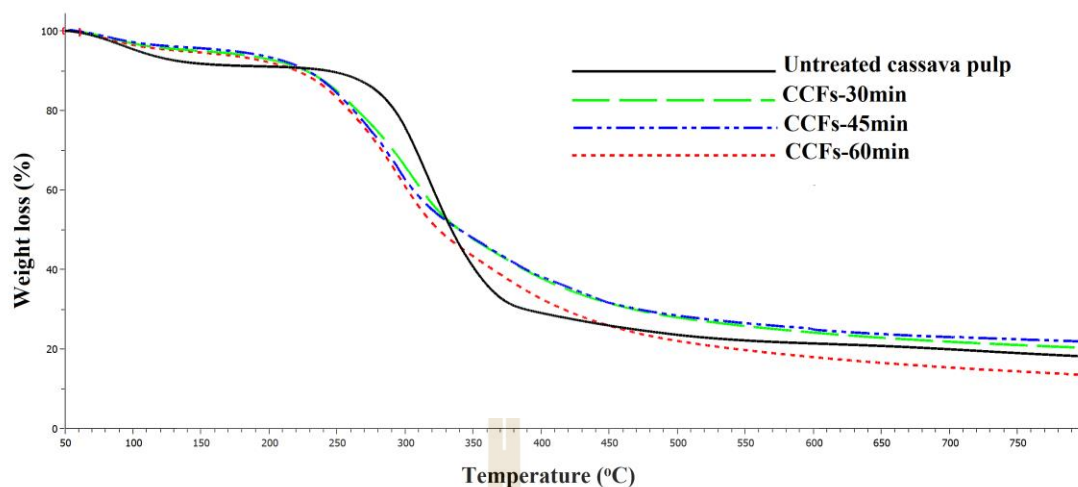


Figure 3.9 TGA curves of untreated cassava pulp and acid treated fibers at different hydrolysis times.

3.5 Conclusions

This work shows that high added-value products can be obtained from an agricultural waste residue. Crystalline cellulose fibers were directly extracted from cassava pulp without any purification. The effects of hydrolysis temperature and time on the crystallinity and thermal stability of obtained cellulose fibers were investigated. Determination of the chemical composition and microscopic observations showed the effects of acid treatment on the surface and components of cassava pulp fibers. Upon treatment, both the cellulose content and crystallinity of the fibers increased. The crystallinity of the extracted cellulose fibers was 44.71 %. The thermal stability of cassava pulp fibers decreased after acid treatment. With the acid concentration and hydrolysis temperature of 6.5 M and 60 °C, respectively, the crystallinity of obtained cellulose fibers did not change significantly with the increase of hydrolysis time from

30 to 60 min. A continuous decrease in the thermal stability of fibers with increasing hydrolysis time and temperature was observed.

It should be noted that the direct acid hydrolysis of cassava pulp without any purification was not effective for the extraction of cellulose nanofibers from cassava pulp. As a next work, the isolation and bleaching of cellulose fibers from cassava pulp before nanofibers extraction should be carried out.

3.6 References

- Alemdar, A., and Sain, M. (2008). Isolation and characterization of nanofibers from agricultural residues—Wheat straw and soy hulls. **Bioresource Technology**. 99: 1664-1671.
- Beck-Candanedo, S., Roman, M., and Gray, D. G. (2005). Effect of reaction conditions on the properties and behavior of wood cellulose nanocrystal suspensions. **Biomacromolecules**. 6: 1048-1054.
- Bledzki, A., and Gassan, J. (1999). Composites reinforced with cellulose based fibres. **Progress in Polymer Science**. 24: 221-274.
- Chen, G., Zhang, B., Zhao, J., and Chen, H. (2013). Improved process for the production of cellulose sulfate using sulfuric acid/ethanol solution. **Carbohydrate Polymers**. 95: 332-337.
- Cherian, B. M., et al. (2010). Isolation of nanocellulose from pineapple leaf fibres by steam explosion. **Carbohydrate Polymers**. 81: 720-725.

- Dai, D., Fan, M., and Collins, P. (2013). Fabrication of nanocelluloses from hemp fibers and their application for the reinforcement of hemp fibers. **Industrial Crops and Products**. 44: 192-199.
- De Morais Teixeira, E., et al. (2011). Sugarcane bagasse whiskers: extraction and characterizations. **Industrial Crops and Products**. 33: 63-66.
- De Morais Teixeira, E., Róz, D., Luzia, A., de Carvalho, A. J. F., and da Silva Curvelo, A. A. (2005). Preparation and characterisation of thermoplastic starches from cassava starch, cassava root and cassava bagasse. **Macromolecular Symposia**. 229: 266-275.
- De Rodriguez, N. L. G., Thielemans, W., and Dufresne, A. (2006). Sisal cellulose whiskers reinforced polyvinyl acetate nanocomposites. **Cellulose**. 13: 261-270.
- Deepa, B., et al. (2011). Structure, morphology and thermal characteristics of banana nano fibers obtained by steam explosion. **Bioresource Technology**. 102: 1988-1997.
- Dufresne, A. (2003). Interfacial phenomena in nanocomposites based on polysaccharide nanocrystals. **Composite Interfaces**. 10: 369-387.
- Habibi, Y., Lucia, L. A., and Rojas, O. J. (2010). Cellulose nanocrystals: Chemistry, self-assembly, and applications. **Chemical Reviews**. 110: 3479-3500.
- Kargarzadeh, H., et al. (2012). Effects of hydrolysis conditions on the morphology, crystallinity, and thermal stability of cellulose nanocrystals extracted from kenaf bast fibers. **Cellulose**. 19: 855-866.

- Klemm, D., Heublein, B., Fink, H. P., and Bohn, A. (2005). Cellulose: fascinating biopolymer and sustainable raw material. **Angewandte Chemie (International ed. in English)**. 44: 3358-3393.
- Li, R., et al. (2009). Cellulose whiskers extracted from mulberry: A novel biomass production. **Carbohydrate Polymers**. 76: 94-99.
- Matsui, K. N., et al. (2004). Cassava bagasse-Kraft paper composites: analysis of influence of impregnation with starch acetate on tensile strength and water absorption properties. **Carbohydrate Polymers**. 55: 237-243.
- Morán, J. I., Alvarez, V. A., Cyras, V. P., and Vázquez, A. (2008). Extraction of cellulose and preparation of nanocellulose from sisal fibers. **Cellulose**. 15: 149-159.
- Pandey, A., et al. (2000). Biotechnological potential of agro-industrial residues. II: cassava bagasse. **Bioresource Technology**. 74: 81-87.
- Peng, B., Dhar, N., Liu, H., and Tam, K. (2011). Chemistry and applications of nanocrystalline cellulose and its derivatives: a nanotechnology perspective. **The Canadian Journal of Chemical Engineering**. 89: 1191-1206.
- Roman, M., and Winter, W. T. (2004). Effect of sulfate groups from sulfuric acid hydrolysis on the thermal degradation behavior of bacterial cellulose. **Biomacromolecules**. 5: 1671-1677.
- Rosa, M., et al. (2010). Cellulose nanowhiskers from coconut husk fibers: Effect of preparation conditions on their thermal and morphological behavior. **Carbohydrate Polymers**. 81: 83-92.

- Segal, L., Creely, J. J., Martin, A. E., and Conrad, C. M. (1959). An Empirical Method for Estimating the Degree of Crystallinity of Native Cellulose Using the X-Ray Diffractometer. **Textile Research Journal**. 29: 786-794.
- Siqueira, G., Bras, J., and Dufresne, A. (2010). Luffa cylindrica as a lignocellulosic source of fiber, microfibrillated cellulose and cellulose nanocrystals. **BioResources**. 5: 727-740.
- Šturcová, A., Davies, G. R., and Eichhorn, S. J. (2005). Elastic modulus and stress-transfer properties of tunicate cellulose whiskers. **Biomacromolecules**. 6: 1055-1061.
- Takagi, H., and Asano, A. (2007). Characterization of “green” composites reinforced by cellulose nanofibers. **Key Engineering Materials**. 334: 389-392.
- Takashi, N., Ikuyo, M., and Koichi, H. (2004). All-cellulose composite. **Macromolecules**. 37: 7683-7687.
- Teixeira, E. d. M., et al. (2009). Cassava bagasse cellulose nanofibrils reinforced thermoplastic cassava starch. **Carbohydrate Polymers**. 78: 422-431.

CHAPTER IV

EXTRACTION OF CELLULOSE MICROFIBERS FROM CASSAVA PULP

4.1 Abstract

Due to the increasing demand for alternatives to unrenovable petroleum supplies, the use of renewable materials for industrial applications is becoming more important. In this regard, cellulose microfibrils extracted from cassava pulp are one of the promising materials. The objective of this work is to develop a chemical treatment to obtain cellulose microfibrils from cassava pulp. The process included alkali treatment and acid hydrolysis treatment. The alkali and acid treatments of cassava pulp were carried out by using NaOH and HCl solutions, respectively. In an effort to find the optimal conditions for these chemical treatments, various reactions with different temperatures and times were performed. Besides that, the sequence of two reactions (alkali treatment and acid hydrolysis treatment) was also varied in order to find out a proper reaction sequence for these chemical treatments. The morphological structure, chemical structure, degree of crystallinity and thermal stability of cellulose microfibrils were investigated using scanning electron microscopy (SEM), Fourier transform infrared (FTIR) spectroscopy, X-ray diffraction (XRD), and thermogravimetric analysis (TGA), respectively. The results demonstrated that this alkali – acid treatment

could remove partially non-cellulosic materials from the structure of fibers and resulted in higher thermal stability and degree of crystallinity.

4.2 Introduction

In terms of biocomposite applications, cellulose microfiber has been used as one of the potential reinforcements. Superior properties of this reinforcement are indicated by its high surface area and specific strength. Cellulose microfibers can be extracted from a variety of cellulosic sources such as plants, bacteria, animals (tunicates) and algae. Cassava pulp is the main byproduct of starch production from cassava tubers. In addition to residual starch, this material contains 15-50 % cellulose fibers (dry weight basis) (Teixeira et al., 2012). These characteristics suggest the possibility of using the cassava pulp as a source of cellulose fibers for the extraction of cellulose microfibers. This not only produces the high-value product but also contributes to solving environmental issues. Cellulose microfibers are composed of both amorphous and crystalline parts and exhibit a web-like structure.

So far, there have been many methods including mechanical and chemical paths, which have been used to extract cellulose microfibers from lignocellulose materials. Among them, acid hydrolysis process is considered as one of the most efficient methods for the isolation of cellulose microfibers from various kinds of cellulosic materials (Rosa et al., 2010); (Teixeira et al., 2009); (Sheltami, Abdullah, Ahmad, Dufresne, and Kargarzadeh, 2012). During acid treatment, disordered amorphous regions of cellulose, which have the greatest surface area, are the first to be affected by the acid reagent. As a result, these regions are hydrolyzed to glucose,

whereas crystalline regions that have a higher resistance to acid attack remain intact (Habibi, Lucia, and Rojas, 2010); (Angles and Dufresne, 2001). The differences in the kinetics of hydrolysis between amorphous and crystalline domains are the main reasons for the acid cleavage event. Some factors such as acid type, acid concentration, hydrolysis time, acid/pulp ratio, and hydrolysis temperature are the main factors influencing on the overall efficiency of the hydrolysis process. The conditions of reaction should be controlled strictly to ensure that the amorphous regions are hydrolyzed. On the other hand, the complete hydrolysis of cellulose to glucose or even carbonization should be avoided. Up to now, hydrochloric, sulfuric, phosphoric, nitric, and hydrobromic acids have been used for cellulose microfibers preparation (Silvério, Neto, Dantas, and Pasquini, 2013); (Sadeghifar, Filpponen, Clarke, Brougham, and Argyropoulos, 2011); (Cherian et al., 2011); (Liu, Zhong, Chang, Li, and Wu, 2010). Nevertheless, sulfuric and hydrochloric acids have been extensively investigated and appear to be the most effective. An acid mixture composed of hydrochloric acid and an organic acid (acetic or butyric) was also used to extract cellulose microfibrils from cotton linter (Braun and Dorgan, 2008). By using this hydrolysis agent, the narrower diameter polydispersity indices of obtained cellulose microfibrils were observed. The dispersibility of cellulose microfibers prepared by hydrolysis in hydrochloric acid is limited, and the flocculation of its aqueous suspension tends to occur (Araki, Wada, Kuga, and Okano, 2000). Conversely, when sulfuric acid is used as a hydrolyzing agent, dispersion of cellulose microfibers in water is improved significantly. It is due to the formation of charged sulfate esters on the surface of fibers by reaction between sulfuric acid and the surface hydroxyl groups of cellulose. However, with the presence of

charged sulfate groups, the thermal stability of obtained cellulose microfibrils was reduced (Roman and Winter, 2004). With increasing applications of cellulose microfibrils as fillers in polymer composites, this issue is important since typical processing temperatures for thermoplastics often exceed 200 °C.

In this study, cellulose microfibrils were extracted from cassava pulp by alkali treatment using sodium hydroxide solution and acid hydrolysis treatment using hydrochloric acid solution. The effects of some reaction factors such as temperature and reaction time on the morphology of obtained fibrils were investigated. Moreover, in order to find out a proper reaction sequence for these chemical treatments, the sequence of alkali treatment and acid treatment was also varied.

4.3 Experimental

4.3.1 Materials

Cassava pulp was obtained from Ratchasima Boonpa Co., Ltd. Hydrochloric acid (37 wt%) and sodium hydroxide were purchased from Carlo. Cellulose membrane (D9402) was supplied from Sigma–Aldrich. All chemical reagents used were of analytical grade.

4.3.2 Preparation of cellulose microfibrils from cassava pulp

4.3.2.1 Alkali treatment

Cassava pulp was ground and separated by sieve. The size of the mesh is 250-425 μm . To remove excess moisture, before being treated with NaOH solution, cassava pulp was dried in an oven at 130 °C for 25 h. About 10 g of cassava pulp was dispersed in 200 ml of sodium hydroxide solution (4 wt% NaOH). The

mixture was transferred to a flask and treatment was performed at 70 °C under vigorously mechanical stirring for 2, 3 and 4 h in a water batch. The solid was then filtered and washed many times with distilled water until the pH reached 6-7.

4.3.2.2 Acid treatment

The acid hydrolysis treatment was performed on raw cassava pulp and alkali treated fibers at a temperature of 50, 60, and 70 °C using 6.5 M hydrochloric acid (HCl) for 45 min under mechanical stirring. The obtained fibers were washed by centrifugation at 9,000 rpm at 25 °C for 10 min. This step had been repeated several times before the suspension was submitted to dialysis against distilled water using a cellulose membrane until the pH reached 6–7. Finally, the resulting suspension was sonicated for 10 min to destroy aggregates and was dried using a freeze dryer.

4.3.3 Characterization of cellulose microfibers

4.3.3.1 Scanning electron microscopy (SEM)

Scanning electron microscopy (SEM) (model JSM6400) was used to observe the surface morphology of obtained cellulose microfibers. Prior to SEM evaluation, the samples were coated with a thin gold film using a vacuum sputtering apparatus. The accelerating voltage was 20 kV.

4.3.3.2 Atomic force microscopy (AFM)

AFM was used to determine the dimensions of obtained cellulose microfibers. This measurement was performed by ParkAFM-XE-120 equipment. A drop of a diluted cellulose microfibers aqueous suspension was deposited onto a freshly cleaved mica surface and air-dried. AFM images were obtained at the ambient temperature in the non-contact mode with a scan rate of 1 Hz and using Si tips.

4.3.3.3 Chemical composition

The chemical composition (dry weight basis) of untreated cassava pulp and chemically treated fibers at each stage of treatment was determined according to a standard method of Animal Feed (EN ISO 13906:2008 and AOAC 973.18). The lignocellulose (cellulose + hemicellulose + lignin) content was estimated by neutral detergent fibers (NDF) method. The (cellulose + lignin) content was determined by acid detergent fibers (ADF) method while the lignin content was measured according to acid detergent lignin (ADL) method. The cellulose content was found by subtracting ADL from ADF. Meanwhile, the hemicellulose content was determined by subtracting ADF from NDF.

4.3.3.4 X-ray diffraction (XRD)

Raw cassava pulp and obtained samples after each chemical treatment were subjected to a powder X-ray diffraction analysis (PXRD). For this analysis, a D8 advanced Bruker AXS diffractometer was used. The diffracted intensity of CuK α radiation (wavelength of 0.1542 nm) was recorded between 5° and 40° (2θ angle range) with a scan rate of 2° min⁻¹ at 40 kV and 40 mA. Samples were analyzed in transmission mode. Before performing XRD analysis, all samples were dried at 50 °C for 12 h in an air-circulating oven. The crystallinity index (CI) was evaluated by using empirical method (Segal, Creely, Martin, and Conrad, 1959) as follows:

$$CI\% = \frac{(I_{002} - I_{am})}{I_{002}} \times 100 \quad (4.1)$$

In which I_{002} is the maximum intensity of diffraction of the (0 0 2) lattice peak at a 2θ angle between 21° and 23° , which represents both crystalline and amorphous materials. I_{am} is the intensity of diffraction of the amorphous material, which is taken at a 2θ angle between 18° and 20° where the intensity is at a minimum (Dai, Fan, and Collins, 2013).

4.3.3.5 Fourier transform infrared spectroscopy (FTIR)

A Bruker/Tensor27 II FT-IR spectrometer using attenuated total reflectance (ATR) equipped with platinum diamond crystal (TYPE A225/QL) was used to obtain the infrared spectrum for cassava pulp and treated fibers. The experiments were carried out in the range of $4000-400\text{ cm}^{-1}$ with a resolution of 4 cm^{-1} and total scans of 64 for each sample.

4.3.3.6 Thermogravimetric analysis (TGA)

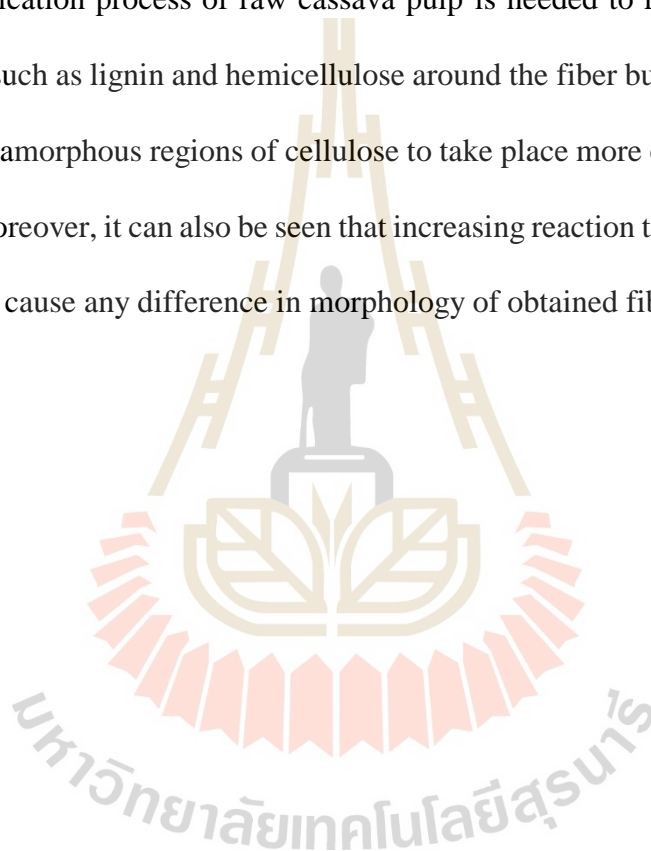
Thermal stability of all samples was determined by TGA measurement performed using a Mettler Toledo thermogravimetric instrument (TGA/DSC1). All measurements were carried out under a nitrogen atmosphere with a gas flow of $100\text{ mL} \cdot \text{min}^{-1}$ by heating the samples from 50 to $800\text{ }^\circ\text{C}$ at a heating rate of $10\text{ }^\circ\text{C} \cdot \text{min}^{-1}$. The sample with a weight between 5 and 10 mg was used for each run.

4.4 Results and discussion

4.4.1 Morphological analysis of the fibers

Figure 4.1 shows the SEM images of untreated cassava pulp and acid treated fibers at three different temperatures. The spherical starch particles on the surface of untreated cassava pulp were observed clearly in Figure 4.1a. However, as

shown in Figure 4.1(b-d), after acid hydrolysis of cassava pulp without alkali pre-treatment step, the starch was removed, and a continuous web-like fibrous network film was observed. This structure consists of cellulose microfibrils. Nevertheless, individual cellulose microfibrils cannot be distinguished. This is attributed to a significant amount of lignin which still exists in the treated fibers. This result indicates that the purification process of raw cassava pulp is needed to remove the cementing components such as lignin and hemicellulose around the fiber bundles. This allows the hydrolysis of amorphous regions of cellulose to take place more efficiently during acid treatment. Moreover, it can also be seen that increasing reaction temperature from 50 to 70 °C did not cause any difference in morphology of obtained fibers.



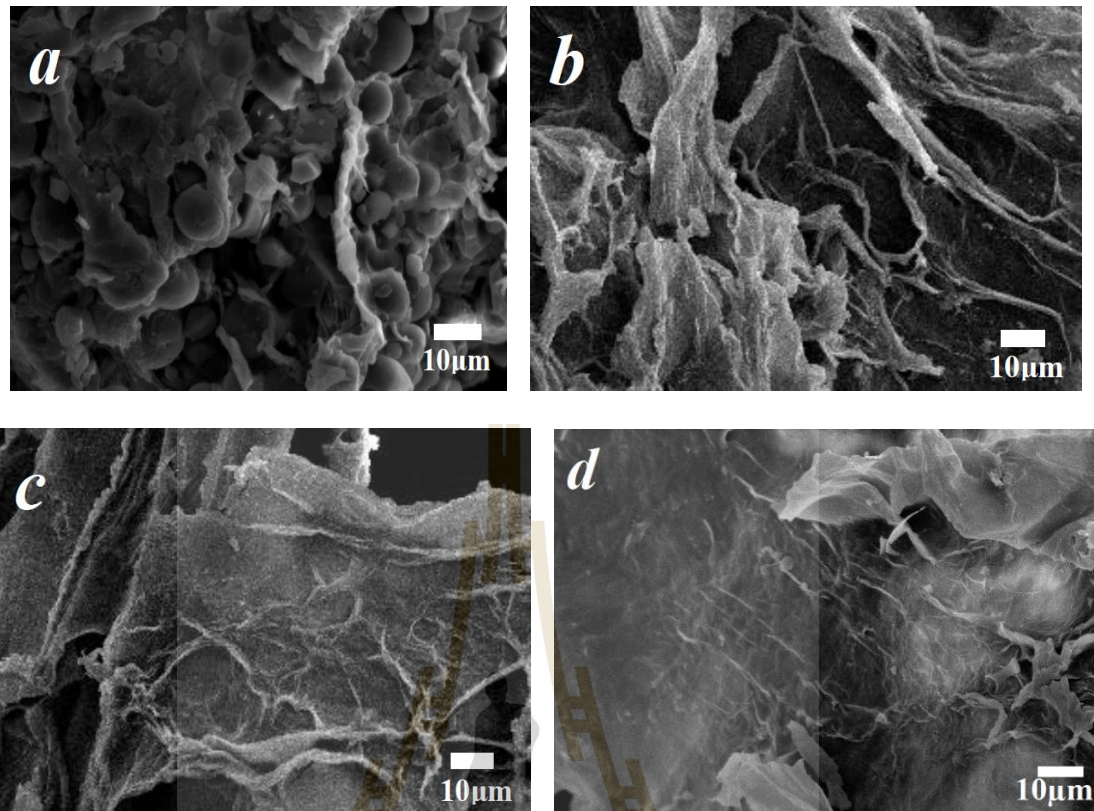


Figure 4.1 SEM micrographs of untreated cassava pulp (a) and acid treated fibers at 50 °C (b), 60 °C (c), and 70 °C (d).

Figure 4.2 presents SEM images of alkali treated fibers at various reaction times. Under controlled conditions, the alkali treatment was expected to remove hemicellulose and lignin partially. This removal helps to isolate cellulose and facilitate the hydrolysis of amorphous regions of cellulose upon acid hydrolysis treatment. As can be seen from Figure 4.2 after alkali treatment, the morphologies of treated fibers show the cell wall structure. This structure indicates the partial defibrillation and opening of fiber bundles. This demonstrates that after alkali treatment, hemicellulose and lignin were removed partially and the continuous

web-like fibrous network film started separating into the individual fibers with a diameter of around 3-6 μm . With the increase of reaction time from 2 to 3 h, the defibrillation occurred more extensively, and very uniform cell wall structure of resulting fibers was observed. However, as reaction time reached 4 h, the treated fibers seemed to be broken in the transverse direction. These results suggest that the reaction time of 3 h was suitable for this treatment reaction. Figure 4.3 shows the difference in morphology of fibers treated with a combination of two reactions (alkali treatment and acid treatment) with different reaction sequences under the same conditions.

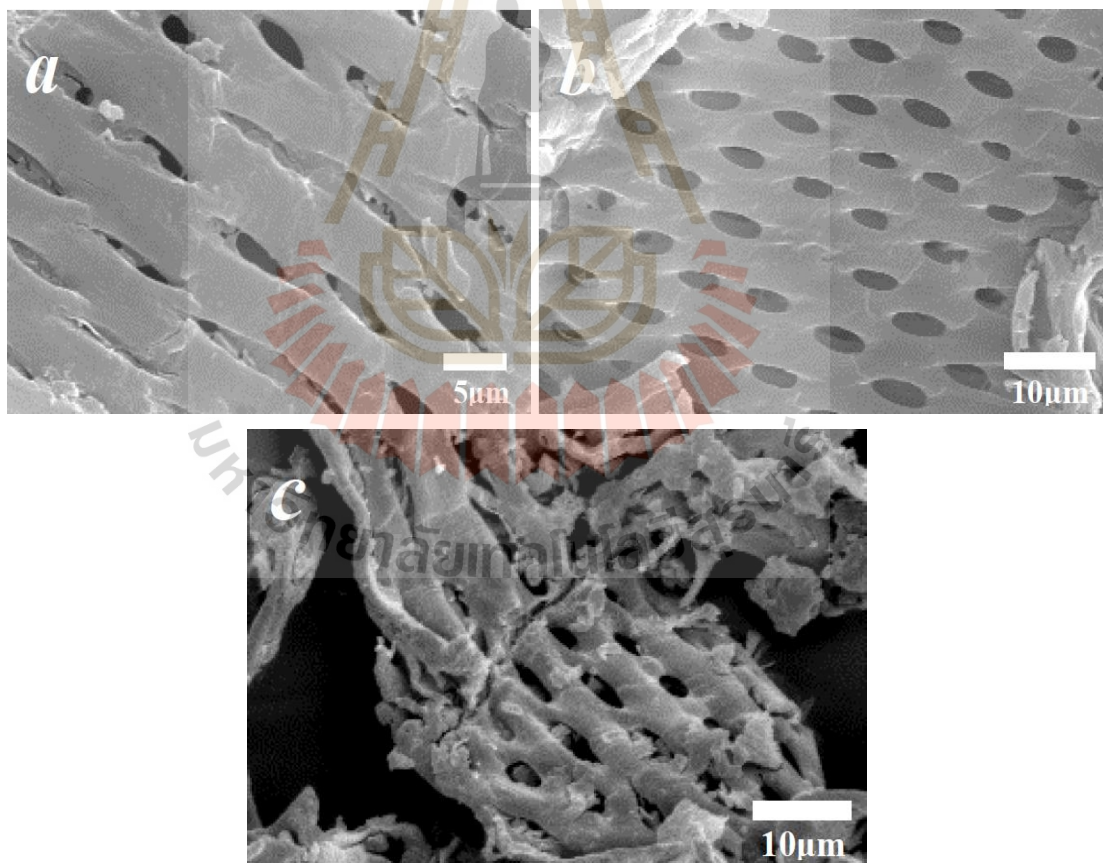


Figure 4.2 SEM images of alkali treated fibers for 2 h (a), 3 h (b), and 4 h (c).

As can be seen from Figure 4.3 when the alkali treatment was carried out before acid treatment (Figure 4.3a), the defibrillation and opening of fiber bundles happened to a higher degree compared to that of treated fibers in which acid treatment was carried out before alkali treatment (Figure 4.3b). The very uniform cell wall structure of resulting cellulose microfibrils with a diameter of around 5 μm was observed. This structure can make this material become a potential reinforcing agent for composite materials. It is thought that the polymeric matrix used to prepare composite can be embedded in the cell walls, which leads to the better dispersion of this filler in the polymeric matrix. As a result, the mechanical properties of resulting composites will be enhanced. The SEM results confirmed that the alkali treatment is necessary to isolate cellulose, as well as eliminate partially the cementing components, which leads to facilitating the hydrolysis process of amorphous domains of cellulose during the acid hydrolysis treatment. In order to determine the dimensions of obtained cellulose microfibrils, AFM analysis was performed. It was observed from Figure 4.4 that the individual cellulose microfibrils have a diameter of around 5 μm . This result is consistent with the SEM result above.

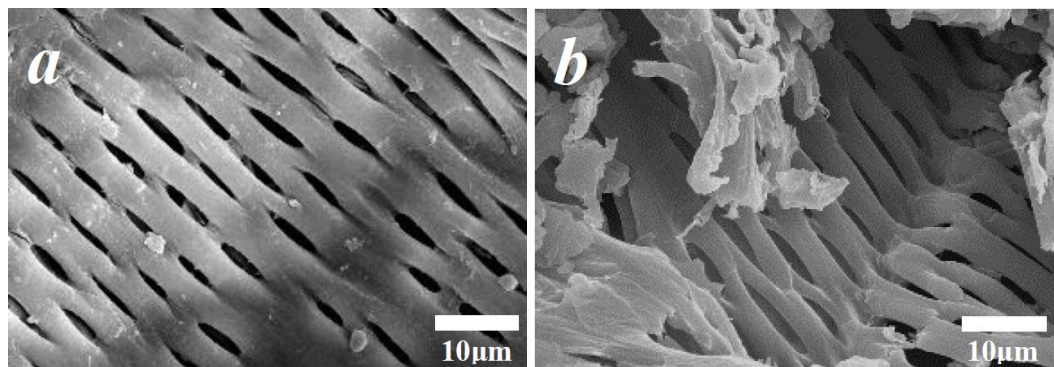


Figure 4.3 SEM images of alkali-acid treated fibers (a) and acid-alkali treated fibers

(b).

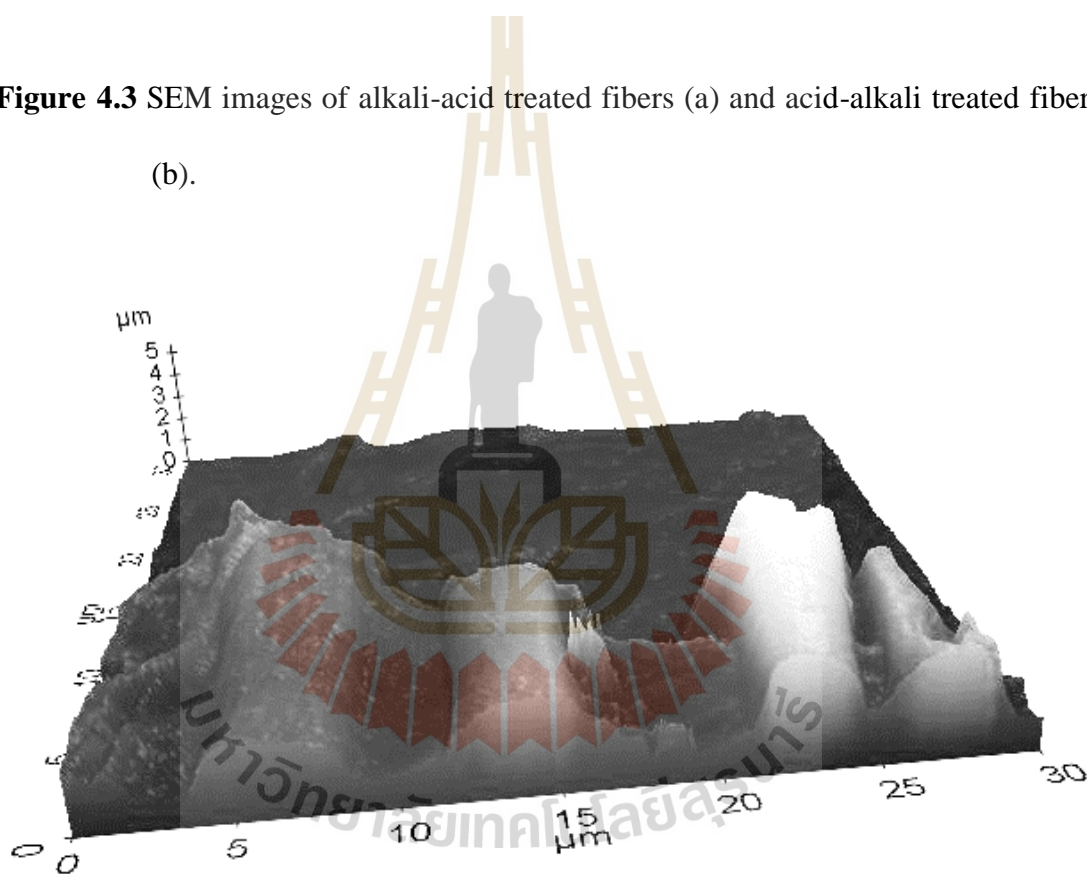


Figure 4.4 3D AFM image of obtained cellulose microfibrils.

4.4.2 Chemical composition of fibers

Table 4.1 shows the chemical composition of the untreated cassava pulp and treated fibers at each stage of treatment. The original cassava pulp contained 21.12

wt% cellulose, 8.64 wt% hemicellulose, 3.53 wt% lignin and 66.71 wt% non-lignocellulose (carbohydrates, starch, protein, lipids, and ash). Upon alkali treatment, the cellulose content of treated fibers increased notably compared to that of untreated cassava pulp. It was observed from Table 4.1 that hemicellulose was eliminated partially by alkali treatment, which decreased from 8.64 wt% to 6.99 wt%. However, the lignin content remained practically constant after alkali treatment. These results indicate that alkali treatment was efficient for removing partially hemicellulose. The lignocellulose contents of acid treated fibers were found to be similar to those of alkali treated fibers. This shows that both alkali and acid treatments were not efficient for eliminating lignin component of the fiber. When the untreated cassava pulp fibers undergo the combination of alkali and acid treatments, we can see that there was a further decrease in the percentage of hemicellulose and lignin, as well as an increase in the percentage of cellulose component present in the fiber. The final fibers obtained after alkali and acid treatments were found to have a higher percentage of cellulose content. Therefore, the reinforcement ability of these fibers is expected to be much higher than that of other fibers that have less percentage of cellulose content. Moreover, as can be seen from Table 4.1 cellulose, hemicellulose, and lignin contents were not influenced significantly by the sequence of alkali treatment and acid hydrolysis treatment. Nevertheless, it is worth noting that the alkali-acid treated fibers show slightly higher cellulose content and lower hemicellulose and lignin contents in relation to acid-alkali treated fibers.

Table 4.1 The chemical composition of untreated cassava pulp and treated fibers at various stages of treatment.

Sample	Lignocellulose			Non-lignocellulose (%)
	Cellulose (%)	Lignin (%)	Hemicellulose (%)	
Cassava pulp	21.12	3.53	8.64	66.71
Alkali treated fibers	65.88	3.13	6.99	24.00
Acid treated fibers	64.07	3.25	7.05	25.63
Acid-alkali treated fibers	71.21	2.94	6.79	19.05
Alkali-acid treated fibers	72.29	2.83	6.81	18.07

4.4.3 X-ray diffraction analysis

X-ray diffraction patterns of untreated cassava pulp and treated fibers are shown in Figure 4.5. These patterns are typical of semicrystalline materials with an amorphous broad hump and crystalline peaks. Crystallinity index analysis is summarized in Table 4.2. It can be noted from Figure 4.5 that all four diffractograms display two well-defined peaks around $2\theta = 15^\circ$ (for 1 0 1 plane) and $2\theta = 22.5^\circ$ (for 0 0 2 plane) characteristic of cellulose (Klemm, Heublein, Fink, and Bohn, 2005). As can be seen from Table 4.2, after alkali treatment or acid treatment, the crystallinity of treated fibers was significantly higher than that of untreated cassava pulp. This is due to the partial removal of amorphous non-cellulosic compounds, which was induced by alkali treatment (Mwaikambo and Ansell, 2006). The higher CI value of acid treated fibers in relation to that of alkali treated fibers can be attributed to the hydrolysis of amorphous regions of cellulose and partial removal of the paracrystalline domains during the acid hydrolysis (Fengel and Wegener, 1983). As expected, by a combination of alkali and acid treatments, a notable increase in crystallinity of cellulose microfibrils compared to that of alkali treated fibers and acid treated fibers was observed (Table

4.2). Interestingly, as alkali treatment was carried out before acid treatment, the crystallinity of obtained cellulose microfibrils was slightly enhanced. This can be explained that after alkali treatment, non-cellulosic materials were removed partially and cellulose was isolated. This caused the hydrolysis of amorphous domains of cellulose to occur more efficiently during acid treatment. As a result, more new hydrogen bonds could be formed through the hydroxyl groups (-OH) on the surface of cellulose. This led to enhancing the crystallinity of attained cellulose microfibrils. This was shown by the stronger and sharper peak at around $2\theta = 22^\circ$ of alkali-acid treated fibers compared to that of acid-alkali treated fibers in the diffraction pattern of cellulose microfibrils (Figure 4.5).

Table 4.2 Crystallinity index of untreated cassava pulp and treated fibers at various stages of treatment.

Sample	Crystallinity index (%)
Cassava pulp	21.59
Alkali treated fibers	46.63
Acid treated fibers	50.95
Acid-alkali treated fibers	57.21
Alkali - acid treated fibers	62.89

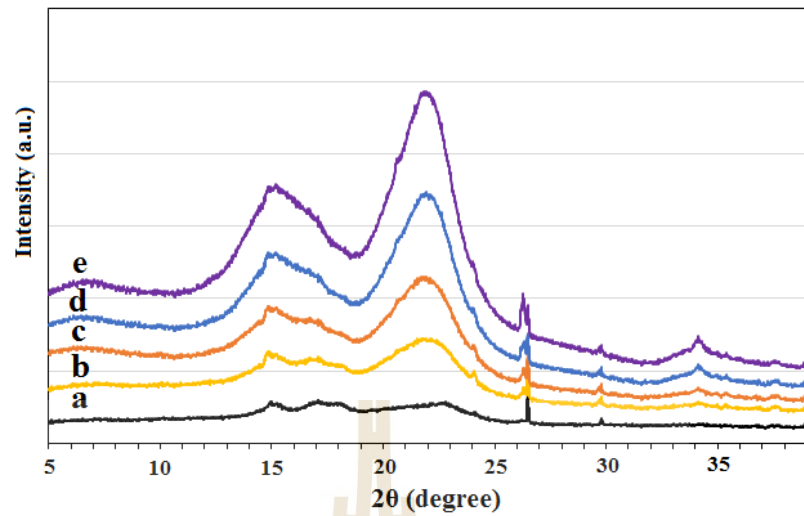


Figure 4.5 X-ray diffraction patterns of untreated cassava pulp (a), alkali treated fibers (b), acid treated fibers (c), acid-alkali treated fibers (d), and alkali-acid treated fibers (e).

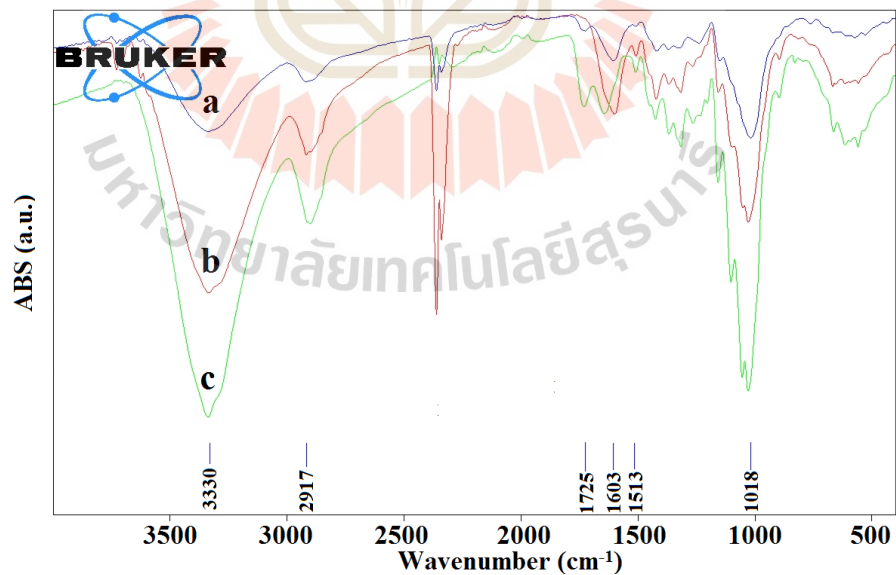


Figure 4.6 FTIR spectra of cassava pulp (a), alkali treated fibers (b), and acid treated fibers (c).

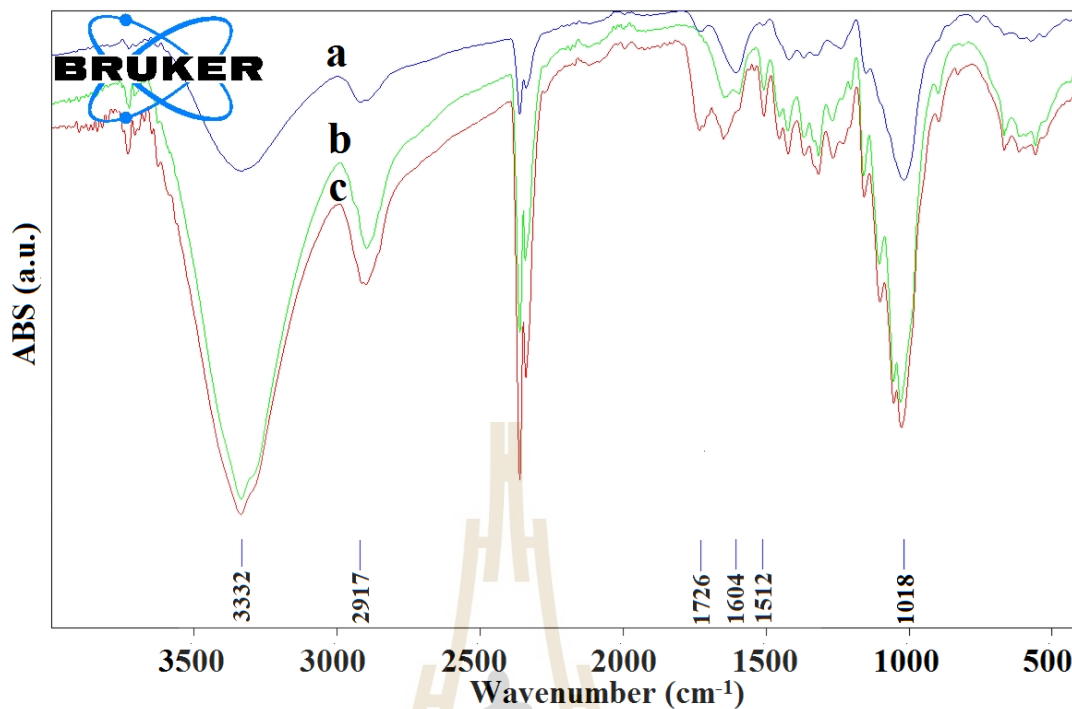


Figure 4.7 FTIR spectra of cassava pulp (a), acid-alkali treated fibers (b), and alkali-acid treated fibers (c).

4.4.4 FTIR spectroscopy analysis

Figure 4.6 shows the FTIR spectra recorded for raw cassava pulp and treated fibers. The peak near 3400 cm^{-1} , which is observed in all spectra, is representative of the C-H and O-H groups. The peak around 1640 cm^{-1} observed in all spectra corresponds to the absorption of water. The peaks of 3400 and 1640 cm^{-1} above are attributed to the stretching of hydrogen bonds and bending of hydroxyl groups bound to the cellulose structure. These results confirmed that after alkali and acid treatments, the chemical structure of cellulose was preserved. The peak present at 1725 cm^{-1} in the spectrum of raw cassava pulp confirmed the presence of hemicellulose

component which contains C=O linkage (Alemdar and Sain, 2008). This peak disappeared upon alkali treatment of cassava pulp indicating the removal of hemicellulose. However, the data shown in Table 4.1 indicate that the hemicellulose content was not entirely removed by alkali treatment. This observation suggests that the absence of carbonyl groups in the FTIR spectrum of alkali treated fibers most probably is due to the cleavage of ester bond and carboxylic group in hemicellulose. Surprisingly, the intensity of this peak increased significantly upon acid treatment. It is maybe ascribed to carboxyl or aldehyde absorption arising from oxidation of the C-OH groups which occurs during acid treatment (Morán, Alvarez, Cyras, and Vázquez, 2008). This explanation can be confirmed by results shown in Figure 4.7. Figure 4.7 reveals that when the acid treatment was carried out before alkali treatment, that peak was not observed. In contrast, when the alkali treatment was conducted before the acid treatment, the presence of that peak was clearly observed. Moreover, the peak present at around 1512 cm^{-1} corresponding to the aromatic skeletal vibration in all spectra indicates the presence of lignin in all samples (Xiao, Sun, and Sun, 2001). This confirms that upon alkali treatment and acid treatment, the lignin component could not be removed efficiently. This result is consistent with the chemical composition of fiber data in Table 4.1.

4.4.5 Thermal stability

Figure 4.8 shows the TGA curves of raw cassava pulp and treated fibers at different stages of treatment. Due to the hydrophilic nature of the lignocellulosic materials, even all samples were dried carefully before TGA measurement, there is the certain moisture content existing in the samples. As a consequence, as shown in Figure

4.8, an initial weight loss of all samples occurred below 100 °C regardless of their treatment. This weight loss is attributed to the vaporization of water existing in all samples. After that, at a higher temperature, a significant weight loss was observed. Figure 4.8 also indicates that after alkali treatment or acid treatment, the thermal stability of materials was improved. This is due to the partial removal of the low thermal stability compositions such as hemicellulose, lignin, and starch. The higher thermal stability of acid treated fibers compared to that of alkali treated fibers is ascribed to the partial removal of starch during acid hydrolysis. Furthermore, the treatment by a combination of two reactions caused an improvement in thermal stability of obtained cellulose microfibrils compared to that of alkali treated or acid treated fibers. This can be ascribed to the combination of partial removal of hemicellulose, lignin, and pectin with partial elimination of starch during the alkali treatment and acid hydrolysis treatment, respectively. Especially, as can be noted from Figure 4.8 that when the acid treatment was carried out before the alkali treatment, the treated fibers showed the higher thermal stability. This can be explained that the partial elimination of starch particles embedded to the surface of fibers during the acid hydrolysis facilitated the interaction between NaOH agent and fibers, which resulted in a more efficient removal of non-cellulosic components during alkali treatment. As a result, the thermal stability of obtained cellulose microfibrils was enhanced. Indeed, the slightly higher lignin content of acid-alkali treated fibers in relation to that of alkali-acid treated fibers (Table 4.1) also contributes to the improvement of thermal stability of attained cellulose microfibrils.

In addition, it is worth noting that the char fraction of untreated cassava pulp and cellulose microfibrils was found to be very high which is in the range of 20–30 % at temperature around 400–600 °C (Figure 4.8).

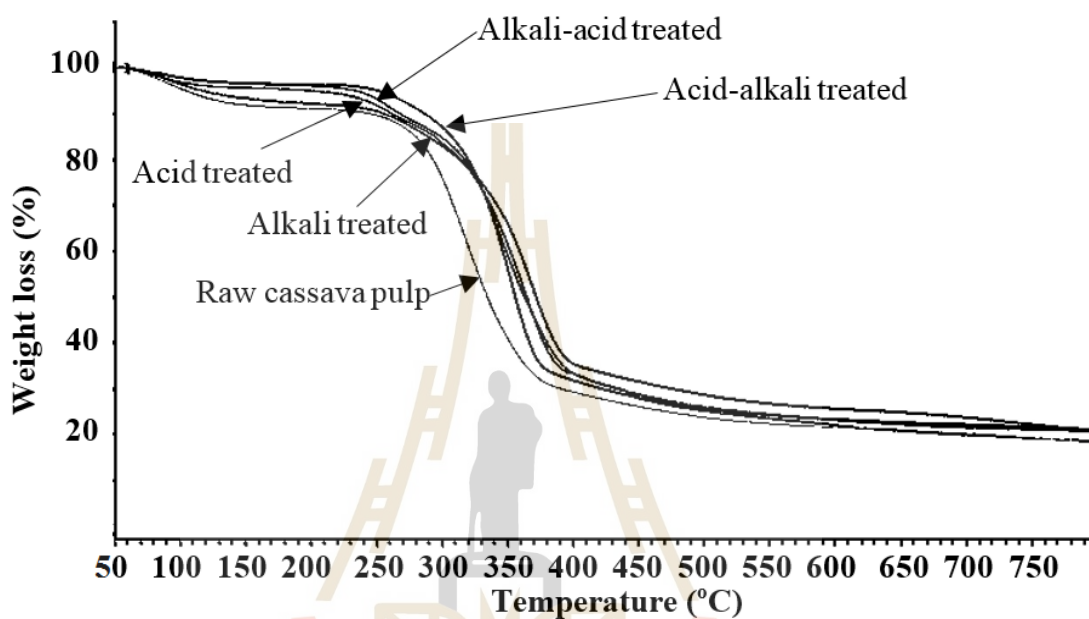


Figure 4.8 TGA curves of raw cassava pulp and treated fibers at various stages of treatment.

4.5 Conclusions

Cellulose microfibrils were successfully prepared from cassava pulp using the combination of alkali and acid hydrolysis treatments. The diameter of obtained cellulose microfibrils determined by AFM analysis was found to be around 5 μm . Amorphous non-cellulosic constituents of cassava pulp fibers were removed partially by alkali treatment. Meanwhile, the starch component was eliminated from the fibers by acid treatment. The cellulose content of attained cellulose microfibrils was

considerably higher than that of untreated cassava pulp. Upon alkali treatment, hemicellulose was removed partially while lignin remained practically constant. The results from XRD and FTIR analyses confirmed that after chemical treatments, the structure of cellulose was maintained. The significantly higher crystallinity of chemically treated fibers compared to that of untreated cassava pulp was observed. The crystallinity of alkali-acid treated fibers was found to be slightly higher than that of acid-alkali treated fibers. More importantly, the obtained cellulose microfibrils exhibited the enhanced thermal stability compared to untreated cassava pulp. Interestingly, the thermal stability of cellulose microfibrils was higher for the reaction sequence in which the acid hydrolysis treatment was carried out before the alkali treatment. Also, it should be noted that the cell wall structure of obtained cellulose microfibrils makes this material become a potential reinforcing agent for biocomposite materials.

It is worth noting that the purification process with only alkali treatment was not effective enough for eliminating completely the cementing components of the fibers. As a consequence, the hydrolysis process during acid treatment did not take place effectively, and the cellulose fibers with nano scale were not obtained. As a next work, the purification with combination of alkali and bleaching treatments should be implemented.

4.6 References

- Alemdar, A., and Sain, M. (2008). Isolation and characterization of nanofibers from agricultural residues—Wheat straw and soy hulls. **Bioresource Technology**. 99: 1664-1671.
- Angles, M. N., and Dufresne, A. (2001). Plasticized starch/tunicin whiskers nanocomposite materials. 2. Mechanical behavior. **Macromolecules**. 34: 2921-2931.
- Araki, J., Wada, M., Kuga, S., and Okano, T. (2000). Birefringent glassy phase of a cellulose microcrystal suspension. **Langmuir**. 16: 2413-2415.
- Braun, B., and Dorgan, J. R. (2008). Single-step method for the isolation and surface functionalization of cellulosic nanowhiskers. **Biomacromolecules**. 10: 334-341.
- Cherian, B. M., et al. (2011). **Cellulose nanocomposites for high-performance applications Cellulose Fibers: Bio-and Nano-Polymer Composites**. Berlin: Springer-Verlag Berlin Heidelberg .
- Dai, D., Fan, M., and Collins, P. (2013). Fabrication of nanocelluloses from hemp fibers and their application for the reinforcement of hemp fibers. **Industrial Crops and Products**. 44: 192-199.
- Fengel, D., and Wegener, G. (1983). **Wood: chemistry, ultrastructure, reactions**. Berlin: Walter de Gruyter.
- Habibi, Y., Lucia, L. A., and Rojas, O. J. (2010). Cellulose nanocrystals: chemistry, self-assembly, and applications. **Chemical Reviews**. 110: 3479-3500.

- Klemm, D., Heublein, B., Fink, H. P., and Bohn, A. (2005). Cellulose: fascinating biopolymer and sustainable raw material. **Angewandte Chemie (International ed. in English)**. 44: 3358-3393.
- Liu, D., Zhong, T., Chang, P. R., Li, K., and Wu, Q. (2010). Starch composites reinforced by bamboo cellulosic crystals. **Bioresource Technology**. 101: 2529-2536.
- Morán, J., Alvarez, V., Cyras, V., and Vázquez, A. (2008). Extraction of cellulose and preparation of nanocellulose from sisal fibers. **Cellulose**. 15: 149-159.
- Mwaikambo, L., and Ansell, M. (2006). Mechanical properties of alkali treated plant fibres and their potential as reinforcement materials. I. Hemp fibres. **Journal of Materials Science**. 41: 2483-2496.
- Roman, M., and Winter, W. T. (2004). Effect of sulfate groups from sulfuric acid hydrolysis on the thermal degradation behavior of bacterial cellulose. **Biomacromolecules**. 5: 1671-1677.
- Rosa, M., et al. (2010). Cellulose nanowhiskers from coconut husk fibers: Effect of preparation conditions on their thermal and morphological behavior. **Carbohydrate Polymers**. 81: 83-92.
- Sadeghifar, H., Filpponen, I., Clarke, S. P., Brougham, D. F., and Argyropoulos, D. S. (2011). Production of cellulose nanocrystals using hydrobromic acid and click reactions on their surface. **Journal of Materials Science**. 46: 7344-7355.
- Segal, L., Creely, J., Martin, A., and Conrad, C. (1959). An empirical method for estimating the degree of crystallinity of native cellulose using the X-ray diffractometer. **Textile Research Journal**. 29: 786-794.

- Sheltami, R. M., Abdullah, I., Ahmad, I., Dufresne, A., and Kargarzadeh, H. (2012). Extraction of cellulose nanocrystals from mengkuang leaves (*Pandanus tectorius*). **Carbohydrate Polymers**. 88: 772-779.
- Silvério, H. A., Neto, W. P. F., Dantas, N. O., and Pasquini, D. (2013). Extraction and characterization of cellulose nanocrystals from corncob for application as reinforcing agent in nanocomposites. **Industrial Crops and Products**. 44: 427-436.
- Teixeira, E. d. M., et al. (2012). Properties of thermoplastic starch from cassava bagasse and cassava starch and their blends with poly (lactic acid). **Industrial Crops and Products**. 37: 61-68.
- Teixeira, E. d. M., et al. (2009). Cassava bagasse cellulose nanofibrils reinforced thermoplastic cassava starch. **Carbohydrate Polymers**. 78: 422-431.
- Xiao, B., Sun, X., and Sun, R. (2001). Chemical, structural, and thermal characterizations of alkali-soluble lignins and hemicelluloses, and cellulose from maize stems, rye straw, and rice straw. **Polymer Degradation and Stability**. 74: 307-319.

CHAPTER V

EXTRACTION OF CELLULOSE NANOFIBERS FROM CASSAVA PULP

5.1 Abstract

Cellulose nanofibers (CNFs) were extracted successfully from cassava pulp (CP) by submitting to alkali, bleaching and acid hydrolysis treatments. The raw CP was mercerized with 4 wt% NaOH solution and then followed by bleaching treatment using a solution made up of equal parts (v:v) of acetate buffer and aqueous chlorite. In order to obtain cellulose nanofibers, the acid hydrolysis treatment of bleached fibers was performed using three different types of acid (HCl, a mixture of HCl/H₂SO₄ (1:2 v/v), and H₂SO₄). In this acid treatment, the effects of acid type, acid concentration, acid/pulp ratio, and hydrolysis time on the crystallinity and thermal stability of obtained cellulose nanofibers were investigated. The morphological structure of the ensuing fibers was examined by scanning electron microscopy (SEM) and transmission electron microscopy (TEM). TEM micrograph revealed that most nanofibers with a diameter in the range of 12-24 nm and immeasurable length were obtained. The results from the chemical composition of fibers indicated that the cellulose content of fibers increased with successive treatments. Fourier transform infrared (FTIR) spectroscopy showed the progressive removal of non-cellulosic components during pre-treatments (alkali and bleaching treatments). An increase in crystallinity of fibers after each stage

of treatment was revealed by X-ray diffraction (XRD). The crystallinity degree of nanofibers increased continuously with increasing acid concentration and acid/pulp ratio but dropped at a certain hydrolysis time under the same acid type. The thermal stability characterized by thermogravimetric analysis (TGA) of nanofibers extracted using H_2SO_4 or a mixture of $\text{HCl}/\text{H}_2\text{SO}_4$ was found to be significantly lower than that of raw cassava pulp fibers and nanofibers extracted using HCl .

5.2 Introduction

Cassava pulp is the solid waste produced as a consequence of starch production. This pulp contains high starch content (50-60 % dry basis) (Sriroth, Chollakup, Chotineeranat, Piyachomkwan, and Oates, 2000). In Thailand, cassava starch is a large and growing industry with about 10 million tons of fresh cassava roots used for the production of starch, generating at least 1 million tons of pulp annually. The main application for the large quantities of waste material produced each year, after drying, is as a low-value animal feed or fertilizer (Sriroth et al. 1999). In addition to residual starch, cassava pulp contains 15-50 % cellulose fibers (dry weight basis) (Teixeira et al. 2012). These characteristics suggest the possibility of using the CP as a source for the extraction of cellulose nanofibers.

Cellulose nanofibers can be obtained by mechanical and chemical paths. By chemical path, so far, acid hydrolysis treatment has proven its efficiency in isolating cellulose nanofibers from various kinds of cellulosic materials. H.A. Silvério et al. investigated the preparation of cellulose nanofibers from corncobs by sulfuric acid hydrolysis treatment (Silvério, Neto, Dantas, and Pasquini, 2013). Pre-treatment steps

including alkali and bleaching treatments were carried out to remove non-cellulosic materials such as hemicellulose and lignin prior to submitting to acid treatment. The results of AFM indicated that the needle-like cellulose nanofibers were obtained. XRD analysis also showed that after acid treatment, the crystallinity of samples increased significantly and structure of cellulose was maintained. The 7-8 nm in diameter and 100-200 nm in lengths cellulose nanofibers were extracted successfully from cotton fibers by using hydrobromic acid as a hydrolyzing agent (Sadeghifar, Filpponen, Clarke, Brougham, and Argyropoulos, 2011). This indicated that besides sulfuric acid, hydrobromic acid was also an effective hydrolyzing agent for the preparation of cellulose nanofibers. Johar et al., studied on the extraction of cellulose nanofibers from rice husk using H₂SO₄ as hydrolyzing agent (Johar, Ahmad, and Dufresne, 2012). The XRD and TGA results showed that after treatment, the crystallinity of obtained nanofibers was higher than that of raw material. However, a significant decrease in the thermal stability of nanofibers compared to that of raw rice husk was observed. In the case of cassava pulp, the remaining starch particles can be eliminated by this acid treatment. During this treatment, amorphous and paracrystalline regions of cellulose are preferentially hydrolyzed, whereas crystalline regions that have a higher resistance to acid attack remain intact (Angles and Dufresne, 2001); (Habibi, Lucia, and Rojas, 2010).

The overall efficiency of the acid hydrolysis treatment and physical properties of obtained cellulose nanofibers are affected by several factors such as acid type, acid concentration, hydrolysis temperature, hydrolysis time, and acid/pulp ratio. Bondeson, Mathew, and Oksman (2006) investigated optimizing the hydrolysis conditions by an

experimental factorial design matrix using microcrystalline cellulose that was derived from Norway spruce (*Picea abies*) as the cellulosic starting material. The factors that were varied during the process were the concentrations of microcrystalline cellulose and sulfuric acid, the hydrolysis time and temperature, and the ultrasonic treatment time. The response that was measured was the median size of the cellulose particles. The authors demonstrated that with a sulfuric acid concentration of 63.5 % (w/w) over a time of approximately 2 h, it was possible to obtain cellulose nanofibers having a length between 200 and 400 nm and a width less than 10 nm. The effects of reaction time and acid/pulp ratio on physical properties of nanofibers obtained by sulfuric acid hydrolysis of bleached softwood sulfite pulp were investigated by Beck-Candanedo, Roman, and Gray (2005). They reported that shorter nanofibers with narrow size polydispersity were produced at longer hydrolysis times. Elazzouzi-Hafraoui et al. (2007) studied the size distribution of cellulose nanofibers resulting from sulfuric acid hydrolysis of cotton treated with 65 % sulfuric acid for 30 min at various temperatures, ranging from 45 to 72 °C. By increasing the temperature, they demonstrated that shorter nanofibers were obtained; however, no apparent influence on the width of the nanofiber was revealed. Corrêa, de Moraes Teixeira, Pessan, and Mattoso (2010) investigated the influence of acid type on the crystallinity and thermal stability of cellulose nanofibers extracted from curaua fibers. The authors reported that the changes in crystallinity indexes due to nature of acid for hydrolysis were slight and not significant. On the other hand, the thermal stability of nanofibers was affected significantly by used acid type. The nanofibers hydrolyzed by H₂SO₄ had lower thermal stability than ones hydrolyzed by HCl.

In this work, cassava pulp was the lignocellulosic material used as the cellulose source to extract cellulose nanofibers. Before being submitted to acid treatment, cassava pulp was treated by alkali and bleaching treatments to remove hemicellulose and lignin. The main objectives of this study were to produce cellulose nanofibers from cassava pulp via acid hydrolysis method, as well as study on the effects of acid type, acid concentration, acid/pulp ratio, and hydrolysis time in the acid hydrolysis treatment on the crystallinity and thermal stability of obtained cellulose nanofibers.

5.3 Materials and methods

5.3.1 Materials

Cassava pulp was supplied by Ratchasima Boonpa Co., Ltd. Sulfuric acid (95.0–98.0 wt%), hydrochloric acid (37 wt%), sodium hydroxide, and glacial acetic acid were purchased from Carlo. Sodium chlorite (NaClO_2 , technical grade, 80 %) and cellulose membrane (D9402) were supplied from Sigma–Aldrich.

5.3.2 Preparation of cellulose nanofibers

5.3.2.1 Alkali treatment

Cassava pulp (CP) was dried in an oven at 130 °C for 25 h to remove excess moisture. About 10 g of CP was dispersed in 200 ml of alkali solution (4 wt% NaOH). The mixture was transferred to a flask and treatment was performed at 70 °C under vigorously mechanical stirring for 3 h in a water batch. The solid was then filtered and washed many times with distilled water until the pH reached 6-7.

5.3.2.2 Bleaching treatment

Following alkali treatment, the bleaching treatment was carried out by a solution made up of equal parts (v:v) of acetate buffer (NaOH and glacial acetic acid) and aqueous chlorite (NaClO_2 in water). This bleaching treatment was performed at 80 °C for 10 h. The bleached fibers were washed repeatedly with distilled water until the pH of the fibers became neutral and subsequently dried using a freeze dryer.

5.3.2.3 Acid hydrolysis treatment

After bleaching treatment, the acid hydrolysis treatment was performed by using three different types of acid (HCl, a mixture of HCl/ H_2SO_4 (1:2 v/v) and H_2SO_4). The concentration of acid was 6.5 M. The reaction temperature and reaction time were kept at 60 °C and 60 min, respectively. After that, the mixture of HCl/ H_2SO_4 (1:2 v/v) was used to investigate the effect of three reaction factors including reaction time, acid concentration, and acid/fibers ratio on the physical properties of obtained cellulose nanofibers. The acid concentration was varied into 5.5, 6.5, and 7.5 M. Three acid/fiber ratios of 100ml/2g, 150ml/2g, and 200ml/2g were used. The reaction time was varied into 30, 60, and 90 min. All reactions were carried out at 60 °C under mechanical stirring. The excess of acid was removed from the ensuing suspension by centrifugation at 9,000 rpm for 10 min. After that, the suspension was submitted to dialysis against distilled water using a cellulose membrane until the pH reached 6–7. Finally, the ultrasonic treatment of fiber suspension was carried out for 10 min to destroy aggregates, and the fiber suspension was dried using a freeze dryer.

5.3.3 Characterization

5.3.3.1 Chemical composition

The chemical composition (dry weight basis) of untreated cassava pulp and chemically treated fibers at each stage of treatment was determined according to a standard method of Animal Feed (EN ISO 13906:2008 and AOAC 973.18). The lignocellulose (cellulose + hemicellulose + lignin) content was estimated by neutral detergent fibers (NDF) method. The (cellulose + lignin) content was determined by acid detergent fibers (ADF) method while the lignin content was measured according to acid detergent lignin (ADL) method. The cellulose content was found by subtracting ADL from ADF. Meanwhile, the hemicellulose content was determined by subtracting ADF from NDF.

5.3.3.2 Transmission electron microscopy (TEM)

TEM (Phillips model Tecnai G2 F30 S/TEM S-Twin) was used to examine the morphology of cellulose nanofibers extracted from cassava pulp. A drop of a diluted suspension (1 wt%) was deposited on the surface of a clean copper grid. The grid was negatively stained with 3 % (w/w) solution of uranyl acetate for 10 s and dried at room temperature. The TEM analysis was carried out with an accelerating voltage of 80 kV. The dimensions of CNFs were determined by using TEM Imaging & Analysis (TIA) software. A hundred CNFs were randomly selected, and a minimum of 100 and 200 measurements were used to determine the average diameter.

5.3.3.3 Scanning electron microscopy (SEM)

Scanning electron microscopy (SEM) (model JSM6400) was used to observe the surface morphology of raw cassava pulp, alkali treated fibers and

bleaching treated fibers. Prior to SEM evaluation, the samples were coated with a thin gold film using a vacuum sputtering apparatus. The accelerating voltage was 20 kV.

5.3.3.4 X-ray diffraction (XRD)

Crystallinity index of cassava pulp, alkali treated fibers, bleaching treated fibers, and cellulose nanofibers was determined by a D8 advanced Bruker AXS diffractometer with a $\text{CuK}\alpha$ radiation source ($\lambda = 0.1542 \text{ nm}$) in the range between 5° and 40° (2θ angle) with a scan rate of 2° min^{-1} at 40 kV and 40 mA. All samples were analyzed in transmission mode. Before performing XRD analysis, all samples were dried at 50°C for 12 h in an air-circulating oven. The crystallinity index (CI) was evaluated by using an empirical method (Segal, Creely, Martin, and Conrad, 1959) as follows:

$$\text{CI}\% = \frac{(I_{002} - I_{am})}{I_{002}} \times 100 \quad (5.1)$$

In which I_{002} is the maximum intensity of diffraction of the (0 0 2) lattice peak at a 2θ angle between 21° and 23° , which represents both crystalline and amorphous materials. I_{am} is the minimum intensity of diffraction taken at a 2θ angle between 18° and 20° (Dai, Fan, and Collins, 2013), which represents the amorphous material.

5.3.3.5 Fourier transform infrared spectroscopy (FTIR)

A Bruker/Tensor27 II FT-IR spectrometer using attenuated total reflectance (ATR) equipped with platinum diamond crystal (TYPE A225/QL) was used to obtain the infrared spectrum for cassava pulp and cellulose nanofibers. The

experiments were carried out in the range of 4000-400 cm^{-1} with a resolution of 4 cm^{-1} and total scans of 64 for each sample. All spectra were normalized using OPUS 7.0 software.

5.3.3.6 Thermogravimetric analysis (TGA)

Thermal stability of all samples was determined by TGA using a Mettler Toledo STARe System (TGA/DSC1) by heating the samples from 30 to 800 $^{\circ}\text{C}$ at a heating rate of 10 $^{\circ}\text{C}/\text{min}$ under a nitrogen atmosphere with a gas flow of 100 ml/min. The sample with a weight between 5 and 10 mg was used for each run.

5.4 Results and discussion

5.4.1 Chemical composition of fibers

The chemical compositions of the untreated cassava pulp and treated fibers at each stage of treatment are summarized in Table 5.1. The original cassava pulp contained 21.12 wt% cellulose, 8.64 wt% hemicellulose, 3.53 wt% lignin and 66.71 wt% non-lignocellulose (carbohydrates, protein, lipids, and ash). Upon chemical treatment, the cellulose content continuously increased as expected. The alkali treatment was efficient in removing partially hemicellulose, which decreased from 8.64 wt% to 6.99 wt% following treatment. The lignin content remained practically constant. Meanwhile, the bleaching treatment efficiently eliminated lignin, which dropped to 1.02 wt% from 3.13 wt%, whereas the hemicellulose content was found to be practically constant upon bleaching treatment. These results indicate that the hemicellulose content and the lignin content were removed partially by alkali treatment and bleaching treatment, respectively. Moreover, as can be seen from Table 5.1, the

non-lignocellulose was removed considerably from 66.71 wt% to 13.88 wt% by pre-treatment steps. After purification, the cellulose content practically quadrupled, while the hemicellulose and lignin contents were removed partially. The treated fibers with low content of hemicellulose and lignin are suitable for the extraction of cellulose nanofibers.

Table 5.1 The chemical composition of untreated cassava pulp and treated fibers at each stage of treatment.

Sample	Lignocellulose			Non-lignocellulose (%)
	Cellulose (%)	Lignin (%)	Hemicellulose (%)	
Cassava pulp	21.12	3.53	8.64	66.71
Alkali treated fibers	65.88	3.13	6.99	24.00
Bleaching treated fibers	78.28	1.02	6.82	13.88

5.4.2 Morphological investigation of the fibers

SEM micrographs of the fibers after each stage of pre-treatment are shown in Figure 5.1. As can be seen from Figure 5.1a, the spherical structure of starch was observed on the surface of untreated cassava pulp. This result indicates that in addition to cellulose fibers, this raw material contains the residual starch. After alkali treatment (Figure 5.1b), the cassava pulp fiber bundles partially started separating into individual fibers. This could indicate the partial removal of the outer non-cellulosic layer composed of materials such as hemicelluloses, lignin, pectin, and other impurities. However, the individual fibers still cannot be distinguished. This is attributed to the retention of the cementing lignin material. Lignin forms a bridge bond with the cellulose ester and acts as a binder in the fiber components (Batra, 1985) thus

preserving the bundle form after alkali treatment. The observed morphology of fibers agrees with the chemical composition data. The effect of the subsequent bleaching treatment on the morphology of fibers is shown in Figure 5.1c. It was observed that the cassava pulp fiber bundles separate extensively into individual fibers. This indicates that lignin was removed mainly because of bleaching treatment.

Figure 5.2a shows transmission electron micrographs obtained for cellulose nanofibers resulting from acid hydrolysis of purified cassava pulp fibers. Under controlled conditions, the amorphous and paracrystalline regions of cellulose are hydrolyzed by acid hydrolysis treatment, whereas the crystalline regions of cellulose that have a high resistance to acid attack remain intact (Habibi, Lucia, and Rojas, 2010). The acid treatment should eventually reduce the size of the fibers from the micron to the nanometer scale (Azizi Samir, Alloin, and Dufresne, 2005). It can be seen from Figure 5.2a that the cellulose nanofibers with the immeasurable length were obtained. The diameter distribution of 100 samples of CNFs is shown in Figure 5.2b. As observed from Figure 5.2b, most cellulose nanofibers displayed a diameter in the range of 12-24 nm. This result indicates that the cellulose nanofibers were successfully extracted from cassava pulp by using acid hydrolysis method.

5.4.3 X-ray diffraction (XRD)

In contrast to hemicellulose and lignin which are amorphous in nature, cellulose has a crystalline structure. This is due to hydrogen bonding interactions and Van der Waals forces between adjacent molecules of cellulose (Zhang and Lynd, 2004). X-ray diffraction analysis was performed to evaluate the crystallinity of the fibers after different chemical treatment stages. Chemical treatment carried out on

natural fibers can affect the crystallinity of cellulose. For example, the acid treatment has no effect on the crystalline domains but destroys the amorphous region of the fiber (Fengel and Wegener, 1983). On the other hand, the stiffness of plant fiber was increased by the alkali treatment. This is due to the fact that the impurities present in the fibers can be removed during this treatment (Mwaikambo and Ansell, 2006). Therefore, in order to assess the effectiveness of the chemical treatment, the crystallinity of chemically treated fibers should be determined and compared to that of untreated fibers. Figure 5.3 shows the diffraction patterns obtained for (a) untreated, (b) alkali treated, (c) bleached, and (d) acid hydrolyzed cassava pulps. They are typical of cellulose I with three well-defined crystalline peaks around $2\theta = 16^\circ$, 22° , and 35° (Klemm, Heublein, Fink, and Bohn, 2005). These peaks become more defined upon chemical treatment as expected. The values of crystallinity index (CI) for various samples are summarized in Table 5.2. It was observed from Table 5.2 that the CI value was increased continuously upon the successive chemical treatments. The cellulose nanofibers have the highest CI value (74.53 %). The diffraction pattern of cellulose nanofibers also displayed the strongest and sharpest peak at around $2\theta = 22^\circ$ compared to that of other samples (Figure 5.3). The higher CI value of purified fibers in relation to that of untreated cassava pulps was ascribed to the progressive removal of amorphous non-cellulosic materials induced by alkali and bleaching treatments. The subsequent increase in the CI value upon acid hydrolysis treatment of purified fibers is due to the partial removal of paracrystalline domains and the dissolution of amorphous cellulosic domains during the acid hydrolysis process. Due to the elimination of amorphous regions of cellulose, the new hydrogen bonds could be formed through the hydroxyl

groups (-OH) on the surface of cellulose. As a result, the crystallinity was increased (Corrêa, de Moraes Teixeira, Pessan, and Mattoso, 2010).

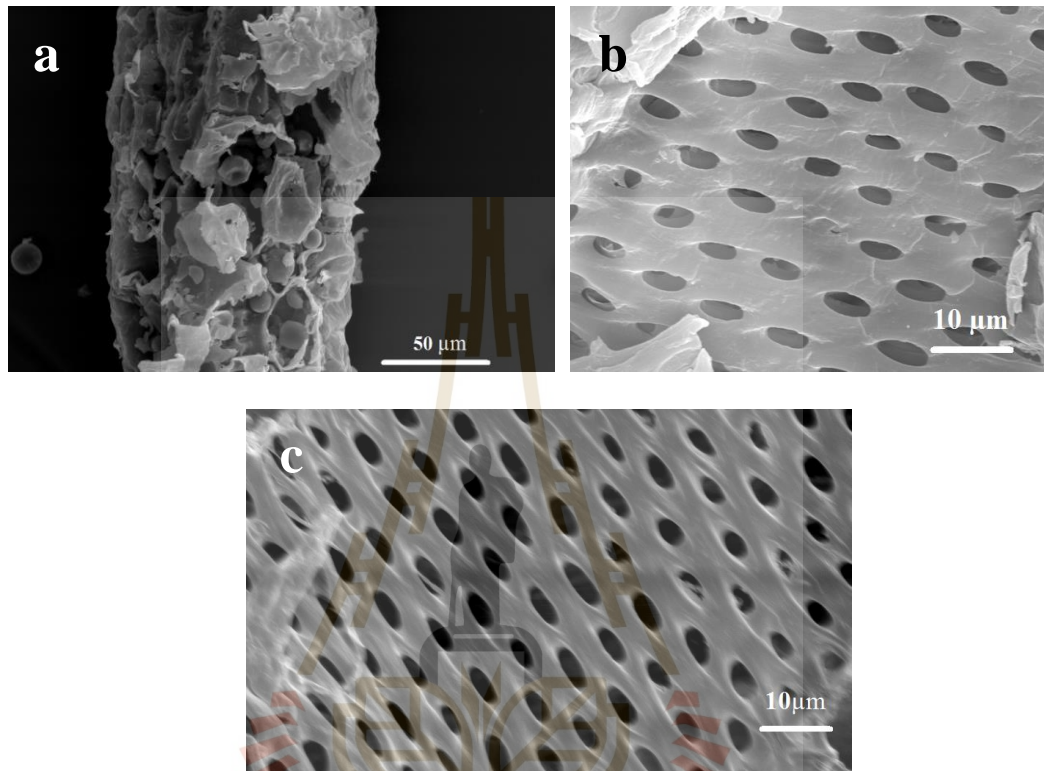


Figure 5.1 Scanning electron micrographs of (a) cassava pulp, (b) alkali-treated fibers, and (c) bleached-treated fibers.

The yields of purified fibers and cellulose nanofibers after acid hydrolysis treatment are listed in Table 5.2. These values were calculated on the basis of the dry weight of raw cassava pulp. As shown in Table 5.2, the cellulose nanofibers yield was approximately 17% of the original cassava pulp weight.

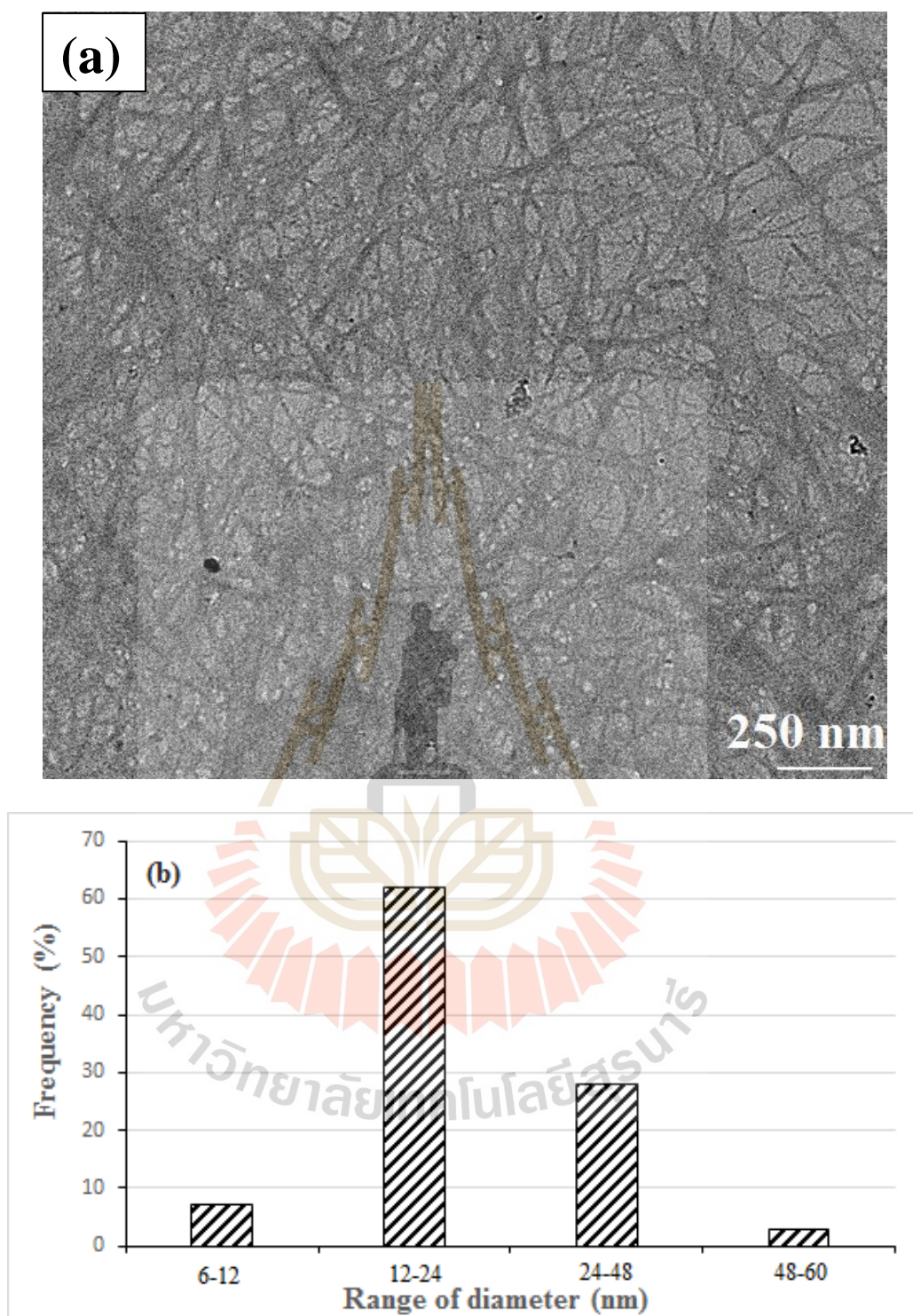


Figure 5.2 (a) Transmission electron micrograph from diluted suspension of cellulose nanofibers, (b) diameter distribution of obtained cellulose nanofibers.

Table 5.2 Crystallinity index (CI) and yield of obtained fibers at different stages of treatment.

Sample	Crystallinity index (%)	Yield (%)
Raw Cassava pulp	21.59	-
Alkali treated cassava pulp	46.63	42.90 ± 0.05
Bleached cassava pulp	66.82	25.31 ± 0.13
Cellulose nanofibers	74.53	16.92 ± 0.11

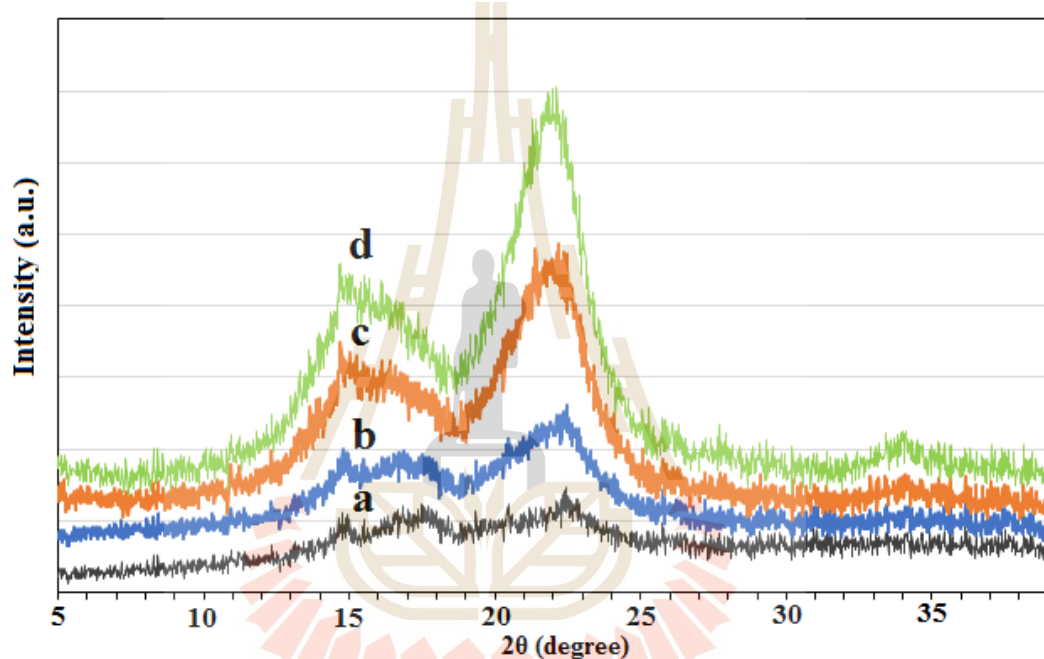


Figure 5.3 X-ray diffraction patterns of (a) raw, (b) alkali treated, (c) bleached, and (d) acid hydrolyzed cassava pulp.

5.4.4 Spectroscopic analysis (FTIR)

Figure 5.4 shows the FTIR spectra of untreated cassava pulp, alkali treated cassava pulp, bleached cassava pulp, and cellulose nanofibers. The absorbance peak around 3400 cm^{-1} , which was observed in all spectra, represents the stretching vibration of O-H groups. The prominent peak located at 1640 cm^{-1} in all spectra

corresponds to the bending vibration of absorbed water molecules. Both sets of peaks are attributed to the stretching of hydrogen bonds and bending of hydroxyl (-OH) groups bound to the cellulose structure. The peak near 2900 cm^{-1} in all spectra is due to the stretching vibration of saturated C-H in cellulose (Kaushik and Singh, 2011). These results indicate that the cellulose component was maintained during the chemical treatments carried out on the cassava pulp fibers.

A shoulder located at 1725 cm^{-1} in the spectrum of untreated cassava pulp can be ascribed to the stretching vibration of carbonyl groups representing the acetyl and uronic ester groups in hemicellulose. This shoulder can also be attributed to the ester linkage of carboxylic groups of p-coumaric and ferulic acids which are dominant constituents of hemicellulose and/or lignin (Alemdar and Sain, 2008). This peak has disappeared after alkali and bleaching treatments of cassava pulp. This indicates that the hemicellulose and lignin contents were removed from the untreated cassava pulp upon chemical treatments. Nevertheless, the data shown in Table 5.1 indicate that the hemicellulose and lignin contents were not entirely removed by these chemical treatments. This observation suggests that the absence of carbonyl groups in the FTIR spectrum most probably is due to the cleavage of ester bond and carboxylic group in hemicellulose and/or lignin.

Moreover, as can be seen from Figure 5.4, a distinct characteristic peak that appeared at around 1500 cm^{-1} in untreated cassava pulp can be assigned to the C=C stretching vibration of the aromatic ring of lignin (Xiao, Sun, and Sun, 2001). This peak still appeared in the alkali treated fiber and finally disappeared in the bleached fiber. These results suggest that the alkali treatment did not effectively remove the lignin and

the subsequent bleaching treatment caused the further removal of lignin. These observations are corroborated by the chemical composition data presented in Table 5.1. The peak located around 1300 cm^{-1} in the spectrum of the chemically treated cassava pulp is representative of a change in the symmetry of the C-H group (Sun, Xu, Sun, Fowler, and Baird, 2005). The band at around 1200 cm^{-1} in the spectra of bleached and acid hydrolyzed cassava pulp refers to the bending frequency of C-H, O-H, or CH_2 . Meanwhile, the absorptions at 1060 cm^{-1} and 890 cm^{-1} appearing in all spectra are attributed to C-O stretching and the glycosidic C-H vibration both of which are characteristic of the cellulose structure (Sun, Tomkinson, Wang, and Xiao, 2000). An increase in the intensity of these two peaks was observed in treated cassava pulp indicating that the treated cassava pulp contained a higher amount of cellulose compared to the untreated one.

In addition, it was noted that compared to the spectrum of bleached cassava pulp, the spectrum of cellulose nanofibers did not display any considerable difference. This indicates that the chemical structure of the samples was not changed after acid hydrolysis treatment.

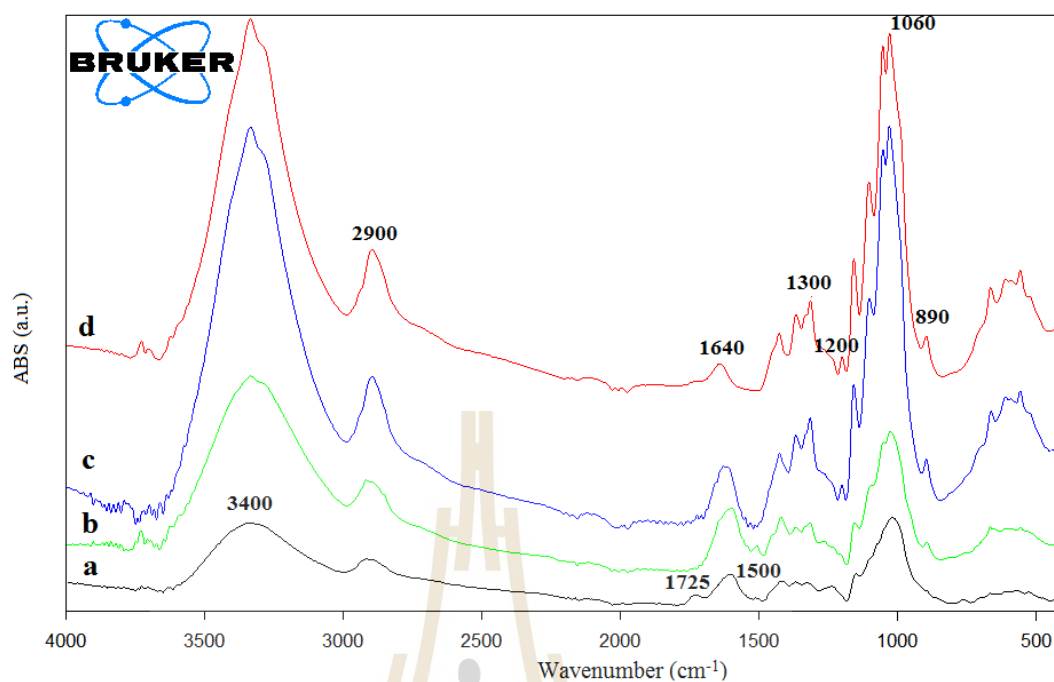


Figure 5.4 FTIR spectra of (a) raw, (b) alkali treated, (c) bleached, and (d) acid hydrolyzed cassava pulp.

5.4.5 Thermal stability

Thermogravimetric analysis (TGA) was performed to evaluate the thermal stability of both untreated and chemically treated cassava pulp fibers. It is thought that study on the thermal stability of cassava pulp fibers is very important in order to estimate their application in reinforced-biocomposite materials because most thermoplastic polymers are processed at temperatures ranging between 150 and 250 °C. Figure 5.5 shows the TGA and derivative thermogravimetry (DTG) curves obtained for untreated, alkali treated, bleached, and acid hydrolyzed cassava pulp. It is clearly seen that there is a small mass loss when these samples are heated from 30 to 130 °C regardless of their treatment. This mass loss in the early stage corresponds to the

evaporation of water because of the hydrophilic character of the lignocellulose fibers. The weight reduction was dependent on the initial moisture content of the analyzed fiber. A sharper weight drop is observed at higher temperatures. As can be seen from Figure 5.5, compared to untreated fiber, the alkali and bleached fibers have considerably higher thermal stability. This is because of the presence of a substantial proportion of low thermal stability components such as hemicellulose, starch, protein, and lipid in the untreated fibers. Their progressive removal by purification process improves the thermal stability of the cassava pulp. However, it was observed that the bleached fiber has slightly lower thermal stability than alkali treated fiber (Figure 5.5). This is attributed to the removal of lignin which has higher decomposition temperature in relation to cellulose (Yang, Yan, Chen, Lee, and Zheng, 2007). These results are very consistent with results obtained from the chemical composition analysis. The acid hydrolysis treatment of the cassava pulp fibers induces a significant decrease of the thermal stability of the material. It is noted that the acid hydrolysis treatment was carried out using a mixture of HCl/H₂SO₄ (1:2 v/v). Therefore, during the hydrolysis, the sulfate groups could be introduced at the outer surface of cellulose. These groups caused the dehydration reaction to take place, which led to lowering the thermal stability of cellulose nanofibers (Corrêa, de Moraes Teixeira, Pessan, and Mattoso, 2010).

Moreover, as can be seen from Figure 5.5, the amounts of residue at temperature around 400–600 °C in untreated cassava pulp fibers were very high which is in the range of 20–30 %. This residue amount or char fraction represents the carbon content of the fibers (Hornsby, Hinrichsen, and Tarverdi, 1997). It was observed that

the acid hydrolysis treatment induces an increase in the char fraction compared to the bleached fibers. This is due to the introduction of sulfated groups acting as a flame retardant (Roman and Winter, 2004).

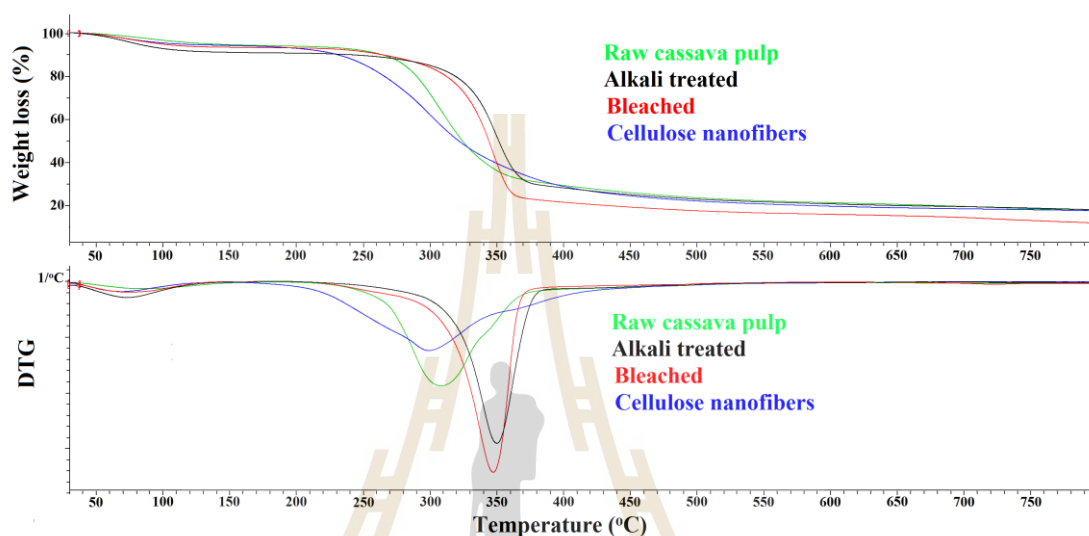


Figure 5.5 TGA and DTG curves of raw, alkali treated, bleached, and acid hydrolyzed cassava pulp.

5.4.6 Effect of acid types on crystallinity and thermal stability of obtained cellulose nanofibers

5.4.6.1 Crystallinity by XRD

As already discussed, removing amorphous components enables –OH groups on the cellulose surface to form new hydrogen bonds, increasing the crystallinity. The changes in crystallinity indexes due to nature of acid for hydrolysis are shown in Table 5.3. As can be seen from Table 5.3, the highest value (76.83 %) corresponds to CNFs-S, which also showed the strongest and sharpest peak at around

$2\theta = 22^\circ$ (Figure 5.6). This is ascribed to more extensive hydrolysis of the amorphous phase during acid treatment using H_2SO_4 . This is due to the fact that H_2SO_4 is stronger than HCl in nature. Thus, during hydrolysis process, the hydrolytic cleavage of glycosidic bonds, which eventually releases individual crystallites, takes place more extensively. As a result, the degree of crystallinity of obtained CNFs was enhanced. This increase in the cellulose fibers crystallinity is expected to increase their stiffness and rigidity, and therefore strength. Thus, it is assumed that the potential mechanical properties and reinforcing capability of treated fibers will increase.

Moreover, as expected, the CI value of CNFs-HS is higher than that of CNFs-H. However, it is worth noting that the changes in crystallinity indexes between CNFs-S and CNFs-HS were slight and not significant. It was also observed from Figure 5.6 that the nature of acid for hydrolysis did not cause any significant difference in the diffraction patterns of obtained CNFs. Nevertheless, the crystalline peak became sharper and stronger for CNFs extracted using H_2SO_4 or a mixture of $\text{HCl}/\text{H}_2\text{SO}_4$.

Table 5.3 Crystallinity index (CI) of cellulose nanofibers extracted using three different types of acid.

Sample	Crystallinity index (%)
CNFs-H	62.51
CNFs-HS	74.53
CNFs-S	76.83

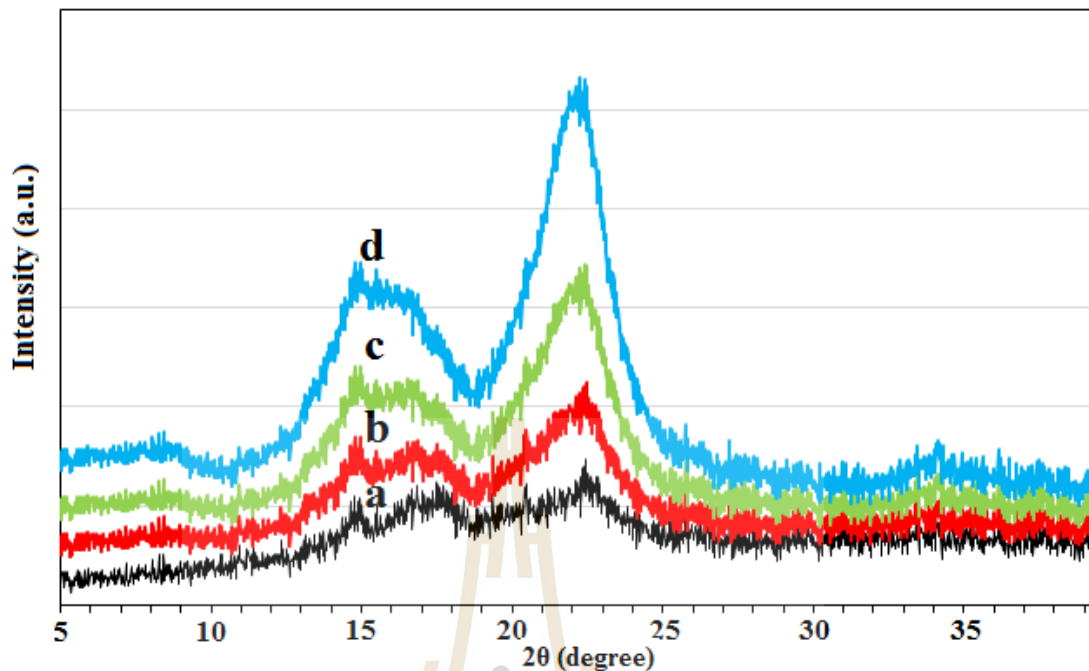


Figure 5.6 X-ray diffraction patterns of (a) raw cassava pulp, (b) CNFs-H, (c) CNFs-HS, and (d) CNFs-S.

5.4.6.2 Thermal stability

Figure 5.7 shows the TG and DTG curves for cassava pulp and nanofibers extracted using three different types of acid. It is clearly seen that the nanofibers hydrolyzed with H_2SO_4 (CNFs-S) presented lower thermal stability than their starting fibers and the other nanofibers. According to Roman and Wang (Roman and Winter, 2004); (Wang, Ding, and Cheng, 2007), the thermal degradation of cellulose containing sulfate groups takes place at lower temperatures because the sulfate groups, introduced at the outer surfaces of cellulose during the hydrolysis, cause a dehydration reaction. On the other hand, the use of HCl increased the thermal stability of nanofibers as observed in Figure 5.7. In addition, the use of only HCl in acid

hydrolysis resulted in narrower peaks (DTG curve) indicating the presence of more homogeneous crystals. The thermal stability of nanofibers hydrolyzed using a mixture of $\text{H}_2\text{SO}_4/\text{HCl}$ (CNFs-HS) was found to be slightly lower than that of raw cassava pulp, but it is better than that of CNFs-S. This suggests that the introduction of HCl in H_2SO_4 solution for hydrolysis resulted in more thermally stable cellulose nanofibers. Moreover, one can see clearly from Figure 5.7, the char fraction of CNFs-S was higher than that of CNFs-HS and CNFs-H. This is attributed to the sulfated groups which act as a flame retardant.

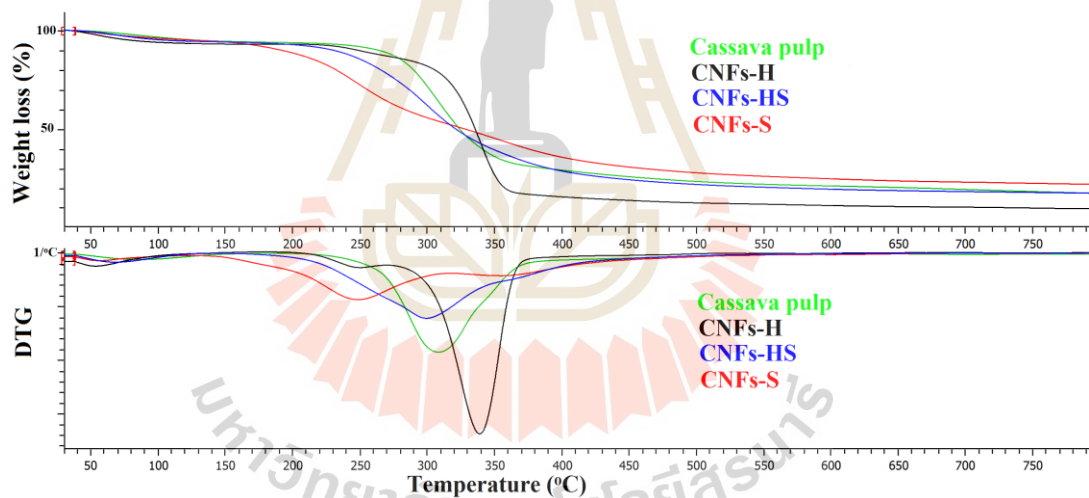


Figure 5.7 TGA and DTG curves of raw cassava pulp and cellulose nanofibers extracted using three different types of acid.

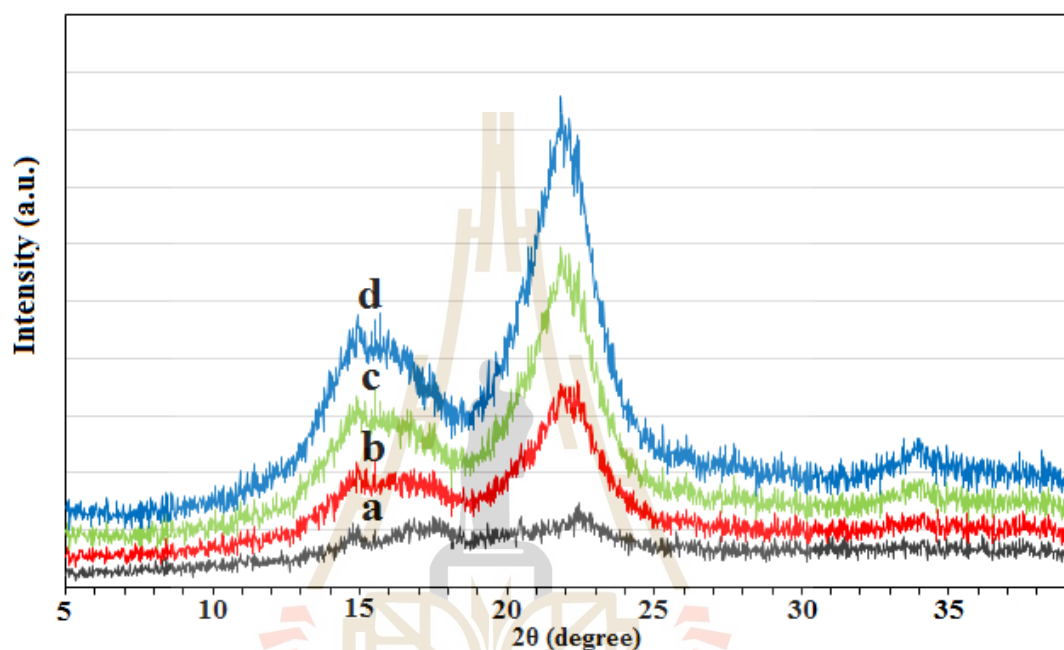
5.4.7 Effect of acid/pulp ratio on crystallinity and thermal stability of obtained cellulose nanofibers

5.4.7.1 Crystallinity by XRD

Crystallinity index of fibers is one of the most important parameters which is needed to determine upon chemical treatment. The higher crystallinity index, the better mechanical properties of fibers. During acid hydrolysis treatment, not only amorphous regions but also crystalline domains could be digested if the reaction conditions are not controlled. Therefore, the crystallinity index of chemical treated fibers should be determined at each stage of treatment. Figure 5.8 shows the XRD patterns of cassava pulp and obtained CNFs at various acid/pulp ratios. These patterns are typical of semicrystalline materials with an amorphous broad hump and crystalline peaks. As can be observed from Figure 5.8, the crystalline peak at around $2\theta = 22^\circ$ became narrower and sharper with increasing acid/pulp ratio. The higher acid/fiber ratio, the sharper crystalline peak. It is attributed to the higher crystallinity of obtained CNFs. From the XRD patterns, the crystallinity index of nanofibers can be determined using Eq. (5.1). Table 5.4 shows the crystallinity index of nanofibers at different acid/pulp ratios. As shown in Table 5.4, the CI value of nanofibers monotonically increased with increasing acid/fiber ratio. It is thought that the hydrolysis at higher acid/pulp ratio led to more extensive hydrolysis of the amorphous regions of cellulose. As a result, more -OH groups on the surface of cellulose could form new hydrogen bonds. This resulted in an increase of crystallinity.

Table 5.4 Crystallinity index (CI) of cellulose nanofibers at various acid/pulp ratios.

Sample	Crystallinity index (%)
CNFs-100ml/2g	70.83
CNFs-150ml/2g	74.53
CNFs-200ml/2g	77.03

**Figure 5.8** X-ray diffraction patterns of (a) raw cassava pulp, (b) CNFs-100ml/2g, (c) CNFs-150ml/2g, and (d) CNFs-200ml/2g.

5.4.7.2 Thermal stability

Figure 5.9 shows the TGA and DTG curves of cassava pulp and nanofibers at various acid/fiber ratios. As can be observed from Figure 5.9, the thermal stability of CNFs was lower than that of raw CP. It is noted that the acid hydrolysis was carried out using a mixture of HCl/H₂SO₄ (1:2 v/v). Therefore, during the hydrolysis, the sulfate groups could be introduced at the outer surface of cellulose. These groups

caused the dehydration reaction to occur. As a consequence, the thermal stability of obtained nanofibers lowered (Corrêa, de Moraes Teixeira, Pessan, and Mattoso, 2010). Furthermore, as shown in Figure 5.9, the thermal stability of nanofibers increased with an increase of acid/fiber ratio from 100ml/2g to 150ml/2g. This is attributed to the increase of crystallinity of CNFs as acid/fiber ratio was increased from 100ml/2g to 150ml/2g (Table 5.4). However, with further increase of acid/fiber ratio from 150ml/2g to 200ml/2g, the thermal stability of nanofibers lowered significantly. This is due to the fact that the higher acid/fiber ratio, the greater amount of sulfate groups introduced at the outer surfaces of cellulose during the hydrolysis. Thus, as acid/fiber ratio was relatively high (200ml/2g), the negative effect caused by sulfate groups on the thermal stability of CNFs dominated the positive effect resulting from the increased crystallinity. As a consequence, the thermal stability of nanofibers lowered. Also, it was noted from Figure 5.9 that the acid/pulp ratio did not cause any significant influence on the char fraction of obtained nanofibers.

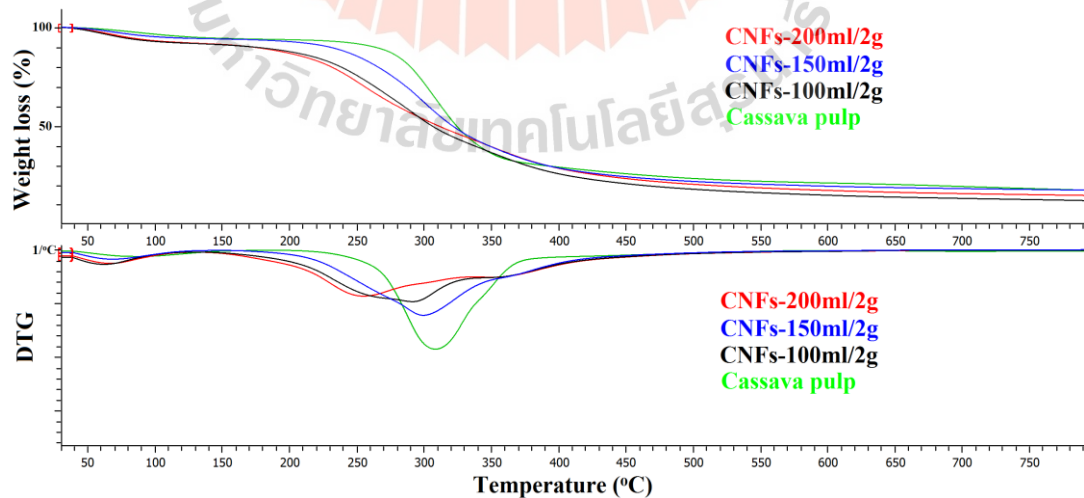


Figure 5.9 TGA and DTG curves of raw cassava pulp and cellulose nanofibers at various acid/fiber ratios.

5.4.8 Effect of hydrolysis time on crystallinity and thermal stability of obtained cellulose nanofibers

5.4.8.1 Crystallinity by XRD

The X-ray diffraction patterns of cellulose nanofibers at various reaction times are shown in Figure 5.10, and the crystallinity values are given in Table 5.5. As shown in Table 5.5, the crystallinity degree of CNFs increased with the increase of reaction time from 30 to 60 min. After that, with further increase of reaction time up to 90 min, a decrease in crystallinity of nanofibers was observed. This suggests that the extraction time of 90 min was severe enough to remove not only the amorphous phase but also to destroy the crystalline part of cellulose. Moreover, it was observed from Figure 5.10 that with an increase in reaction time, the XRD patterns of CNFs changed slightly. The peaks at around 22.5° and 15° of the CNFs-60min seem sharper than those of the CNFs-30min and CNFs-90min. This result indicates that 60 min of hydrolysis was long enough to remove most of the amorphous regions in nanofibers. The relative intensity of the peak at around 22.5° increased with an increase of hydrolysis time from 30 to 60 min. However, with further hydrolysis, particularly as hydrolysis time reached 90 min, the cellulose crystalline regions in the nanofibers were partially destroyed due to corrosion from the concentrated acid solution. This kind of damage in the cellulose crystalline regions led to a decrease in crystallinity of obtained nanofibers. It was verified by the reduction in relative intensity of the peak at around 22.5° as hydrolysis time reached 90 min (Figure 5.10).

5.4.8.2 Thermal stability

The TG and DTG curves for cassava pulp and nanofibers at various hydrolysis times are presented in Figure 5.11. As observed in Figure 5.11, the highest thermal stability of nanofibers was observed for the CNFs-60min sample. The thermal stability of nanofibers was enhanced with the increase of reaction time from 30 to 60 min. However, with further increase of reaction time, the thermal stability of nanofibers was dropped. More sulfated regions of cellulose degrade at lower temperatures, while regions less accessed by the sulfate groups of the acid tend to be more thermally stable (Li et al. 2009). Thus, the condition of hydrolysis for 90 min resulted in a major cellulose sulfation, also contributing to the cellulose degradation by dehydration reactions, hence causing damages in the crystal structure of cellulose. Because less sulfation occurred when hydrolysis was carried out for 30 min, this effect was minimized. Nevertheless, as can be seen from Figure 5.11, CNFs-30min had lower thermal stability than CNFs-60min. This is due to the lower crystallinity of CNFs-30min sample compared to that of CNFs-60min sample, as was verified by XRD analysis. This indicates that the hydrolysis time of 30 min is not long enough to allow the hydrolysis of the amorphous phase of cellulose to take place completely.

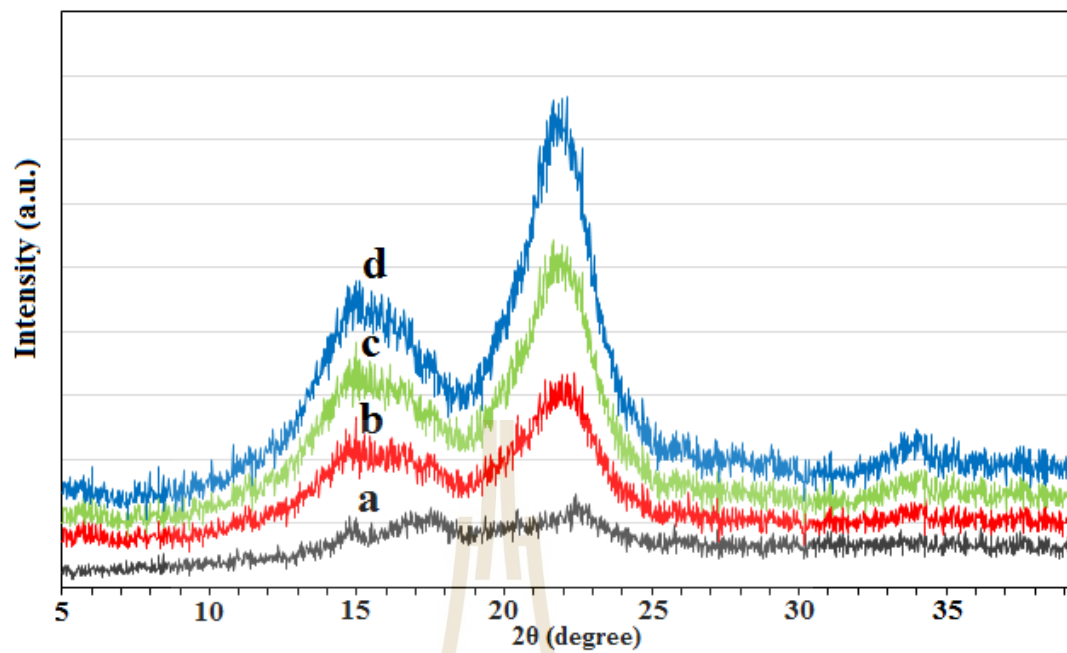


Figure 5.10 X-ray diffraction patterns of (a) raw cassava pulp, (b) CNFs-30min, (c) CNFs-90min, and (d) CNFs-60min.

Table 5.5 Crystallinity index (CI) of cellulose nanofibers at various hydrolysis times.

Sample	Crystallinity index (%)
CNFs-30min	67.90
CNFs-60min	74.53
CNFs-90min	70.50

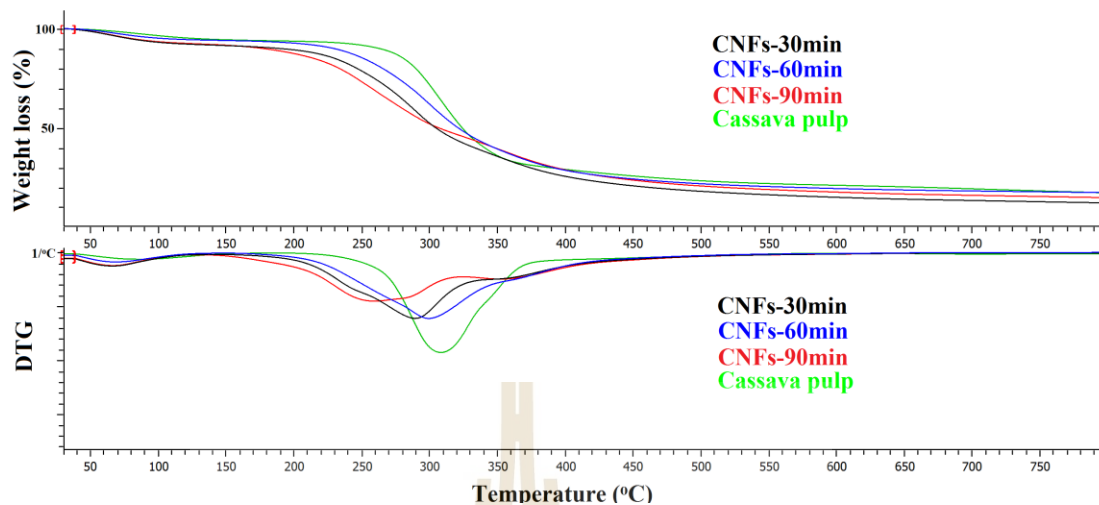


Figure 5.11 TGA and DTG curves of raw cassava pulp and cellulose nanofibers at various hydrolysis times.

5.4.9 Effect of acid concentration on crystallinity and thermal stability of obtained cellulose nanofibers

5.4.9.1 Crystallinity by XRD

The X-ray diffraction patterns and crystallinity index of cellulose nanofibers at various acid concentrations are shown in Figure 5.12 and Table 5.6, respectively. As observed in Figure 5.12, the relative intensity of the peak at around 22.5° increased continuously with the increase of acid concentration from 5.5 to 7.5 M. This corresponds to the highest crystallinity of CNFs-7.5M sample compared to that of the other samples hydrolyzed at lower acid concentration conditions (Table 5.6). It is thought that hydrolysis at a very low acid concentration (5.5 M) reduced the amorphous component from the starting pulp; however, the conditions are inadequate to structurally realign the crystallites or reduce the crystallite size. As a result, nanofibers

with lower crystallinity are produced. In addition, as can be seen from Table 5.6, a very slight increase of crystallinity of nanofibers was observed as acid concentration was increased from 6.5 to 7.5 M. This suggests that using an acid concentration of 6.5 M is an economic choice for this hydrolysis process.

Table 5.6 Crystallinity index (CI) of cellulose nanofibers at various acid concentrations.

Sample	Crystallinity index (%)
CNFs-5.5M	66.61
CNFs-6.5M	74.53
CNFs-7.5M	74.90

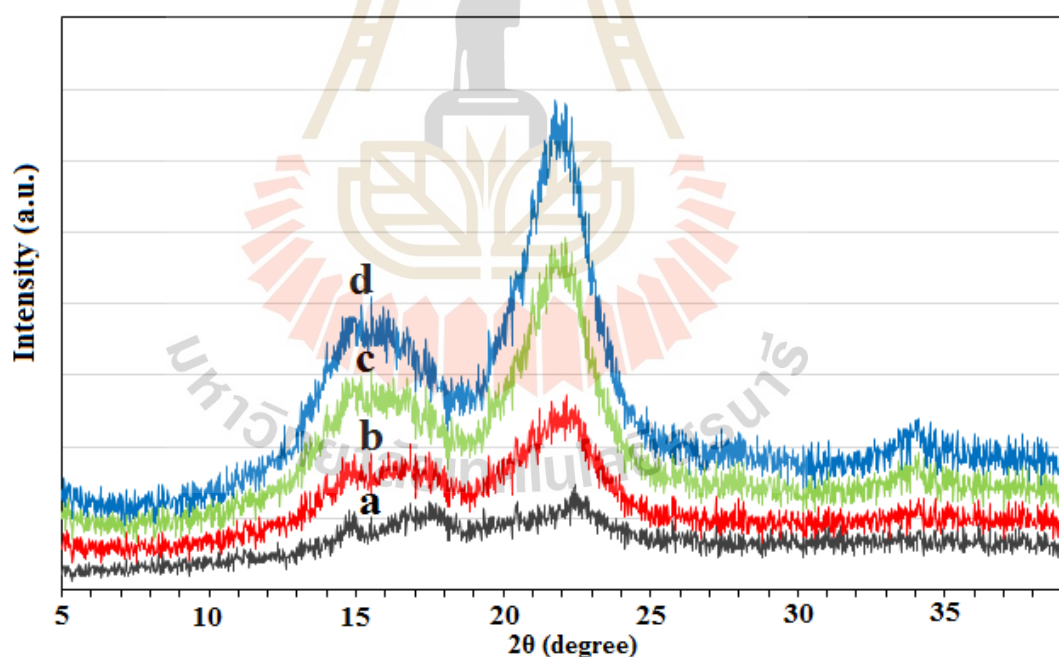


Figure 5.12 X-ray diffraction patterns of (a) raw cassava pulp, (b) CNFs-5.5M, (c) CNFs-6.5M, and (d) CNFs-7.5M.

5.4.9.2 Thermal stability

Acid hydrolysis of cassava pulp fibers using a mixture of HCl/H₂SO₄ is a heterogeneous process involving the diffusion of the acid into the pulp fibers, the cleavage of the glycosidic bond in cellulose, and the possible sulfation of cellulosic hydroxyl groups (i.e., conversion of cellulose-OH to cellulose-OSO₃H). Thus, it is expected that hydrolysis at higher acid concentration could lead to the greater degree of sulfation of the cellulose materials. This means that more sulfate (–OSO₃H) groups could be introduced to the surfaces of the crystalline cellulose materials. As discussed, these sulfate groups caused the dehydration reaction to take place, which led to lowering the thermal stability of obtained nanofibers. As observed from the TG and DTG curves of nanofibers at various acid concentrations (Figure 5.13), the thermal degradation of CNFs took place at lower temperatures as acid concentration was increased from 6.5 to 7.5 M. This is due to the higher degree of sulfation of CNFs-7.5M sample in relation to that of CNFs-6.5M sample. On the other hand, the thermal stability of CNFs-5.5M was surprisingly slightly lower than that of CNFs-6.5M, as observed in Figure 5.13. This could be explained by the very low crystallinity degree of CNFs-5.5M sample (Table 5.6). Thus, even the sulfation level of CNFs-5.5M sample was lower than that of CNFs-6.5M sample, the negative effect caused by the low crystallinity on the thermal stability of CNFs-5.5M was dominant. As a result, the thermal stability of CNFs-6.5M was slightly higher than that of CNFs-5.5M.

Moreover, as can be seen from Figure 5.13, the hydrolysis at an acid concentration of 5.5 M resulted in the lowest amount of residue. This is ascribed to the less sulfated groups acting as a flame retardant in the CNFs-5.5M sample.

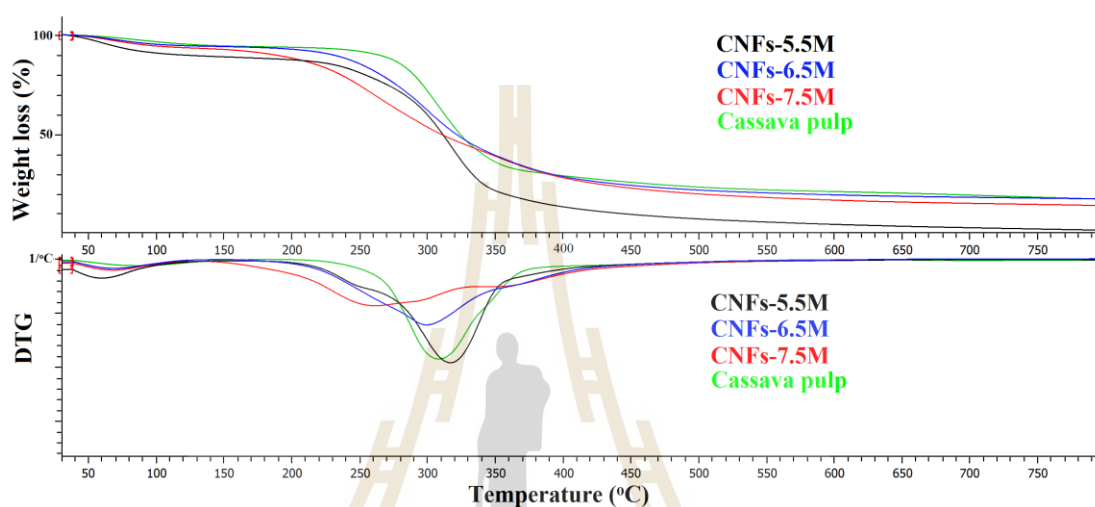


Figure 5.13 TGA and DTG curves of raw cassava pulp and cellulose nanofibers at various acid concentrations.

5.5 Conclusions

Cellulose nanofibers with a diameter in the range of 12-24 nm and immeasurable length were extracted successfully from cassava pulp by submitting to alkali, bleaching, and acid hydrolysis treatments under different conditions. It was observed that the alkali treatment was efficient in removing hemicellulose while the bleaching treatment was efficient for the removal of lignin. Chemical composition determination, morphological investigation, infrared spectroscopy, and X-ray diffraction analyses confirmed the removal of non-cellulosic materials. The chemical

treatments induced an increase of the cellulose content from 21.12 % to 78.28 %, and of the crystallinity index from 21.59 % to 74.53 %. Under the same reaction conditions, the crystallinity of nanofibers hydrolyzed using H₂SO₄ or a mixture of HCl/H₂SO₄ was higher than that of ones hydrolyzed using HCl. On the other hand, the thermal stability of nanofibers hydrolyzed using HCl was found to be significantly higher than that of the starting material and ones hydrolyzed using H₂SO₄ or a mixture of HCl/H₂SO₄. The introduction of HCl in H₂SO₄ solution for hydrolysis resulted in more thermally stable nanofibers with the slightly lower crystallinity. For the same acid type (using a mixture of HCl/H₂SO₄ (1:2 v/v)), the increase in acid concentration and acid/pulp ratio in the acid hydrolysis treatment resulted in nanofibers with higher crystallinity degree and a decrease in thermal stability at certain conditions (7.5 M and 200ml/2g, respectively). With the same acid concentration and acid/pulp ratio, the crystallinity and thermal stability of nanofibers dropped considerably at a certain hydrolysis time (90 min).

As a next work, the effect of the resulting cellulose nanofibers as a reinforcing phase in a poly(lactic acid) matrix is worth to be investigated.

5.6 References

- Alemdar, A., and Sain, M. (2008). Isolation and characterization of nanofibers from agricultural residues—Wheat straw and soy hulls. **Bioresource Technology**. 99: 1664-1671.
- Angles, M. N., and Dufresne, A. (2001). Plasticized starch/tunicin whiskers nanocomposite materials. 2. Mechanical behavior. **Macromolecules**. 34: 2921-2931.

- Azizi Samir, M. A. S., Alloin, F., and Dufresne, A. (2005). Review of recent research into cellulosic whiskers, their properties and their application in nanocomposite field. **Biomacromolecules**. 6: 612-626.
- Batra, S. (1985). Other long vegetable fibres: abaca, banana, sisal, henequen, flax, ramie, hemp, sunn, and coir. **Handbook of Fiber Science and Technology**. 4: 727-807.
- Beck-Candanedo, S., Roman, M., and Gray, D. G. (2005). Effect of reaction conditions on the properties and behavior of wood cellulose nanocrystal suspensions. **Biomacromolecules**. 6: 1048-1054.
- Bondeson, D., Mathew, A., and Oksman, K. (2006). Optimization of the isolation of nanocrystals from microcrystalline cellulose by acid hydrolysis. **Cellulose**. 13: 171-180.
- Corrêa, A. C., de Moraes Teixeira, E., Pessan, L. A., and Mattoso, L. H. C. (2010). Cellulose nanofibers from curaua fibers. **Cellulose**. 17: 1183-1192.
- Dai, D., Fan, M., and Collins, P. (2013). Fabrication of nanocelluloses from hemp fibers and their application for the reinforcement of hemp fibers. **Industrial Crops and Products**. 44: 192-199.
- Elazzouzi-Hafraoui, S., et al. (2007). The shape and size distribution of crystalline nanoparticles prepared by acid hydrolysis of native cellulose. **Biomacromolecules**. 9: 57-65.
- Fengel, D., and Wegener, G. (1983). **Wood: chemistry, ultrastructure, reactions**. Berlin: Walter de Gruyter.

- Habibi, Y., Lucia, L. A., and Rojas, O. J. (2010). Cellulose nanocrystals: Chemistry, self-assembly, and applications. **Chemical Reviews**. 110: 3479-3500.
- Hornsby, P., Hinrichsen, E., and Tarverdi, K. (1997). Preparation and properties of polypropylene composites reinforced with wheat and flax straw fibres: part I fibre characterization. **Journal of Materials Science**. 32: 443-449.
- Johar, N., Ahmad, I., and Dufresne, A. (2012). Extraction, preparation and characterization of cellulose fibres and nanocrystals from rice husk. **Industrial Crops and Products**. 37: 93-99.
- Kaushik, A., and Singh, M. (2011). Isolation and characterization of cellulose nanofibrils from wheat straw using steam explosion coupled with high shear homogenization. **Carbohydrate Research**. 346: 76-85.
- Klemm, D., Heublein, B., Fink, H. P., and Bohn, A. (2005). Cellulose: fascinating biopolymer and sustainable raw material. **Angewandte Chemie (International ed. in English)**. 44: 3358-3393.
- Li, R., et al. (2009). Cellulose whiskers extracted from mulberry: A novel biomass production. **Carbohydrate Polymers**. 76: 94-99.
- Mwaikambo, L., and Ansell, M. (2006). Mechanical properties of alkali treated plant fibres and their potential as reinforcement materials. I. Hemp fibres. **Journal of Materials Science**. 41: 2483-2496.
- Roman, M., and Winter, W. T. (2004). Effect of sulfate groups from sulfuric acid hydrolysis on the thermal degradation behavior of bacterial cellulose. **Biomacromolecules**. 5: 1671-1677.

- Sadeghifar, H., Filpponen, I., Clarke, S. P., Brougham, D. F., and Argyropoulos, D. S. (2011). Production of cellulose nanocrystals using hydrobromic acid and click reactions on their surface. **Journal of Materials Science**. 46: 7344-7355.
- Segal, L., Creely, J. J., Martin, A. E., and Conrad, C. M. (1959). An Empirical Method for Estimating the Degree of Crystallinity of Native Cellulose Using the X-Ray Diffractometer. **Textile Research Journal**. 29: 786-794.
- Silvério, H. A., Neto, W. P. F., Dantas, N. O., and Pasquini, D. (2013). Extraction and characterization of cellulose nanocrystals from corncob for application as reinforcing agent in nanocomposites. **Industrial Crops and Products**. 44: 427-436.
- Sriroth, K., Chollakup, R., Chotineeranat, S., Piyachomkwan, K., and Oates, C. G. (2000). Processing of cassava waste for improved biomass utilization. **Bioresource Technology**. 71: 63-69.
- Sriroth, K., et al. (1999). Cassava starch granule structure–function properties: influence of time and conditions at harvest on four cultivars of cassava starch. **Carbohydrate Polymers**. 38: 161-170.
- Sun, R., Tomkinson, J., Wang, Y., and Xiao, B. (2000). Physico-chemical and structural characterization of hemicelluloses from wheat straw by alkaline peroxide extraction. **Polymer**. 41: 2647-2656.
- Sun, X., Xu, F., Sun, R., Fowler, P., and Baird, M. (2005). Characteristics of degraded cellulose obtained from steam-exploded wheat straw. **Carbohydrate Research**. 340: 97-106.

- Teixeira, E. d. M., et al. (2012). Properties of thermoplastic starch from cassava bagasse and cassava starch and their blends with poly (lactic acid). **Industrial Crops and Products**. 37: 61-68.
- Wang, N., Ding, E., and Cheng, R. (2007). Thermal degradation behaviors of spherical cellulose nanocrystals with sulfate groups. **Polymer**. 48: 3486-3493.
- Xiao, B., Sun, X., and Sun, R. (2001). Chemical, structural, and thermal characterizations of alkali-soluble lignins and hemicelluloses, and cellulose from maize stems, rye straw, and rice straw. **Polymer Degradation and Stability**. 74: 307-319.
- Yang, H., Yan, R., Chen, H., Lee, D. H., and Zheng, C. (2007). Characteristics of hemicellulose, cellulose and lignin pyrolysis. **Fuel**. 86: 1781-1788.
- Zhang, Y. H. P., and Lynd, L. R. (2004). Toward an aggregated understanding of enzymatic hydrolysis of cellulose: noncomplexed cellulase systems. **Biotechnology and Bioengineering**. 88: 797-824.

CHAPTER VI

GLYCIDYL METHACRYLATE GRAFTED POLY(LACTIC ACID)

6.1 Abstract

Glycidyl methacrylate (GMA) was grafted onto poly (lactic acid) (PLA) by an internal mixer using dicumyl peroxide (DCP) as an initiator. The results from proton nuclear magnetic resonance ($^1\text{H-NMR}$), carbon-13 nuclear magnetic resonance ($^{13}\text{C-NMR}$) and gel permeation chromatograph (GPC) indicated that the grafting reaction of GMA onto PLA took place successfully. In order to obtain the optimal mixing conditions, the grafting reaction was carried out at various GMA contents and mixing times. The GMA content was varied into 5, 10 and 15 wt% of PLA. The mixing time was varied into 7, 10 and 14 min. Physical properties including rheological, morphological, thermal, mechanical properties and crystallization behavior of glycidyl methacrylate grafted poly (lactic acid) (PLA-g-GMA) were studied and compared with those of PLA. With the same mixing time, GMA content of 10 wt% was found to give the highest elongation at break and impact strength of PLA-g-GMA. The weight-average molecular weights, the number-average molecular weights, and the polydispersity index of PLA increased after grafting with GMA. PLA-g-GMA, prepared with GMA content of 10 and 15 wt%, showed melt crystallization upon cooling. This was different from PLA and PLA-g-GMA prepared

with GMA content of 5 wt%, which did not undergo crystallization upon cooling from the melt. At a given amount of GMA, the mixing time of 10 min was found to give the highest grafting yield, elongation at break and impact strength of PLA-g-GMA. After grafting, the brittle behavior of amorphous PLA was changed to the ductile behavior of semicrystalline PLA-g-GMA. With its superior mechanical properties compared to those of pure PLA, PLA-g-GMA can be considered to be used as a new generation of biodegradable polymers, which can be applied in many industrial applications.

6.2 Introduction

Due to the environmental issue related to non-degradable plastic wastes, the research and development of biodegradable polymers have recently received considerable attention. Owing to its renewability, biodegradability, good mechanical properties and being easily processed, poly (lactic acid), a synthetic aliphatic polyester derived from biomasses, has been emerging as an alternative to conventional petroleum-based polymeric materials (Garlotta, Doane, Shogren, Lawton, and Willett, 2003). However, PLA is still more expensive than many petroleum-derived commodity plastics. It has some poor physical properties such as slow crystallization rate, high brittleness, and low heat stability (Rudnik, 2010) which hinder PLA to be used for various end-use applications.

So far, in addition to solution copolymerization, melt grafting process by using an internal mixer has been extensively used in order to prepare many of the functionalized reactive polymers because of the relative simplicity and cost efficiency of this method (Gaylord and Mishra, 1983); (De Roover et al., 1995); (Ho, Su, Wu,

and Chen, 1993). Free radical grafting of PLA with monomers containing reactive groups has been considered to be a potential approach to modifying basic properties of pristine PLA (Pesetskii and Makarenko, 2002); (Burton, Woodhead, Coates, and Gough, 2010). Also, it is an effective method to produce the compatibilizing agent for PLA-based polymer blends.

Due to its dual functionality, which consists of epoxy and acrylic groups, GMA has been increasingly used as a grafting monomer. It is thought that the epoxy group of GMA can react with many other groups, such as hydroxyl and carboxyl groups. Meanwhile, acrylic groups allow the free-radical grafting of GMA onto the polymer chains to occur (Cho, Eom, Kim, and Park, 2008); (Xu, Tang, and Zhu, 2012); (Li and Xie, 2012); (Chen, Wong, and Baker, 1996); (Huang and Liu, 1998). Xu et al. (2015) studied on grafting GMA onto polypropylene (PP) by melt grafting using a homemade reactive corotating twin-screw extruder. Dicumyl peroxide (DCP) was used as a radical initiator. The authors reported that the GMA grafted PP had higher crystallization temperature, higher melting temperature, higher crystallinity, and slightly higher thermal stability compared to the neat PP. The grafting of GMA onto isotactic polybutene-1 (iPB) using di-tert-butyl peroxide (DTBP) as an initiator via a radical-initiated melt grafting reaction was investigated by Zhao, Zhou, Chen, and Han (2015). The grafting process was carried out using an internal mixer. They demonstrated that at 180 °C, while increasing the GMA concentration, the grafting degree increased, and the grafting efficiency decreased. At a given amount of GMA, increasing DTBP concentration could increase the grafting degree and grafting efficiency, while the degradation of iPB became substantial. Compared to the unmodified iPB, the melting peaks and crystallinity of iPB-g-GMA were lower, while

the crystallization temperature and the crystallization rate increased. Mohanty and Nayak (2015) investigated grafting GMA onto PLA by melt blending PLA with GMA in an internal mixer using benzoyl peroxide (BPO) and dicumyl peroxide (DCP) as initiators. They reported that the percentage of grafting achieved using BPO was higher than that obtained by DCP at a given amount of GMA.

Depending on the selected polymer used for modification and medium of grafting reaction, the grafting mechanism may be different. In the case of PLA, the mechanism of grafting GMA onto PLA chain using melt polymerization reaction has been reported (Liu, Jiang, and Chen, 2012). This possible mechanism was described by three main steps involving in the grafting reaction. As can be seen from Figure 6.1 the grafting reaction starts with the decomposition of peroxide initiator followed by generation of peroxy radical. This free radical captured a tertiary hydrogen from PLA chain to form PLA macroradical. Then GMA grafting reaction can occur through step (2) and step (3). Besides that, it was reported that the epoxy group of GMA could react with hydroxyl groups and carboxyl end groups of PLA in the melt mixing (Jeong and Xanthos, 2007). Furthermore, the crosslinking reaction through step (1) can occur during the grafting reaction. It is worth noting that during grafting reaction, the homopolymerization of GMA can happen due to the high activation of GMA monomer with respect to free radical polymerization reaction (Matyjaszewski, Coca, and Jasieczek, 1997).

Even the radical grafting of GMA onto polyolefin in melt mixing process has been investigated extensively, there have been very few studies focusing on the grafting of GMA onto PLA and effects of GMA content and mixing time on physical properties of obtained PLA-g-GMA. Therefore, in this study, we report on the

grafting of GMA onto PLA with different GMA contents and mixing times using dicumyl peroxide (DCP) as an initiator in the internal mixer.

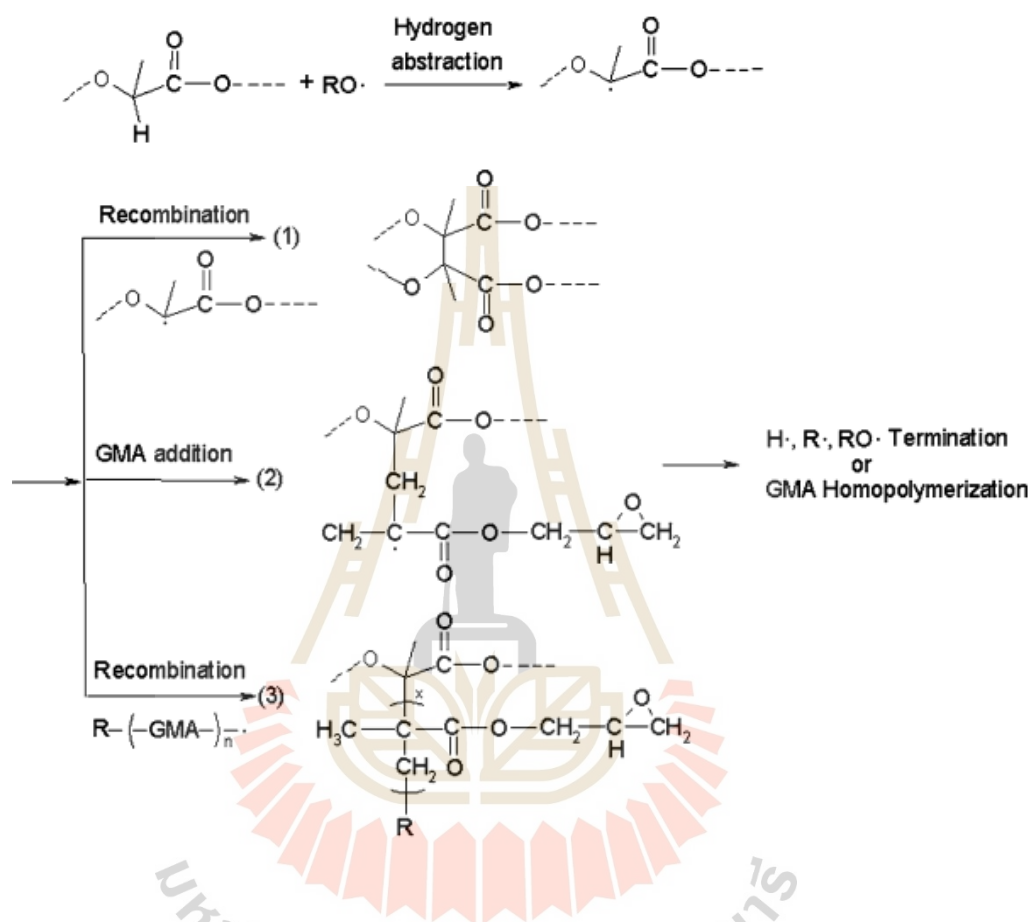


Figure 6.1 Mechanism of the grafting of GMA onto the PLA chain (Liu et al., 2012).

PLA-g-GMA obtained from this study can be used to replace for pristine PLA having many drawbacks in many industrial applications. Furthermore, with the chemical structure containing hydrophilic chain and oleophilic chain, the obtained PLA-g-GMA can be used as a potential compatibilizer in natural fibers reinforced PLA-based biocomposites.

6.3 Materials and methods

6.3.1 Materials

Commercial PLA (PLA 4043D) was purchased from NatureWorks LLC. Dicumyl peroxide (DCP, 99 %), glycidyl methacrylate (GMA, 99 %), dichlorobenzene (DCB), chloroform (HPLC grade), and methanol were supplied from Sigma-Aldrich[®]. Before being used for grafting, GMA was purified by basic alumina pack column to remove inhibitor and stored in the refrigerator at about 5 °C.

6.3.2 Preparation of PLA-g-GMA

The grafting of GMA onto PLA chain was carried out by an internal mixer (Haake Rheomix, 3000p). Before being used, PLA pellet was dried at 70 °C for 2 h. The grafting reaction was carried out under the temperature and mixing speed of 170 °C, and 60 rpm, respectively. With the same mixing time, GMA content was varied into 5, 10, and 15 wt% of PLA. The obtained grafted samples were labeled as PLA-g-GMA5%, PLA-g-GMA10%, and PLA-g-GMA15%, respectively. Under the same GMA content, the mixing time was varied into 7, 10, and 14 min. The obtained samples were labeled as PLA-g-GMA7min, PLA-g-GMA10min, and PLA-g-GMA14min, respectively. The number of the labeled names indicated the used GMA content and mixing time, respectively. Before grafting, GMA was stored in the refrigerator at 5 °C. The concentration of DCP used was 0.2 wt% of PLA. The grafting procedure is described as follows:

First, determined amounts of PLA and DCP were premixed before being charged into the mixing chamber. After 2 min of mixing, GMA was added into the chamber. After the addition of GMA, the mixing chamber was closed immediately to minimize the loss of GMA due to vaporization.

6.3.3 Purification of prepared PLA-g-GMA

In order to remove unreacted GMA and possible homopolymer of GMA, which may be generated during the grafting reaction, the obtained samples were dissolved in DCB (5 wt% solution) at 120 °C after mixing (Cho et al., 2008). After that, the solution was poured into a large excess of methanol to precipitate PLA-g-GMA. The obtained white PLA-g-GMA precipitate was washed several times with methanol to remove the residual GMA and homopolymer of GMA completely. After purification process, the pure white PLA-g-GMA was dried in a vacuum oven at 70 °C for 24 h.

6.3.4 Characterization of PLA-g-GMA

6.3.4.1 Nuclear magnetic resonance (NMR)

The percentage of GMA grafted on PLA was determined by ¹H-NMR analysis. ¹H-NMR spectra of PLA, PLA-g-GMA, and GMA monomer were recorded on a Varian model Inova 300 NMR spectrophotometer at 25 °C and 300 MHz using CDCl₃ as a solvent and tetramethylsilane (TMS) as an internal standard. The graft content was determined by calculating the relative area of the characteristic peaks of PLA and GMA. It was examined by Eq. (6.1) (Liu et al., 2012). The GMA grafting efficiency, which is defined as grafted GMA divided by initial GMA concentration, was determined by Eq. (6.2) (Cho et al., 2008). The ¹³C-NMR analysis was performed to confirm the grafting of GMA onto PLA chain. The ¹³C-NMR measurements were carried out at room temperature on a Bruker Biospin DPX-300 at 75 MHz.

$$\% \text{grafting} = \frac{\text{relative - area - of - characteristic - peak - of - GMA}}{\text{relative - area - of - characteristic - peak - of - PLA}} \times 100 \quad (6.1)$$

$$\text{Grafting efficiency} = \frac{\% \text{grafting}}{\text{initial - GMA - concentration}} \quad (6.2)$$

6.3.4.2 Fourier Transform Infrared (FTIR) Spectroscopy

The measurements of structural characterization of PLA and PLA-g-GMA were conducted by Fourier transform infrared spectroscopy Bruker Tensor 27 using attenuated total reflectance (ATR) equipped with platinum diamond crystal (TYPE A225/QL). Spectra were obtained at 4 cm^{-1} resolution and 32 scans in the wavenumber range from 4000 to 400 cm^{-1} . All samples were dried in a vacuum oven at $60 \text{ }^{\circ}\text{C}$ for 24 h before testing. All spectra were normalized using OPUS 7.0 software.

6.3.4.3 Gel permeable chromatography (GPC)

The molecular weight and polydispersity index (PDI) of pure PLA and PLA-g-GMA were obtained by Gel Permeable Chromatography (GPC, Agilent 1200) using chloroform (HPLC grade) as a solvent with a flow rate of 0.5 ml/min . The calibration was carried out by using polystyrene standards (Polyscience Co.). All samples were measured at $40 \text{ }^{\circ}\text{C}$.

6.3.4.4 Rheological properties

Shear viscosities at various shear rates of pure PLA and PLA-g-GMA were measured using Gottfert capillary rheometer (model RG 20) at $170 \text{ }^{\circ}\text{C}$. Melt flow index (MFI) of pure PLA and PLA-g-GMA was characterized using a melt flow indexer (Kayeness, 4004). All measurements were performed according to

ASTM D1238 at 170 °C with a load of 2.16 kg. The results are reported in terms of the weight of the extrudate in gram per 10 min.

6.3.4.5 Mechanical properties

Compression molding was used to prepare the test specimens for mechanical properties testing. After drying in an oven at 70 °C for 2 h, all samples were compression molded at 170 °C for 10 min. Tensile properties of all compression molded samples were obtained according to ASTM D638 using an Instron Universal Testing Machine (UTM 5565) with a load cell of 5 kN. The unnotched Izod impact strengths of pure PLA and PLA-g-GMA were obtained according to ASTM D256 by using Instron CEAST 9050 Pendulum Impact System.

6.3.4.6 X-ray diffraction (XRD)

The difference in the crystalline structure of pure PLA and PLA-g-GMA before and after the tensile test was investigated using a diffractometer (AXS Nanostar-D8 Discover, Bruker) equipped with a CuK α generator ($\lambda = 1.5404$ Å) at 40 kV and 40 mA, in a 2θ range from 5 to 90°.

6.3.4.7 Morphological properties

The tensile fractured surfaces of all samples were observed by a scanning electron microscope (SEM, model JEOL JSM6010LV). Before testing, the specimens were coated with gold. An acceleration voltage of 10 kV was used to obtain SEM images.

6.3.4.8 Thermal properties

The nonisothermal crystallization behavior of pure PLA and PLA-g-GMA was investigated using a differential scanning calorimetry (DSC) (model: DSC204F1 Phoenix). The samples were first heated to 200 °C with the rate of

5 °C/min and kept at 200 °C for 5 min (First heating scan). After that, they were cooled to 40 °C with the rate of 5 °C/min (Cooling scan). Then they were heated again to 200 °C with the rate of 5 °C/min (Second heating scan). Enthalpy of crystallization (ΔH_c) was determined from the area under the peak of the thermograms from the cooling scan. Enthalpy of cold crystallization (ΔH_{cc}) was obtained from the area under the recrystallization peak of the thermograms from the second heating scan. Enthalpy of melting (ΔH_m) was determined from the area under the melting peak of the thermograms from the second heating scan. The degree of crystallinity ($\%X_c$) of pure PLA and PLA-g-GMA was examined by Eq. (6.3) (Huang et al., 1998):

$$\%X_c = \frac{\Delta H_m}{\Delta H_{mo}} \times 100 \quad (6.3)$$

In which ΔH_m is the measured melting enthalpy (in J/g) from the second heating scan and ΔH_{mo} is the theoretical melting enthalpy of completely crystalline PLA (93.7 J/g) (Fischer, Sterzel, and Wegner, 1973).

6.4 Results and discussion

6.4.1 Characterization of glycidyl methacrylate grafted poly (lactic acid)

6.4.1.1 Spectroscopic analysis

The FTIR spectra of pure PLA and PLA-g-GMA are shown in Figure 6.2. The spectrum of pure PLA indicated the peaks at 3000–2940 cm^{-1} , 1761 cm^{-1} , and 1190–1090 cm^{-1} , which are associated with CH_3 stretching, C=O stretching, and the O–C=O stretching, respectively (Orozco, Brostow, Chonkaew, and Lopez,

2009). The peaks at 910 cm^{-1} , 1150 cm^{-1} , 1761 cm^{-1} , and 3000 cm^{-1} were observed in the spectrum of PLA-g-GMA. Compared to the spectrum of pure PLA, the spectrum of PLA-g-GMA presented a small new peak appeared at 910 cm^{-1} , which is attributed to the asymmetric stretching of the epoxy group. This evidence indicates that the GMA was successfully grafted onto PLA chain.

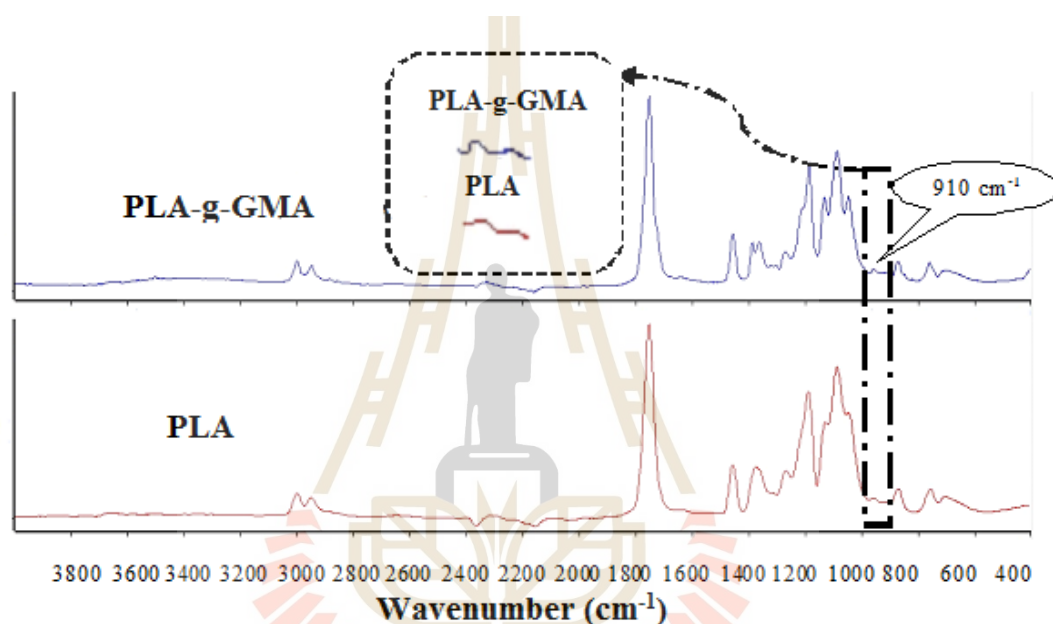


Figure 6.2 FTIR spectra of pure PLA and PLA-g-GMA, [GMA] = 10 wt%, mixing time = 10 min.

NMR analysis was also used to confirm the grafting of GMA onto PLA. As seen in Figure 6.3, $^1\text{H-NMR}$ spectra of PLA and PLA-g-GMA show two peaks at 5.2 and 1.6 ppm, which represent methine protons and methyl protons of PLA chain, respectively. After grafting, the lower relative area of the peak of methyl protons was observed, and the chemical shift of methyl protons was slightly shifted to

a higher value. It is attributed to the deshielding effect of electron withdrawing groups in the chemical structure of GMA leading to the reduction of electron density around a methyl proton nucleus. Moreover, compared to the spectrum of pure PLA, the spectrum of PLA-g-GMA exhibited the new and weak peaks appeared at 0.9-4.3 ppm. These peaks represent the protons 1-7 in the chemical structure of GMA as shown in Figure 6.3. Moreover, from $^1\text{H-NMR}$ spectrum of GMA, it can be observed that the chemical shifts of all peaks, which are associated with GMA constitutional unit of proton CH, CH_2 , and CH_3 , are different from those in the spectrum of PLA-g-GMA. This observation demonstrates that the new multipeak belong to GMA grafted on PLA chain. These results confirmed that GMA was successfully grafted onto PLA chain. The similar results were reported by another study (Liu et al., 2012).

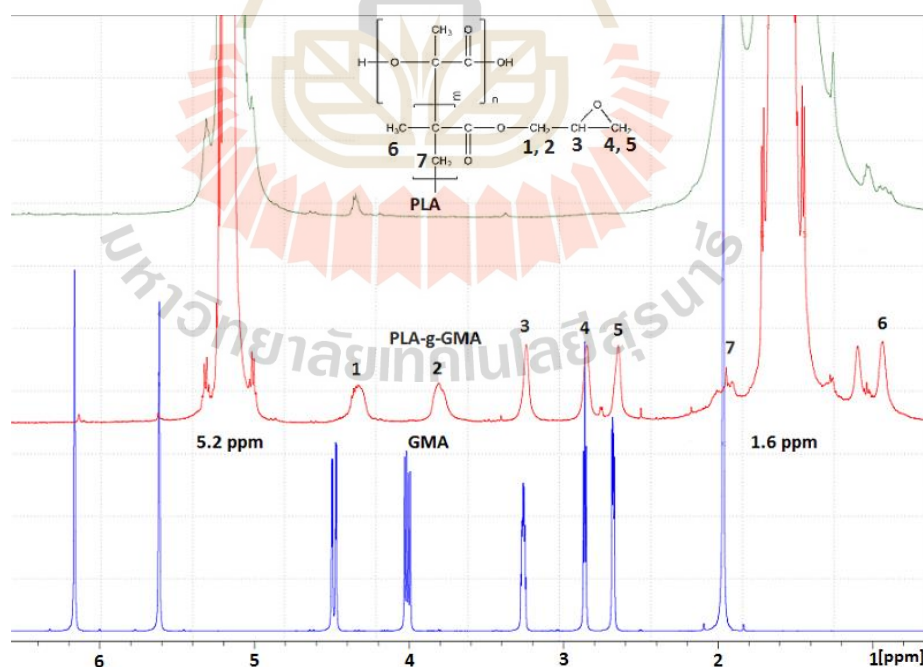


Figure 6.3 $^1\text{H-NMR}$ spectra of PLA, GMA and PLA-g-GMA, [GMA] = 10 wt%, mixing time = 10 min.

Furthermore, ^{13}C -NMR analysis in the spectrum of PLA-g-GMA (Figure 6.4) presented two new peaks at 49.07 and 44.71 ppm, indicating the carbons of the epoxy group of GMA. In order to confirm that these two peaks belong to the carbons of the epoxy group of GMA grafted on PLA chain, the ^{13}C -NMR analysis of GMA was also carried out. It can be observed from Figure 6.4 that the chemical shifts of two peaks, which are attributed to the carbons of the epoxy group of GMA, are different from those in the spectrum of PLA-g-GMA. Moreover, after grafting, the peak at 135.87 ppm indicating the carbon of double bond in the chemical structure of GMA was disappeared (Appendix A). This indicates the formation of chemical bonding between GMA and PLA chains. These results further demonstrate that grafting of GMA on PLA chain occurred successfully. In addition, the intensity of signals at 17 and 70 ppm of methyl carbon (CH_3) and ($-\text{O}-\text{CH}$) carbon of PLA before and after grafting with GMA was quite similar.

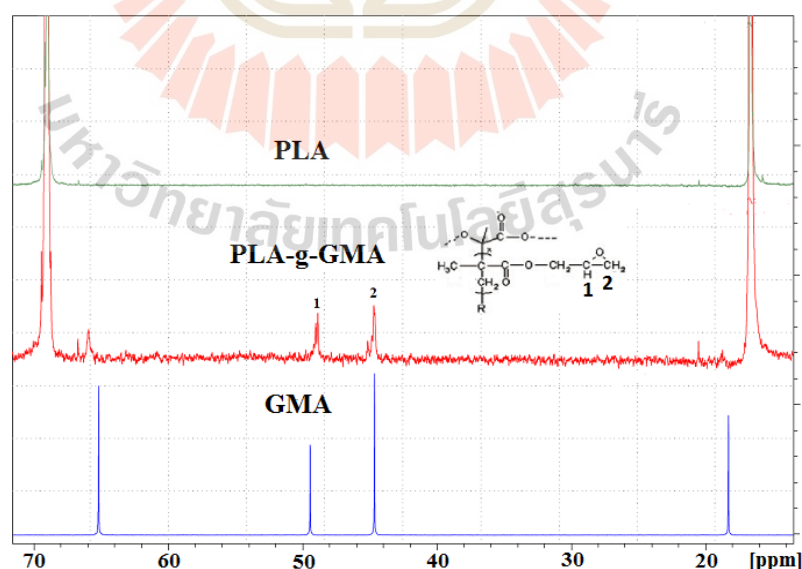


Figure 6.4 ^{13}C -NMR spectra of pure PLA, GMA and PLA-g-GMA, [GMA] = 10 wt%, mixing time = 10 min.

6.4.1.2 GPC analysis

Gel permeation chromatogram of pure PLA and PLA-g-GMA was shown in Figure 6.5. The weight-average molecular weights (\bar{M}_w), the number-average molecular weights (\bar{M}_n), and the polydispersity index (*PDI*) of PLA and PLA-g-GMA were shown in Table 6.1. PLA-g-GMA has higher \bar{M}_w , \bar{M}_n , and *PDI* than PLA. These results indicate that the chain extension through step (1) as illustrated in Figure 6.1 may occur while the chain scission reaction did not take place during grafting reaction.

Moreover, as shown in Figure 6.5, the new and small shoulder peak was observed in GPC diagram of PLA-g-GMA. This is attributed to the presence of fractions having higher molecular weight than pure PLA. This observation also confirmed that GMA was grafted successfully onto PLA chain. This result is consistent with the NMR results discussed earlier.

Table 6.1 The weight-average molecular weights (\bar{M}_w), the number-average molecular weights (\bar{M}_n), and the polydispersity index (*PDI*) of PLA and PLA-g-GMA. [GMA]=10 wt%, mixing time = 10 min.

Sample	\bar{M}_w	\bar{M}_n	<i>PDI</i>
PLA	160,777	79,119	2.032
PLA-g-GMA	205,618	79,610	2.583

6.4.1.3 Rheological properties

Flow curves of PLA and PLA-g-GMA were shown in Figure 6.6. It revealed that viscosity at all shear rate ranges of PLA-g-GMA was higher than that of PLA. This corresponds to the higher molecular weights of PLA-g-GMA

compared to that of PLA (Table 6.1). Melt flow index (MFI) of PLA and PLA-g-GMA shown in Table 6.2 are in good agreement with the viscosity data. PLA-g-GMA showed lower MFI than PLA indicating the higher viscosity. These results suggest that degradation of PLA through chain scission did not occur during the grafting process.

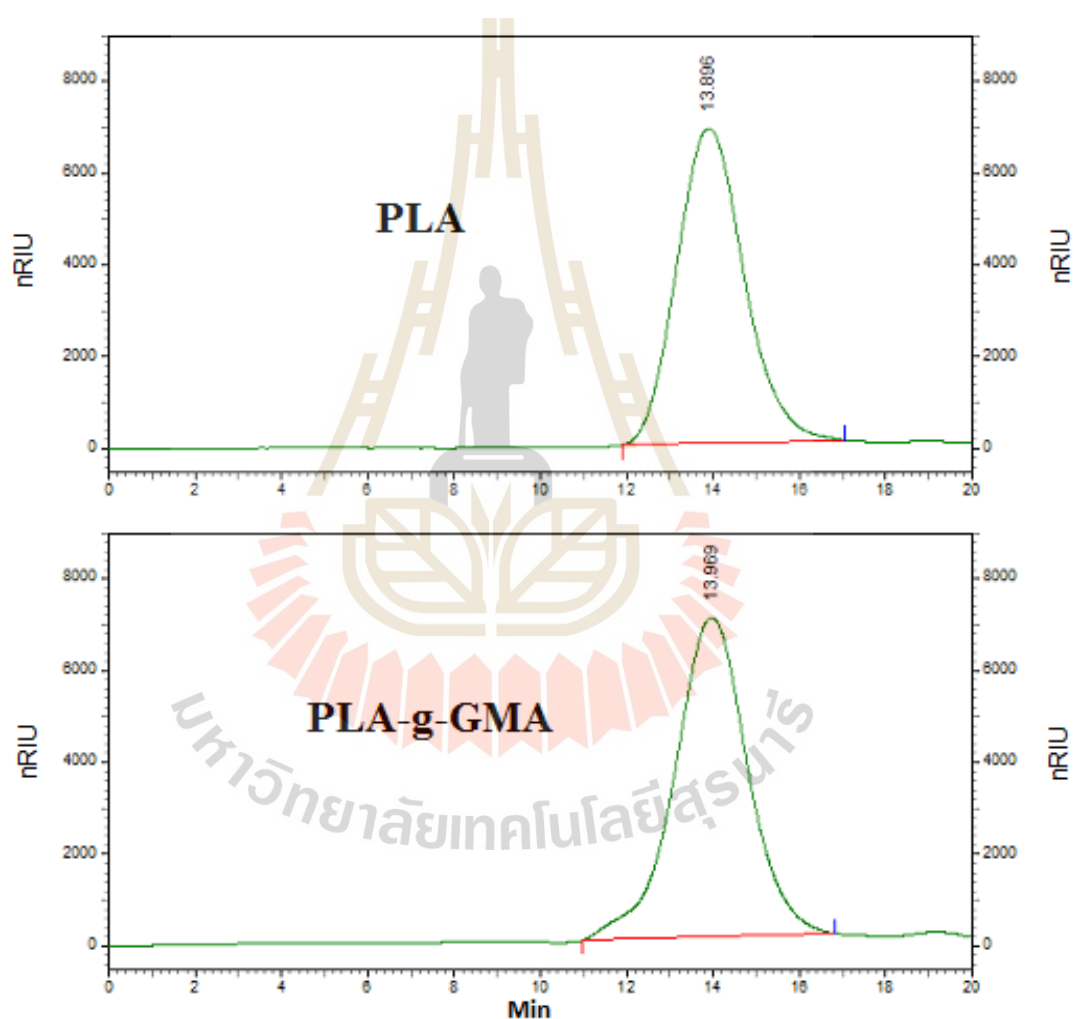


Figure 6.5 Gel permeation chromatogram of PLA and PLA-g-GMA, [GMA] = 10 wt%, mixing time = 10 min.

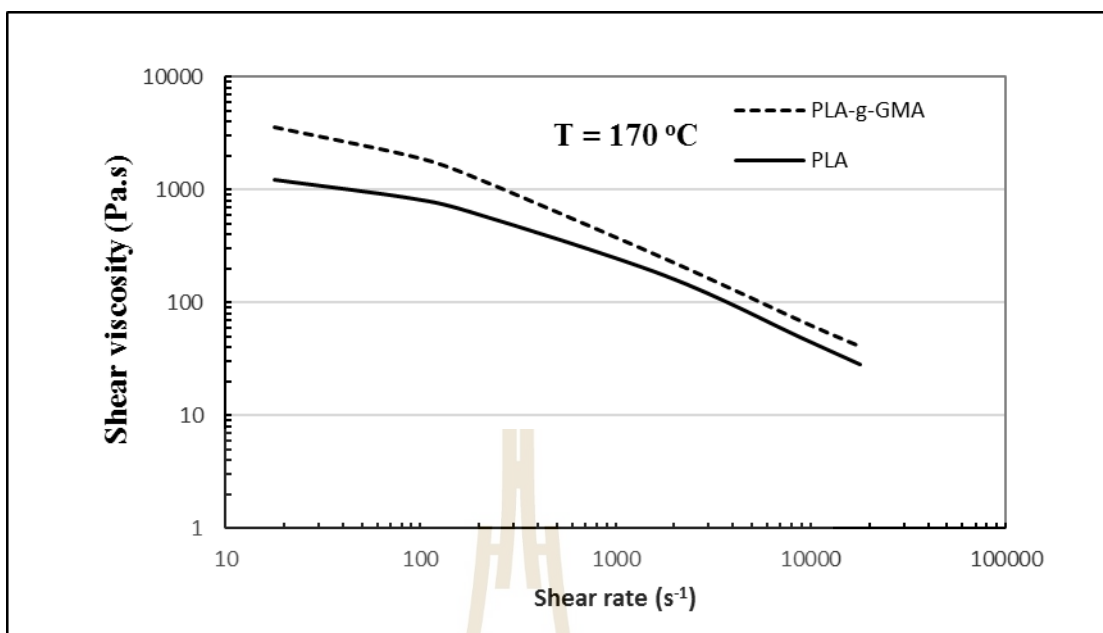


Figure 6.6 Shear viscosity of pure PLA and PLA-g-GMA at various shear rates.

[GMA] = 10 wt%, mixing time = 10 min.

Table 6.2 MFI of pure PLA and PLA-g-GMA, [GMA] =10 wt%, mixing time = 10 min.

Sample	MFI (g/10min)
PLA	2.75 ± 0.05
PLA-g-GMA	0.690 ± 0.002

6.4.1.4 X-ray diffraction (XRD) analysis

The X-ray diffraction analysis was carried out to investigate the change in crystallization behavior of PLA after grafting. Figure 6.7 shows the XRD patterns of pure PLA and PLA-g-GMA before and after tensile test. One can see that pure PLA showed a broad amorphous hump with no clear diffraction patterns. This pattern is typical of amorphous materials. Conversely, the XRD pattern of PLA-g-GMA showed the new diffraction peaks around 2θ at 12° , 14° , 16° , 19° and 22° . This

pattern is typical of semicrystalline materials. The change in XRD patterns indicates the difference in crystallization behavior of PLA after being grafted with GMA. These results are similar to those of the investigation of Lai, Hung, Kao, Liu, and Wang (2013) where the annealing treatment at 125 °C for 2.5 h was applied to neat PLA. Interestingly, after applying tensile stress, XRD pattern of pure PLA did not show any considerable difference compared to that of pure PLA before applying tensile stress. However, as observed in Figure 6.7, XRD pattern of PLA-g-GMA has changed apparently after the tensile test. The intensity of diffraction peak around 2θ at 16° decreased, whereas the significant increase of intensity of diffraction peak around 2θ at 29° was observed. Surprisingly, the diffraction peaks around 2θ at 14° , 19° , and 22° disappeared. The appearance of the new peaks around 2θ at 35° , 39° , 42.5° , 47° , 48° , 57° , 60° , 64° , 65° , 70° , 72.5° , 81° , and 83.5° were also observed in the XRD pattern of PLA-g-GMA after the tensile test. This shows that the crystallization behavior of PLA-g-GMA was changed after applying tensile stress.

6.4.1.5 Morphological investigation of PLA and PLA-g-GMA

SEM images (600x magnification) of the tensile fractured surfaces of pure PLA and PLA-g-GMA are shown in Figure 6.8a and Figure 6.8b, respectively. Compared to the smooth fractured surface of pure PLA, the rougher fractured surface of PLA-g-GMA was observed.

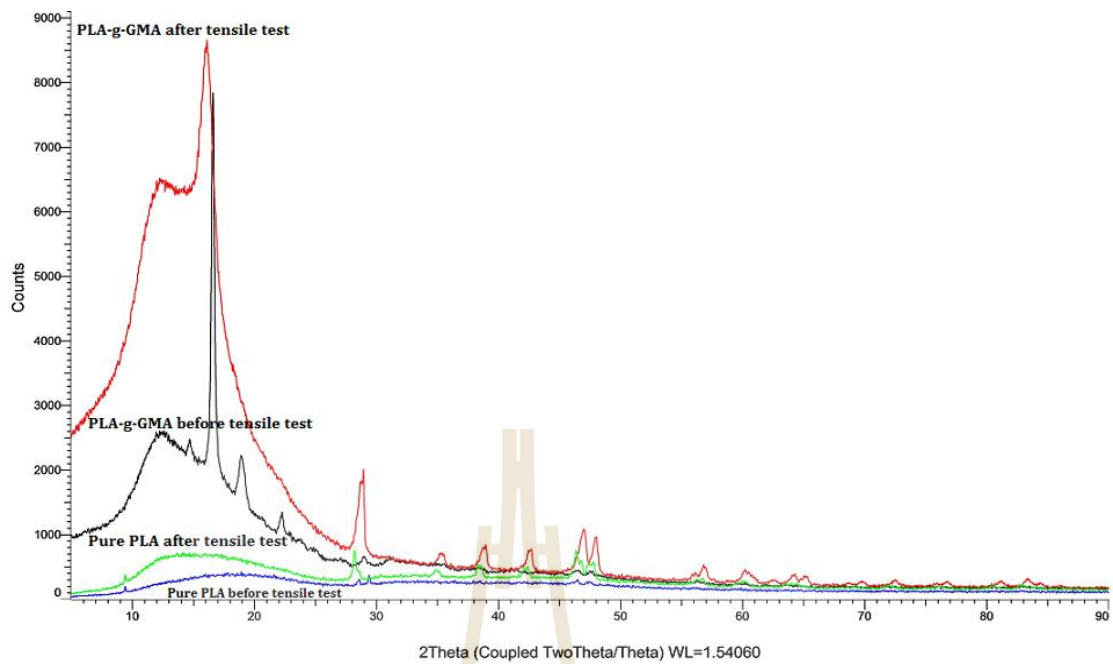


Figure 6.7 XRD patterns of PLA and PLA-g-GMA before and after the tensile test, [GMA] = 10 wt%, mixing time = 10 min.

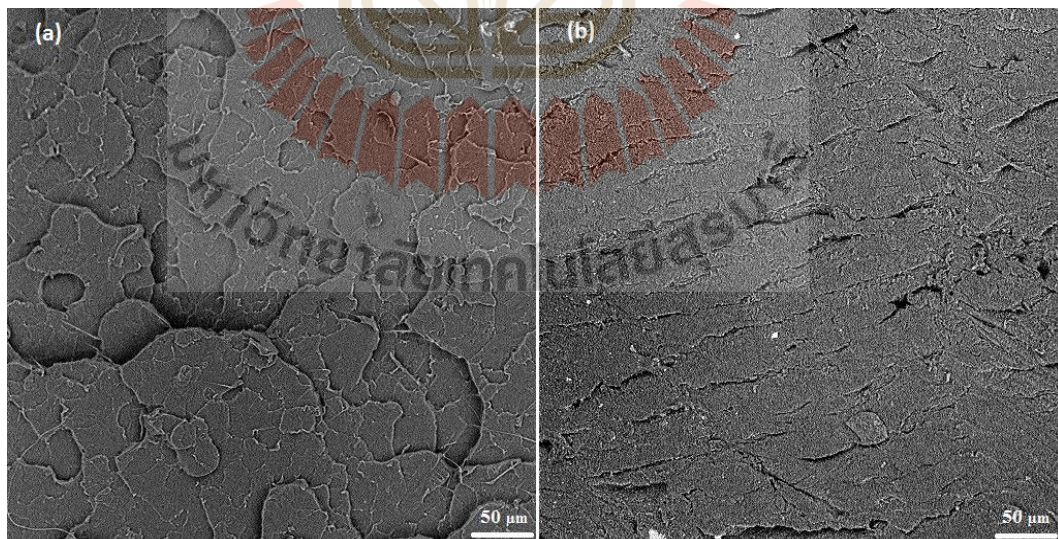


Figure 6.8 SEM images of tensile fractured surface of pure PLA (a) and PLA-g-GMA (b), [GMA] = 10 wt%, mixing time = 10 min.

6.4.2 Effect of GMA content on GMA grafting and physical properties of PLA-g-GMA

6.4.2.1 Grafting yield and efficiency by $^1\text{H-NMR}$ analysis

The effect of GMA concentration on the grafting yield was determined by calculating the relative areas of characteristic peaks of GMA and PLA from $^1\text{H-NMR}$ spectra, which are shown in Table 6.3 and Figure 6.9.

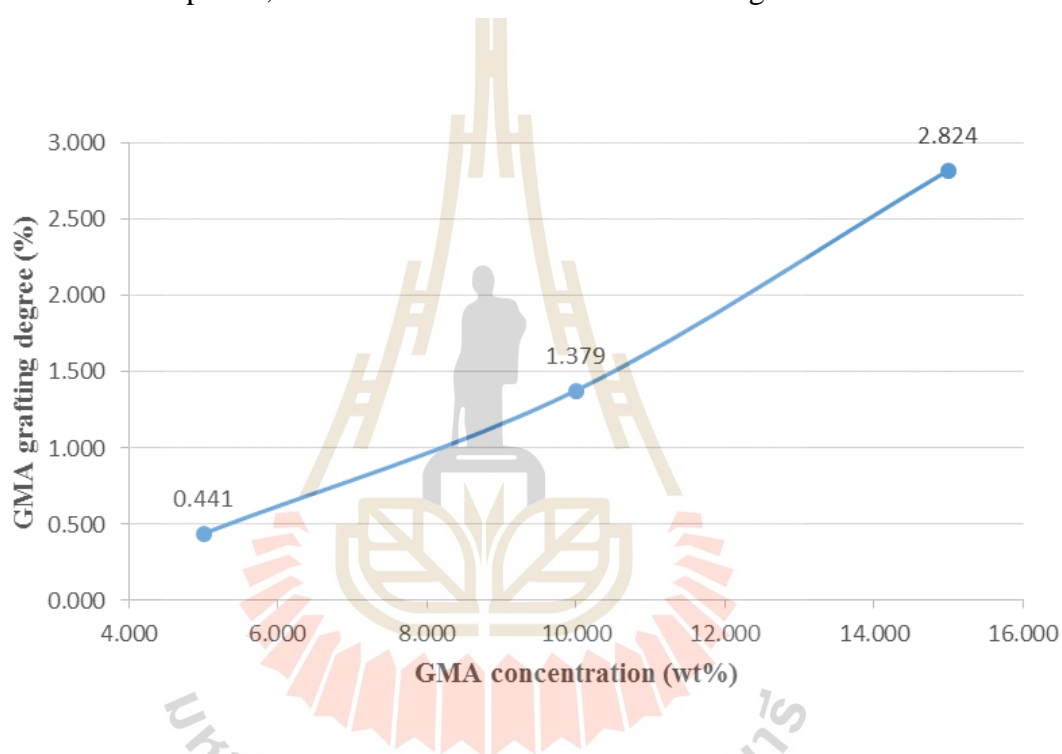


Figure 6.9 Effect of GMA monomer content on GMA grafting yield, mixing time = 10 min.

It revealed that the percentage of GMA grafted on PLA chain increased with increasing GMA concentration. The same tendency was observed in the case that GMA was grafted on polycaprolactone (Kim, Jung, Kim, and Park, 2004). The grafting yield increased from 0.441 to 2.824 % as the GMA concentration increased from 5 to 15 wt%. It is relatively lower than that of the study of Liu et al.

(2012) where benzoyl peroxide was used as an initiator and the grafting percentage increased from 1.8 to 11.0 % as the GMA concentration was varied from 5 to 20 wt%. Moreover, as can be clearly seen from Figure 6.10, the GMA grafting efficiency increased from 0.088 to 0.188 with the increase of GMA concentration from 5 to 15 wt%. This indicates that when the GMA concentration increases from 5 to 15 wt%, GMA grafting still exceeds the GMA homopolymerization in rate. Therefore, the GMA grafting efficiency based on initial GMA concentration increases. These results were found to be opposite to those elsewhere where the GMA was grafted on HDPE and LDPE by melt mixing (Cho et al., 2008); (Wei, Chionna, Galoppini, and Pracella, 2003).

Table 6.3 The relative area of characteristic peaks of PLA and GMA calculated from $^1\text{H-NMR}$ spectra of PLA-g-GMA at various GMA contents, mixing time = 10 min.

Sample	Relative area	
	Characteristic peak of PLA	Characteristic peak of GMA
PLA-g-GMA5%	4.313	0.019
PLA-g-GMA10%	4.279	0.059
PLA-g-GMA15%	4.426	0.125

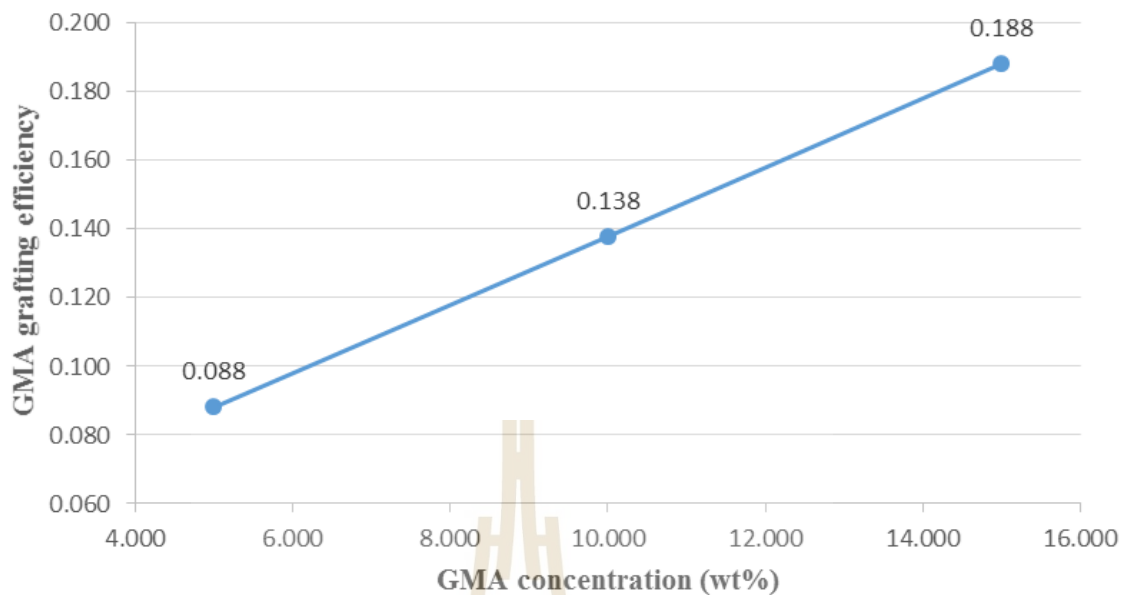


Figure 6.10 Effect of GMA monomer content on GMA grafting efficiency, mixing time = 10 min.

6.4.2.2 Mechanical properties

Effect of GMA content on mechanical properties of PLA-g-GMA was investigated by the tensile and impact tests. Stress-strain curves of PLA and PLA-g-GMA at different GMA contents were shown in Figure 6.11. After applying tensile stress, necking and cold drawing can be observed in PLA-g-GMA10% and PLA-g-GMA15% samples indicating the reorientation of the molecular chain. This implies that the strain-induced crystallization can take place easier for PLA-g-GMA10% and PLA-g-GMA15% compared to PLA and PLA-g-GMA5% which indicated the brittle fracture. It was observed from Figure 6.12 that the tensile strength of PLA and PLA-g-GMA5% was found to be higher than that of PLA-g-GMA10% and PLA-g-GMA15%. However, the elongation at break of PLA-g-

GMA10% and PLA-g-GMA15% was considerably higher than that of PLA (Figure 6.13). From this result, it can be thought that when GMA content was high enough (10 wt% and 15 wt%), PLA-g-GMA can crystallize under cooling from the melt. Their molecular chain can rearrange under tensile stress. This phenomenon is similar to other semicrystalline polymers. Conversely, it did not occur in the case of pure PLA and PLA-g-GMA5% (GMA content was low) where PLA did not crystallize under cooling from the melt. As a result, they are amorphous materials under solid state. This implied the difficulty of their molecular chain to rearrange under tensile stress. These results are consistent with XRD results which indicated that PLA before and after the tensile test was an amorphous material. These show the difference in crystallization behavior between pure PLA and PLA-g-GMA (high GMA content) under applied tensile stress.

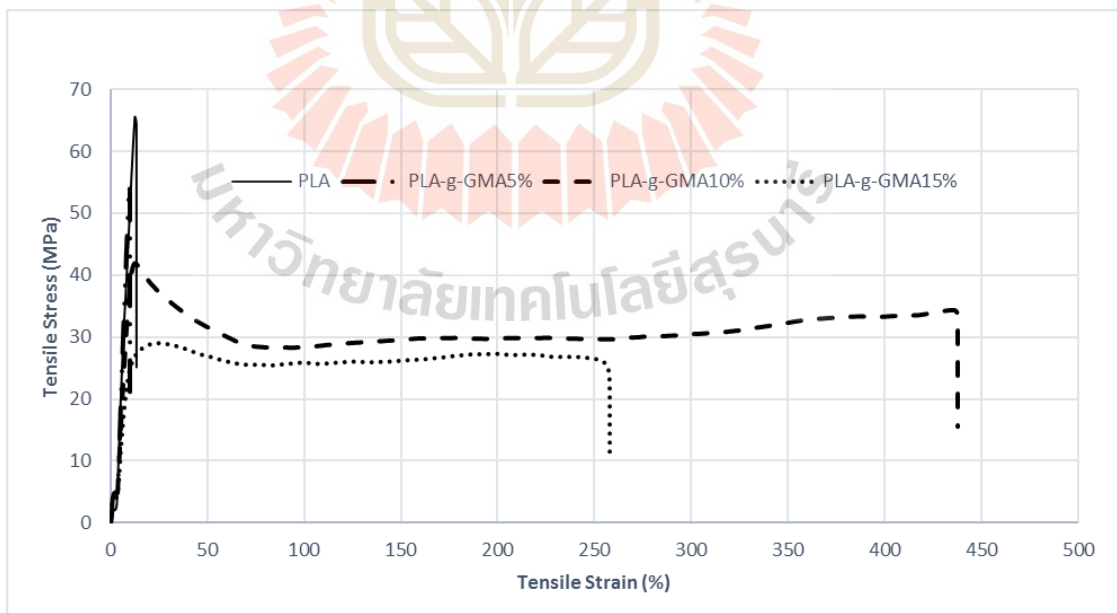


Figure 6.11 Stress-strain curves of pure PLA and PLA-g-GMA at different GMA contents, mixing time = 10 min.

Moreover, one can see from Figure 6.13 that the elongation at break of PLA-g-GMA increased significantly with the increase of GMA concentration from 5 to 10 wt%. This is attributed to the increase of GMA grafting yield as GMA concentration increased from 5 to 10 wt% as observed in Figure 6.9. Nevertheless, it decreased when the GMA content reached 15 wt%. Meanwhile, the tensile strength decreased continuously as GMA concentration increased from 5 to 15 wt% (Figure 6.12).

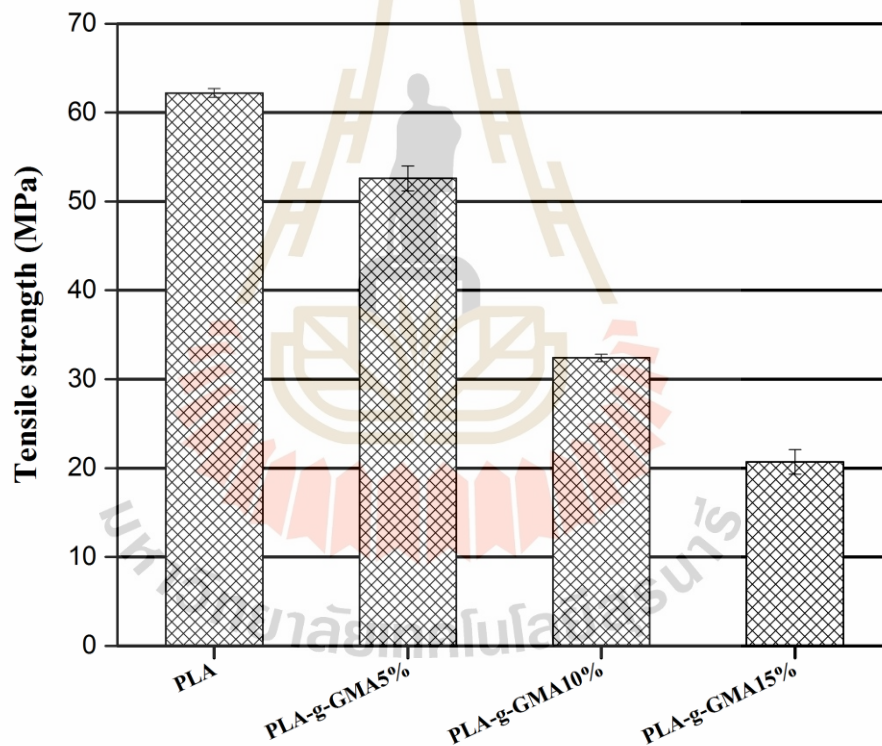


Figure 6.12 Effect of GMA content on tensile strength of PLA-g-GMA, mixing time = 10 min.

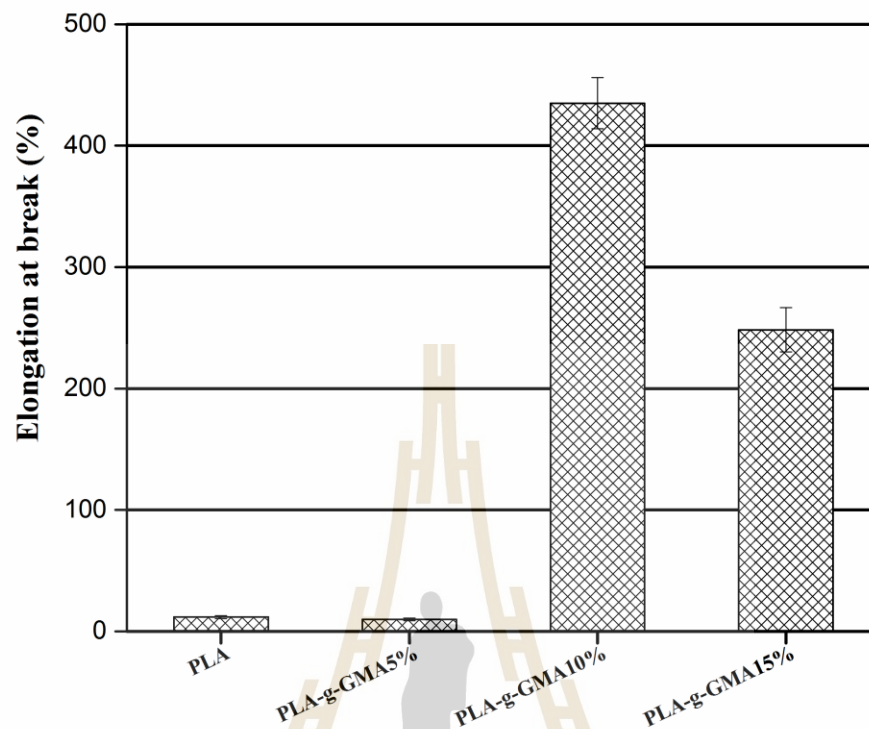


Figure 6.13 Effect of GMA content on elongation at break of PLA-g-GMA, mixing time = 10 min.

Figure 6.14 shows that the impact strength of PLA-g-GMA was higher than that of pure PLA. It was considerably influenced by the GMA content. The impact strength of PLA-g-GMA increased as GMA concentration was increased from 5 to 10 wt%. However, it decreased as GMA concentration was increased from 10 to 15 wt%. The highest impact strength was obtained with PLA-g-GMA prepared with GMA content of 10 wt%. It is due to the smaller size of crystals of PLA-g-GMA10% leading to higher number of tie-molecules, resulting in an increase of

impact strength (Zhang et al., 2002). These results indicated that the GMA content of 10 wt% was optimal for the elongation at break and impact strength of PLA-g-GMA.

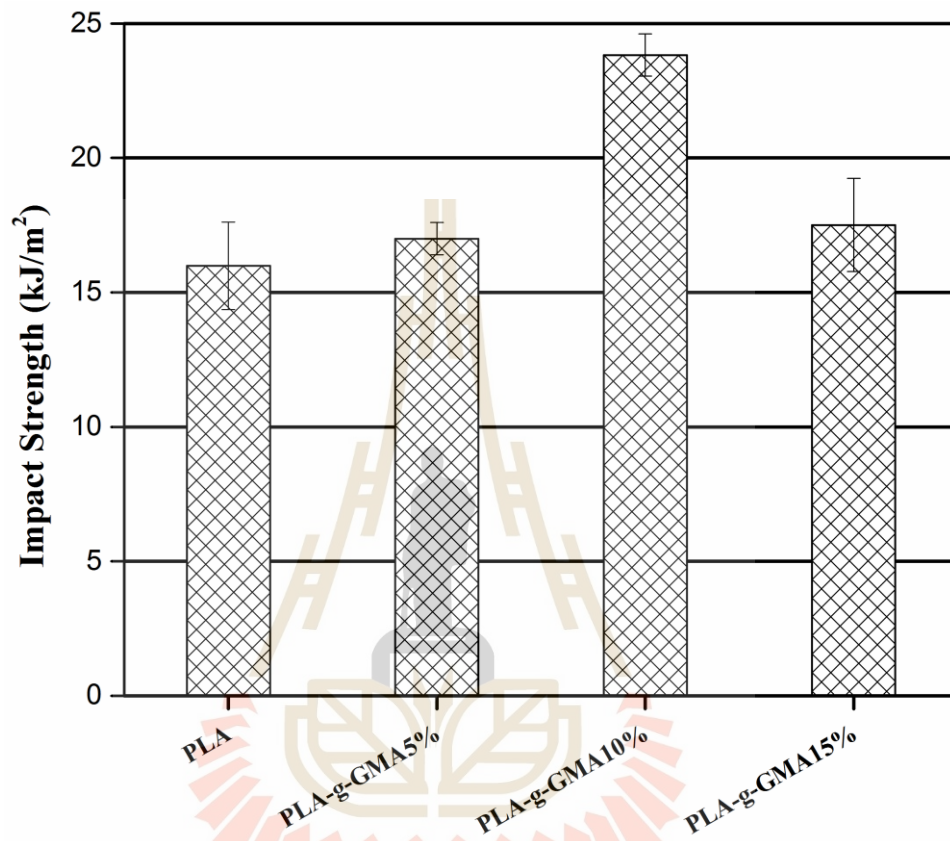


Figure 6.14 Effect of GMA content on impact strength of PLA-g-GMA, mixing time = 10 min.

6.4.2.3 Thermal properties

DSC thermograms during cooling and heating of PLA and PLA-g-GMA with different GMA contents were shown in Figure 6.15 and Figure 6.16, respectively. From the cooling scan (Figure 6.15), one can see that PLA and PLA-g-GMA5% could not undergo crystallization, whereas PLA-g-GMA10% and

PLA-g-GMA15% exhibited melt crystallization upon cooling. These results were in good agreement with XRD results. It also confirmed for the explanation mentioned in the tensile properties results. It is possibly thought that when the GMA grafting degree was high enough, PLA-g-GMA could induce PLA crystallization to occur under cooling from the melt. Moreover, when GMA concentration was increased from 10 to 15 wt%, the crystallization peak shifted to a higher temperature. This reflects the faster crystallization of PLA under cooling. This result indicates that PLA-g-GMA accelerates the crystallization of PLA more significantly as GMA content was increased. The quite similar phenomenon was found in the study of Song et al. (2012) where the crystallization of PLA under cooling was accelerated by a nanoscale zinc citrate complex as a nucleating agent.

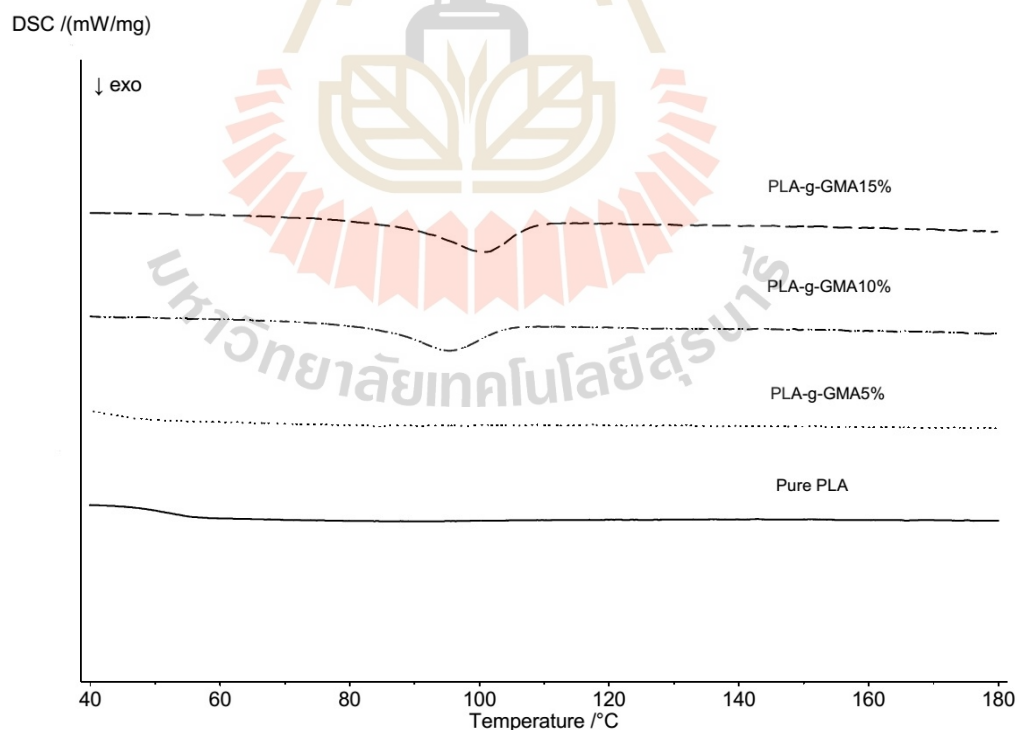


Figure 6.15 DSC thermograms of PLA and PLA-g-GMA at different GMA contents (cooling scan), mixing time = 10 min.

As observed in Figure 6.16, pure PLA and PLA-g-GMA5% presented the sharp cold crystallization peaks upon heating. Meanwhile, PLA-g-GMA10% and PLA-g-GMA15% showed very weak cold crystallization peaks. It is due to the fact that PLA and PLA-g-GMA5% did not undergo melt crystallization under cooling (Figure 6.15). Therefore, the reorientation of their chain can occur easily upon heating. In contrast to that, the packed crystals of PLA-g-GMA10% and PLA-g-GMA15% generated under cooling (Figure 6.15) could not rearrange upon heating. As a result, the very weak cold crystallization peaks were observed with respect to PLA-g-GMA10% and PLA-g-GMA15% samples.

In addition, the apparent double melting peak located at lower and higher temperature was observed in the second heating scan for pure PLA, which relates to the less organized crystals and well-organized crystals, respectively (Chen et al., 2014). The lower temperature peak (T_{m1}) is attributed to melting of primary crystals formed upon cooling from the melt, and the higher one (T_{m2}) corresponds to melting of crystals generated from recrystallization upon heating (Yasuniwa, Tsubakihara, Sugimoto, and Nakafuku, 2004). In the case of PLA-g-GMA samples, the melting peak shifted to a lower temperature. It is because almost crystals of PLA-g-GMA were generated upon cooling from the melt. Therefore, they are thermally less stable than those of pure PLA formed from the reorientation of the chains under heating (Zhou, Green, and Joo, 2006). The higher GMA content was used, the lower melting temperature was observed. Furthermore, it is thought that crystals of PLA-g-GMA almost generated from the melt upon cooling were more homogeneous than those of pure PLA. As a result, when GMA content was high enough (10 wt% and 15 wt%), almost single melting peak was observed. The values of enthalpy of

crystallization (ΔH_c), enthalpy of cold crystallization (ΔH_{cc}), enthalpy of melting (ΔH_m), crystallization temperature (T_c), cold crystallization temperature (T_{cc}), melting temperatures (T_{m1} and T_{m2}), and degree of crystallinity ($\%X_c$) of pure PLA and PLA-g-GMA were shown in Table 6.4. As observed in Table 6.4, the crystallinity of PLA-g-GMA was lower than that of PLA. The higher GMA content, the lower crystallinity of PLA-g-GMA. It is thought that the existence of the GMA segments would be expected to hinder the motion and folding of the PLA molecular chains and bring defects to the crystals. As discussed, the grafting degree increased with increasing GMA content (Figure 6.9). The increase of the grafting degree increased the amount of the GMA segments, which made the impeditive effect evident. As a consequence, the crystallinity of PLA-g-GMA was lower than that of PLA and lowered with the increase of GMA content.

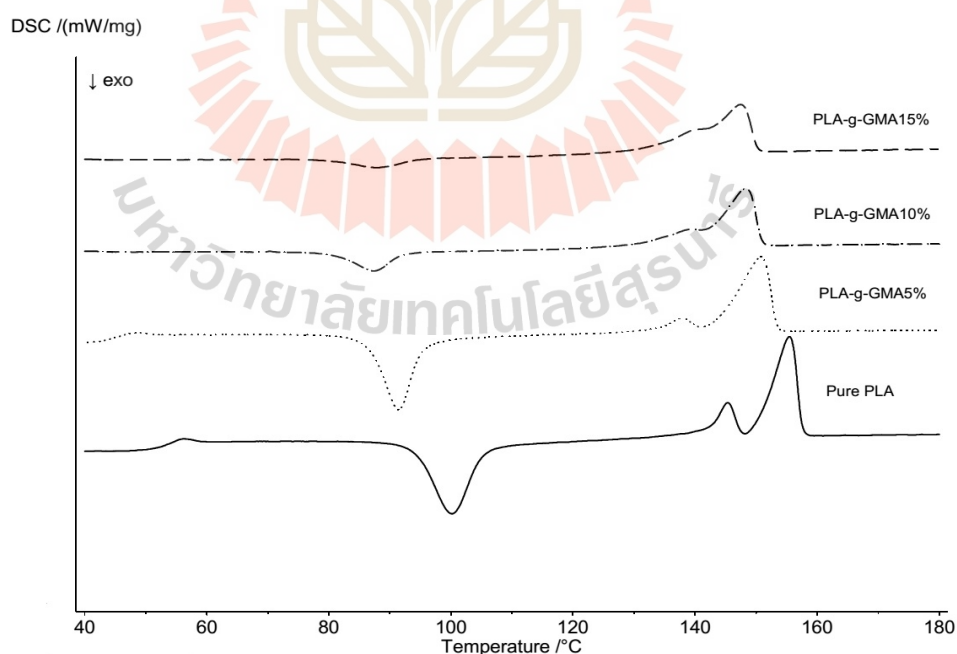


Figure 6.16 DSC thermograms of PLA and PLA-g-GMA at various GMA contents (second heating scan), mixing time = 10 min.

Table 6.4 Thermal properties of pure PLA and PLA-g-GMA at different GMA contents, mixing time = 10 min.

Sample	Thermal properties							
	T_c (°C)	T_{cc} (°C)	T_{m1} (°C)	T_{m2} (°C)	ΔH_c (J/g)	ΔH_{cc} (J/g)	ΔH_m (J/g)	$\%X_c$ (%)
PLA	-	100.2	145.3	155.5	0.00	29.80	31.23	33.33
PLA-g-GMA5%	-	91.4	137.8	150.8	0.00	24.77	28.04	29.93
PLA-g-GMA10%	95.4	87.3	139.4	148.3	11.35	7.20	22.96	24.50
PLA-g-GMA15%	101.0	87.9	140.0	147.5	15.51	3.94	22.06	23.54

6.4.3 Effect of mixing time on GMA grafting and physical properties of PLA-g-GMA

6.4.3.1 Grafting yield by $^1\text{H-NMR}$ analysis

The effect of mixing time on grafting yield was determined by calculating the relative area of characteristic peaks of GMA and PLA from $^1\text{H-NMR}$ spectra. Calculated results were shown in Table 6.5 and Figure 6.17. As can be seen from Figure 6.17, the percentage of GMA grafted onto PLA chain increased from 1.123 to 1.379 % as the mixing time was increased from 7 to 10 min. However, with the further increase of mixing time up to 14 min, the grafting yield decreased from 1.379 to 1.128 %. The reason for this decline may be attributed to the depolymerization of GMA which has taken place as the mixing time is too long.

Table 6.5 The relative area of characteristic peaks of GMA and PLA calculated from $^1\text{H-NMR}$ spectra of PLA-g-GMA at various mixing times.

Sample	Relative area	
	Characteristic peak of PLA	Characteristic peak of GMA
PLA-g-GMA7min	4.275	0.048
PLA-g-GMA10min	4.279	0.059
PLA-g-GMA14min	4.345	0.049

6.4.3.2 Mechanical properties

Effect of mixing time on mechanical properties of PLA-g-GMA was shown in Figures (6.18-6.21). It was observed from Figure 6.18 that PLA-g-GMA showed the ductile fracture with necking and cold drawing in the stress-strain curve. In contrast to that, the brittle fracture of pure PLA was demonstrated. The elongation at break of PLA-g-GMA was significantly higher than that of PLA (Figure 6.20). From this result, it can be thought that the reorientation of the molecular chains of PLA-g-GMA can occur under tensile force. This phenomenon did not take place in the case of pure PLA. This indicated the difference in crystallization behavior between pure PLA and PLA-g-GMA under applied tensile force.

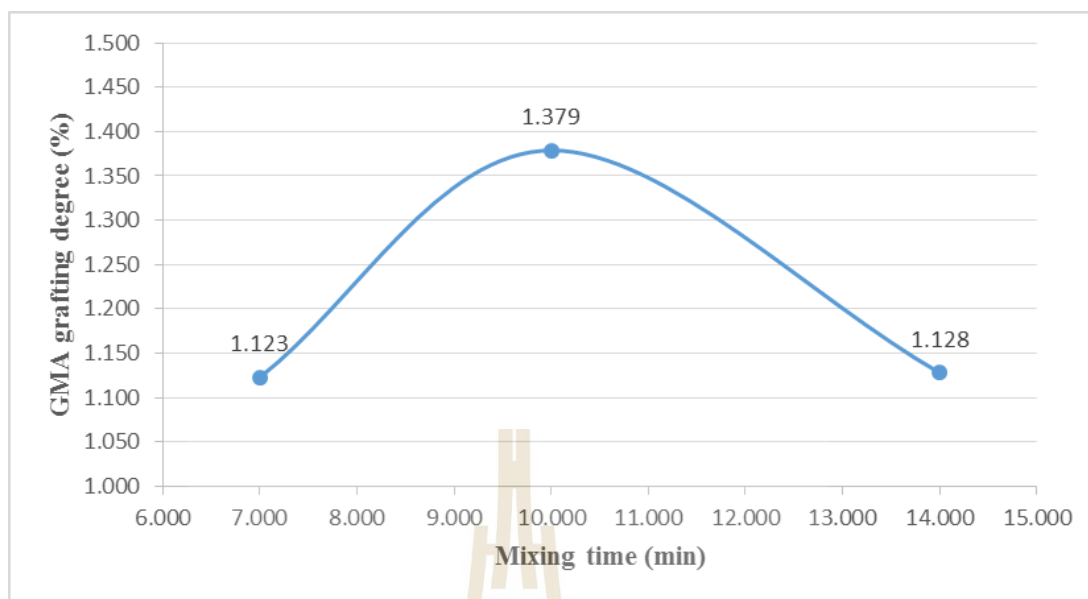


Figure 6.17 Effect of mixing time on GMA grafting yield, [GMA] = 10 wt%.

However, as observed from Figure 6.19, the tensile strength of PLA-g-GMA significantly decreased compared to that of pure PLA. This decrease is ascribed to the reduction of crystallinity of PLA after grafting. Figure 6.20 exhibits that the elongation at break of PLA-g-GMA increased slightly with the increase of mixing time from 7 to 10 min. This is due to the increase of GMA grafting yield as mixing time was increased from 7 to 10 min (Figure 6.17). On the other hand, it significantly decreased when the mixing time reached 14 min. It has been known that PLA is highly sensitive to heat, therefore, if the mixing time was kept too long, the degradation of PLA chain can occur easily. Furthermore, the GMA grafting yield had a tendency to drop at a certain mixing time as observed in Figure 6.17 and another research in which GMA was grafted onto HDPE (Cho et al., 2008).

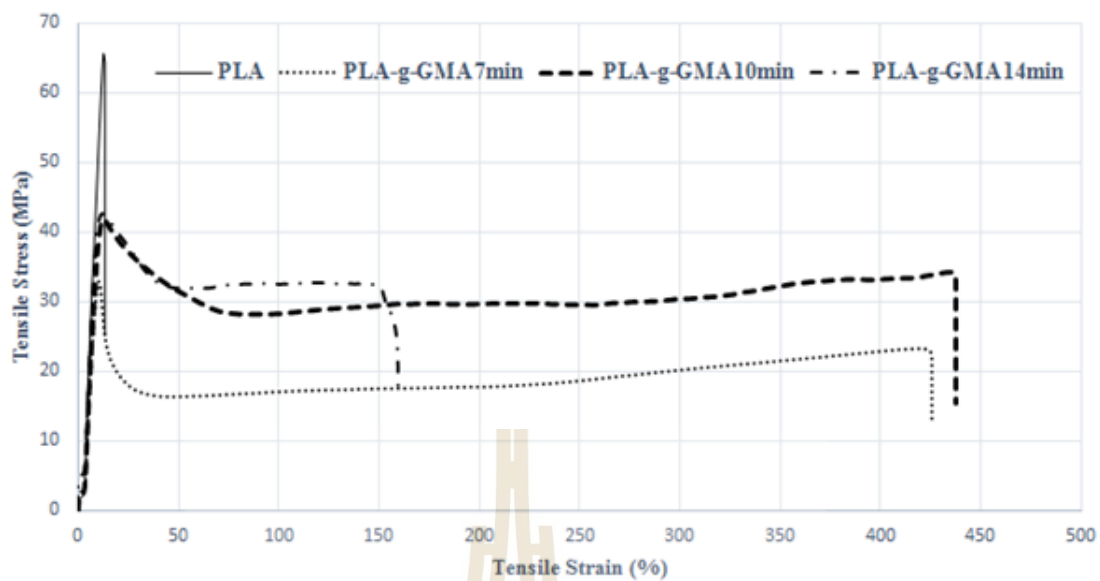


Figure 6.18 Stress-strain curves of pure PLA and PLA-g-GMA at various mixing times, [GMA] = 10 wt%.

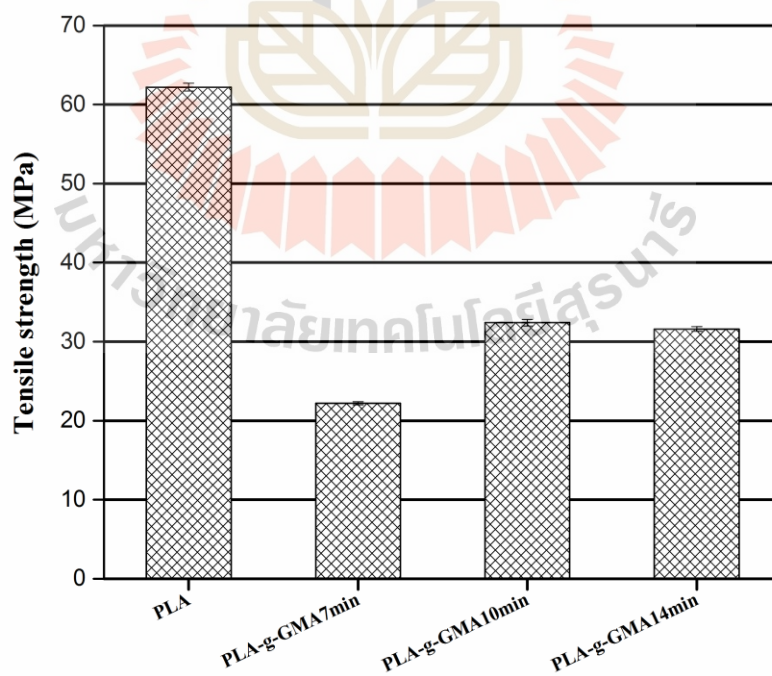


Figure 6.19 Effect of mixing time on tensile strength of PLA-g-GMA, [GMA] = 10 wt%.

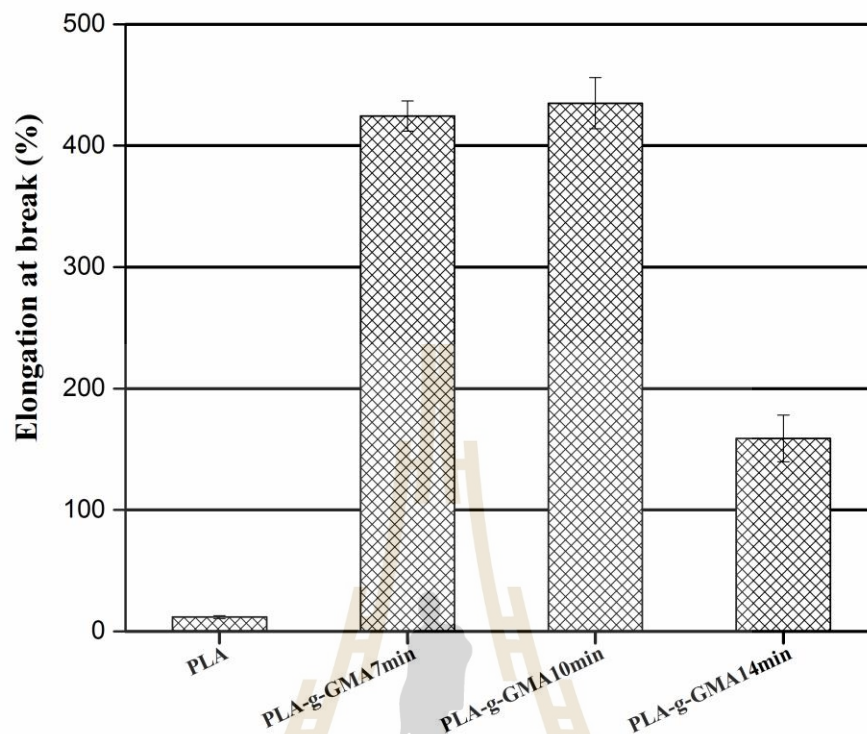


Figure 6.20 Effect of mixing time on elongation at break of PLA-g-GMA, [GMA] = 10 wt%.

Figure 6.21 shows that the impact strength of PLA-g-GMA was considerably higher than that of pure PLA. However, it was not significantly influenced by the mixing time. The impact strength of PLA-g-GMA increased slightly as mixing time was increased from 7 to 10 min. Conversely, it decreased as mixing time was increased from 10 to 14 min. This decrease is due to the reduction of GMA grafting yield and degradation of PLA chain as the mixing time was kept too long. From the mechanical properties results, it can be stated that the mixing time of 10 min was optimal for the elongation at break and impact strength of PLA-g-GMA.

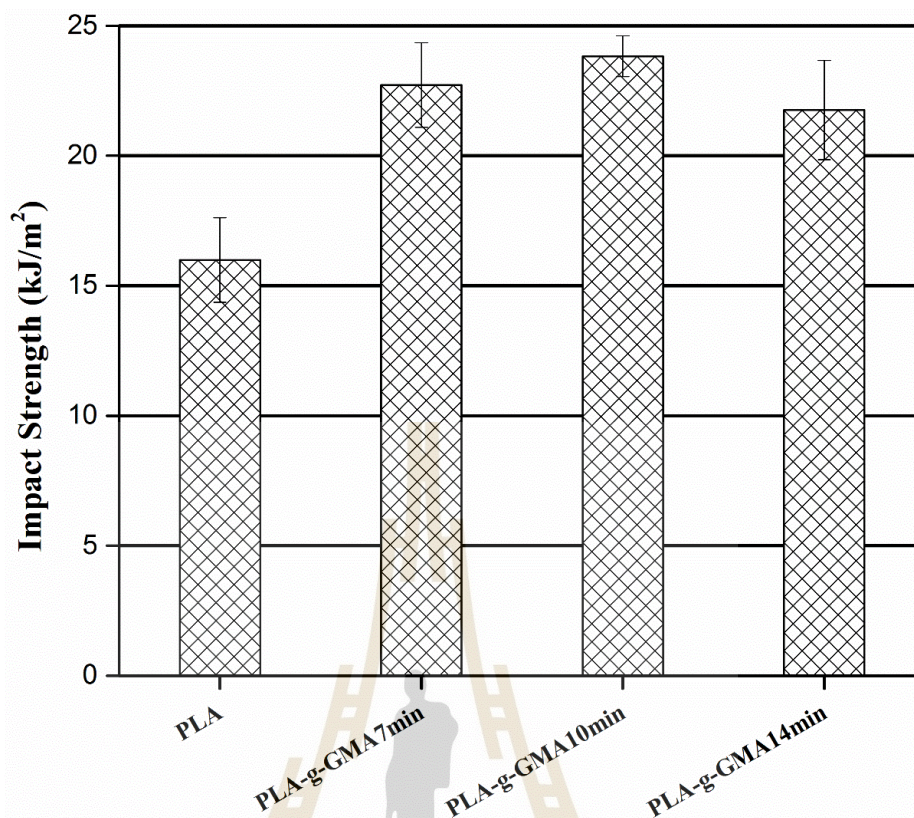


Figure 6.21 Effect of mixing time on impact strength of PLA-g-GMA, [GMA] = 10 wt%.

6.4.3.3 Thermal properties

DSC thermograms during cooling and heating of PLA and PLA-g-GMA at various mixing times were shown in Figure 6.22 and Figure 6.23, respectively. As observed from the cooling scan (Figure 6.22) that pure PLA and PLA-g-GMA7min did not show crystallization from the melt upon cooling. PLA-g-GMA10min and PLA-g-GMA14min samples, however, underwent melt crystallization upon cooling. This indicated the difference in crystallization behavior between pure PLA and PLA-g-GMA as the mixing time was long enough so that the grafting reaction could take place effectively.

It was observed from the heating scan (Figure 6.23) that pure PLA and PLA-g-GMA7min presented the strong cold crystallization peaks upon heating. Meanwhile, PLA-g-GMA10min and PLA-g-GMA14min showed very weak cold crystallization peaks. The reason for this difference is due to the fact that PLA and PLA-g-GMA7min did not undergo melt crystallization under cooling (Figure 6.22). Therefore, the reorientation of their chain can occur easily upon heating. Conversely, the packed crystals of PLA-g-GMA10min and PLA-g-GMA14min, which were generated under cooling could not rearrange upon heating. As a consequence, the very weak cold crystallization peaks were observed with respect to PLA-g-GMA10min and PLA-g-GMA14min samples.

Moreover, as can be seen clearly from Figure 6.23 that the melting temperature of PLA-g-GMA was not influenced considerably by mixing time in the range of 7-14 min. The values of enthalpy of crystallization (ΔH_c), enthalpy of cold crystallization (ΔH_{cc}), enthalpy of melting (ΔH_m), crystallization temperature (T_c), cold crystallization temperature (T_{cc}), melting temperatures (T_{m1} and T_{m2}), and degree of crystallinity ($\%X_c$) of pure PLA and PLA-g-GMA at various mixing times were shown in Table 6.6. The degree of crystallinity of PLA-g-GMA did not change significantly with respect to mixing time. It was observed from Table 6.6 that at a given amount of GMA, the mixing time of 10 min was found to give the lowest crystallinity of PLA-g-GMA. This is ascribed to the highest grafting degree as the mixing time was 10 min (Figure 6.17). The highest grafting degree led to the largest amount of GMA segments which hinder the motion and folding of the PLA molecular chains.

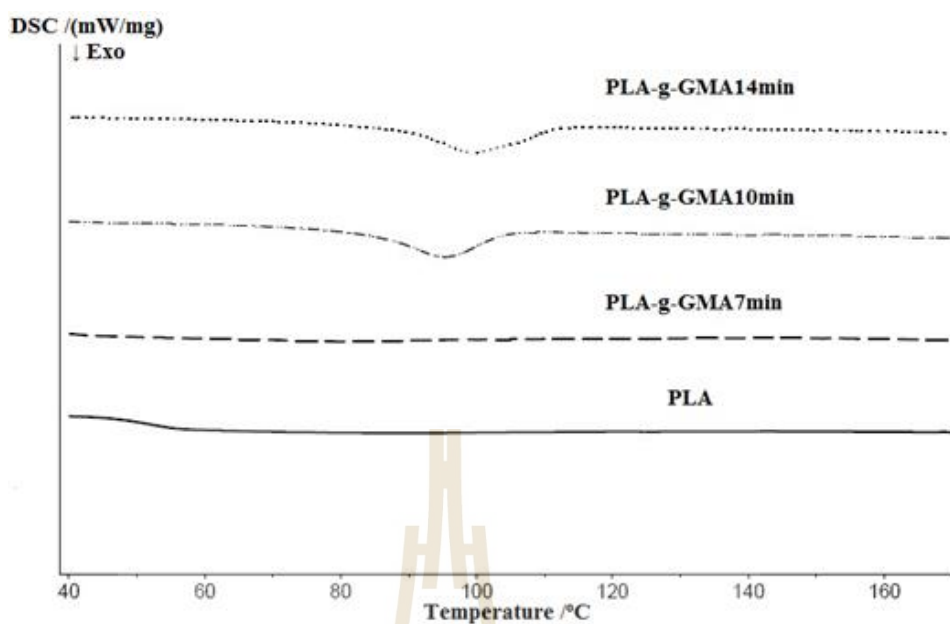


Figure 6.22 DSC thermograms of PLA and PLA-g-GMA at various mixing times (cooling scan), [GMA] = 10 wt%.

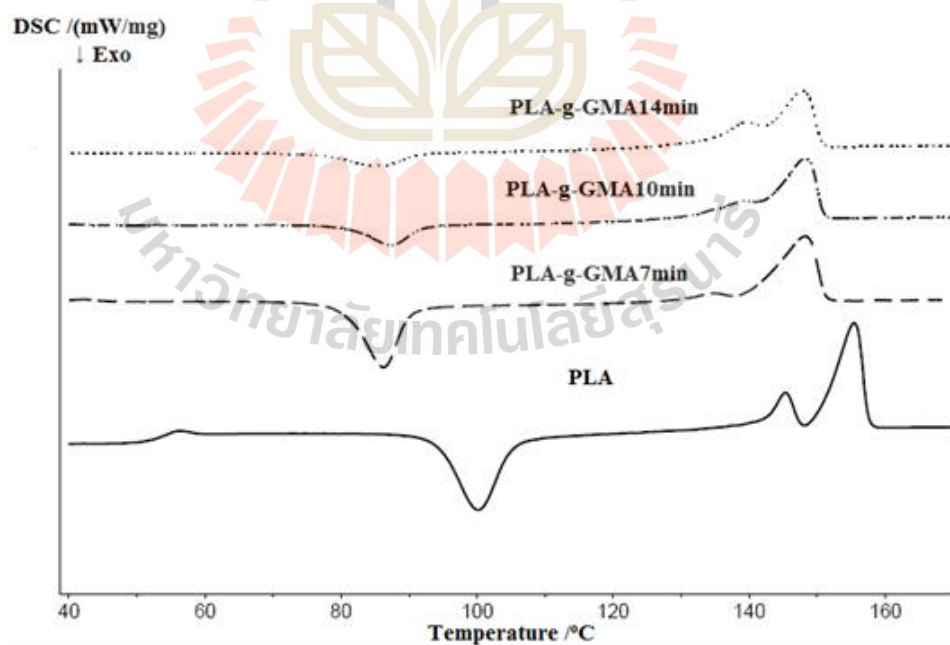


Figure 6.23 DSC thermograms of PLA and PLA-g-GMA at various mixing times (second heating scan), [GMA] = 10 wt%.

Table 6.6 Thermal properties of PLA and PLA-g-GMA at different mixing times, [GMA] = 10 wt%.

Sample	Thermal properties							
	T_c	T_{cc}	T_{m1}	T_{m2}	ΔH_c	ΔH_{cc}	ΔH_m	$\%X_c$
	(°C)	(°C)	(°C)	(°C)	(J/g)	(J/g)	(J/g)	(%)
PLA	-	100.2	145.3	155.5	0.00	29.80	31.23	33.33
PLA-g-GMA7min	-	86.3	135.2	148.2	0.00	21.50	24.52	26.17
PLA-g-GMA10min	95.3	87.3	139.4	148.3	13.26	7.34	22.96	24.50
PLA-g-GMA14min	99.5	84.9	139.6	147.9	14.38	5.38	23.88	25.49

6.5 Conclusions

By the confirmation of NMR, FTIR, and GPC analyses, it can be stated that glycidyl methacrylate was successfully grafted onto poly (lactic acid) by melt mixing method which can be applied for industrial scale production.

The physical properties of PLA-g-GMA were found to be considerably different from those of pure PLA. Compared to the smooth fractured surface of pure PLA, PLA-g-GMA showed the rougher fractured surface. The elongation at break and impact strength of PLA-g-GMA were significantly higher than those of pure PLA. However, the melt temperature and crystallinity of PLA-g-GMA were slightly lower than those of PLA. After being grafted with GMA, viscosity and weight-average molecular weights of PLA-g-GMA were higher than those of pure PLA. It implied that with the mixing temperature, mixing time, and GMA content of 170 °C, 10 min, and 10 wt%, respectively, degradation of PLA chain did not occur during grafting reaction. By grafting of GMA onto PLA chain, especially, crystallization behavior of PLA was changed from brittle amorphous PLA to ductile semicrystalline PLA-g-GMA. This was confirmed by XRD, DSC, SEM, and tensile test results.

Moreover, it was also found that GMA grafting yield, mechanical properties and crystallization behavior of PLA-g-GMA were affected by GMA content and mixing time. The optimal elongation at break and impact strength were obtained for PLA-g-GMA prepared with the GMA content and mixing time of 10 wt% and 10 min, respectively.

6.6 References

- Burton, E. L., Woodhead, M., Coates, P., and Gough, T. (2010). Reactive grafting of glycidyl methacrylate onto polypropylene. **Journal of Applied Polymer Science**. 117: 2707-2714.
- Chen, L. F., Wong, B., and Baker, W. (1996). Melt grafting of glycidyl methacrylate onto polypropylene and reactive compatibilization of rubber toughened polypropylene. **Polymer Engineering & Science**. 36: 1594-1607.
- Chen, R.-y., et al. (2014). Poly(lactic acid)/poly(butylene succinate)/calcium sulfate whiskers biodegradable blends prepared by vane extruder: Analysis of mechanical properties, morphology, and crystallization behavior. **Polymer Testing**. 34: 1-9.
- Cho, K. Y., Eom, J. Y., Kim, C. H., and Park, J. K. (2008). Grafting of glycidyl methacrylate onto high-density polyethylene with reaction time in the batch mixer. **Journal of Applied Polymer Science**. 108: 1093-1099.
- De Roover, B., et al. (1995). Molecular characterization of maleic anhydride-functionalized polypropylene. **Journal of Polymer Science Part A: Polymer Chemistry**. 33: 829-842.

- Fischer, E. W., Sterzel, H., and Wegner, G. (1973). Investigation of the structure of solution grown crystals of lactide copolymers by means of chemical reactions. **Kolloid-Z.u.Z.Polymere**. 251: 980-990.
- Garlotta, D., Doane, W., Shogren, R., Lawton, J., and Willett, J. (2003). Mechanical and thermal properties of starch-filled poly (D, L-lactic acid)/poly (hydroxy ester ether) biodegradable blends. **Journal of Applied Polymer Science**. 88: 1775-1786.
- Gaylord, N. G., and Mishra, M. K. (1983). Nondegradative reaction of maleic anhydride and molten polypropylene in the presence of peroxides. **Journal of Polymer Science: Polymer Letters Edition**. 21: 23-30.
- Ho, R., Su, A., Wu, C., and Chen, S. (1993). Functionalization of polypropylene via melt mixing. **Polymer**. 34: 3264-3269.
- Huang, H., and Liu, N. (1998). Nondegradative melt functionalization of polypropylene with glycidyl methacrylate. **Journal of Applied Polymer Science**. 67: 1957-1963.
- Huang, J., et al. (1998). Crystallization and microstructure of poly (l-lactide-co-meso-lactide) copolymers. **Macromolecules**. 31: 2593-2599.
- Jeong, B. J., and Xanthos, M. (2007). Reactive modification of PBT with applications in low density extrusion foaming. **Polymer Engineering & Science**. 47: 244-253.
- Kim, C.-H., Jung, K.-M., Kim, J.-S., and Park, J.-K. (2004). Modification of Aliphatic Polyesters and Their Reactive Blends with Starch. **Journal of Polymers and the Environment**. 12: 179-187.

- Lai, S. M., Hung, K. C., Kao, H. C., Liu, L. C., and Wang, X. F. (2013). Synergistic effects by compatibilization and annealing treatment of metallocene polyethylene/PLA blends. **Journal of Applied Polymer Science**. 130: 2399-2409.
- Li, J.-L., and Xie, X.-M. (2012). Reconsideration on the mechanism of free-radical melt grafting of glycidyl methacrylate on polyolefin. **Polymer**. 53: 2197-2204.
- Liu, J., Jiang, H., and Chen, L. (2012). Grafting of glycidyl methacrylate onto poly (lactide) and properties of PLA/starch blends compatibilized by the grafted copolymer. **Journal of Polymers and the Environment**. 20: 810-816.
- Matyjaszewski, K., Coca, S., and Jasieczek, C. B. (1997). Polymerization of acrylates by atom transfer radical polymerization. Homopolymerization of glycidyl acrylate. **Macromolecular Chemistry and Physics**. 198: 4011-4017.
- Mohanty, S., and Nayak, S. K. (2015). Effect of poly (lactic acid)-graft-glycidyl methacrylate as a compatibilizer on properties of poly (lactic acid)/banana fiber biocomposites. **Polymers for Advanced Technologies**. 27: 515-524.
- Orozco, V. H., Brostow, W., Chonkaew, W., and Lopez, B. L. (2009). Preparation and characterization of poly (lactic acid)-g-maleic anhydride + starch blends. **Macromolecular Symposia**. 277: 69-80.
- Pesetskii, S., and Makarenko, O. (2002). Grafting of glycidyl methacrylate to polypropylene in an extruder, initiated with organic peroxides. **Russian Journal of Applied Chemistry**. 75: 629-635.
- Rudnik, E. (2010). **Compostable polymer materials**. Amsterdam: Elsevier.
- Song, P., et al. (2012). Rapid crystallization of poly (l-lactic acid) induced by a nanoscaled zinc citrate complex as nucleating agent. **Polymer**. 53: 4300-4309.

- Wei, Q., Chionna, D., Galoppini, E., and Pracella, M. (2003). Functionalization of LDPE by Melt Grafting with Glycidyl Methacrylate and Reactive Blending with Polyamide-6. **Macromolecular Chemistry and Physics**. 204: 1123-1133.
- Xu, T., Tang, Z., and Zhu, J. (2012). Synthesis of polylactide-graft-glycidyl methacrylate graft copolymer and its application as a coupling agent in polylactide/bamboo flour biocomposites. **Journal of Applied Polymer Science**. 125: E622-E627.
- Xu, X., et al. (2015). Thermal Behavior of Polypropylene-g-glycidyl Methacrylate Prepared by Melt Grafting. **Journal of Macromolecular Science, Part B**. 54: 32-44.
- Yasuniwa, M., Tsubakihara, S., Sugimoto, Y., and Nakafuku, C. (2004). Thermal analysis of the double-melting behavior of poly (L-lactic acid). **Journal of Polymer Science Part B: Polymer Physics**. 42: 25-32.
- Zhang, X., et al. (2002). Effect of nucleating agent on the structure and properties of polypropylene/poly(ethylene-octene) blends. **European Polymer Journal**. 38: 1-6.
- Zhao, Y., Zhou, Y., Chen, J., and Han, L. (2015). Grafting of glycidyl methacrylate onto isotactic polybutene-I initiated by di-tert-butyl peroxide. **Journal of Elastomers and Plastics**. 47: 262-276.
- Zhou, H., Green, T. B., and Joo, Y. L. (2006). The thermal effects on electrospinning of polylactic acid melts. **Polymer**. 47: 7497-7505.

CHAPTER VII

BIOCOMPOSITES OF POLY(LACTIC ACID) AND CELLULOSE NANOFIBERS FROM CASSAVA PULP

7.1 Abstract

In this study, synchrotron small angle X-ray scattering (SAXS) technique was applied to study the crystallization behavior of poly (lactic acid) (PLA)/cellulose nanofibers (CNFs) composites. Mechanical, morphological, and thermal properties of the composites were elucidated as well. PLA/CNFs composites were prepared by melt mixing in an internal mixer. Glycidyl methacrylate (GMA) grafted poly (lactic acid) (PLA-g-GMA) was used as a compatibilizer between CNFs and PLA. CNFs were extracted from cassava pulp (CP) by acid hydrolysis method. Effect of CNFs content on crystallization behavior and physical properties of the composites was studied. The SAXS results showed that with the addition of 0.1 wt% CNFs and using PLA-g-GMA as a compatibilizer, the crystallization rate of composites significantly increased. The paracrystalline model was applied and well fitted to the SAXS data. The average long period (L) and lamellar thickness (L_c) determined by applying the paracrystalline model of PLA, PLA-g-GMA, and PLA/PLA-g-GMA/CNFs composites exhibited a slight decrease in the very early stages of crystallization, then become time independent. The fiber content of 0.1 wt% was found to give the highest crystallization rate of both PLA/CNFs and PLA/PLA-g-GMA/CNFs composites. A notably higher impact strength of PLA/CNFs and PLA/PLA-g-GMA/CNFs composites in relation to that of pure PLA

was observed. However, the tensile strength, elongation at break, and thermal stability of PLA/CNFs and PLA/PLA-g-GMA/CNFs composites did not change significantly compared to that of pure PLA. An improvement in impact strength of composites with the addition of PLA-g-GMA was observed. The enhanced interfacial adhesion between PLA and CNFs by PLA-g-GMA was confirmed by scanning electron microscopy (SEM). With the increase of CNFs content from 0.1 to 0.5 wt%, the impact strength of composites decreased. Meanwhile, there was no significant influence of CNFs content on thermal stability of obtained composites.

7.2 Introduction

Due to its good mechanical properties and easy production from its monomer, poly (lactic acid) is one of the most studied biodegradable polymers. However, some poor physical properties such as high brittleness, low crystallization rate, and low thermal stability limited its industrial applications. The combination between PLA and biodegradable fillers like cellulose nanofibers was found to improve mechanical properties and thermal stability of obtained composites (Oksman, Skrifvars, and Selin, 2003).

With the rising concern toward environmental issues, the studies on fiber-reinforced polymer composites which use both materials from renewable resources have received considerable attention. Owing to some advantages, such as abundance, renewability, low density, high specific strength and modulus, and low cost, natural fibers have been used to replace for synthetic fibers in many fiber-reinforced polymer composites (Wambua, Ivens, and Verpoest, 2003); (Mohanty, Misra, and Hinrichsen, 2000); (John and Thomas, 2008).

So far, cellulose nanofibers have been used as fillers in many composites studies (Espino-Pérez et al., 2013); (Lin, Huang, Chang, Feng, and Yu, 2011); (Sanchez-Garcia and Lagaron, 2010); (Pei, Zhou, and Berglund, 2010). Ahmad and Luyt (2012) studied CNFs reinforced PLA composites with various CNFs contents by using an internal mixer. The results from TEM images showed the poor dispersion of freeze-dried pristine CNFs in PLA matrix. The enhanced storage modulus and reduced thermal stabilities of obtained composites compared to those of neat PLA were observed. In another research, CNFs were incorporated into PLA matrix by using melt extrusion technique in a twin-screw microextruder. The surface-modification of CNFs with functional trialkoxysilanes was carried out to improve the compatibility between PLA and CNFs. Thermomechanical and thermal analyses showed that these CNFs act as nanoreinforcing agent for PLA matrix, enhancing the crystallinity degree and reinforcing the thermomechanical properties of PLA matrix (Raquez et al., 2012). Besides that, cellulose nanofibers have proven to be effective nucleating agents for the crystallization of PLA. DSC results revealed the higher degree of crystallinity for obtained composites as 2.5 wt% CNFs were added into PLA by using a fully automated laboratory two roll mill (Frone, Berlioz, Chailan, and Panaitescu, 2013).

Cellulose nanofibers used as filler in this study were extracted from cassava pulp using acid hydrolysis method (Ruangudomsakul, Ruksakulpiwat, and Ruksakulpiwat, 2015). Cassava pulp is the solid waste during starch production from cassava tubers (Sriroth, Chollakup, Chotineeranat, Piyachomkwan, and Oates, 2000). In Thailand, the production of starch generates at least 1 million tons of cassava pulp annually (Sriroth et al., 1999). In addition to residual starch, cassava pulp contains 15-50 % cellulose fibers (dry weight basis) (Teixeira et al., 2012). Extracting successfully

CNFs from cassava pulp not only generates the high-value product but also contributes to solving environmental issues. The extraction process was carried out by the combination of pre-treatments such as alkali and bleaching treatments and acid hydrolysis treatment. The results from TEM images showed that cellulose nanofibers with a diameter and length of 8-15 nm and 200-800 nm, respectively, were obtained. The crystallinity of CNFs determined by X-ray diffraction technique was found to be significantly higher than that of raw cassava pulp (Ruangudomsakul et al., 2015).

One of the biggest challenges as dispersing CNFs into polymer matrices is the highly hydrophilic character of this filler. It hinders the dispersion of CNFs in non-polar polymer matrices. Because of the strong particle–particle interactions and poor polymer wetting on the hydrophilic CNFs surface, the agglomeration of CNFs was prone to occur during melt mixing (Ahmad and Luyt, 2012); (Raquez et al., 2012). To overcome this drawback, one of the efficient methods is using a surfactant. Bondeson and Oksman (2007) investigated the preparation of biodegradable nanocomposites based on 5 wt% CNFs and PLA using an extrusion process. An anionic surfactant (5, 10 and 20 wt%) was solution blended to the CNFs suspension; water was eliminated by freeze-drying of the surfactant/CNFs system prior to melt-mixing in the PLA matrix. The results showed that as increasing surfactant content, the dispersion of CNFs in PLA was improved. However, at the same time, degradation of PLA matrix occurred. Tensile strength and elongation at break of composites were also found to be enhanced. Using a master batch of PLA/CNFs is also an efficient method to improve the dispersion of CNFs in PLA matrix. By this approach, the nanolevel dispersion of CNFs in PLA was obtained (Bitinis et al., 2013); (Jonoobi, Harun, Mathew, and Oksman, 2010). In addition, a two-step process where solvent mixing and melt mixing were carried out

sequentially was also used to enhance the dispersion of CNFs in PLA matrix (Arias, Heuzey, Huneault, Ausias, and Bendahou, 2015). In this method, first, CNFs were solution blended with a carrier polymer, and then in the second step, the CNFs-carrier polymer mixture was melt blended with the polymer matrix to prepare the composites.

PLA-g-GMA, prepared by grafting of GMA onto PLA chain via free-radical polymerization, was used as a compatibilizer in this study in order to improve the compatibility between CNFs and PLA matrix. The preparation of PLA-g-GMA was carried out by melt mixing method using an internal mixer. The experimental results from $^1\text{H-NMR}$ spectrum indicated that the grafting reaction of GMA onto PLA took place successfully. After grafting, the brittle fracture behavior of PLA was changed to ductile fracture behavior. PLA-g-GMA showed significantly higher elongation at break in relation to pure PLA (Nguyen, Ruksakulpiwat, and Ruksakulpiwat, 2016). With the chemical structure containing hydrophilic chain and oleophilic chain, PLA-g-GMA has been used as a potential compatibilizer in natural fibers reinforced PLA-based biocomposites (Xu, Tang, and Zhu, 2012).

By using the most powerful X-radiation source as a synchrotron, the recording of detailed scattering patterns with high accuracy during short exposure times could be obtained. This enables the monitoring of crystallization process of polymeric materials in real time. The isothermal crystallization behavior of poly(L-lactic acid) (PLLA) and its copolymers from the melt was investigated by synchrotron small-angle X-ray scattering (SAXS) (Wang et al., 2001); (Cho et al., 2003). The results showed that the long period of crystalline lamellar of PLLA decreased in the very early stages during primary crystallization.

In this work, the effects of CNFs and CNFs content on the crystallization rate of composites with and without using PLA-g-GMA as a compatibilizer were investigated by small angle X-ray scattering technique with synchrotron radiation. Moreover, the influences of PLA-g-GMA and CNFs content on morphological, mechanical and thermal characteristics of PLA were also elucidated.

7.3 Materials and methods

7.3.1 Materials

A commercial grade of PLA (PLA 4043D) was purchased from NatureWorks. Cellulose nanofibers were extracted from cassava pulp by using acid hydrolysis method in our laboratory. The preparation and characterization of CNFs were given in details in Chapter V. PLA-g-GMA was prepared by melt mixing using an internal mixer. The details of this grafting reaction can be found in Chapter VI.

7.3.2 Preparation of PLA composites

PLA composites were prepared using an internal mixer (Haake Rheomix, 3000p) at a temperature of 170 °C. Before mixing, PLA and CNFs were dried in an oven at 70 °C for 2 h and 50 °C for 24 h, respectively. The ratio of composites is shown in Table 7.1. The mixing time and mixing speed were kept at 10 min and 60 rpm, respectively. Before being charged into the mixing chamber, the determined amounts of PLA, PLA-g-GMA and CNFs were premixed. All compositions of composites were charged into the mixing chamber at the same time.

Table 7.1 Composition of composites

Symbol	PLA (wt%)	PLA-g-GMA (wt%)	CNFs (wt%)
PLA	100	-	-
PLA/CNFs0.1	99.9	-	0.1
PLA/CNFs0.3	99.7	-	0.3
PLA/CNFs0.5	99.5	-	0.5
PLA/PLA-g-GMA/CNFs0.1	79.9	20	0.1
PLA/PLA-g-GMA/CNFs0.3	79.7	20	0.3
PLA/PLA-g-GMA/CNFs0.5	79.5	20	0.5

7.3.3 Characterization

7.3.3.1 Morphological properties

The morphologies of the tensile fractured surface of compression molded samples were observed by a scanning electron microscope (SEM, model JEOL JSM6010LV). The specimens were coated with gold before the examination. All SEM images were collected under an acceleration voltage of 10 kV.

7.3.3.2 SAXS analyses

Isothermal crystallization behaviors of PLA and composites were determined by SAXS technique. The synchrotron SAXS experiments were performed at BL1.3W beamline of the Siam Photon Laboratory, Synchrotron Light Research Institute, Nakhon-Ratchasima, Thailand. The wavelength was 1.38 Å and the sample-to-detector was set at 2.4 m. Silver behenate (AgBH) with $d = 3.838$ nm was used as a standard material for calibrating the scattering angle. A CCD detector (Rayonix SX 165) with a diameter of 165 mm was used to capture the scattering patterns. An ionization chamber installed in front of the sample holder and a photodiode attached in front of a beam stop were used to monitor the beam intensity before and

after the sample, respectively. The schematic diagram of the SAXS BL1.3W beamline is shown in Figure 7.1.

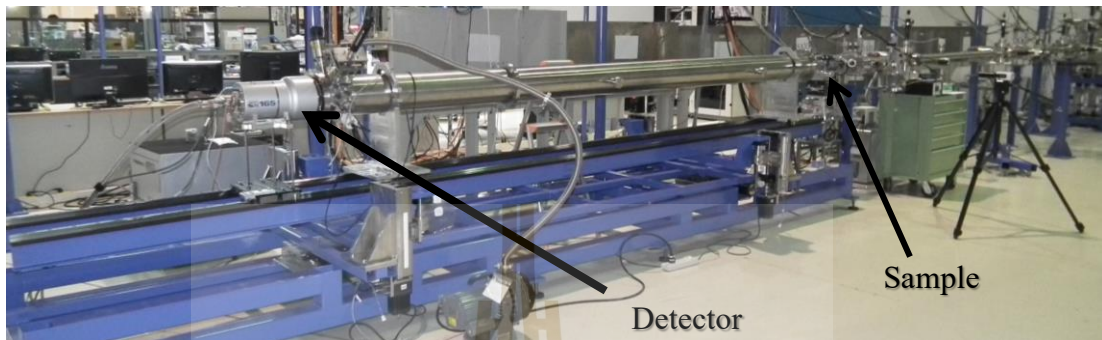


Figure 7.1 Schematic diagram of the SAXS BL1.3W beamline.

The samples with the same thickness were filled into the sample cell with Kapton windows. The specimens were heated from room temperature to 200 °C and kept for 5 min to eliminate any possible crystalline phase completely. Then the samples were quenched to 120 °C and the synchrotron SAXS measurements were carried out at different crystallization times with the exposure time of 10 s. The 2D SAXS patterns were reduced to 1D SAXS profile by circularly averaging the 2D patterns using the SAXSIT program (Soontaranon and Rugmai, 2012). After that, the profile was corrected for beam intensity, sample transmission, background scattering and converted to Lorentz-corrected SAXS profile by multiplying by q^2 (Vonk and Kortleve, 1967). The scattering vector is given by (Glatter and Kratky, 1982):

$$q = (4\pi/\lambda) \sin \theta \quad (7.1)$$

In which λ and 2θ are the wavelength of the X-ray source and the scattering angle, respectively.

The scattering angle is given by:

$$2\theta = \tan^{-1} (D/L) \quad (7.2)$$

In which D is the distance from the origin to the point on the detector plane, calculated using the pixel size, and L is the sample-to-detector distance.

The total scattering intensity is proportional to the difference of electron density of crystalline and amorphous phases, and the volume fraction of crystalline phase in the semi-crystalline polymers. Therefore, the change of total scattering intensity can regard as the change of crystallinity (Luo et al., 2011); (Lee et al., 2004); (Verma, Marand, and Hsiao, 1996); (Koberstein and Stein, 1983); (Ivanov, Legras, and Jonas, 1999); (Ivanov, Amalou, and Magonov, 2001). The SAXS peak can be attributed to the lamellar structure in the spherulites of PLA (Wang et al., 2001). In this research, the SAXS patterns of pure PLA and its composites were recorded to investigate the effects of CNFs and CNFs content on the crystallization behavior of PLA composites.

The morphological parameters such as the average long period of lamellar structure (L) and the average lamellar thickness (L_c) of PLA, PLA-g-GMA, and PLA/PLA-g-GMA/CNFs composites were determined by applying the paracrystalline diffraction method. It should be noticed that the average long period of lamellar structure can also be obtained from the first maximum at the lowest scattering angle by applying Bragg's law ($L_B = 2\pi / q_{\max}$, where q_{\max} is scattering vector at

maximum intensity) in the SAXS profiles (Luo et al., 2001); (Zhou and Wilkes, 1997); (Xia, Sue, Wang, Avila-Orta, and Hsiao, 2001). However, in most cases, the values determined by this simple method do not agree quantitatively with the structures seen by electron microscopy (Dismore and Statton, 1966). Compared to Bragg's law method, the paracrystalline diffraction method is more physically meaningful because it takes into account the nonideal periodicity of macrolattices in semicrystalline polymers. With this method, the size fluctuations of amorphous layer and crystalline component are assumed to contribute to the long-range disorder of the lattice. Thus, each of the two phases are treated equally in defining the structure of the paracrystalline macrolattice (Crist, 1973). Besides determining the average long period, this method can also provide the average lamellar thickness parameter. These parameters can be obtained by fitting the SAXS curves to the equation (Vaĭnshteĭn, 1966):

$$I(q) = C * \left\{ I_0 \exp(-\sigma_{in}^2 q^2) \frac{|F(q, L)|^2 S(q)}{1 + q^2 \xi^2} + a q^{-x} + \frac{b}{1 + (|q - q_0| \xi_0)^m} \right\} + k \quad (7.3)$$

In which C , I_0 , a , b , x , and k are positive adjustable parameters.

The first term in Eq. (7.3) represents for crystalline part and describes the SAXS peak. The second term is given by the power-law function and describes the underlying diffusive scattering. The third term is given by the Ornstein-Zernike function and represents for the scattering of random chains. The fourth term is given by the broad peak and describes the scattering of amorphous soft materials. The exponential $\exp(-\sigma_{in}^2 q^2)$

comes from the smoothing of crystalline-amorphous interface. The averaged crystalline lamella form factor is expressed as:

$$\overline{|F(q, L)|^2} = \frac{1}{\sqrt{2\pi}\sigma_L} \int_{-\infty}^{\infty} |F(q, x)|^2 \exp\left(-\frac{(x-L)^2}{2\sigma_L^2}\right) dy \quad (7.4)$$

The form factor of crystalline lamella with thickness L is given by:

$$F(q, L) = \frac{\sin\left(\frac{qL}{2}\right)}{\frac{qL}{2}} \quad (7.5)$$

The structure factor $S(q)$ corresponds to the interference between the scattered X-ray of the neighboring lamellae aligning in one dimension, which is expressed as:

$$S(q) = \frac{1 - |G(q)|^2}{1 - 2|G(q)| \cos(q\alpha) + |G(q)|^2} \quad (7.6)$$

Where α is the average long period. $G(q)$ is the Fourier transform of Gaussian long period distribution function:

$$G(q) = \mathcal{F}[H(y)] \quad (7.7)$$

With the Gaussian long period distribution function is given by:

$$H(y) = \frac{1}{\sqrt{2\pi}\sigma_a} \exp\left(-\frac{(y-\alpha)^2}{2\sigma_a^2}\right) \quad (7.8)$$

In which σ is standard deviation of the long period distribution.

The measured SAXS intensity profiles were fitted by using a Matlab based module (SAXSIT) (Soontaranon and Rugmai, 2012).

The fiber content of 0.1 wt% was selected to investigate the effect of CNFs on the crystallization behavior of PLA/PLA-g-GMA/CNFs composites. In this analysis, SAXS measurements were carried out at 200 °C and 120 °C at different crystallization times (5, 10, 20, 30, 40, 50, and 60 min). Moreover, in order to investigate the effect of fiber content on the crystallization behavior of PLA/CNFs and PLA/PLA-g-GMA/CNFs composites, SAXS analysis was measured at 120 °C at three different crystallization times (0, 5, and 10 min).

7.3.3.3 Thermal properties

Thermal stability of PLA and its composites was evaluated via thermogravimetric analysis (TGA), which was performed using a Mettler Toledo STARe System (TGA/DSC1) by heating the samples from room temperature to 600 °C at a heating rate of 10 °C/min under a nitrogen atmosphere. The sample with a weight between 5 and 10 mg was used for each run.

Differential scanning calorimetry (DSC) (model: DSC204F1 Phoenix) was used to obtain thermal properties of specimens by heating the samples from 40 to 200 °C at a rate of 5 °C/min (First heating scan). After keeping the specimens

at 200 °C for 5 min, they were cooled to 40 °C at 5 °C/min. Then they were heated again to 200 °C at 5 °C/min (Second heating scan). The degree of crystallinity (% X_c) of PLA and composites was determined by Eq. (7.9):

$$\%X_c = \frac{\Delta H_m}{\Delta H_{mo} \times W_{PLA}} \times 100 \quad (7.9)$$

In which ΔH_m is the measured melting enthalpy (J/g) from the second heating scan, ΔH_{mo} is the theoretical melting enthalpy of completely crystalline PLA (93.7 J/g), and W_{PLA} is the PLA weight fraction in the composites (Cheung, Lau, Tao, and Hui, 2008).

7.3.3.4 Mechanical properties

Compression molding (LabTech, LP20-B) was used to prepare the test specimens for mechanical properties testing. After drying in an oven at 70 °C for 2 h, all samples were compression molded at 170 °C for 10 min. Tensile properties of PLA and its composites were measured according to ASTM D638 using an Instron Universal Testing Machine (UTM 5565) with a load cell of 5 kN. The unnotched Izod impact strength of PLA and its composites was obtained according to ASTM D256 using Instron CEAST 9050 Pendulum Impact System.

7.4 Results and discussion

7.4.1 Morphological properties

Figure 7.2(a-g) shows SEM images of the tensile fractured surface of pure PLA and its composites. Compared to pure PLA, PLA/CNFs0.1 did not show any

significant differences in morphology. No visible microscale agglomerations of CNFs were observed (Figure 7.2b). As CNFs content was increased (up to 0.3 and 0.5 wt%), however, the rougher fractured surfaces and some microscale agglomerations of CNFs were observed. The higher CNFs content was used; the rougher surfaces and the bigger size of microscale agglomerations of CNFs were observed (Figure 7.2(c,d)). Generally, a relatively good dispersion was obtained in composite with low fiber content (0.1 wt%).

For composites with using PLA-g-GMA as a compatibilizer, the better dispersion of CNFs in PLA was achieved, especially for PLA/PLA-g-GMA/CNFs0.1 (Figure 7.2e) and PLA/PLA-g-GMA/CNFs0.3 (Figure 7.2f) composites. Compared to PLA/CNFs composites, PLA/PLA-g-GMA/CNFs composites showed the smoother surfaces at all studied fiber contents (0.1, 0.3, and 0.5 wt%). As shown in Figure 7.2f, the dispersion of CNFs in PLA is still relatively good with fiber content up to 0.3 wt%. Nevertheless, with further increase of fiber content up to 0.5 wt%, a slightly coarse surface and some small agglomerations were observed (Figure 7.2g). The more detailed micrographs of PLA/CNFs0.5 and PLA/PLA-g-GMA/CNFs0.5 composites are shown in Figure 7.3. From the graph of PLA/CNFs0.5 composite (Figure 7.3a), one can see that the gaping holes and voids between fibers and matrix are visible. This indicates the poor interfacial adhesion between fibers and matrix. Conversely, as shown in Figure 7.3b, by the addition of PLA-g-GMA, no voids between fibers and matrix were observed. This indicates that the interfacial adhesion between fibers and matrix was improved. This improvement is attributed to the compatibilizing effect of PLA-g-GMA. On the one hand, the hydroxyl groups (-OH) on the surface of cellulose nanofibers can react with the epoxy groups of GMA on PLA-g-GMA, on the other hand, the physical

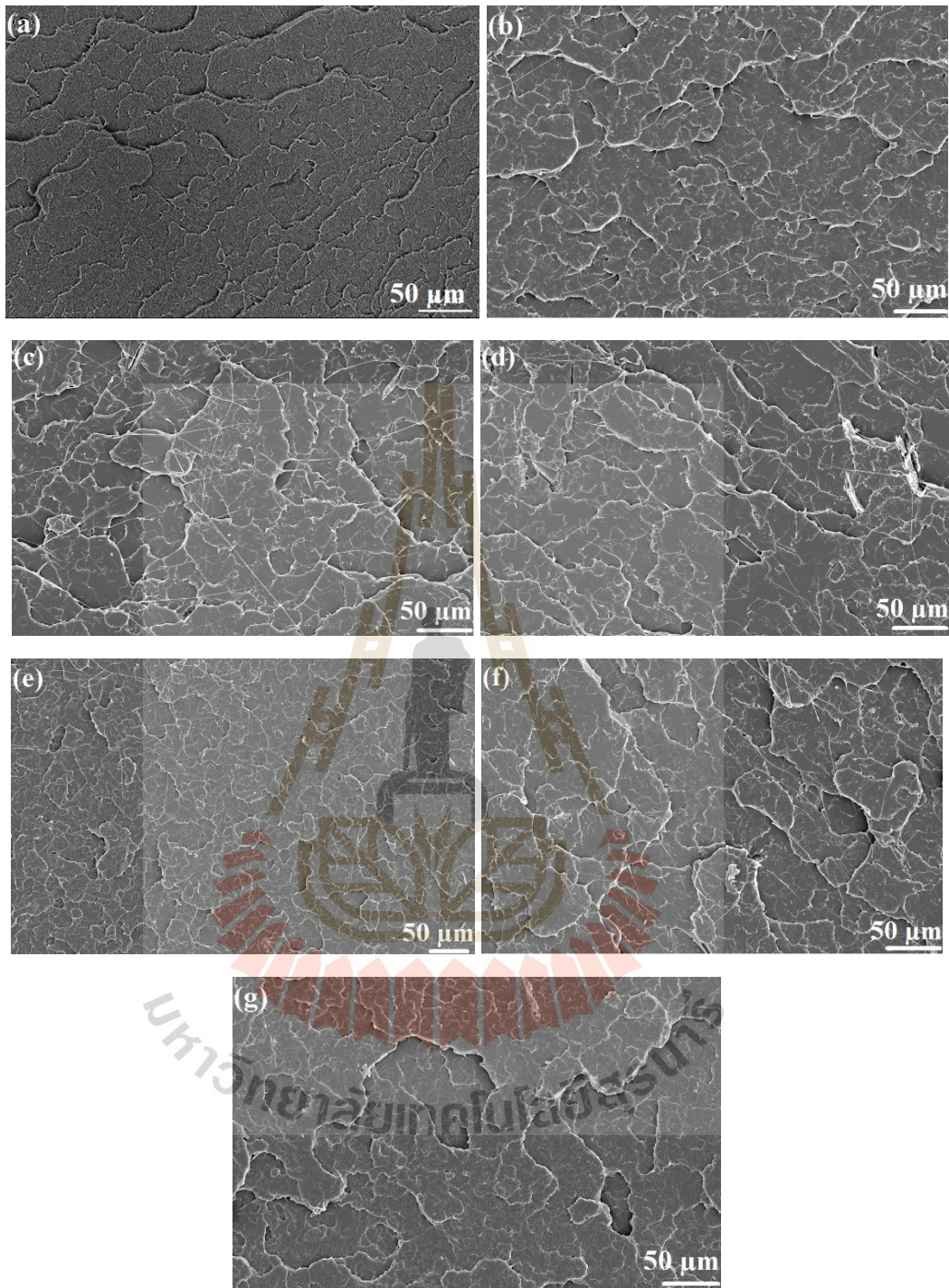


Figure 7.2 SEM micrographs of the tensile fractured surfaces of pure PLA (a), PLA/CNFs0.1 (b), PLA/CNFs0.3 (c), PLA/CNFs0.5 (d), PLA/PLA-g-GMA/CNFs0.1 (e), PLA/PLA-g-GMA/CNFs0.3 (f), and PLA/PLA-g-GMA/CNFs0.5 (g).

entanglements between PLA chains of the matrix and PLA chains of PLA-g-GMA can be formed during mixing.

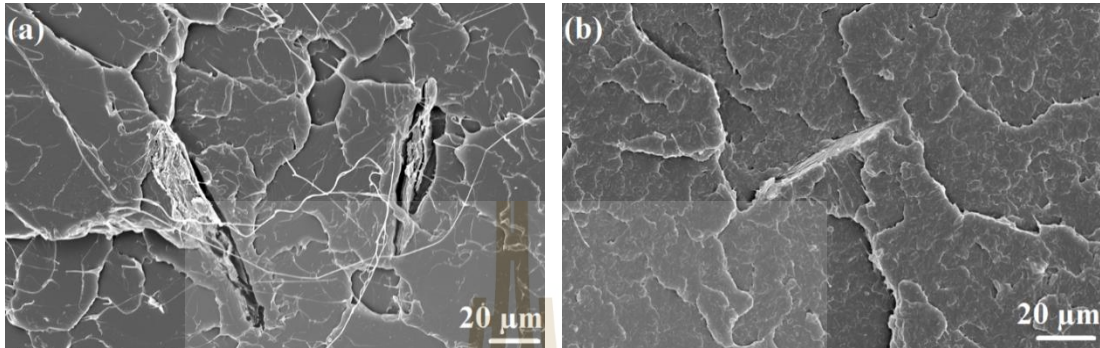


Figure 7.3 Detailed view of the tensile fractured surfaces of PLA/CNFs0.5 (a) and PLA/PLA-g-GMA/CNFs0.5 (b) composites showing the interfacial adhesion between fibers and PLA matrix.

7.4.2 Isothermal crystallization behavior by SAXS

Figure 7.4 shows Lorentz-corrected SAXS profiles of PLA, PLA-g-GMA, and PLA/PLA-g-GMA/CNFs0.1 composite obtained at 200 °C. As shown in Figure 7.4, no SAXS peaks were observed in all samples. This confirms that all samples do not contain any crystalline part before it was cooled down. The Lorentz-corrected SAXS profiles of PLA, PLA-g-GMA, and PLA/PLA-g-GMA/CNFs0.1 composite at 120 °C at different crystallization times are shown in Figures (7.5-7.11).

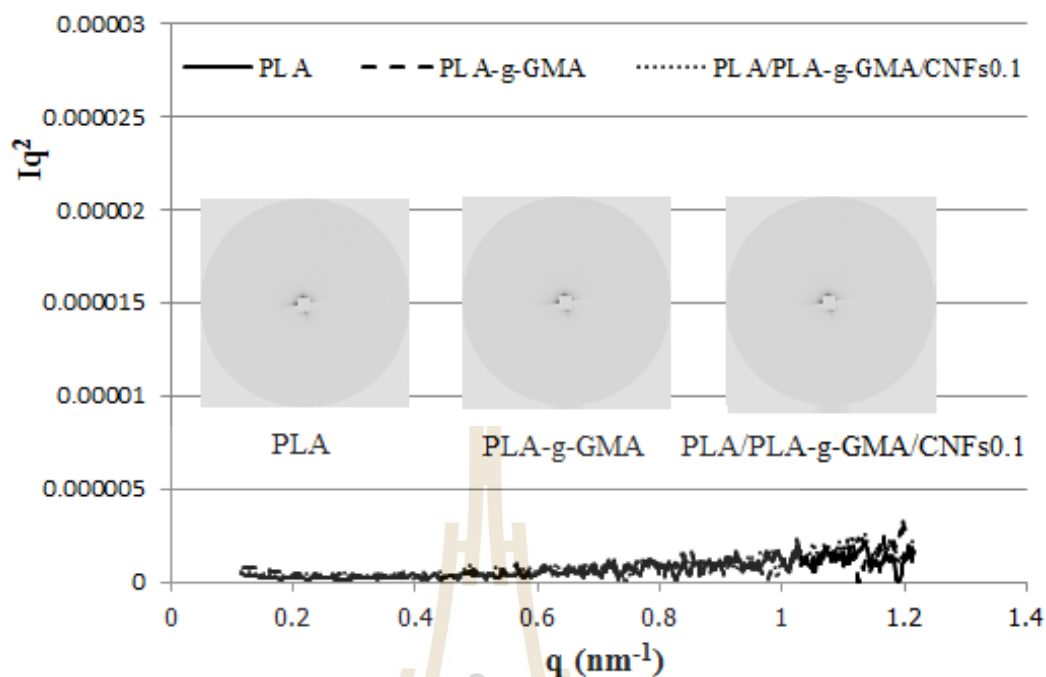


Figure 7.4 Lorentz-corrected SAXS profiles of pure PLA, PLA-g-GMA, and PLA/PLA-g-GMA/CNFs0.1 composite obtained at 200 °C. The insets show the 2D-SAXS patterns of these samples.

As can be seen from Figure 7.5, after 5 min of crystallization time, no scattering peak was observed for pure PLA. This demonstrates that no crystallization of PLA took place within 5 min of crystallization time at 120 °C. Conversely, the clear scattering peaks were observed for PLA-g-GMA and PLA/PLA-g-GMA/CNFs0.1 composite. It indicates that PLA has longer induction time for crystallization compared to that of PLA-g-GMA and PLA/PLA-g-GMA/CNFs0.1 composite. Moreover, as shown in Figure 7.5, the intensity of the scattering peak of the composite is significantly higher than that of PLA-g-GMA. From this result, it can be seen that the crystallinity

of composite is higher than that of pure PLA and PLA-g-GMA after 5 min of crystallization time.

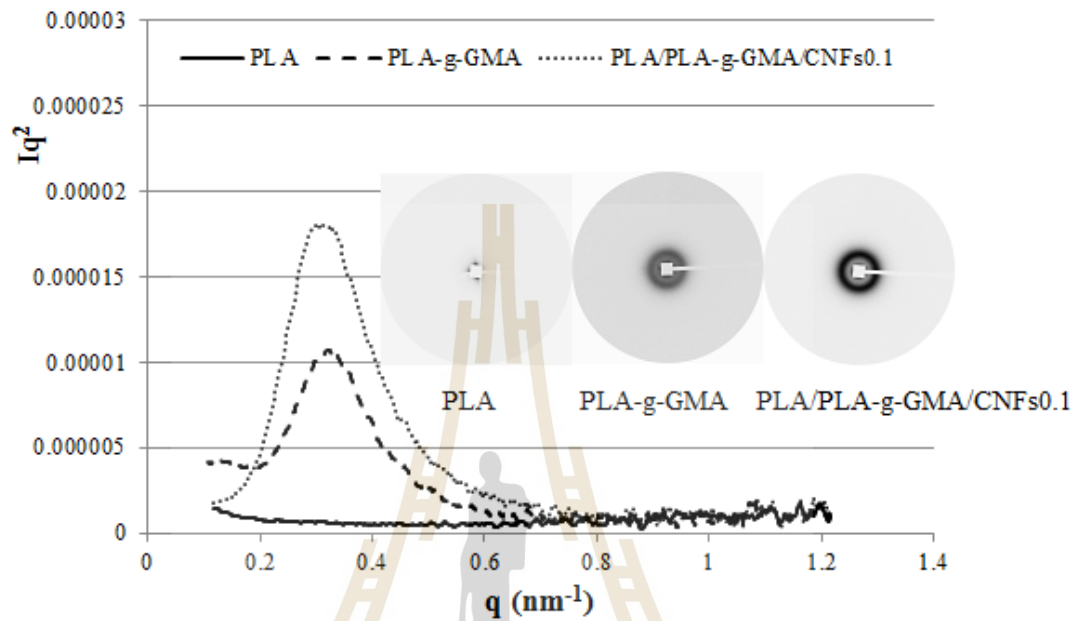


Figure 7.5 Lorentz-corrected SAXS profiles of pure PLA, PLA-g-GMA, and PLA/PLA-g-GMA/CNFs0.1 composite obtained at 120 °C after 5 min of crystallization time. The insets show the 2D-SAXS patterns of these samples.

After 10 min of crystallization time (Figure 7.6), the crystallization of PLA was shown with a small scattering peak appeared in the scattering profile of pure PLA. This means that PLA has started to crystallize at the time between 5 to 10 min of crystallization time. Meanwhile, the scattering intensity of PLA-g-GMA and the composite continued increasing, especially for the composite, the scattering intensity

increased dramatically. It indicates the faster crystallization of the composite compared to those of pure PLA and PLA-g-GMA.

It can be seen from Figure 7.7 that after 20 min of crystallization time, the intensity of scattering peaks of the composite stayed constant compared to that at 10 min. It implies that the crystallization process of the composite has already finished after 10 min of crystallization time. In contrast to the composite, PLA and PLA-g-GMA continued to crystallize as shown by the increased scattering intensity. Notably, the SAXS profile of PLA exhibited the apparent scattering peak with significantly increased intensity. However, the SAXS peak of PLA appeared at higher q position compared to that of PLA-g-GMA and the composite. It indicates the smaller long spacing in the lamellar stack.

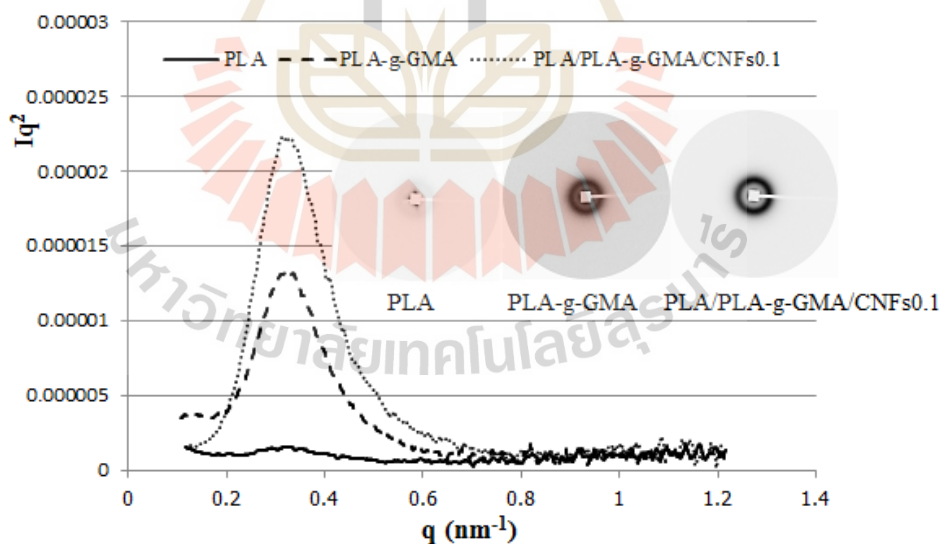


Figure 7.6 Lorentz-corrected SAXS profiles of pure PLA, PLA-g-GMA, and PLA/PLA-g-GMA/CNFs0.1 composite obtained at 120 °C after 10 min of crystallization time. The insets show the 2D-SAXS patterns of these samples.

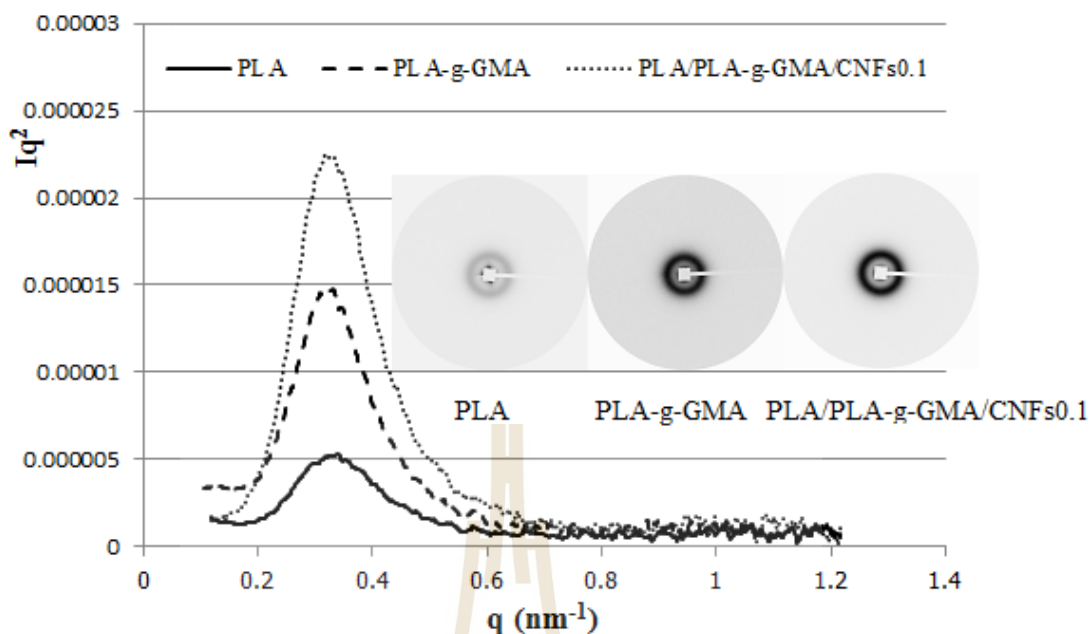


Figure 7.7 Lorentz-corrected SAXS profiles of pure PLA, PLA-g-GMA, and PLA/PLA-g-GMA/CNFs0.1 composite obtained at 120 °C after 20 min of crystallization time. The insets show the 2D-SAXS patterns of these samples.

The SAXS profiles of PLA, PLA-g-GMA, and the composite after 30 min of crystallization time are shown in Figure 7.8. As can be seen from Figure 7.8, the scattering peak of the composite did not show any difference in the intensity and q position compared to that at 10 and 20 min of crystallization time. A slight increase in the intensity of SAXS peak of PLA-g-GMA was observed. Meanwhile, the intensity of SAXS peak of PLA increased considerably compared to that at 20 min of crystallization time. This result indicates that the crystallization process of PLA and PLA-g-GMA has not finished yet after 20 min of crystallization time.

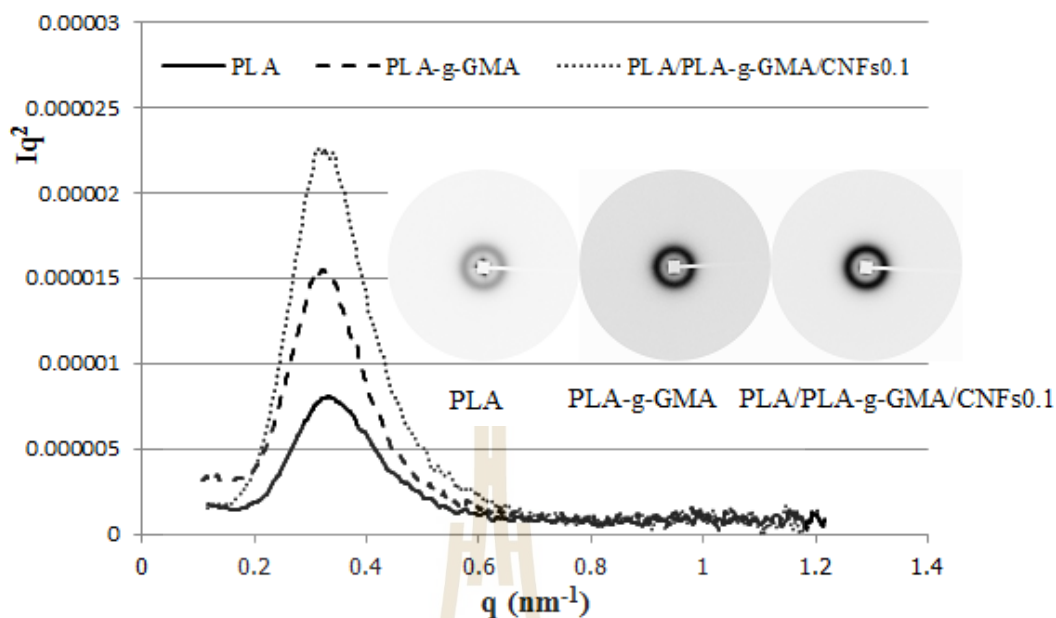


Figure 7.8 Lorentz-corrected SAXS profiles of pure PLA, PLA-g-GMA, and PLA/PLA-g-GMA/CNFs0.1 composite obtained at 120 °C after 30 min of crystallization time. The insets show the 2D-SAXS patterns of these samples.

After 40 min of crystallization time (Figure 7.9), the intensity of SAXS peak of PLA-g-GMA stayed constant compared to that at 30 min. It implies that the crystallization process of PLA-g-GMA seemed to finish after 30 min of crystallization time. However, for PLA, it appears that the crystallization process has not finished yet because the intensity of SAXS peak at 40 min shows a significant increase compared to that at 30 min of crystallization time. The intensity of SAXS peak of PLA still shows a slight increase after 50 min of crystallization time (Figure 7.10), whereas there is no difference in intensity of SAXS peak of PLA at 60 min (Figure 7.11) compared to that

at 50 min. From this result, it can be stated that the crystallization process of PLA has been completed after 50 min of crystallization time.

In order to see more clearly the effect of CNFs on the crystallization rate of the composite, the maximum $I(q)q^2$ was plotted versus *crystallization time* as shown in Figure 7.12. The slope of the curve of the composite was considerably higher than that of pure PLA and PLA-g-GMA. This result indicates that the crystallization rate of PLA was improved significantly by the addition of 0.1 wt% CNFs and using PLA-g-GMA as a compatibilizer. The well dispersed CNFs acted as nucleating agents for the crystallization of PLA, which contributes to fastening the crystallization rate of the composite.

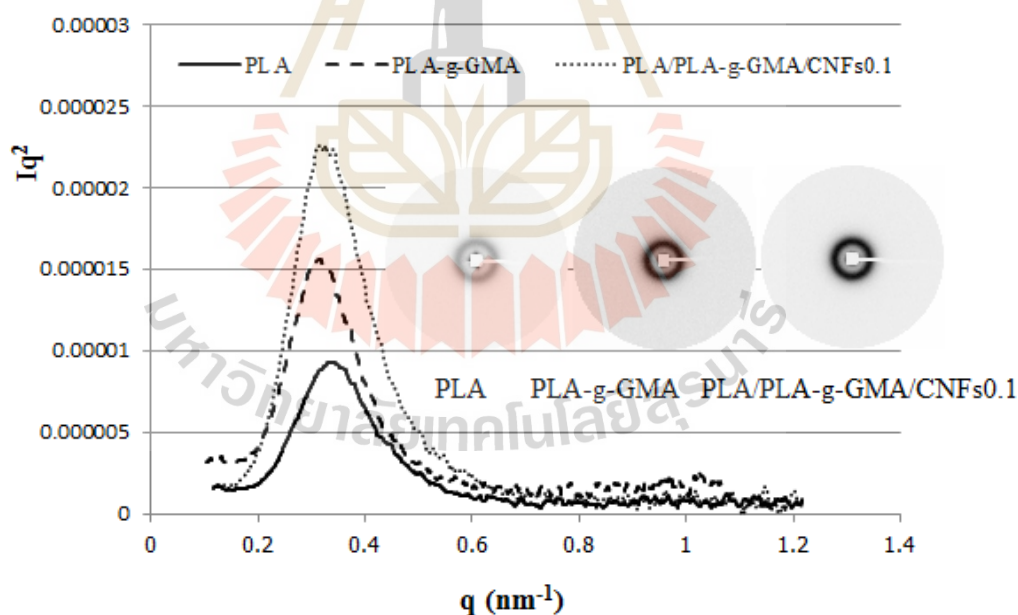


Figure 7.9 Lorentz-corrected SAXS profiles of pure PLA, PLA-g-GMA, and PLA/PLA-g-GMA/CNFs0.1 composite obtained at 120 °C after 40 min of crystallization time. The insets show the 2D-SAXS patterns of these samples.

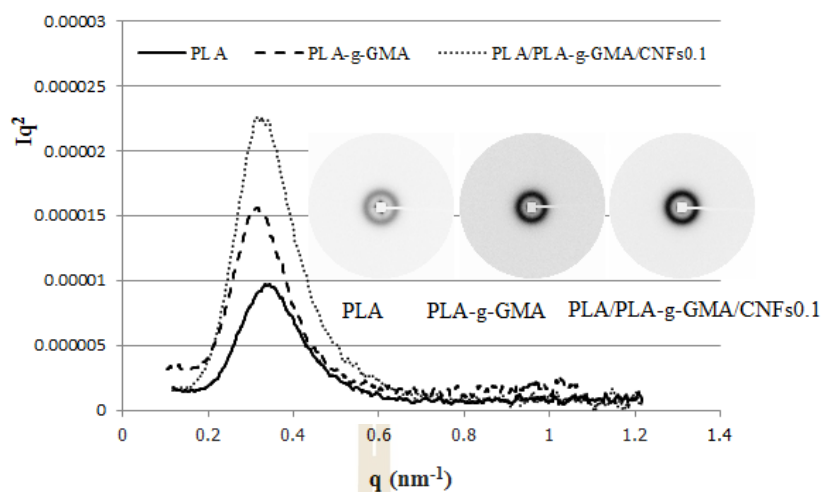


Figure 7.10 Lorentz-corrected SAXS profiles of pure PLA, PLA-g-GMA, and PLA/PLA-g-GMA/CNFs0.1 composite obtained at 120 °C after 50 min of crystallization time. The insets show the 2D-SAXS patterns of these samples.

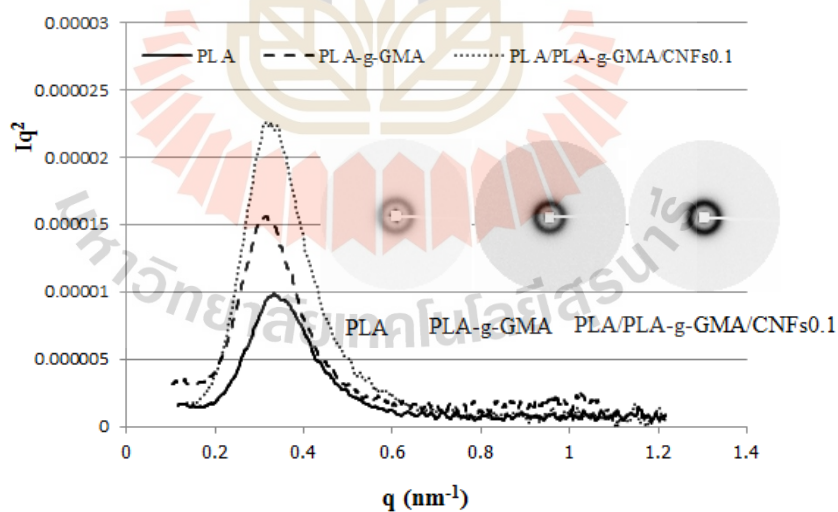


Figure 7.11 Lorentz-corrected SAXS profiles of pure PLA, PLA-g-GMA, and PLA/PLA-g-GMA/CNFs0.1 composite obtained at 120 °C after 60 min of crystallization time. The insets show the 2D-SAXS patterns of these samples.

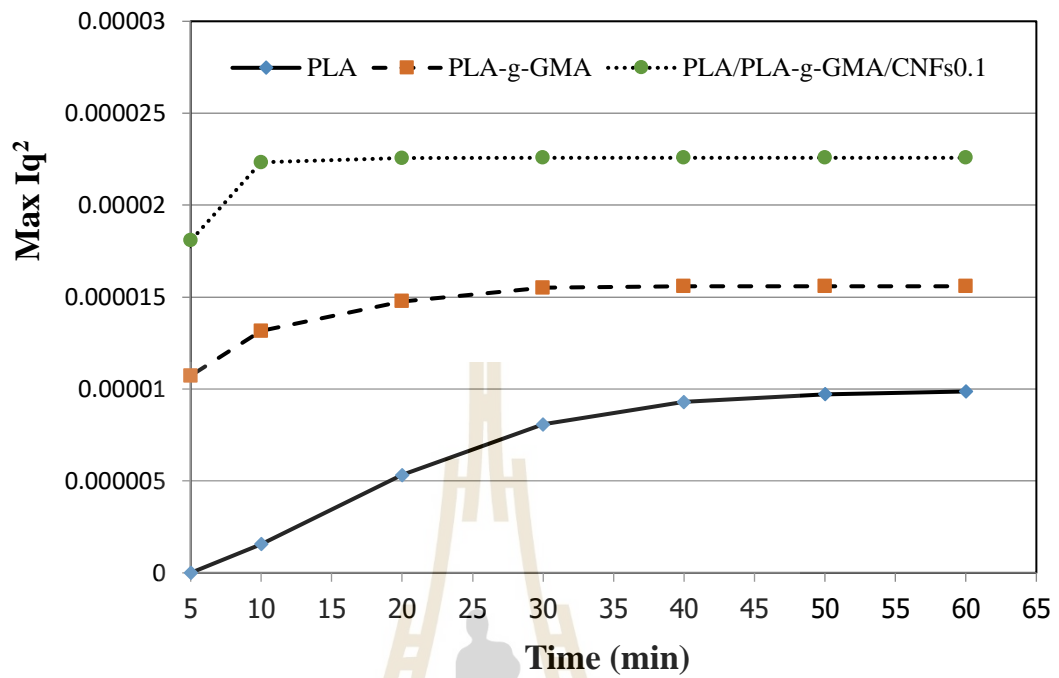


Figure 7.12 The plot of the changes of maximum Iq^2 versus *crystallization time* of PLA, PLA-g-GMA, and PLA/PLA-g-GMA/CNFs0.1 composite.

The experimental data and its fitting curve using paracrystalline model (Eq. (7.3)) of PLA, PLA-g-GMA and PLA/PLA-g-GMA/CNFs0.1 composites at 120 °C after 20 min of crystallization time are shown in Figure. 7.13. The similar fitting procedures were conducted at other crystallization times.

The L and L_c values were obtained from fitting the experimental data to the paracrystalline model of PLA, PLA-g-GMA and PLA/PLA-g-GMA/CNFs0.1 composites at different crystallization times shown in Figure. 7.14. The average long period and lamellar thickness of PLA, PLA-g-GMA, and PLA/PLA-g-GMA/CNFs0.1 composites decreased very slightly in the early stages of crystallization, then became

time independent. The initial decrease in L and L_c values is larger for PLA-g-GMA. Such behavior could be interpreted by the lamellar stack insertion process which is related to the crystallization of thinner, possibly more defective lamellar stacks between existing primary stacks consisting of lamella with larger thickness (Cho et al., 2003). Similar results have been reported by several authors in isothermal crystallization of various semi-crystalline polymers such as PLLA (Wang et al., 2001); (Cho et al., 2003), polystyrene (PS) (Rastogi, Goossens, and Lemstra, 1998), and polyester terephthalate (PET) (Lee et al., 2003). Additionally, as can be seen from Figure. 7.14, L and L_c values of PLA and PLA-g-GMA were slightly lower than those of PLA/PLA-g-GMA/CNFs0.1 composites. This could be attributed to the secondary crystallization which produced thinner lamellae thickness, resulting in the reduction of the average long period and lamellar thickness (Wang, Hsiao, Sauer, and Kampert, 1999).

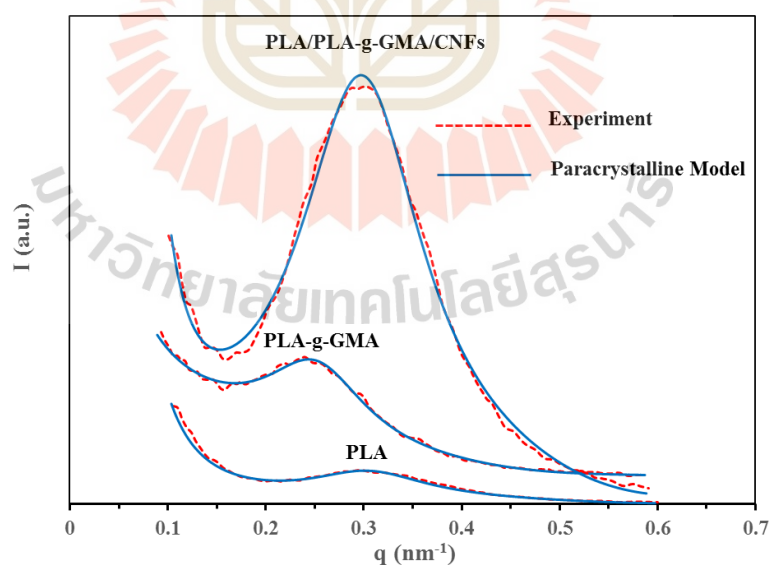


Figure 7.13 The SAXS curves from the experimental data and fitting results using the paracrystalline model of PLA, PLA-g-GMA, and PLA/PLA-g-GMA/CNFs0.1 composites at 120 °C after 20 min of crystallization time.

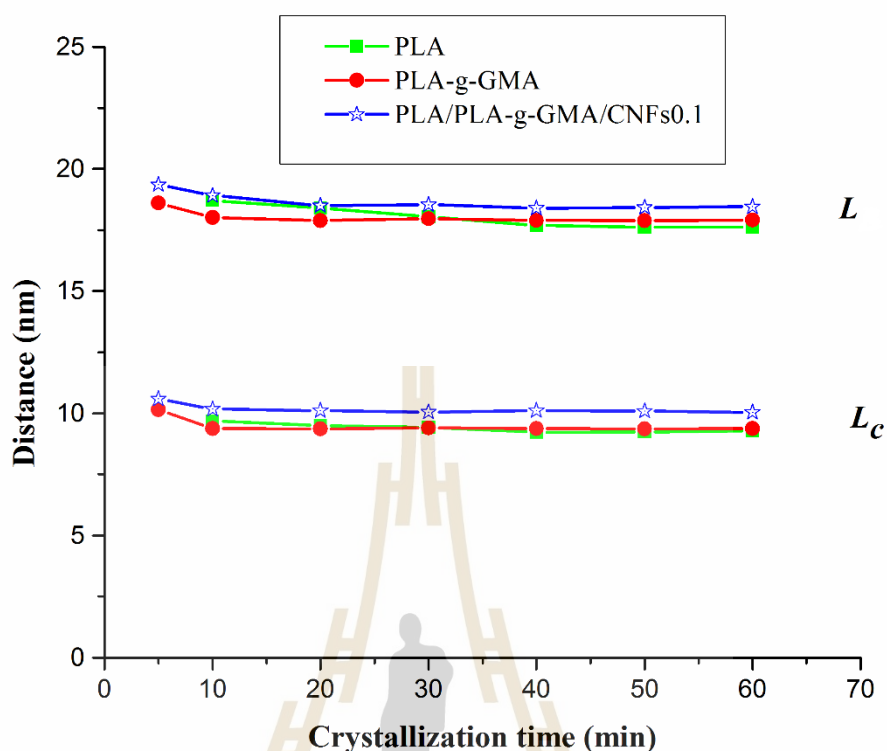


Figure 7.14 Crystallization time dependence of the average long period (L) and lamellar thickness (L_c) of PLA, PLA-g-GMA, and PLA/PLA-g-GMA/CNFs0.1 composites crystallized at 120 °C.

7.4.3 Effect of PLA-g-GMA and fiber content on the crystallization behavior of PLA/CNFs composites

Figure 7.15 shows Lorentz-corrected SAXS profiles of PLA/CNFs composites with various fiber contents at the beginning of melt crystallization at 120 °C. As shown in Figure 7.15, no SAXS peaks were observed in all samples. This confirms that all crystals were melted upon heating or before cooling down to desired crystallization temperature. After 5 min of crystallization time (Figure 7.16), there was no difference in SAXS profiles of PLA/CNFs composites at various fiber contents

compared to those at 0 min of crystallization time. However, after 10 min of crystallization time (Figure 7.17), the crystallization of PLA/CNFs0.1, PLA/CNFs0.3, and PLA/CNFs0.5 composites was observed by the small scattering peaks appeared in the scattering profile of these three samples. Compared to SAXS profile of PLA/CNFs0.3 and PLA/CNFs 0.5 composites, SAXS profile of PLA/CNFs0.1 composite showed the highest scattering peak.

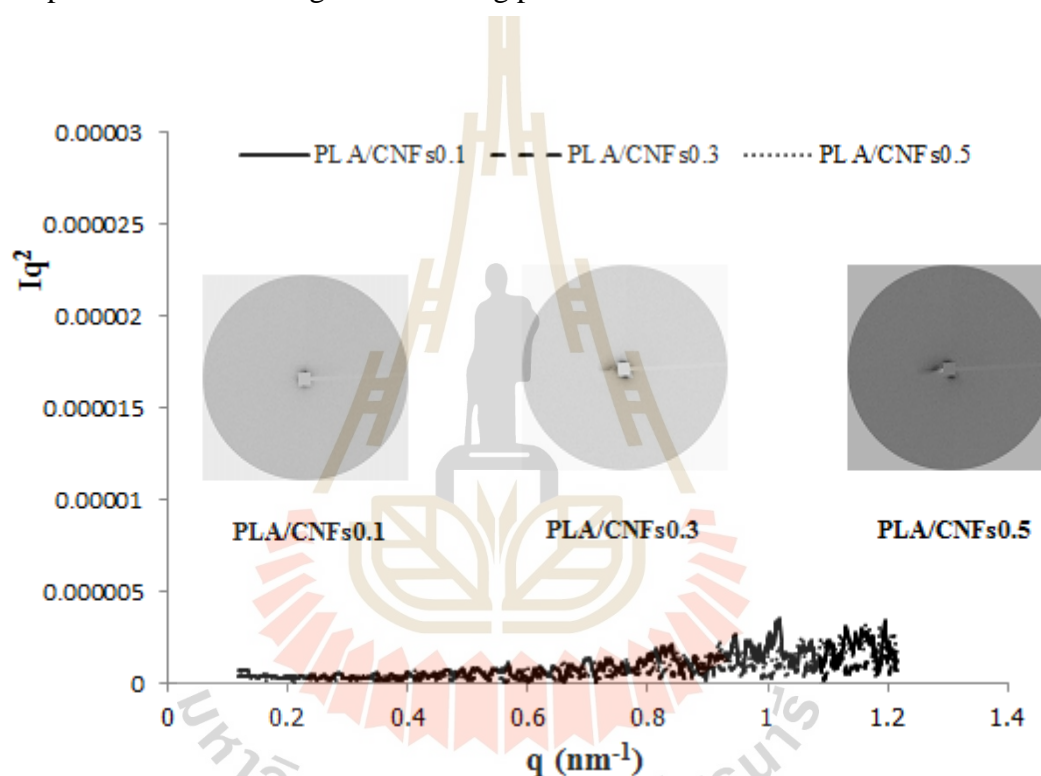


Figure 7.15 Lorentz-corrected SAXS profiles of PLA/CNFs composites with various fiber contents obtained at 120 °C at 0 min of crystallization time. The insets show the 2D-SAXS patterns of the respective samples.

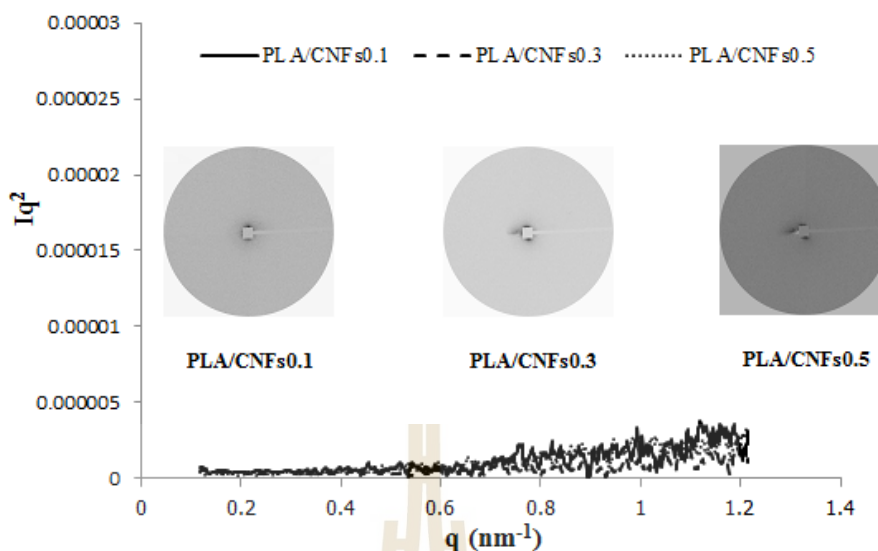


Figure 7.16 Lorentz-corrected SAXS profiles of PLA/CNFs composites with various fiber contents obtained at 120 °C after 5 min of crystallization time. The insets show the 2D-SAXS patterns of the respective samples.

As observed from Figure 7.17 the intensity of scattering peak slightly decreased with increasing fiber content. Furthermore, there was no significant difference in intensity of scattering peak of PLA/CNFs0.3 and PLA/CNFs0.5 composites. It indicates that increasing fiber content from 0.3 to 0.5 wt% did not cause any considerable change in crystallinity of PLA/CNFs composites. Generally, from SAXS results, the slow crystallization rate was observed for PLA/CNFs composites with various fiber contents. The fiber content of 0.1 wt% was found to give the highest crystallization rate of PLA/CNFs composites.

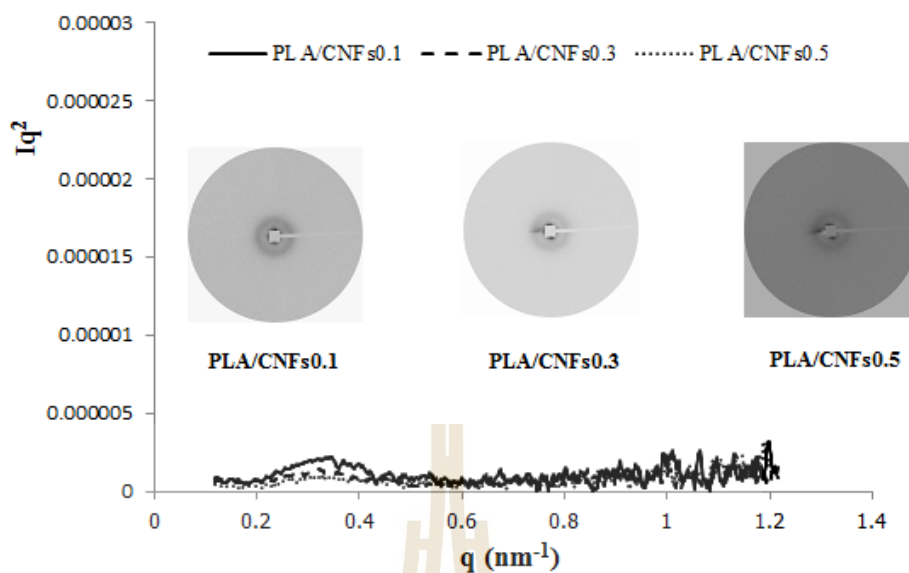


Figure 7.17 Lorentz-corrected SAXS profiles of PLA/CNFs composites with various fiber contents obtained at 120 °C after 10 min of crystallization time. The insets show the 2D-SAXS patterns of the respective samples.

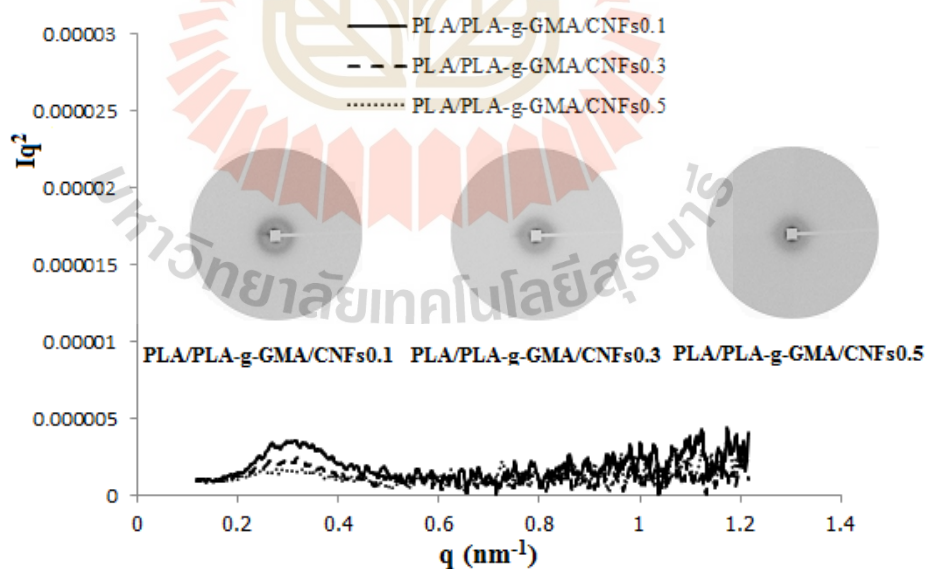


Figure 7.18 Lorentz-corrected SAXS profiles of PLA/PLA-g-GMA/CNFs composites with various fiber contents obtained at 120 °C at 0 min of crystallization time. The insets show the 2D-SAXS patterns of the respective samples.

In the case of PLA/PLA-g-GMA/CNFs composites with using PLA-g-GMA as a compatibilizer, the small scattering peaks were observed in the SAXS profile of all samples with various fiber contents at 0 min of crystallization time (Figure 7.18). This is entirely different from PLA/CNFs composites without PLA-g-GMA with no scattering peak was observed even after 5 min of crystallization time. The lower fiber content, the higher intensity of scattering peak. Additionally, at the beginning of crystallization, a very slight difference in intensity of scattering peak of PLA/PLA-g-GMA/CNFs0.3 and PLA/PLA-g-GMA/CNFs0.5 composites was observed.

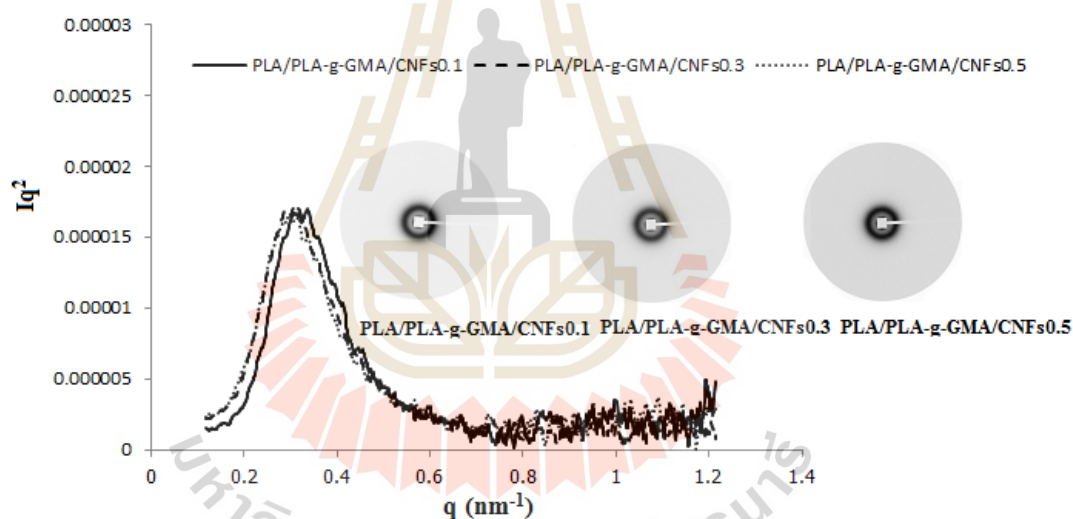


Figure 7.19 Lorentz-corrected SAXS profiles of PLA/PLA-g-GMA/CNFs composites with various fiber contents obtained at 120 °C after 5 min of crystallization time. The insets show the 2D-SAXS patterns of the respective samples.

As can be seen from Figure 7.19 that after 5 min of crystallization time, the intensity of the scattering peak of PLA/PLA-g-GMA/CNFs0.1, PLA/PLA-g-

GMA/CNFs0.3, and PLA/PLA-g-GMA/CNFs0.5 composites increased significantly compared to that at 0 min of crystallization time. Moreover, there was no considerable difference in intensity of scattering peak of PLA/PLA-g-GMA/CNFs composites as fiber content was increased from 0.1 to 0.5 wt%. After 10 min of crystallization time (Figure 7.20), the SAXS profile exhibits that the intensity of the scattering peak of all samples continued increasing compared to that after 5 min of crystallization time. However, the intensity of the scattering peak of PLA/PLA-g-GMA/CNFs0.1 composite increased more significantly and showed the highest value compared to that of other samples. It indicates that the fiber content of 0.1 wt% was found to give the highest crystallization rate of PLA/PLA-g-GMA/CNFs composites. Also, it is worth noting that increasing fiber content from 0.3 to 0.5 wt% did not cause any significant change in the crystallization rate of PLA/PLA-g-GMA/CNFs composites. Especially, compared to PLA/CNFs composites, PLA/PLA-g-GMA/CNFs composites with various fiber contents show significantly higher scattering intensity after 10 min of crystallization time.

The plot of maximum Iq^2 versus *crystallization time* of PLA/CNFs and PLA/PLA-g-GMA/CNFs composites with various fiber contents is shown in Figure 7.21. As can be observed from Figure 7.21 that the slope of the curves of PLA/PLA-g-GMA/CNFs composites is significantly higher than that of PLA/CNFs composites at all fiber contents. This indicates that the crystallization rate of PLA/PLA-g-GMA/CNFs is faster than that of PLA/CNFs. Moreover, as shown in Figure 7.21, increasing fiber content led to lower slope of the curves for both PLA/CNFs and PLA/PLA-g-GMA/CNFs composites, which indicates the slower crystallization rate. It is due to the agglomerations of fibers that can be formed as the fiber loading was increased (Figure

7.2). From SAXS results of PLA/CNFs and PLA/PLA-g-GMA/CNFs composites, it can be stated that the crystallization rate of PLA/PLA-g-GMA/CNFs composites is faster than that of PLA/CNFs composites at all fiber contents. It is thought that PLA-g-GMA used as a compatibilizer makes the dispersion of CNFs in PLA matrix better. The well dispersed CNFs could act as nucleating agents for the crystallization of PLA. Furthermore, it should be noted that the fiber content of 0.1 wt% was found to give the highest crystallization rate of both PLA/CNFs and PLA/PLA-g-GMA/CNFs composites. Increasing fiber content from 0.3 to 0.5 wt% did not cause any considerable difference in the crystallization rate of composites with and without using PLA-g-GMA.

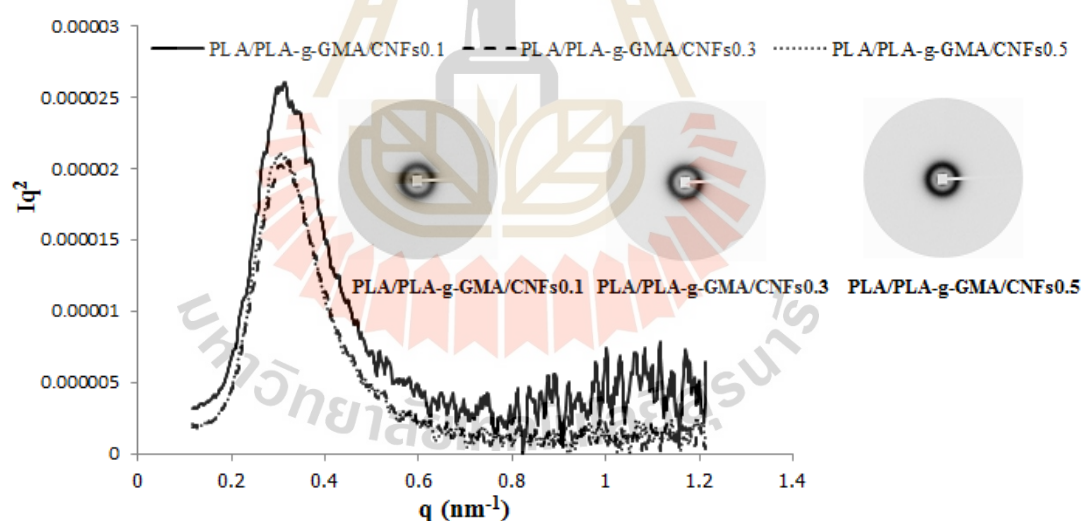


Figure 7.20 Lorentz-corrected SAXS profiles of PLA/PLA-g-GMA/CNFs composites with various fiber contents obtained at 120 °C after 10 min of crystallization time. The insets show the 2D-SAXS patterns of the respective samples.

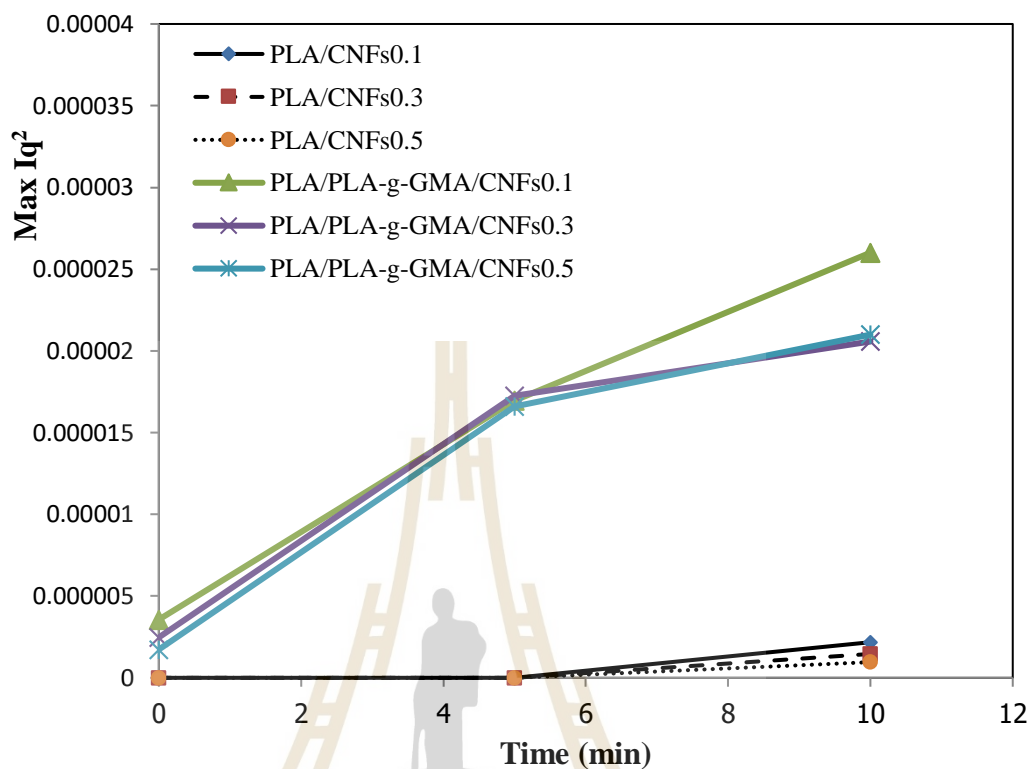


Figure 7.21 The plot of the changes of maximum Iq^2 versus *crystallization time* of PLA/CNFs and PLA/PLA-g-GMA/CNFs composites with various fiber loadings.

7.4.4 Thermal properties

Thermal stability of PLA and its composites was investigated by TGA. The residual mass % as a function of temperature for pure PLA and the composites at various fiber contents is shown in Figures (7.22 and 7.24). As observed from Figure 7.22, the TGA and DTG curves of pure PLA and PLA/CNFs composites show only one degradation step between 310 °C and 390 °C. It was observed that the thermal stability of PLA/CNFs composites was not significantly different compared to that of pure PLA.

A slight decrease of thermal stability of PLA/CNFs composites was observed as CNFs content increased from 0.1 to 0.5 wt%. This might be attributed to the higher water content induced by the presence of the cellulosic nanofiller. With the increase of fiber content, the agglomerations of fiber on the surface due to poor dispersion could accelerate the water absorption of composites. This lead to lowering the thermal stability of obtained PLA/CNFs composites (Pandey, Chu, Kim, Lee, and Ahn, 2009). In addition, the increased thermal conductivity of the polymer after cellulose nanofibers addition was also suggested as the reason for reduced thermal stability of the composites (Ten, Turtle, Bahr, Jiang, and Wolcott, 2010). Figure 7.22 also reveals that the char yield increased with the addition of CNFs.

In the case of using PLA-g-GMA as a compatibilizer, the thermal stability of PLA/PLA-g-GMA/CNFs composites was found to be higher than that of PLA/CNFs composites (Figure 7.23). This could be due to the better dispersion of CNFs and the improved interaction between PLA and fibers, which led to reducing the chain mobility. As a result, the thermal stability was enhanced. This result was in agreement with another study in which the strong hydrogen bonding between hydroxyl groups of cellulose and the PVA matrix was suggested to improve the thermal stability of the host polymer (Lee et al., 2009). Additionally, it was observed from Figure 7.24 that there was no considerable difference in thermal stability of PLA/PLA-g-GMA/CNFs composites with the increase of CNFs content. The char yield of PLA/PLA-g-GMA/CNFs composites was higher than that of pure PLA.

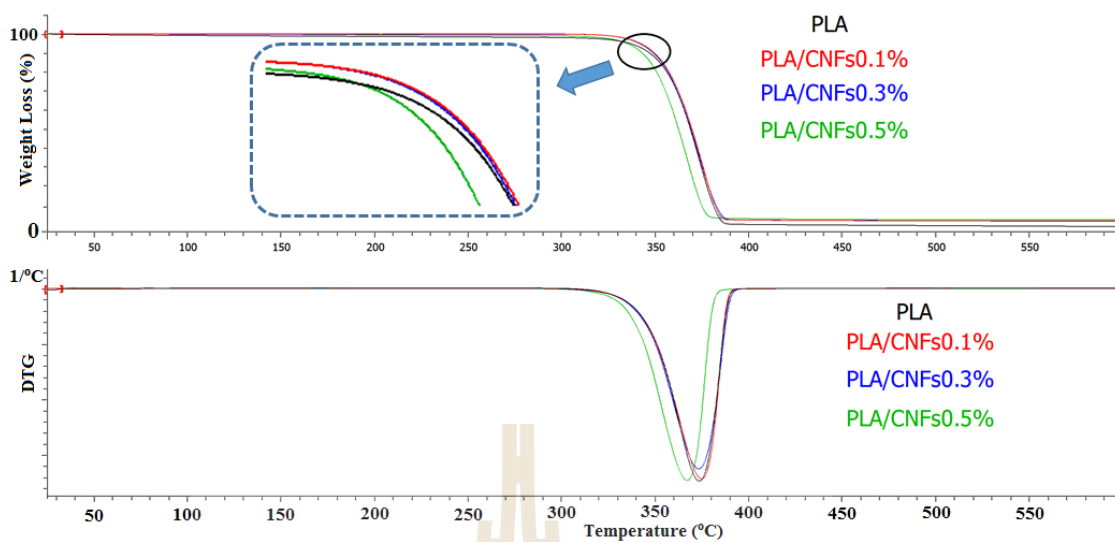


Figure 7.22 TGA and DTG curves of pure PLA and PLA/CNFs composites with different fiber loadings.

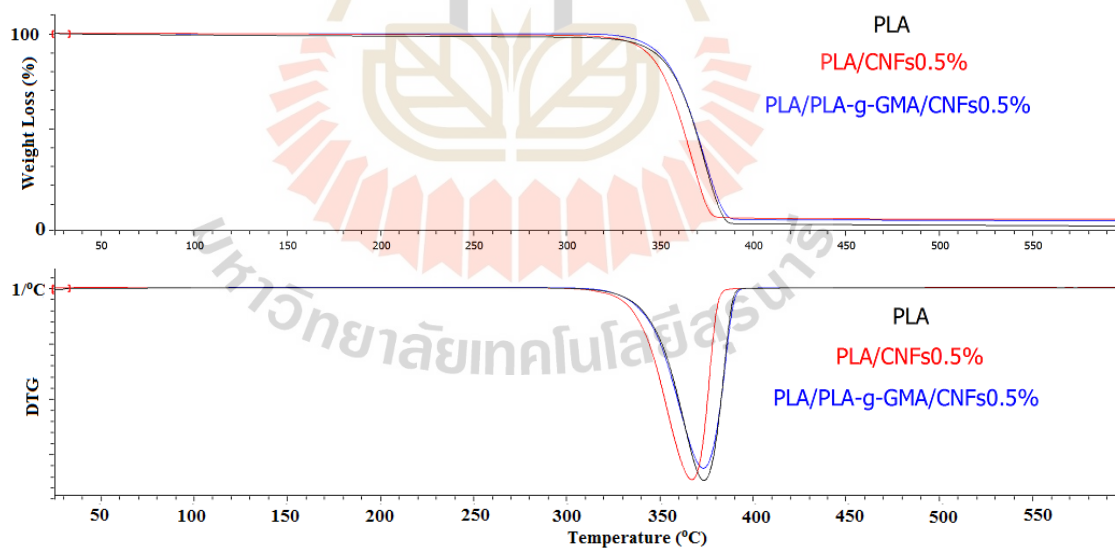


Figure 7.23 TGA and DTG curves of pure PLA, PLA/CNFs0.5, and PLA/PLA-g-GMA/CNFs0.5 composites.

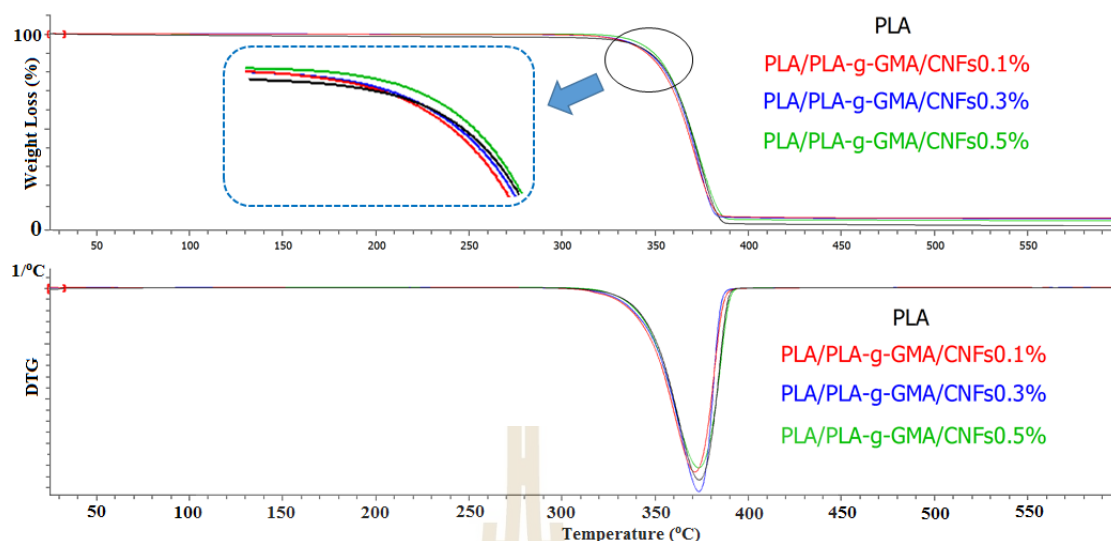


Figure 7.24 TGA and DTG curves of pure PLA and PLA/PLA-g-GMA/CNFs composites with different fiber loadings.

The non-isothermal crystallization and melting behavior of PLA and its composites were investigated by DSC. DSC thermograms of pure PLA and composites during the cooling scan are shown in Figure 7.25. From this graph, one can see that pure PLA and PLA/CNFs composites with various fiber contents did not show melt crystallization upon cooling. In contrast to that, with using PLA-g-GMA as a compatibilizer, the melt crystallization peaks were observed for all PLA/PLA-g-GMA/CNFs composites. This indicates that PLA-g-GMA induced the melt crystallization of PLA upon cooling. Furthermore, as seen in Figure 7.25, there was no significant change in crystallization temperature of the composites as fiber content was increased from 0.1 to 0.5 wt%.

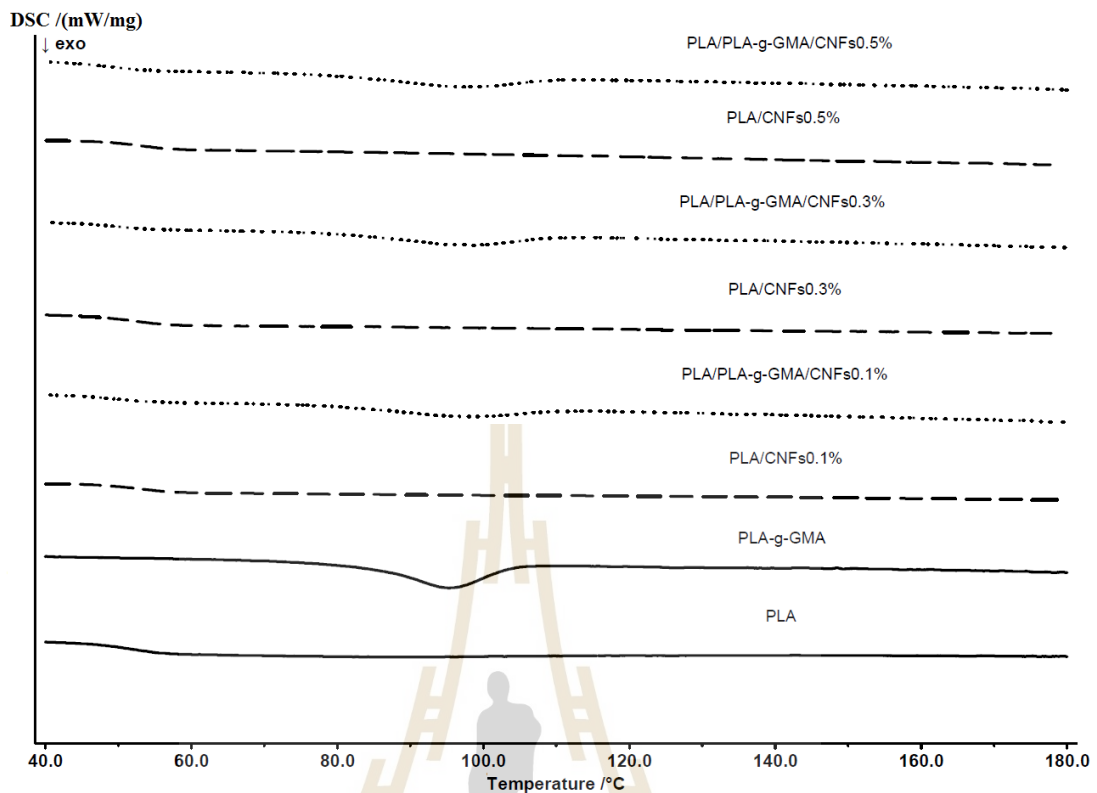


Figure 7.25 DSC thermograms of PLA and composites with various fiber loadings (cooling cycle).

Figure 7.26 shows DSC thermograms of pure PLA and its composites during the second heating scan. As observed in Figure 7.26 and Table 7.2, with the addition of CNFs, the glass transition temperature (T_g) of PLA/CNFs biocomposites slightly increased in comparison with that of pure PLA. It is due to the restriction of chain mobility with the presence of CNFs. The T_g values of PLA/CNFs biocomposites were found to not change significantly with increasing fibers content from 0,1 to 0.5 wt%. By using PLA-g-GMA as a compatibilizer, a slight decrease in T_g values of biocomposites was observed.

Moreover, it was observed from Figure 7.26 that PLA/CNFs composites exhibited a slightly higher cold crystallization temperature compared to pure PLA. This indicates that without using PLA-g-GMA as a compatibilizer, the addition of cellulose nanofibers did not induce any improvement in the crystallization rate of PLA. Nevertheless, as PLA-g-GMA was used, the broader cold crystallization peaks appeared at lower temperatures as compared to the cold crystallization of pure PLA. The lower cold crystallization temperature is an indication of faster crystallization induced by cellulose nanofibers which acted as nucleating agents for PLA (Kang, Lee, Lee, Narayan, and Shin, 2008). Cellulose nanofibers allow heterogeneous nucleation mechanism which induces a decrease of the free energy barrier and fastens the crystallization. In addition, it was observed from Figure 7.26 that the cold crystallization temperatures of PLA/CNFs and PLA/PLA-g-GMA/CNFs composites were not significantly influenced by the increase of fiber content.

The melting temperatures (T_{m1} and T_{m2}) of PLA/CNFs composites were found to be slightly higher than those of pure PLA. The lower temperature peak (T_{m1}) is attributed to the melting of crystals formed upon cooling from the melt, and the higher one (T_{m2}) corresponds to the melting of crystals generated from cold crystallization upon heating (Yasuniwa, Tsubakihara, Sugimoto, and Nakafuku, 2004). The PLA/PLA-g-GMA/CNFs composites, however, showed slightly lower melting temperatures compared to pure PLA and PLA/CNFs composites. The degree of crystallinity (X_c) calculated based on Eq. (7.9) indicated that PLA/PLA-g-GMA/CNFs composites had higher crystallinity compared to PLA/CNFs composites at all fiber loadings used. This result is consistent with the SAXS result. By using PLA-g-GMA as a compatibilizer, the crystallinity of PLA in the composites was enhanced. This

enhancement was induced by the improved dispersion of cellulose nanofibers in the PLA matrix (Figure 7.2). As a result, more crystals were able to nucleate and grow on the increased surface area of the interfaces due to a growing number of nucleating particles (Pei et al., 2010). Besides that, as can be seen from Table 7.2 the X_c values of PLA/CNFs and PLA/PLA-g-GMA/CNFs composites did not change significantly with the increase of fiber content from 0.1 to 0.5 wt%. The values of T_g , enthalpy of crystallization (ΔH_c), enthalpy of cold crystallization (ΔH_{cc}), enthalpy of melting (ΔH_m), crystallization temperature (T_c), cold crystallization temperature (T_{cc}), melting temperatures (T_{m1} and T_{m2}), and degree of crystallinity ($\%X_c$) of pure PLA and composites are shown in Table 7.2.

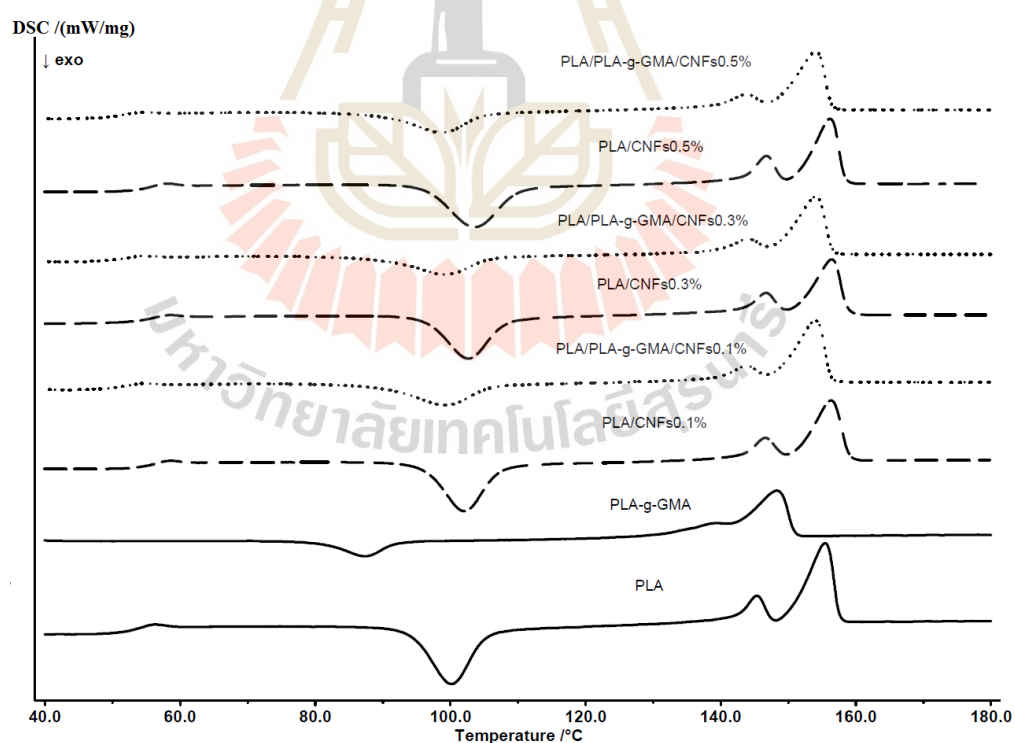


Figure 7.26 DSC thermograms of PLA and composites with various fiber loadings (second heating cycle).

Table 7.2 Thermal properties of the pure PLA, PLA-g-GMA, and composites with different fiber contents.

Sample	Thermal properties								
	T_g (°C)	T_c (°C)	T_{cc} (°C)	T_{m1} (°C)	T_{m2} (°C)	ΔH_c (J/g)	ΔH_{cc} (J/g)	ΔH_m (J/g)	$\%X_c$ (%)
PLA	53.9	-	100.2	145.3	155.5	-	29.80	31.23	33.33
PLA-g-GMA	39.5	95.4	87.3	139.4	148.3	11.35	7.20	22.96	24.50
PLA/CNFs0.1	55.6	-	102.1	146.7	156.3	-	22.04	24.87	26.57
PLA/CNFs0.3	55.8	-	102.7	146.8	156.4	-	20.23	21.83	23.37
PLA/CNFs0.5	56.1	-	103.7	146.7	156.2	-	22.19	25.17	27.00
PLA/PLA-g-GMA/CNFs0.1	52.7	98.1	99.3	143.9	154.0	3.83	10.97	25.44	33.98
PLA/PLA-g-GMA/CNFs0.3	53.3	98.1	99.3	144.0	154.0	4.41	9.09	23.45	31.40
PLA/PLA-g-GMA/CNFs0.5	53.5	98.1	98.8	143.8	154.1	4.39	10.87	23.98	32.19

7.4.5 Mechanical properties

The mechanical properties of PLA and its composites are shown in Figures (7.27-7.30). Figure 7.27 shows the tensile modulus of pure PLA and its composites at various fiber contents. The tensile modulus of PLA increased 5.9 % from 846 MPa to 896 MPa with the addition of 0.5 wt% cellulose nanofibers without using PLA-g-GMA. This can be associated with the restrictions of macromolecular mobility and deformability imposed by the presence of CNFs. The tensile modulus of PLA/CNFs composites increased with increasing CNFs loading because the increase in CNFs content restricted the mobility of the PLA chains. With using PLA-g-GMA as a compatibilizer, the tensile modulus of composites was slightly improved (reached a value of 940 MPa with the addition of 0.5 wt% CNFs). The increased composite stiffness depends on the CNF content and uniformity of reinforcement dispersion (Tawakkal, Talib, Abdan, and Ling, 2012). In this case, the enhanced tensile modulus

of PLA/PLA-g-GMA/CNFs composites can be attributed to the better dispersion of CNFs nanofillers due to the presence of PLA-g-GMA (Figure 7.2).

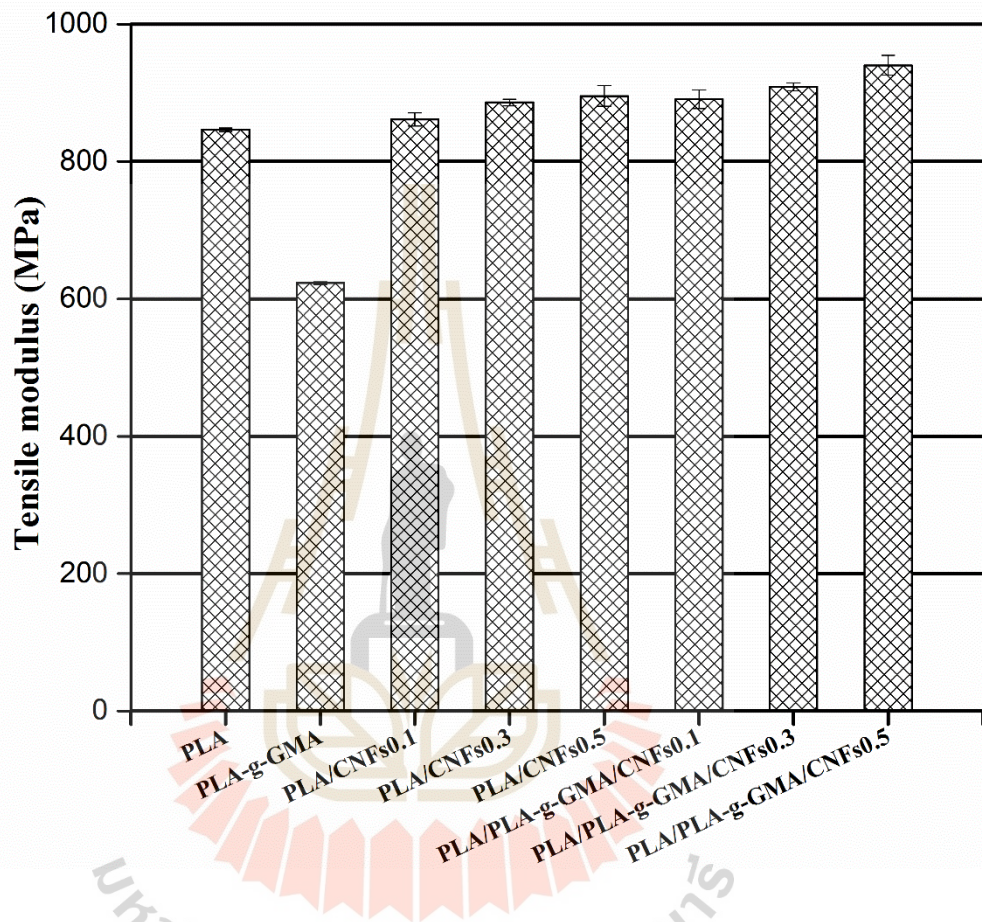


Figure 7.27 Tensile modulus of PLA, PLA-g-GMA, and composites with different fiber loadings.

The tensile strength of pure PLA and its composites is shown in Figure 7.28. Compared to PLA, the PLA/CNFs composites did not show any improvements in tensile strength. This is due to the poor interfacial adhesion between CNFs and PLA matrix (Figure 7.3). Bitinis et al. (2013) also reported tensile strength was maintained

or lowered with the addition of unmodified and modified cellulose nanofibers in PLA/natural rubber (NR) blend when NR was fixed at 10 wt% and the CNFs loading was varied from 1 to 5 wt%. As observed in Figure 7.28, by using PLA-g-GMA, the tensile strength of PLA/PLA-g-GMA/CNFs composites was found to be slightly improved as compared to that of PLA/CNFs composites at all used fiber loadings (with the addition of only 0.1 wt% CNFs in PLA resulted in a 5.2 % increase in the tensile strength compared to pure PLA). The reason for the improvement in tensile strength can be attributed to the better dispersion of CNFs and the enhanced interfacial adhesion between PLA and CNFs as PLA-g-GMA was used as a compatibilizer (Figure 7.2e). This reduces the voids at the fiber-matrix interface and allows better stress transfer from the PLA matrix to the CNFs. Additionally, the slightly increased degree of crystallinity (Table 7.2) also contributed to the improvement of tensile strength of PLA/PLA-g-GMA/CNFs composites. Figure 7.28 also shows that increasing fiber content from 0.1 to 0.5 wt% did not cause a significant change in the tensile strength of PLA/PLA-g-GMA/CNFs composites. The tensile strength of PLA/PLA-g-GMA/CNFs composites slightly decreased with increasing fiber content.

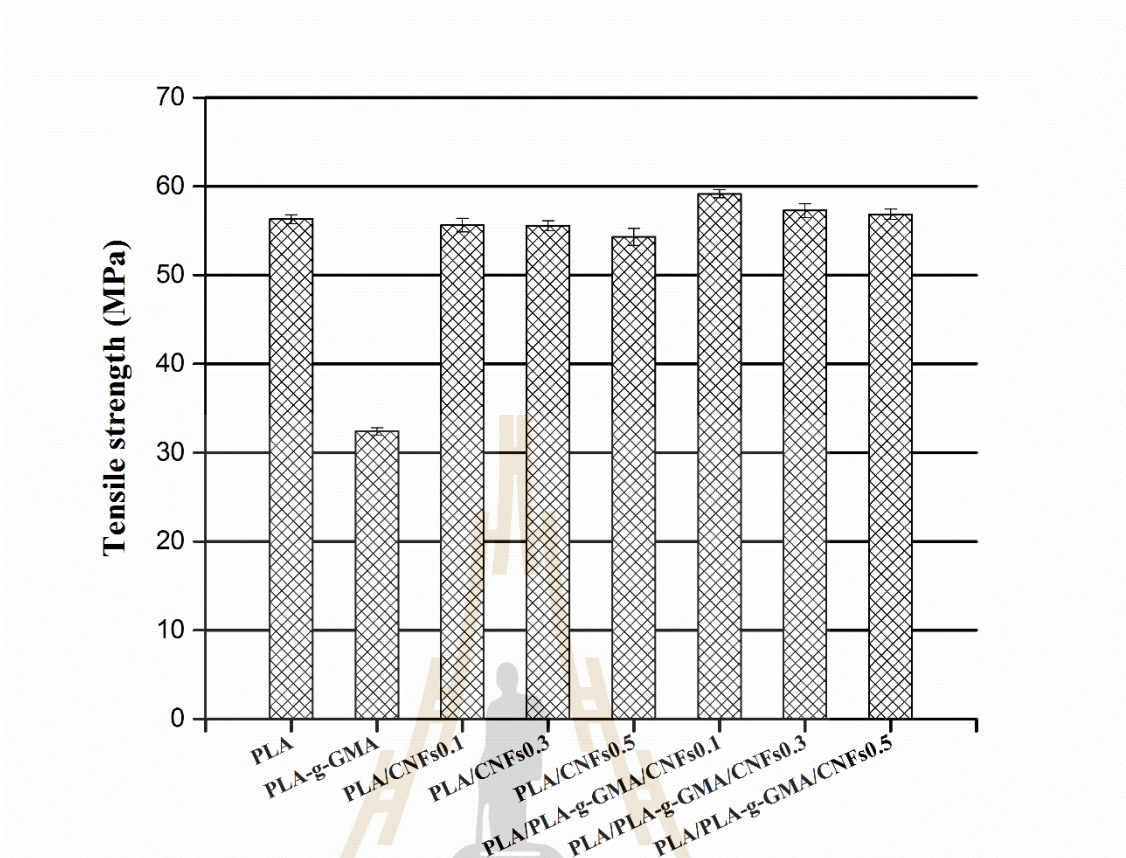


Figure 7.28 Tensile strength of PLA, PLA-g-GMA, and composites with different fiber loadings.

Figure 7.29 shows that there was no significant difference in elongation at break of pure PLA and PLA/CNFs composites. The elongation at break slightly lowered with the increase of fiber loading. With using PLA-g-GMA as a compatibilizer, the elongation at break of PLA/PLA-g-GMA/CNFs composites did not show considerable improvement in relation to that of PLA/CNFs composites.

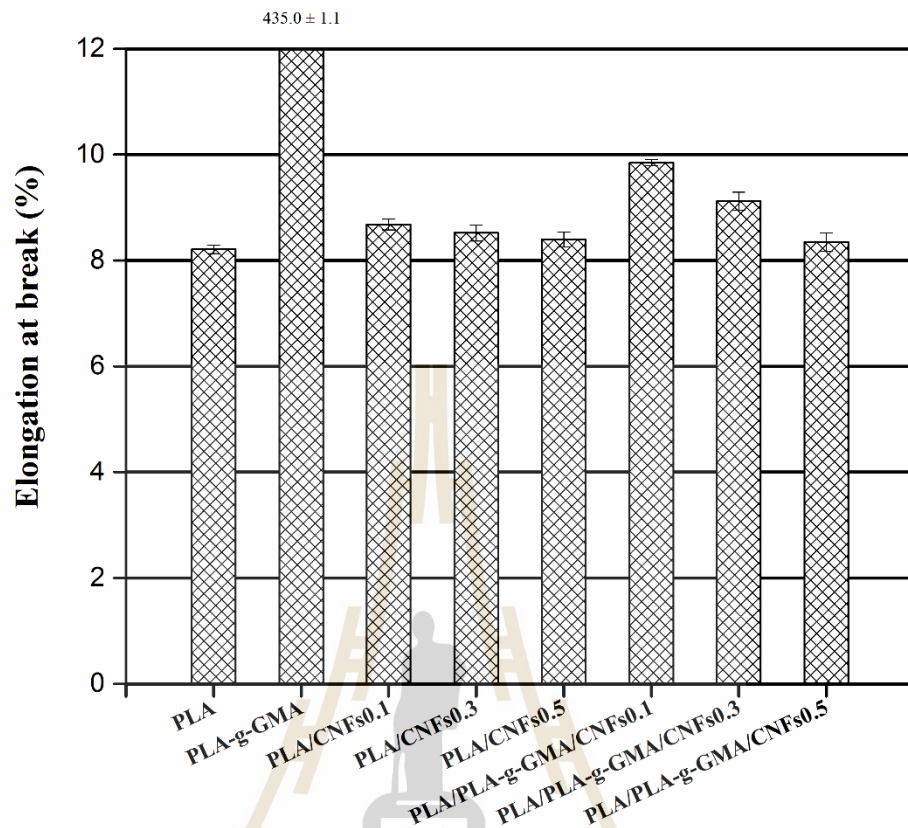


Figure 7.29 Elongation at break of PLA, PLA-g-GMA, and composites with different fiber loadings.

The impact strength of pure PLA and its composites is shown in Figure 7.30. The impact strength of PLA/CNFs composites was higher than that of pure PLA, particularly for the composites with low fiber content (0.1 wt% and 0.3 wt%). With increasing fiber loading from 0.1 to 0.5 wt%, the impact strength of PLA/CNFs composites decreased. This is due to the poor dispersion of CNFs in PLA matrix as CNFs content was increased (Figure 7.2). This might result in stress concentration regions that require less energy to initiate cracks. With the addition of PLA-g-GMA,

the impact strength of composites was improved. The PLA/PLA-g-GMA/CNFs0.1 composite achieved the highest impact strength (22.6 kJ/m²) with a 41 % and 7.6 % increase compared to pure PLA and PLA/CNFs0.1 composite, respectively. This improvement can be attributed to the better dispersion of CNFs with the presence of PLA-g-GMA. The well-dispersed CNFs acted as a nucleating agent and increased the crystallization rate of PLA, resulting in a reduction in PLA spherulite size. As a result, the impact strength of composites was enhanced. This result was in agreement with SAXS result.

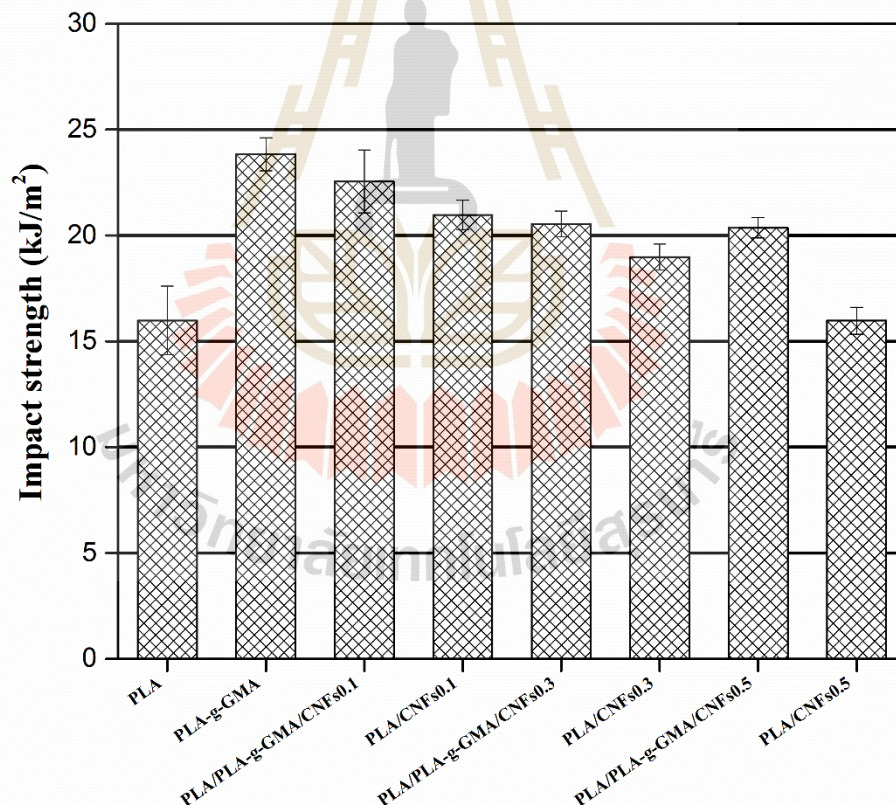


Figure 7.30 Impact strength of PLA, PLA-g-GMA, and composites with different fiber loadings.

7.5 Conclusions

The PLA composites with various cellulose nanofibers contents were prepared by melt mixing using an internal mixer. The PLA-g-GMA was used as a compatibilizer to enhance the interfacial adhesion between fibers and PLA matrix.

The morphology studies by SEM of pure PLA and its composites showed that by using PLA-g-GMA as a compatibilizer, the better dispersion of fibers, as well as the enhanced interfacial adhesion between fibers and PLA, were achieved. However, some visible microscale agglomerations of CNFs were observed as fiber loading was increased up to 0.5 wt%. Compared to the tensile fractured surfaces of PLA/CNFs composites, the tensile fractured surfaces of PLA/PLA-g-GMA/CNFs composites were smoother at all studied fiber loadings.

The synchrotron SAXS study indicated that by the addition of only 0.1 wt% cellulose nanofibers and using PLA-g-GMA as a compatibilizer, the crystallization rate of PLA in composites was enhanced considerably. Moreover, the DSC study also showed that the cold crystallization peak of PLA/PLA-g-GMA/CNFs composites was shifted to a lower temperature as compared to pure PLA and PLA/CNFs composites with a slight improvement in the degree of crystallinity for PLA/PLA-g-GMA/CNFs0.1 composite. These results demonstrated the role of the well-dispersed cellulose nanofibers as nucleating agents, which enhanced the crystallization rate of PLA. Increasing fiber content from 0.1 to 0.5 wt% led to the decrease of the crystallization rate of composites with and without using PLA-g-GMA.

The evaluation of the mechanical properties of PLA and its composites showed that the addition of only 0.1 wt% cellulose nanofibers with using PLA-g-GMA as a compatibilizer resulted in a 5.3 % increase in the tensile modulus, a 5.2 % increase in

the tensile strength, a 21 % increase in the elongation at break, and a 41 % increase in the impact strength of composites compared to those of pure PLA.

This work indicates that the melt compounding of PLA with a small content of cellulose nanofibers using PLA-g-GMA as a compatibilizer is a quite promising method to achieve the improved crystallization rate and mechanical properties of PLA.

7.6 References

- Ahmad, E., and Luyt, A. (2012). Morphology, thermal, and dynamic mechanical properties of poly (lactic acid)/sisal whisker nanocomposites. **Polymer Composites**. 33: 1025-1032.
- Arias, A., Heuzey, M.-C., Huneault, M. A., Ausias, G., and Bendahou, A. (2015). Enhanced dispersion of cellulose nanocrystals in melt-processed polylactide-based nanocomposites. **Cellulose**. 22: 483-498.
- Bitinis, N., et al. (2013). Poly (lactic acid)/natural rubber/cellulose nanocrystal bionanocomposites Part I. Processing and morphology. **Carbohydrate Polymers**. 96: 611-620.
- Bondeson, D., and Oksman, K. (2007). Dispersion and characteristics of surfactant modified cellulose whiskers nanocomposites. **Composite Interfaces**. 14: 617-630.
- Cheung, H.-Y., Lau, K.-T., Tao, X.-M., and Hui, D. (2008). A potential material for tissue engineering: Silkworm silk/PLA biocomposite. **Composites Part B: Engineering**. 39: 1026-1033.

- Cho, J., et al. (2003). Crystallization and structure formation of poly(l-lactide-co-meso-lactide) random copolymers: a time-resolved wide- and small-angle X-ray scattering study. **Polymer**. 44: 711-717.
- Crist, B. (1973). Small-angle x-ray scattering of semicrystalline polymers. I. Review of existing models. **Journal of Polymer Science: Polymer Physics Edition**. 11: 635-661.
- Dismore, P., and Statton, W. (1966). **Small-angle scattering from fibrous and partially oriented systems**. New York: Interscience.
- Espino-Pérez, E., et al. (2013). Influence of chemical surface modification of cellulose nanowhiskers on thermal, mechanical, and barrier properties of poly (lactide) based bionanocomposites. **European Polymer Journal**. 49: 3144-3154.
- Frone, A. N., Berlioz, S., Chailan, J.-F., and Panaitescu, D. M. (2013). Morphology and thermal properties of PLA–cellulose nanofibers composites. **Carbohydrate Polymers**. 91: 377-384.
- Glatter, O., and Kratky, O. (1982). **Small angle X-ray scattering**. Massachusetts: Academic press.
- Ivanov, D. A., Amalou, Z., and Magonov, S. N. (2001). Real-time evolution of the lamellar organization of poly(ethylene terephthalate) during crystallization from the melt: high-temperature atomic force microscopy study. **Macromolecules**. 34: 8944-8952.
- Ivanov, D. A., Legras, R., and Jonas, A. M. (1999). Interdependencies between the evolution of amorphous and crystalline regions during isothermal cold crystallization of poly(ether–ether–ketone). **Macromolecules**. 32: 1582-1592.

- John, M. J., and Thomas, S. (2008). Biofibres and biocomposites. **Carbohydrate Polymers**. 71: 343-364.
- Jonoobi, M., Harun, J., Mathew, A. P., and Oksman, K. (2010). Mechanical properties of cellulose nanofiber (CNF) reinforced polylactic acid (PLA) prepared by twin screw extrusion. **Composites Science and Technology**. 70: 1742-1747.
- Kang, K. S., Lee, S. I., Lee, T. J., Narayan, R., and Shin, B. Y. (2008). Effect of biobased and biodegradable nucleating agent on the isothermal crystallization of poly (lactic acid). **Korean Journal of Chemical Engineering**. 25: 599-608.
- Koberstein, J. T., and Stein, R. S. (1983). Small-angle x-ray scattering measurements of diffuse phase-boundary thicknesses in segmented polyurethane elastomers. **Journal of Polymer Science: Polymer Physics Edition**. 21: 2181-2200.
- Lee, B., et al. (2004). Secondary crystallization behavior of poly (ethylene isophthalate-co-terephthalate): Time-resolved small-angle X-ray scattering and calorimetry studies. **Macromolecules**. 37: 4174-4184.
- Lee, B., et al. (2003). Time-resolved X-ray scattering and calorimetric studies on the crystallization behaviors of poly(ethylene terephthalate) (PET) and its copolymers containing isophthalate units. **Polymer**. 44: 2509-2518.
- Lee, S.-Y., et al. (2009). Nanocellulose reinforced PVA composite films: effects of acid treatment and filler loading. **Fibers and Polymers**. 10: 77-82.
- Lin, N., Huang, J., Chang, P. R., Feng, J., and Yu, J. (2011). Surface acetylation of cellulose nanocrystal and its reinforcing function in poly (lactic acid). **Carbohydrate Polymers**. 83: 1834-1842.

- Luo, J., et al. (2011). Mechanisms of nucleation and crystal growth in a nascent isotactic polypropylene/poly (ethylene-co-octene) in-reactor alloy investigated by temperature-resolved synchrotron SAXS and DSC methods. **Polymer**. 52: 4590-4599.
- Mohanty, A., Misra, M., and Hinrichsen, G. (2000). Biofibres, biodegradable polymers and biocomposites: an overview. **Macromolecular Materials and Engineering**. 276: 1-24.
- Nguyen, T. C., Ruksakulpiwat, C., and Ruksakulpiwat, Y. (2016). The study on the grafting of glycidyl methacrylate onto poly(lactic acid) in an internal mixer. **Walailak Journal of Science and Technology (WJST)**. 13: 1037-1046.
- Oksman, K., Skrifvars, M., and Selin, J.-F. (2003). Natural fibres as reinforcement in polylactic acid (PLA) composites. **Composites Science and Technology**. 63: 1317-1324.
- Pandey, J., Chu, W., Kim, C., Lee, C., and Ahn, S. (2009). Bio-nano reinforcement of environmentally degradable polymer matrix by cellulose whiskers from grass. **Composites Part B: Engineering**. 40: 676-680.
- Pei, A., Zhou, Q., and Berglund, L. A. (2010). Functionalized cellulose nanocrystals as biobased nucleation agents in poly (l-lactide)(PLLA)-crystallization and mechanical property effects. **Composites Science and Technology**. 70: 815-821.
- Raquez, J.-M., et al. (2012). Surface-modification of cellulose nanowhiskers and their use as nanoreinforcers into polylactide: a sustainably-integrated approach. **Composites Science and Technology**. 72: 544-549.

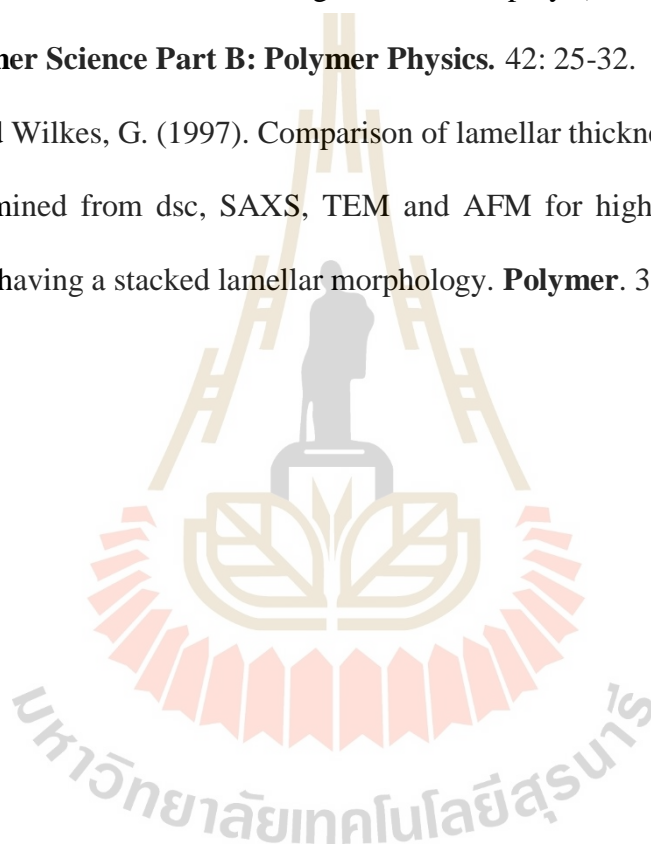
- Rastogi, S., Goossens, J. G. P., and Lemstra, P. J. (1998). An in situ SAXS/WAXS/Raman spectroscopy study on the phase behavior of syndiotactic polystyrene (sPS)/solvent systems: compound formation and solvent (dis)ordering. **Macromolecules**. 31: 2983-2998.
- Ruangudomsakul, W., Ruksakulpiwat, C., and Ruksakulpiwat, Y. (2015). Preparation and characterization of cellulose nanofibers from cassava pulp. **Macromolecular Symposia**. 354: 170-176.
- Sanchez-Garcia, M. D., and Lagaron, J. M. (2010). On the use of plant cellulose nanowhiskers to enhance the barrier properties of polylactic acid. **Cellulose**. 17: 987-1004.
- Soontaranon, S., and Rugmai, S. (2012). Small angle X-ray scattering at Siam photon laboratory. **Chinese Journal of Physics**. 50: 204-210.
- Sriroth, K., Chollakup, R., Chotineeranat, S., Piyachomkwan, K., and Oates, C. G. (2000). Processing of cassava waste for improved biomass utilization. **Bioresource Technology**. 71: 63-69.
- Sriroth, K., et al. (1999). Cassava starch granule structure–function properties: influence of time and conditions at harvest on four cultivars of cassava starch. **Carbohydrate Polymers**. 38: 161-170.
- Tawakkal, I. S. M., Talib, R. A., Abdan, K., and Ling, C. N. (2012). Mechanical and physical properties of kenaf-derived cellulose (KDC)-filled polylactic acid (PLA) composites. **BioResources**. 7: 1643-1655.
- Teixeira, E. d. M., et al. (2012). Properties of thermoplastic starch from cassava bagasse and cassava starch and their blends with poly (lactic acid). **Industrial Crops and Products**. 37: 61-68.

- Ten, E., Turtle, J., Bahr, D., Jiang, L., and Wolcott, M. (2010). Thermal and mechanical properties of poly (3-hydroxybutyrate-co-3-hydroxyvalerate)/cellulose nanowhiskers composites. **Polymer**. 51: 2652-2660.
- Vaǐnshteĭn, B. K. (1966). **Diffraction of X-rays by chain molecules**. New York: Elsevier.
- Verma, R., Marand, H., and Hsiao, B. (1996). Morphological changes during secondary crystallization and subsequent melting in poly (ether ether ketone) as studied by real time small angle X-ray scattering. **Macromolecules**. 29: 7767-7775.
- Vonk, C. G., and Kortleve, G. (1967). X-ray small-angle scattering of bulk polyethylene. **Kolloid-Z.u.Z.Polymere**. 220: 19-24.
- Wambua, P., Ivens, J., and Verpoest, I. (2003). Natural fibres: can they replace glass in fibre reinforced plastics? **Composites Science and Technology**. 63: 1259-1264.
- Wang, Z.-G., et al. (2001). Time-resolved isothermal crystallization of absorbable PGA-co-PLA copolymer by synchrotron small-angle X-ray scattering and wide-angle X-ray diffraction. **Polymer**. 42: 8965-8973.
- Wang, Z.-G., Hsiao, B., Sauer, B., and Kampert, W. (1999). The nature of secondary crystallization in poly (ethylene terephthalate). **Polymer**. 40: 4615-4627.
- Xia, Z., Sue, H.-J., Wang, Z., Avila-Orta, C. A., and Hsiao, B. S. (2001). Determination of crystalline lamellar thickness in poly (ethylene terephthalate) using small-angle X-ray scattering and transmission electron microscopy. **Journal of Macromolecular Science, Part B**. 40: 625-638.

Xu, T., Tang, Z., and Zhu, J. (2012). Synthesis of polylactide-graft-glycidyl methacrylate graft copolymer and its application as a coupling agent in polylactide/bamboo flour biocomposites. **Journal of Applied Polymer Science**. 125: E622-E627.

Yasuniwa, M., Tsubakihara, S., Sugimoto, Y., and Nakafuku, C. (2004). Thermal analysis of the double-melting behavior of poly (L-lactic acid). **Journal of Polymer Science Part B: Polymer Physics**. 42: 25-32.

Zhou, H., and Wilkes, G. (1997). Comparison of lamellar thickness and its distribution determined from dsc, SAXS, TEM and AFM for high-density polyethylene films having a stacked lamellar morphology. **Polymer**. 38: 5735-5747.



CHAPTER VIII

CONCLUSIONS

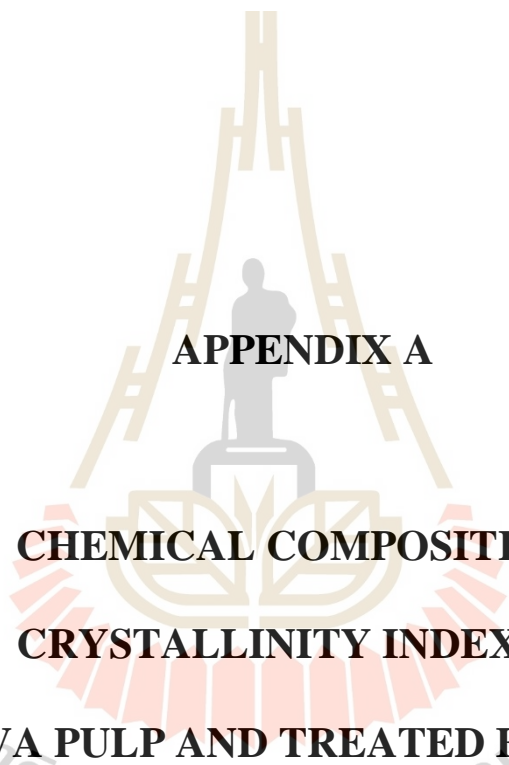
In this research, crystalline cellulose fibers were directly extracted from cassava pulp without any purification by using sulfuric acid hydrolysis treatment. After hydrolysis, both the cellulose content and crystallinity of the fibers increased. However, the thermal stability of treated fibers was found to be lower than that of untreated cassava pulp. The influence of hydrolysis time and temperature on the crystallinity and thermal stability of obtained fibers was investigated. The crystallinity of acid treated fibers did not change significantly with the increase of hydrolysis time and temperature. On the other hand, the thermal stability of treated fibers decreased continuously with the increase of hydrolysis time and temperature. Cellulose microfibrils with a diameter of around 5 μm were successfully prepared from cassava pulp by a combination of alkali and acid hydrolysis treatments. By alkali treatment, amorphous non-cellulosic constituents of cassava pulp fibers were removed partially while starch component was eliminated from the fibers by acid treatment. The chemical composition result showed that the cellulose content of obtained cellulose microfibrils was significantly higher than that of untreated cassava pulp. The results from XRD and TGA analyses revealed the considerably higher crystallinity and thermal stability of chemically treated fibers compared to those of untreated cassava pulp. The effect of the sequence of alkali treatment and acid treatment on crystallinity and thermal stability of cellulose microfibrils was investigated. The crystallinity of alkali-acid treated fibers was slightly

higher than that of acid-alkali treated fibers. Nevertheless, the thermal stability of acid-alkali treated fibers was found to be higher than that of alkali-acid treated fibers. Cellulose nanofibers were extracted successfully from cassava pulp by submitting to alkali, bleaching and acid hydrolysis treatments. The TEM and diameter distribution results indicated that most of the CNFs had a diameter in the range of 12-24 nm and immeasurable length. From the chemical composition data, it was confirmed that hemicellulose was removed partially by alkali treatment while lignin was eliminated efficiently by bleaching treatment. By using a mixture of HCl/H₂SO₄ (1:2 v/v) as the hydrolysis reagent, a significant increase in the crystallinity degree of CNFs in relation to that of untreated cassava pulp fibers was observed. On the other hand, the thermal stability of CNFs was lower than that of untreated fibers. The influences of acid nature, acid concentration, acid/pulp ratio and hydrolysis time on the crystallinity and thermal stability of CNFs were elucidated. With the same conditions, using H₂SO₄ or a mixture of HCl/H₂SO₄ as the hydrolysis reagent resulted in the higher crystallinity of nanofibers compared to that of ones hydrolyzed using HCl. Meanwhile, the thermal stability of nanofibers hydrolyzed using HCl was significantly superior to that of ones hydrolyzed using H₂SO₄ or a mixture of HCl/H₂SO₄. With the same hydrolysis reagent (a mixture of HCl/H₂SO₄ (1:2 v/v)) and a given hydrolysis time, the increase in acid concentration and acid/pulp ratio resulted in nanofibers with higher crystallinity degree and reduction in thermal stability at certain conditions (7.5 M and 200ml/2g, respectively). With the given acid concentration and acid/pulp ratio, a significant drop at a particular hydrolysis time (90 min) in the crystallinity and thermal stability of nanofibers was observed. Glycidyl methacrylate was grafted onto PLA by melt mixing method using dicumyl peroxide (DCP) as an initiator. From the GPC results, it was found that weight-average

molecular weight of PLA-g-GMA was higher than that of PLA. It implied that degradation of PLA chains did not occur during grafting reaction. The elongation at break and impact strength of PLA-g-GMA were found to be significantly higher than those of PLA. After grafting, particularly the brittle behavior of amorphous PLA was changed to the ductile behavior of semicrystalline PLA-g-GMA. The effects of GMA content and mixing time on physical properties of PLA-g-GMA were studied. With the GMA content of 10 wt% and mixing time of 10 min, the highest elongation at break and impact strength of PLA-g-GMA were shown. PLA/CNFs composites were prepared by melt compounding. The influences of CNFs and CNFs content on the crystallization behavior and mechanical, morphological and thermal properties of PLA/CNFs composites were investigated. The results from SAXS analysis indicated that with the addition of CNFs, the crystallization rate of PLA in the PLA/CNFs composites was slightly improved. Nonetheless, the crystallization rate of PLA/CNFs composites was not affected considerably by CNFs content. The impact strength of PLA/CNFs composites was enhanced with the addition of CNFs. On the other hand, there was no significant change in the tensile strength, elongation at break, and thermal stability of PLA/CNFs composites in relation to those of PLA. PLA-g-GMA was used as a compatibilizer for PLA/CNFs composites. The effects of PLA-g-GMA on the crystallization behavior and morphological, mechanical, and thermal properties of PLA/CNFs composites were elucidated. With the addition of PLA-g-GMA, the better dispersion of CNFs and the improved PLA-CNFs adhesion were observed by SEM micrographs. The SAXS and DSC results showed that the crystallization rate of PLA in PLA/PLA-g-GMA/CNFs composites was significantly higher than that of neat PLA and PLA/CNFs composites. Through these results, the role of the well-dispersed

cellulose nanofibers as nucleating agents enhancing the crystallization rate of PLA was proved. The addition of only 0.1 wt% CNFs and using PLA-g-GMA as a compatibilizer resulted in a 41 % increase in the impact strength of composites compared to that of neat PLA. Moreover, with the addition of PLA-g-GMA, a slight improvement in the tensile strength and elongation at break of composites was observed.

In general, the reinforcement efficiency of CNFs in these composite systems is relatively low. It is due to the relatively poor dispersion and distribution of CNFs in PLA matrix and low fiber content used. It should be noted that because of the strong hydrogen bonds between CNFs, CNFs have tendency to agglomerate during drying. Therefore, dispersing CNFs into PLA matrix by melt compounding is a big challenge in this research field. For future works, the investigation on improving the dispersion and distribution of CNFs in melt-processed PLA-based biocomposites should be implemented. Some approaches such as using a master batch of PLA/CNFs, a surfactant, and a miscible polymer carrier (PEO) are worthwhile to investigate. Moreover, the works on enhancement of thermal stability of CNFs should be carried out. Using a weak base to neutralize the sulfate groups on the surface of CNFs is suggested.



APPENDIX A

**CHEMICAL COMPOSITION,
CRYSTALLINITY INDEX OF
CASSAVA PULP AND TREATED FIBERS, AND
FULL-RANGE ^{13}C -NMR SPECTRA OF GMA AND
PLA-g-GMA**

Table A1 Chemical composition of untreated cassava pulp and treated fibers at various stages of treatment.

Sample	NDF	ADF	ADL	Lignocellulose			Non Lignocellulose (%)
				Cellulose (%)	Lignin (%)	Hemicellulose (%)	
Cassava pulp	33.2898	24.6509	3.5329	21.1180	3.5329	8.6389	66.7102
Alkali treated fibers	76.0028	69.0166	3.1341	65.8825	3.1341	6.9862	23.9972
Bleaching treated fibers	86.1279	79.3045	1.0231	78.2814	1.0231	6.8234	13.8721
Acid treated fibers_H ₂ SO ₄	75.1866	68.0868	3.2812	64.8055	3.2812	7.0998	24.8134
Acid treated fibers_HCl	74.3692	67.3223	3.2547	64.0676	3.2547	7.0469	25.6308
Acid-alkali treated fibers	80.9459	74.1545	2.9411	71.2134	2.9411	6.7914	19.0541
Alkali-acid treated fibers	81.9347	75.1286	2.8341	72.2945	2.8341	6.8060	18.0653

Table A2 Intensity and crystallinity index of cassava pulp and crystalline cellulose fibers at different hydrolysis temperatures and times.

Sample	2 theta (degree)		Intensity (a.u)		Crystallinity Index (%)
	I_{am}	I_{002}	I_{am}	I_{002}	
Raw cassava pulp	19.412	22.963	2498	3186	21.59
CCFs-50	18.903	22.191	1391	2366	41.21
CCFs-60	18.652	21.845	1259	2277	44.71
CCFs-70	18.862	22.155	1560	2786	44.01
CCFs-30min	18.929	21.988	1333	2398	44.41
CCFs-60min	18.905	22.377	1175	2137	45.02

Table A3 Intensity and crystallinity index of cassava pulp and cellulose microfibrils at different stages of treatment.

Sample	2 theta (degree)		Intensity (a.u)		Crystallinity Index (%)
	I_{am}	I_{002}	I_{am}	I_{002}	
Raw cassava pulp	19.412	22.963	2498	3186	21.59
Alkali treated	18.595	22.179	2535	4750	46.63
Acid treated	18.779	22.318	2093	4267	50.95
Alkali-acid treated	18.984	22.417	3624	9766	62.89
Acid-alkali treated	18.771	22.339	2518	5884	57.21

Table A4 Intensity and crystallinity index of cassava pulp and cellulose nanofibers at different stages of treatment.

Sample	2 theta (degree)		Intensity (a.u)		Crystallinity Index (%)
	I_{am}	I_{002}	I_{am}	I_{002}	
Raw cassava pulp	19.412	22.963	2498	3186	21.59
Alkali treated	18.595	22.179	2535	4750	46.63
Bleaching treated fibers	18.616	22.357	658	1983	66.82
Cellulose nanofibers	19.107	22.030	67.5	265	74.53

Table A5 Crystallinity index of cellulose nanofibers extracted using three different types of acid.

Sample	2 theta (degree)		Intensity (a.u)		Crystallinity Index (%)
	I_{am}	I_{002}	I_{am}	I_{002}	
CNFs-H	18.780	22.481	734	1958	62.51
CNFs-HS	19.107	22.030	67.5	265	74.53
CNFs-S	19.065	22.439	1256	5421	76.83

Table A6 Crystallinity index of cellulose nanofibers at various acid/pulp ratios.

Sample	2 theta (degree)		Intensity (a.u)		Crystallinity Index (%)
	I_{am}	I_{002}	I_{am}	I_{002}	
CNFs-100ml/2g	18.432	22.182	42	144	70.83
CNFs-150ml/2g	19.107	22.030	67.5	265	74.53
CNFs-200ml/2g	18.225	22.214	54.9	239	77.03

Table A7 Crystallinity index of cellulose nanofibers at various hydrolysis times.

Sample	2 theta (degree)		Intensity (a.u)		Crystallinity Index (%)
	I_{am}	I_{002}	I_{am}	I_{002}	
CNFs-30min	18.553	22.285	65.8	205	67.90
CNFs-60min	19.107	22.030	67.5	265	74.53
CNFs-90min	18.288	21.988	64.6	219	70.50

Table A8 Crystallinity index of cellulose nanofibers at various acid concentrations.

Sample	2 theta (degree)		Intensity (a.u)		Crystallinity Index (%)
	I_{am}	I_{002}	I_{am}	I_{002}	
CNFs-5.5M	19.128	22.627	951	2848	66.61
CNFs-6.5M	19.107	22.030	67.5	265	74.53
CNFs-7.5M	18.575	22.153	50.2	200	74.90

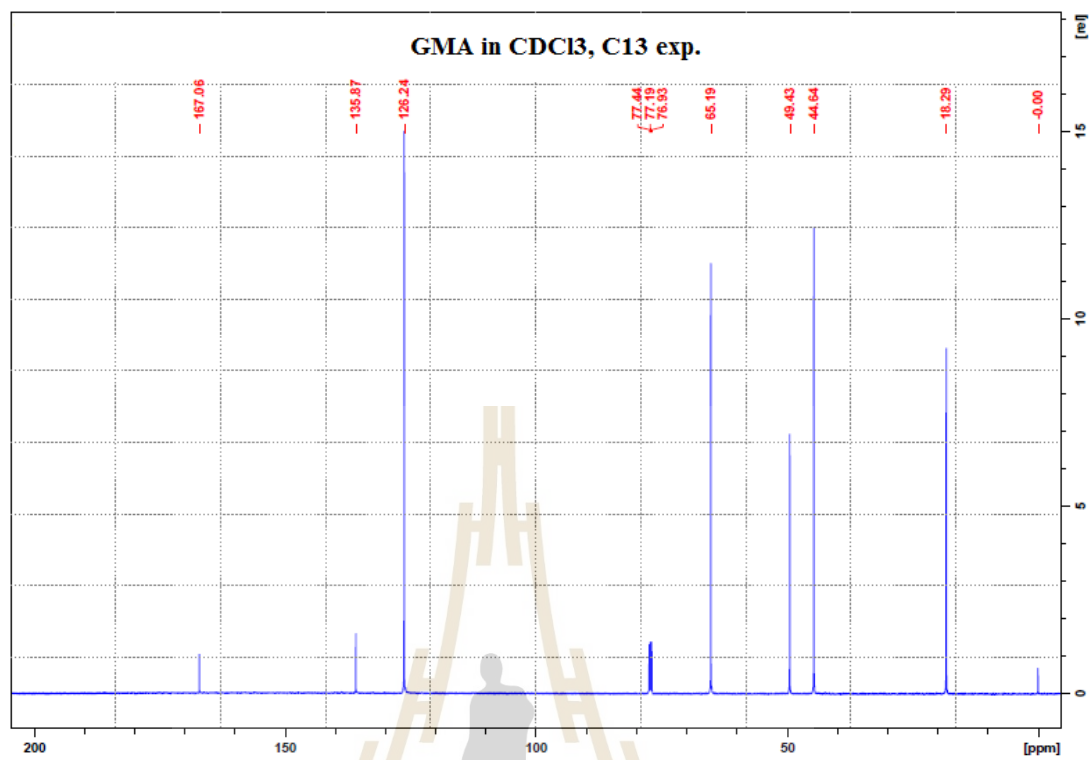


Figure A1 Full-range ¹³C-NMR spectrum of GMA.

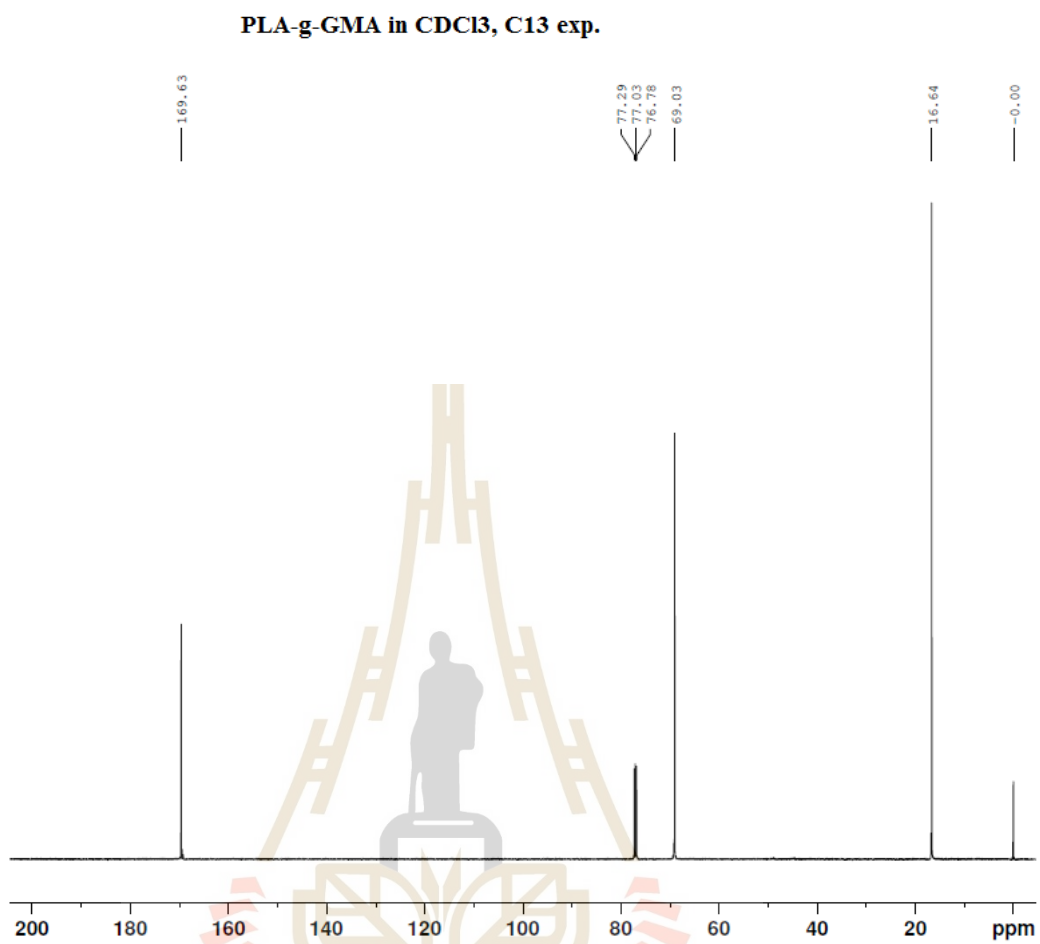
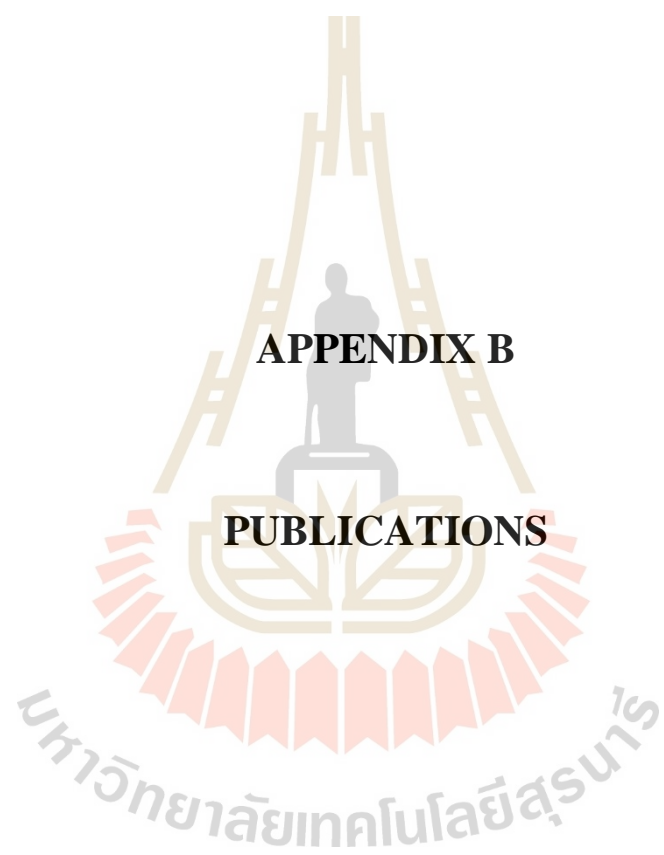


Figure A2 Full-range ¹³C-NMR spectrum of PLA-g-GMA.



APPENDIX B

PUBLICATIONS

List of publications

- Nguyen, T. C., Ruksakulpiwat, C., Soontaranon, S., Rugmai, S., and Ruksakulpiwat, Y. (2017). Crystallization behavior studied by synchrotron small-angle x-ray scattering of poly(lactic acid)/cellulose nanofibers composites. **Composites Science and Technology**. 143: 106-115.
- Nguyen, T. C., Ruksakulpiwat, C., and Ruksakulpiwat, Y. (2016). The study on the grafting of glycidyl methacrylate onto poly(lactic acid) in an internal mixer. **Walailak Journal of Science and Technology (WJST)**. 13: 1037-1046.
- Nguyen, T. C., Ruksakulpiwat, C., and Ruksakulpiwat, Y. (2016). Effect of glycidyl methacrylate (GMA) content on grafting yield and mechanical properties of GMA grafted poly (lactic acid) prepared by melt mixing method. **Key Engineering Materials**. 709: 27-31.
- Nguyen, T. C., Ruksakulpiwat, C., and Ruksakulpiwat, Y. (2017). Effect of acid/fiber ratio on physical properties of cellulose nanofibers extracted from cassava pulp. **Materials Science Forum**. 890: 103-107.
- Nguyen, T. C., Ruksakulpiwat, C., and Ruksakulpiwat, Y. (2017). Extraction of cellulose microfibrils from cassava pulp. **Key Engineering Materials**. 723: 427-433.
- Nguyen, T. C., Ruksakulpiwat, C., and Ruksakulpiwat, Y. Biocomposites of poly(lactic acid) and cellulose nanofibers from cassava pulp. **Key Engineering Materials**. (In publication).



ELSEVIER

Contents lists available at ScienceDirect

Composites Science and Technology

journal homepage: <http://www.elsevier.com/locate/compscitech>

Crystallization behavior studied by synchrotron small-angle X-ray scattering of poly (lactic acid)/cellulose nanofibers composites

Thanh Chi Nguyen^a, Chaiwat Ruksakulpiwat^a, Supagorn Rugmai^b, Siriwat Soontaranon^b, Yupaporn Ruksakulpiwat^{a,*}^a School of Polymer Engineering, Institute of Engineering, Suranaree University of Technology, Nakhon Ratchasima 30000, Thailand^b Synchrotron Light Research Institute (Public Organization), Nakhon Ratchasima 30000, Thailand

ARTICLE INFO

Article history:

Received 16 December 2016

Received in revised form

15 February 2017

Accepted 21 February 2017

Available online 9 March 2017

Keywords:

PLA biocomposites

Cellulose nanofibers

Synchrotron SAXS

Crystallization

Morphological properties

ABSTRACT

In this study, synchrotron small angle X-ray scattering (SAXS) technique was applied to study the crystallization behavior of poly (lactic acid) (PLA)/cellulose nanofibers (CNFs) biocomposites. Morphological properties of the biocomposites were elucidated as well. PLA/CNFs biocomposites were prepared by melt mixing in an internal mixer. Glycidyl methacrylate (GMA) grafted poly (lactic acid) (PLA-g-GMA) was used as a compatibilizer between CNFs and PLA. CNFs were extracted from cassava pulp (CP) by acid hydrolysis method. Effect of CNFs content on the crystallization behavior of the biocomposites was studied. The SAXS results showed that with the addition of 0.1 wt% CNFs and using PLA-g-GMA as a compatibilizer, the crystallization rate of biocomposites significantly increased. The paracrystalline model was applied and well fitted to the SAXS data. The average long period (L) and lamellar thickness (L_c) determined by applying the paracrystalline model of PLA, PLA-g-GMA, and PLA/PLA-g-GMA/CNFs biocomposites exhibited a slight decrease in the very early stages of crystallization, then become time independent. The fiber content of 0.1 wt% was found to give the highest crystallization rate of both PLA/CNFs and PLA/PLA-g-GMA/CNFs biocomposites. The enhanced interfacial adhesion between PLA and CNFs by PLA-g-GMA was confirmed by scanning electron microscopy (SEM).

© 2017 Elsevier Ltd. All rights reserved.

1. Introduction

Due to its good mechanical properties and easy production from its monomer, poly (lactic acid) is one of the most studied biodegradable polymers. However, some poor physical properties such as high brittleness, low crystallization rate, and low thermal stability limited its industrial applications. The combination between PLA and biodegradable fillers like cellulose nanofibers was found to improve mechanical properties and thermal stability of obtained composites [1].

With the rising concern toward environmental issues, the studies on fiber-reinforced polymer composites which use both materials from renewable resources have received considerable attention. Owing to some advantages, such as abundance, renewability, low density, high specific strength and modulus, and low cost [2–4], natural fibers have been used to replace for synthetic

fibers in many fiber-reinforced polymer composites [4].

So far, cellulose nanofibers have been used as fillers in many biocomposites studies [5–8]. Ahmad et al. studied CNFs reinforced PLA biocomposites with various CNFs contents by using an internal mixer [9]. The results from TEM images showed the poor dispersion of freeze-dried pristine CNFs in PLA matrix. The enhanced storage modulus and reduced thermal stabilities of obtained composites compared to those of pure PLA were observed. In another research, CNFs were incorporated into PLA matrix by using melt extrusion technique in a twin-screw microextruder. The surface-modification of CNFs with functional trialkoxysilanes was carried out to improve the compatibility between PLA and CNFs. Thermomechanical and thermal analyses showed that these CNFs act as nanoreinforcing agents for PLA matrix, enhancing the crystallinity degree and reinforcing the thermomechanical properties of PLA matrix [10]. Besides that, cellulose nanofibers have proven to be effective nucleating agents for the crystallization of PLA. DSC results revealed the higher degree of crystallinity for obtained composites as 2.5 wt% CNFs were added into PLA by using a fully automated laboratory two roll mill [11].

* Corresponding author.

E-mail address: yupa@sut.ac.th (Y. Ruksakulpiwat).

Cellulose nanofibers used as filler in this study were extracted from cassava pulp using acid hydrolysis method [12]. Cassava pulp is the solid waste during starch production from cassava tubers [13]. In Thailand, the production of starch generates at least 1 million tons of cassava pulp annually [14]. In addition to residual starch, cassava pulp contains 15–50% cellulose fibers (dry weight basis) [15]. Extracting successfully CNFs from cassava pulp not only generates the high-value product but also contributes to solving environmental issues. The extraction process was carried out by the combination of pre-treatments such as alkali and bleaching treatments and acid hydrolysis treatment. The results from TEM images showed that cellulose nanofibers with a diameter and length of 8–15 nm and 200–800 nm, respectively, were obtained. The crystallinity of CNFs determined by X-ray diffraction technique was found to be significantly higher than that of raw cassava pulp [12].

One of the biggest challenges as dispersing CNFs into polymer matrices is the highly hydrophilic character of this filler. It hinders the dispersion of CNFs in non-polar polymer matrices. Because of the strong particle–particle interactions and poor polymer wetting on the hydrophilic CNFs surface, the agglomeration of CNFs was prone to occur during melt mixing [9,10]. In order to overcome this drawback, one of the efficient methods is using a surfactant. Bondeson et al. investigated the preparation of biodegradable nanocomposites based on 5 wt% CNFs and PLA using an extrusion process [16]. An anionic surfactant (5, 10 and 20 wt%) was solution blended to the CNFs suspension, water was eliminated by freeze-drying of the surfactant/CNFs system prior to melt-mixing in the PLA matrix. The results showed that as increasing surfactant content, the dispersion of CNFs in PLA was improved. However, at the same time, degradation of PLA matrix occurred. Using a master batch of PLA/CNFs is also an efficient method to improve the dispersion of CNFs in PLA matrix. By this method, the nanolevel dispersion of CNFs in PLA was obtained [17,18]. In addition, a two-step process where solvent-mixing and melt-mixing were carried out sequentially was also used to enhance the dispersion of CNFs in PLA matrix [19]. In this method, first, CNFs was solution blended with a carrier polymer and then, in the second step, the CNFs-carrier polymer mixture was melt blended with the polymer matrix to prepare the composites.

PLA-g-GMA, prepared by grafting of GMA onto PLA chain via free-radical polymerization, was used as a compatibilizer in this study in order to improve the compatibility between CNFs and PLA matrix. The preparation of PLA-g-GMA was carried out by melt mixing method using an internal mixer. The experimental results from ^1H NMR spectrum indicated that the grafting reaction of GMA onto PLA took place successfully. After grafting, the brittle fracture behavior of PLA was changed to ductile fracture behavior. PLA-g-GMA showed significantly higher elongation at break in relation to pure PLA [20]. With the chemical structure containing hydrophilic chain and oleophilic chain, PLA-g-GMA has been used as a potential compatibilizer in natural fibers reinforced PLA-based biocomposites [21].

By using the most powerful X-radiation source as a synchrotron, the recording of detailed scattering patterns with high accuracy during short exposure times could be obtained. This enables the monitoring of crystallization process of polymeric materials in real time. The isothermal crystallization behavior of poly(L-lactic acid) (PLLA) and its copolymers from the melt was investigated by synchrotron small-angle X-ray scattering (SAXS) [22,23]. The results showed that the long period and lamellar thickness of PLLA decreased in the very early stages during primary crystallization.

In this work, the effects of CNFs and CNFs content on the crystallization rate of biocomposites with and without using PLA-g-GMA as a compatibilizer were investigated by small angle X-ray scattering technique with synchrotron radiation. Moreover, the

influences of PLA-g-GMA and CNFs content on morphological characteristics of PLA biocomposites were also elucidated.

2. Materials and methods

2.1. Materials

A commercial grade of PLA (PLA 4043D) was purchased from Nature Works. Cellulose nanofibers were extracted from cassava pulp by using acid hydrolysis method in our laboratory. The preparation and characterization of CNFs were given in details in another publication [12]. PLA-g-GMA was prepared by melt mixing using an internal mixer. The details of this grafting reaction can be found in our previous publication [20].

2.2. Preparation of PLA biocomposites

PLA composites were prepared using an internal mixer (Hakke Rheomix, 3000p) at a temperature of 170 °C. Before mixing, PLA and CNFs were dried in an oven at 70 °C for 2 h and 50 °C for 24 h, respectively. The ratio of biocomposites is shown in Table 1. The mixing time and mixing speed were kept at 10 min and 60 rpm, respectively. Before being charged into the mixing chamber, the determined amounts of PLA, PLA-g-GMA and CNFs were premixed. All compositions of composites were charged into the mixing chamber at the same time.

2.3. Characterization

2.3.1. Morphological properties

The morphologies of the tensile fractured surface of compression molded samples were observed by a scanning electron microscope (SEM, model JEOL JSM6010LV). The specimens were coated with gold prior to the examination. All SEM images were collected under an acceleration voltage of 10 kV.

2.3.2. SAXS analyses

Isothermal crystallization behavior of pure PLA and its biocomposites was determined by SAXS technique. The synchrotron SAXS experiments were performed at BL1.3 W beamline of the Siam Photon Laboratory, Synchrotron Light Research Institute, Nakhon-Ratchasima, Thailand. The wavelength was 1.38 Å and the sample-to-detector was set at 2.4 m. Silver behenate (AgBH) with $d = 3.838$ nm was used as a standard material for calibrating the scattering angle. A CCD detector (Rayonix SX 165) with a diameter of 165 mm was used to capture the scattering patterns. An ionization chamber installed in front of the sample holder and a photodiode attached in front of a beam stop were used to monitor the beam intensity before and after the sample, respectively. The schematic diagram of the SAXS BL1.3 W beamline is shown in Fig. 1.

The specimens with the same thickness were filled into the sample cell with Kapton windows. The specimens were heated from room temperature to 200 °C and kept for 5 min to completely

Table 1
The composition of biocomposites.

Symbol	PLA (wt%)	PLA-g-GMA (wt%)	CNFs (wt%)
PLA	100	–	–
PLA/CNFs0.1	99.9	–	0.1
PLA/CNFs0.3	99.7	–	0.3
PLA/CNFs0.5	99.5	–	0.5
PLA/PLA-g-GMA/CNFs0.1	79.9	20	0.1
PLA/PLA-g-GMA/CNFs0.3	79.7	20	0.3
PLA/PLA-g-GMA/CNFs0.5	79.5	20	0.5

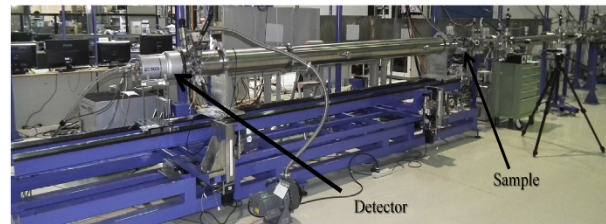


Fig. 1. Schematic diagram of the SAXS BL13W beamline.

eliminate any possible crystalline phase. Then the specimens were quenched to 120 °C and the synchrotron SAXS measurements were carried out at different crystallization times with the exposure time of 10 s. The 2D SAXS patterns were reduced to 1D SAXS profile by circularly averaging the 2D patterns using the SAXSIT program [24]. After that, the profile was corrected for beam intensity, sample transmission, background scattering and converted to Lorentz-corrected SAXS profile by multiplying by q^2 [25]. The scattering vector is given by Ref. [26]:

$$q = (4\pi/\lambda) \sin \theta \quad (1)$$

where λ and 2θ are the wavelength of the X-ray source and the scattering angle, respectively.

The scattering angle is given by:

$$2\theta = \tan^{-1}(D/L) \quad (2)$$

where D is the distance from the origin to the point on the detector plane, calculated using the pixel size, and L is the sample-to-detector distance.

The total scattering intensity is proportional to the difference of electron density of crystalline and amorphous phases, and the volume fraction of crystalline phase in the semi-crystalline polymers. Therefore, the change of total scattering intensity can regard as the change of crystallinity [27–32]. The SAXS peak can be attributed to the lamellar structure in the spherulites of PLA [22]. In this research, the SAXS patterns of pure PLA and its biocomposites were recorded in order to investigate the effects of CNFs and CNFs content on the crystallization behavior of PLA biocomposites.

The morphological parameters such as the average long period of lamellar structure (L) and the average lamellar thickness (L_c) of PLA, PLA-g-GMA, and PLA/PLA-g-GMA/CNFs biocomposites were determined by using the paracrystalline diffraction method. It should be noticed that the average long period of lamellar structure can also be obtained from the first maximum at the lowest scattering angle by applying Bragg's law ($L_B = 2\pi/q_{\max}$, where q_{\max} is scattering vector at maximum intensity) in the SAXS profiles [27,33–38]. However, in most cases, the values determined by this simple method do not agree quantitatively with the structures seen by electron microscopy [39]. Compared to Bragg's law method, the paracrystalline diffraction method is more physically meaningful because it takes into account the nonideal periodicity of macrolattices in semicrystalline polymers. With this method, the size fluctuations of amorphous layer and crystalline component are assumed to contribute to the long-range disorder of the lattice. Thus, each of the two phases are treated equally in defining the structure of the paracrystalline macrolattice [40]. Besides determining the average long period, this method can also provide the average lamellar thickness parameter. These parameters can be obtained by fitting the SAXS curves to the equation [41]:

$$I(q) = C^* \left\{ I_0 \exp(-\sigma_{in}^2 q^2) \overline{|F(q, L)|^2} S(q) - a q^{-x} + \frac{b}{1 + q^2 \xi^2} + \frac{I_{ob}}{1 - (|q - q_0|/\xi_0)^m} \right\} + k \quad (3)$$

in which C , I_0 , a , b , x , and k are positive adjustable parameters. The first term in Eq. (3) represents for crystalline part and describes the SAXS peak. The second term is given by the power-law function and describes the underlying diffusive scattering. The third term is given by the Ornstein-Zernike function and represents for the scattering of random chains. The fourth term is given by the broad peak and describes the scattering of amorphous soft materials. The exponential $\exp(-\sigma_{in}^2 q^2)$ comes from the smoothing of crystalline-amorphous interface. The averaged crystalline lamella form factor is expressed as:

$$\overline{|F(q, L)|^2} = \frac{1}{\sqrt{2\pi}\sigma_L} \int_{-\infty}^{\infty} |F(q, x)|^2 \exp\left(-\frac{(x-L)^2}{2\sigma_L^2}\right) dy \quad (4)$$

The form factor of crystalline lamella with thickness L is given by:

$$F(q, L) = \frac{\sin\left(\frac{qL}{2}\right)}{\frac{qL}{2}} \quad (5)$$

The structure factor $S(q)$ corresponds to the interference between the scattered X-ray of the neighboring lamellae aligning in one dimension, which is expressed as:

$$S(q) = \frac{1 - |G(q)|^2}{1 - 2|G(q)|\cos(q\alpha) + |G(q)|^2} \quad (6)$$

where α is the average long period. $G(q)$ is the Fourier transform of Gaussian long period distribution function:

$$G(q) = \mathcal{F}[H(y)] \quad (7)$$

With the Gaussian long period distribution function is given by:

$$H(y) = \frac{1}{\sqrt{2\pi}\sigma_a} \exp\left(-\frac{(y-\alpha)^2}{2\sigma_a^2}\right) \quad (8)$$

in which σ is standard deviation of the long period distribution.

The measured SAXS intensity profiles were fitted by using a Matlab based module (SAXSIT) [24].

The fiber content of 0.1 wt% was selected to investigate the effect of CNFs on the crystallization behavior of PLA/PLA-g-GMA/CNFs

biocomposites. In this analysis, SAXS measurements were carried out at 120 °C at different crystallization times (5, 10, 20, 30, 40, 50, and 60 min). Moreover, in order to investigate the effect of fiber content on the crystallization behavior of PLA/CNFs and PLA/PLA-g-GMA/CNFs biocomposites, SAXS analysis was measured at 120 °C at three different crystallization times (0, 5, and 10 min).

3. Results and discussion

3.1. Morphological properties

Fig. 2a-g shows SEM images of the tensile fractured surface of pure PLA and its biocomposites. Compared to pure PLA, PLA/

CNFs0.1 did not show any significant differences in morphology. No visible microscale agglomerations of CNFs were observed (Fig. 2b). As CNFs content was increased (up to 0.3 and 0.5 wt%), however, the rougher fractured surfaces and some microscale agglomerations of CNFs were observed. The higher CNFs content was used; the rougher surfaces and the bigger size of microscale agglomerations of CNFs were observed (Fig. 2c,d). Generally, a relatively good dispersion was obtained in biocomposite with low fiber content (0.1 wt%).

For biocomposites with using PLA-g-GMA as a compatibilizer, the better dispersion of CNFs in PLA was achieved, especially for PLA/PLA-g-GMA/CNFs0.1 (Fig. 2e) and PLA/PLA-g-GMA/CNFs0.3 (Fig. 2f) biocomposites. Compared to PLA/CNFs biocomposites,

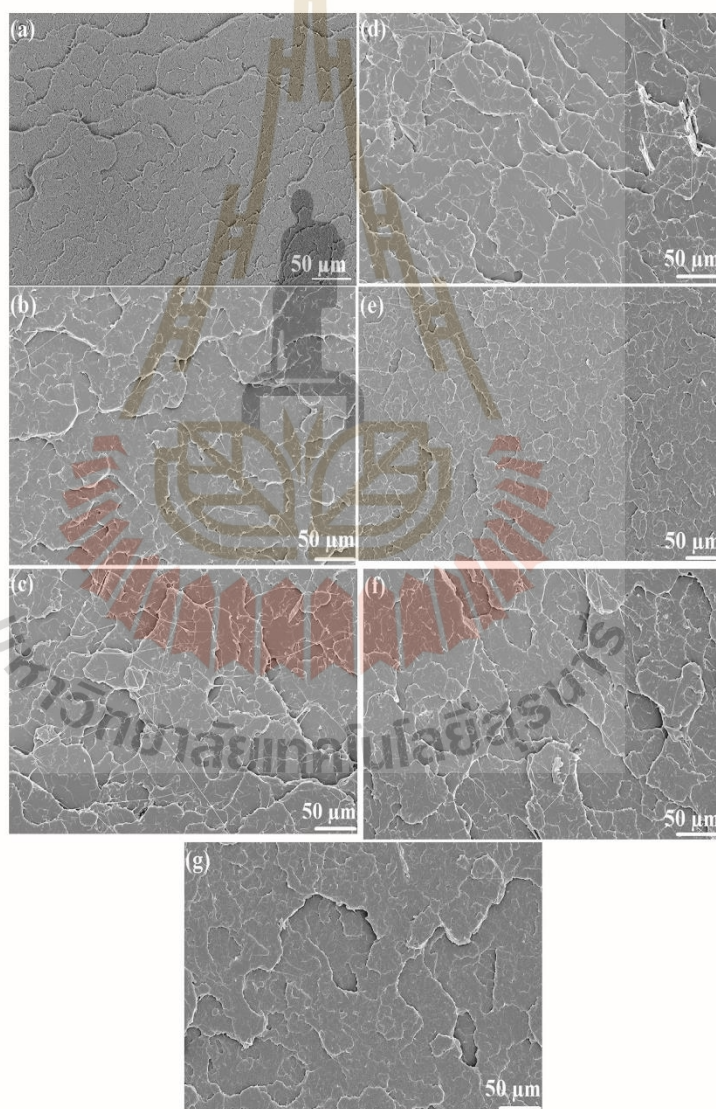


Fig. 2. SEM micrographs of the tensile fractured surfaces of pure PLA (a), PLA/CNFs0.1 (b), PLA/CNFs0.3 (c), PLA/CNFs0.5 (d), PLA/PLA-g-GMA/CNFs0.1 (e), PLA/PLA-g-GMA/CNFs0.3 (f), and PLA/PLA-g-GMA/CNFs0.5 (g).

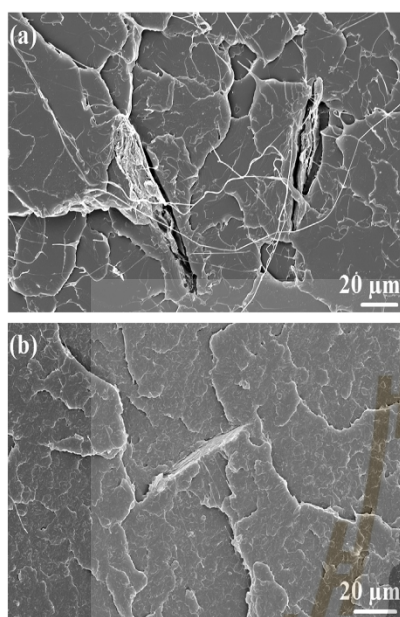


Fig. 3. Detailed view of the tensile fractured surfaces of PLA/CNFs0.5 (a) and PLA/PLA-g-GMA/CNFs0.5 (b) biocomposites showing the interfacial adhesion between fibers and PLA matrix.

PLA/PLA-g-GMA/CNFs biocomposites showed the smoother surfaces at all studied fiber contents (0.1, 0.3, and 0.5 wt%). As shown in Fig. 2f, the dispersion of CNFs in PLA is still relatively good with fiber content up to 0.3 wt%. Nevertheless, with further increase of fiber content up to 0.5 wt%, a slightly coarse surface and some small agglomerations were observed (Fig. 2g). The more detailed micrographs of PLA/CNFs0.5 and PLA/PLA-g-GMA/CNFs0.5 biocomposites are shown in Fig. 3. From the graph of PLA/CNFs0.5 biocomposite

(Fig. 3a), one can see that the gaping holes and voids between fibers and matrix are visible. This indicates the poor interfacial adhesion between fibers and matrix. Conversely, as shown in Fig. 3b, by the addition of PLA-g-GMA, no voids between fibers and matrix were observed. This indicates that the interfacial adhesion between fibers and matrix was improved. This improvement is attributed to the compatibilizing effect of PLA-g-GMA. On the one hand, the hydroxyl groups ($-OH$) on the surface of cellulose nanofibers can react with the epoxy groups of GMA on PLA-g-GMA, on the other hand, the physical entanglements between PLA chains of the matrix and PLA chains of PLA-g-GMA can be formed during mixing.

3.2. Isothermal crystallization behavior by SAXS

The Lorentz-corrected SAXS profiles of PLA, PLA-g-GMA, and PLA/PLA-g-GMA/CNFs0.1 biocomposites at 120 °C at different crystallization times are shown in Figs. 4–6. As can be seen from Fig. 4, after 5 min of crystallization time, no scattering peak was observed for pure PLA. This demonstrates that no crystallization of PLA took place within 5 min of crystallization time at 120 °C. Conversely, the clear scattering peaks were observed for PLA-g-GMA and PLA/PLA-g-GMA/CNFs0.1 biocomposites (Figs. 5–6). It indicates that PLA has longer induction time for crystallization compared to that of PLA-g-GMA and PLA/PLA-g-GMA/CNFs0.1 biocomposite. Moreover, as shown in Figs. 5 and 6, the intensity of the scattering peak of the biocomposite is significantly higher than that of PLA-g-GMA. From this result, it can be seen that the crystallinity of biocomposite is higher than that of pure PLA and PLA-g-GMA after 5 min of crystallization time.

After 10 min of crystallization time, the crystallization of PLA was shown with a small scattering peak appeared in the scattering profile of pure PLA. This means that PLA has started to crystallize at the time between 5 and 10 min of crystallization time. Meanwhile, the scattering intensity of PLA-g-GMA and the biocomposite continued increasing, especially for the biocomposite, the scattering intensity increased dramatically. It indicates the faster crystallization of the biocomposite compared to that of pure PLA and PLA-g-GMA.

It can be seen from Fig. 6 that after 20 min of crystallization time, the intensity of scattering peaks of the biocomposite stayed

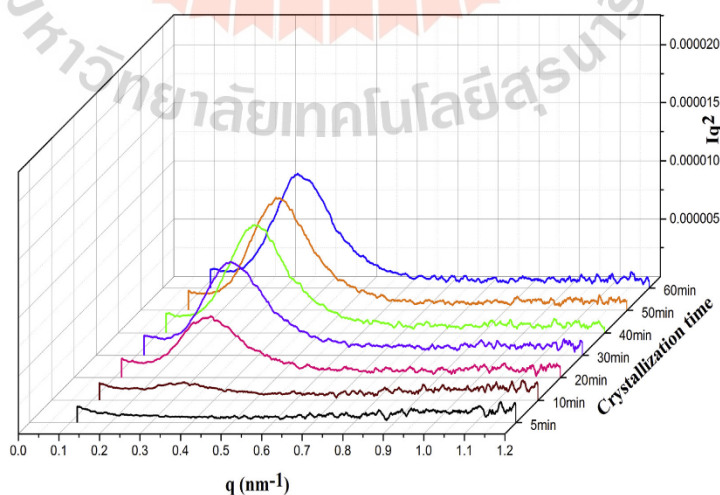


Fig. 4. Lorentz-corrected SAXS profiles of PLA obtained at 120 °C at different crystallization times.

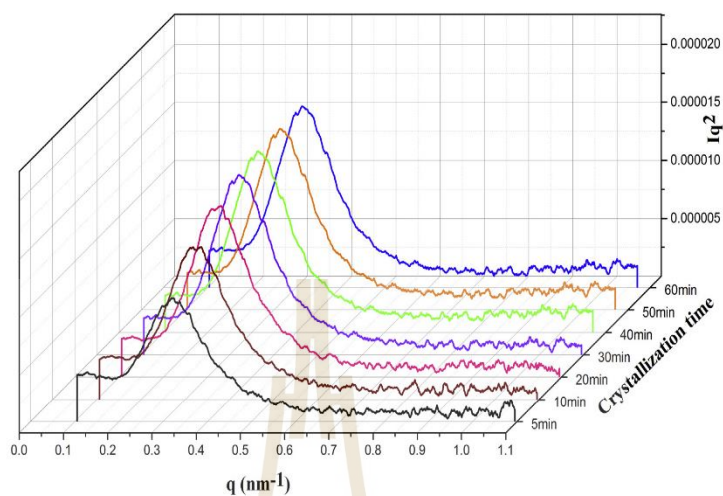


Fig. 5. Lorentz-corrected SAXS profiles of PLA-g-GMA obtained at 120 °C at different crystallization times.

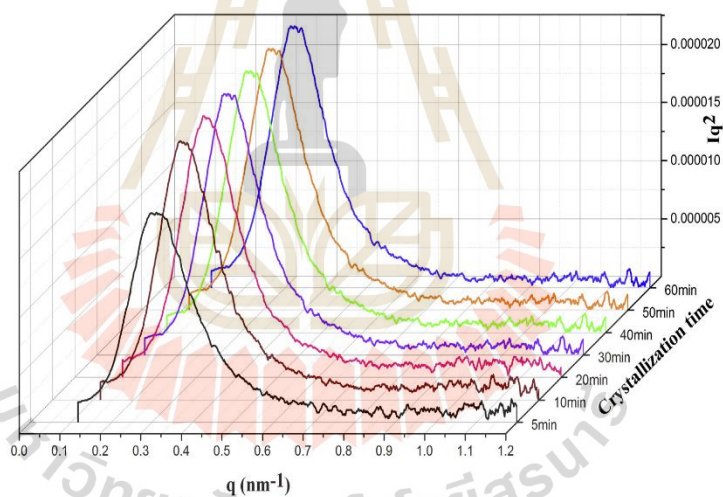


Fig. 6. Lorentz-corrected SAXS profiles of PLA/PLA-g-GMA/CNFs biocomposites obtained at 120 °C at different crystallization times.

constant compared to that at 10 min. It implies that the crystallization process of the biocomposite has already finished after 10 min of crystallization time. In contrast to the biocomposite, PLA and PLA-g-GMA continued to crystallize as shown by the increased scattering intensity (Figs. 4–5). Especially, the SAXS profile of PLA exhibited the obvious scattering peak with significantly increased intensity.

After 30 min of crystallization time, the scattering peak of the biocomposite did not show any difference in the intensity and q position compared to that at 10 and 20 min of crystallization time. A slight increase in the intensity of SAXS peak of PLA-g-GMA was observed. Meanwhile, the intensity of SAXS peak of PLA increased considerably compared to that at 20 min of crystallization time. This result indicates that the crystallization process of PLA and PLA-g-GMA has not finished yet after 20 min of crystallization time.

After 40 min of crystallization time, the intensity of SAXS peak of PLA-g-GMA stayed constant compared to that at 30 min. It implies that the crystallization process of PLA-g-GMA seemed to finish after 30 min of crystallization time. However, for PLA, it seems that the crystallization process has not finished yet because the intensity of SAXS peak at 40 min shows a significant increase compared to that at 30 min of crystallization time. The intensity of SAXS peak of PLA still shows a slight increase after 50 min of crystallization time, whereas there is no difference in intensity of SAXS peak of PLA at 60 min compared to that at 50 min (Fig. 4). From this result, it can be stated that the crystallization process of PLA has completed after 50 min of crystallization time.

In order to see more clearly the effect of CNFs on the crystallization rate of the biocomposite, the maximum $I(q)q^2$ was plotted versus crystallization time as shown in Fig. 7. The slope of the curve

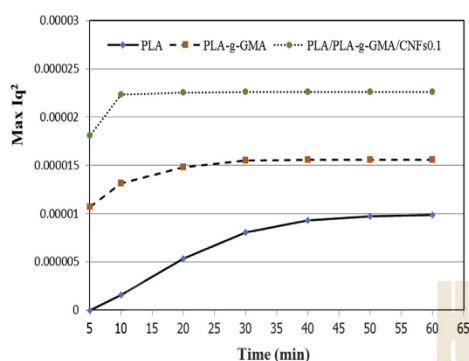


Fig. 7. The plot of the changes of maximum lq^2 versus crystallization time of PLA, PLA-g-GMA, and PLA/PLA-g-GMA/CNFs biocomposites.

of the biocomposite was considerably higher than that of pure PLA and PLA-g-GMA. This result indicates that the crystallization rate of PLA was improved significantly by the addition of 0.1 wt% CNFs and using PLA-g-GMA as a compatibilizer. The well dispersed CNFs acted as nucleating agents for the crystallization of PLA, which contributes to fastening the crystallization rate of the biocomposite.

The experimental data and its fitting curve using paracrystalline model (Equation (3)) of PLA, PLA-g-GMA and PLA/PLA-g-GMA/CNFs biocomposites at 120 °C after 20 min of crystallization time are shown in Fig. 8. The similar fitting procedures were conducted at other crystallization times.

The L and L_c values were obtained from fitting the experimental data to the paracrystalline model of PLA, PLA-g-GMA, and PLA/PLA-g-GMA/CNFs biocomposites at different crystallization times shown in Fig. 9. The average long period and lamellar thickness of PLA, PLA-g-GMA, and PLA/PLA-g-GMA/CNFs biocomposites decreased very slightly in the early stages of crystallization, then became time independent. The initial decrease in L and L_c values is larger for PLA-g-GMA. Such behavior could be interpreted by the lamellar stack insertion process which is related to the crystallization of thinner, possibly more defective lamellar stacks between existing primary stacks consisting of lamella with larger thickness

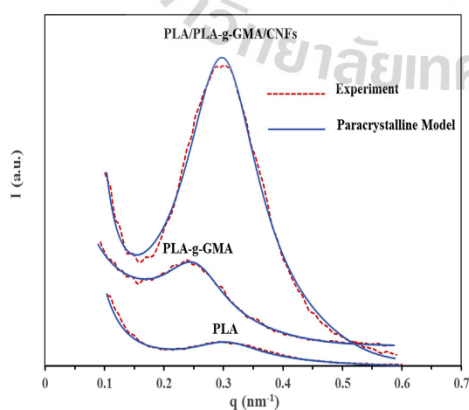


Fig. 8. The SAXS curves from the experimental data and fitting results using the paracrystalline model of PLA, PLA-g-GMA, and PLA/PLA-g-GMA/CNFs biocomposites at 120 °C after 20 min of crystallization time.

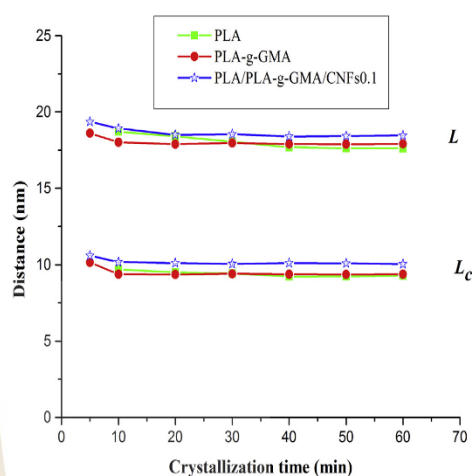


Fig. 9. Crystallization time dependence of the average long period (L) and lamellar thickness (L_c) of PLA, PLA-g-GMA, and PLA/PLA-g-GMA/CNFs biocomposites crystallized at 120 °C.

[23]. Similar results have been reported by several authors in isothermal crystallization of various semi-crystalline polymers such as PLLA [22,23], polystyrene (PS) [42], and polyester terephthalate (PET) [43]. Additionally, as can be seen from Fig. 9, L and L_c values of PLA and PLA-g-GMA were slightly lower than those of PLA/PLA-g-GMA/CNFs biocomposites. This could be attributed to the secondary crystallization which produced thinner lamellae thickness, resulting in the reduction of the average long period and lamellar thickness [44].

3.3. Effect of PLA-g-GMA and fiber content on the crystallization behavior of PLA/CNFs biocomposites

Fig. 10 shows Lorentz-corrected SAXS profiles of PLA/CNFs biocomposites with various fiber contents at 120 °C after 5 min of crystallization time. As shown in Fig. 10, no SAXS peaks were observed for all samples with different fiber contents. In contrast, for PLA/PLA-g-GMA/CNFs biocomposites, the apparent scattering peaks were observed in the SAXS profile of all samples with various fiber contents after 5 min of crystallization time (Fig. 11). This indicates the role of PLA-g-GMA as a compatibilizer improving the dispersion of CNFs in PLA matrix. The well dispersed CNFs acted as nucleating agents for the crystallization of PLA, which contributes to the reduction in induction time for crystallization of PLA/PLA-g-GMA/CNFs biocomposites. Moreover, as can be seen from Fig. 11, there was no considerable difference in intensity of scattering peak of PLA/PLA-g-GMA/CNFs biocomposites as fiber content was increased from 0.1 to 0.5 wt%.

The plot of maximum lq^2 versus crystallization time of PLA/CNFs and PLA/PLA-g-GMA/CNFs biocomposites with various fiber contents is shown in Fig. 12. As can be observed from Fig. 12, the slope of the curves of PLA/PLA-g-GMA/CNFs biocomposites is significantly higher than that of PLA/CNFs biocomposites at all fiber contents. This indicates that the crystallization rate of PLA/PLA-g-GMA/CNFs is faster than that of PLA/CNFs. Moreover, as shown in Fig. 12, increasing fiber content led to lower slope of the curves for both PLA/CNFs and PLA/PLA-g-GMA/CNFs biocomposites, which indicates the slower crystallization rate. It is due to the agglomerations of fibers that can be formed as the fiber loading was

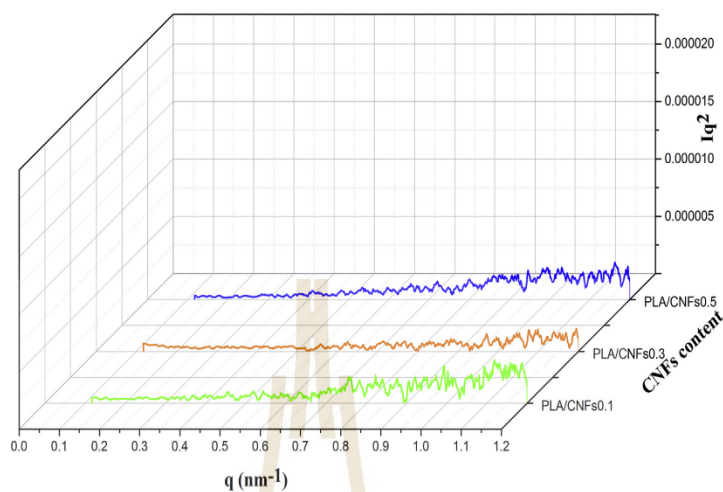


Fig. 10. Lorentz-corrected SAXS profiles of PLA/CNFs biocomposites with various fiber contents obtained at 120 °C after 5 min of crystallization time.

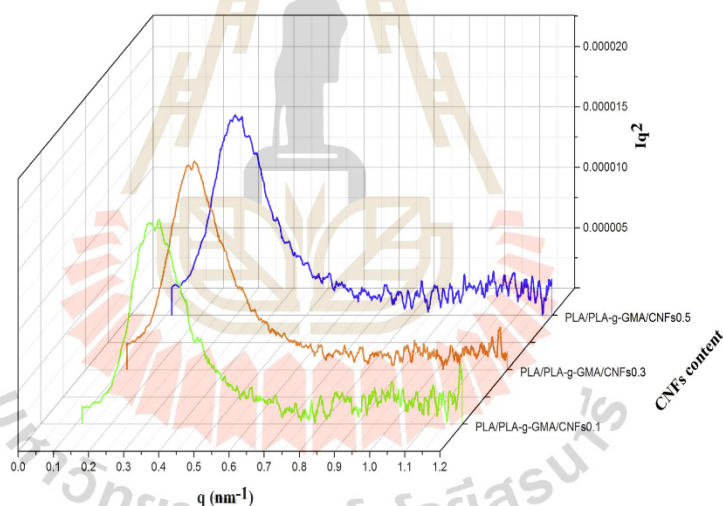


Fig. 11. Lorentz-corrected SAXS profiles of PLA/PLA-g-GMA/CNFs biocomposites with various fiber contents obtained at 120 °C after 5 min of crystallization time.

increased (Fig. 2). From SAXS results of PLA/CNFs and PLA/PLA-g-GMA/CNFs biocomposites, it can be stated that the crystallization rate of PLA/PLA-g-GMA/CNFs biocomposites is faster than that of PLA/CNFs biocomposites at all fiber contents. It is thought that PLA-g-GMA used as a compatibilizer makes the dispersion of CNFs in PLA matrix become better. The well dispersed CNFs could act as nucleating agents for the crystallization of PLA. Furthermore, it should be noted that the fiber content of 0.1 wt% was found to give the highest crystallization rate of both PLA/CNFs and PLA/PLA-g-GMA/CNFs biocomposites.

4. Conclusions

The PLA biocomposites with various cellulose nanofibers contents were prepared by melt mixing using an internal mixer. The

PLA-g-GMA was used as a compatibilizer to enhance the interfacial adhesion between fibers and PLA matrix.

The morphology studies by SEM of pure PLA and its biocomposites showed that by using PLA-g-GMA as a compatibilizer, the better dispersion of fibers, as well as the enhanced interfacial adhesion between fibers and PLA, were achieved. However, some visible microscale agglomerations of CNFs were observed as fiber loading was increased up to 0.5 wt%. Compared to the tensile fractured surfaces of PLA/CNFs biocomposites, the tensile fractured surfaces of PLA/PLA-g-GMA/CNFs biocomposites were smoother at all studied fiber loadings.

The synchrotron SAXS study indicated that by the addition of only 0.1 wt% cellulose nanofibers and using PLA-g-GMA as a compatibilizer, the crystallization rate of PLA in biocomposites was enhanced considerably. This result demonstrated the role of the

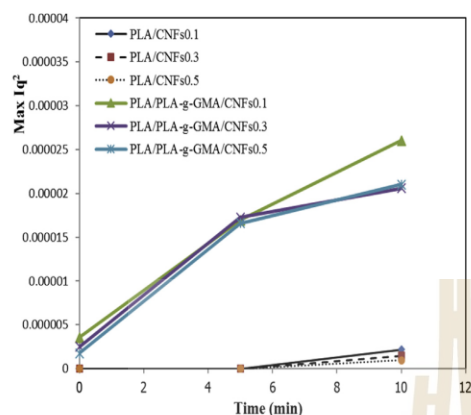


Fig. 12. The plot of the changes of maximum Iq^2 versus crystallization time of PLA/CNFs and PLA/PLA-g-GMA/CNFs biocomposites with various fiber contents.

well-dispersed cellulose nanofibers as nucleating agents, which enhanced the crystallization rate of PLA. Nevertheless, increasing fiber content from 0.1 to 0.5 wt% led to the decrease of the crystallization rate of biocomposites with and without using PLA-g-GMA.

This work indicates that the melt compounding of PLA with a small content of cellulose nanofibers using PLA-g-GMA as a compatibilizer is a quite promising method to achieve the improved crystallization rate of PLA.

Acknowledgements

The authors would like to express gratitude to the SUT-PhD Scholarship for Asian Countries Program of Suranaree University of Technology, Thailand for the financial support and Siam Synchrotron Light Research Institute for the SAXS instrument.

References

- [1] K. Oksman, M. Skrifvars, J.-F. Selin, Natural fibres as reinforcement in poly(lactic acid) (PLA) composites, *Compos. Sci. Technol.* 63 (9) (2003) 1317–1324.
- [2] P. Wambua, J. Ivens, I. Verpoest, Natural fibres: can they replace glass in fibre reinforced plastics? *Compos. Sci. Technol.* 63 (9) (2003) 1259–1264.
- [3] A. Mohanty, M. Misra, G. Hinrichsen, Biofibres, biodegradable polymers and biocomposites: an overview, *Macromol. Mater. Eng.* 276 (1) (2000) 1–24.
- [4] M.J. John, S. Thomas, Biofibres and biocomposites, *Carbohydr. Polym.* 71 (3) (2008) 343–364.
- [5] E. Espino-Pérez, J. Bras, V. Ducret, A. Guinault, A. Dufresne, S. Doménech, Influence of chemical surface modification of cellulose nanowhiskers on thermal, mechanical, and barrier properties of poly(lactide) based bionanocomposites, *Eur. Polym. J.* 49 (10) (2013) 3144–3154.
- [6] N. Lin, J. Huang, P.R. Chang, J. Feng, J. Yu, Surface acetylation of cellulose nanocrystal and its reinforcing function in poly(lactic acid), *Carbohydr. Polym.* 83 (4) (2011) 1834–1842.
- [7] M.D. Sanchez-Garcia, J.M. Lagaron, On the use of plant cellulose nanowhiskers to enhance the barrier properties of polylactic acid, *Cellulose* 17 (5) (2010) 987–1004.
- [8] A. Pei, Q. Zhou, L.A. Berglund, Functionalized cellulose nanocrystals as bio-based nucleating agents in poly(l-lactide)(PLLA)-crystallization and mechanical property effects, *Compos. Sci. Technol.* 70 (5) (2010) 815–821.
- [9] E. Ahmad, A. Luyt, Morphology, thermal, and dynamic mechanical properties of poly(lactic acid)/sisal whisker nanocomposites, *Polym. Compos.* 33 (6) (2012) 1025–1032.
- [10] J.-M. Raquez, Y. Murena, A.-L. Goffin, Y. Habibi, B. Ruelle, F. DeBuij, P. Dubois, Surface-modification of cellulose nanowhiskers and their use as nano-reinforcers into polylactide: a sustainably-integrated approach, *Compos. Sci. Technol.* 72 (5) (2012) 544–549.
- [11] A.N. Frone, S. Berlioz, J.-F. Chailan, D.M. Panaitescu, Morphology and thermal properties of PLA–cellulose nanofibers composites, *Carbohydr. Polym.* 91 (1) (2013) 377–384.
- [12] W. Ruangudomsakul, C. Ruksakulpiwat, Y. Ruksakulpiwat, Preparation and characterization of cellulose nanofibers from cassava pulp, *Macromol. Symp.* 354 (1) (2015) 170–176.
- [13] K. Sriroth, R. Chollakup, S. Chotineeranat, K. Piyachomkwan, C.G. Oates, Processing of cassava waste for improved biomass utilization, *Bioresour. Technol.* 71 (1) (2000) 63–69.
- [14] K. Sriroth, V. Santisopasri, C. Petchalanuwat, K. Kurotjanawong, K. Piyachomkwan, C.G. Oates, Cassava starch granule structure–function properties: influence of time and conditions at harvest on four cultivars of cassava starch, *Carbohydr. Polym.* 38 (2) (1999) 161–170.
- [15] E.D.M. Teixeira, A.A.S. Curvelo, A.C. Correia, J.M. Marconcini, G.M. Glenn, L.H.C. Mattoso, Properties of thermoplastic starch from cassava bagasse and cassava starch and their blends with poly(lactic acid), *Indus. Crops Prod.* 37 (1) (2012) 61–68.
- [16] D. Bondeson, K. Oksman, Dispersion and characteristics of surfactant modified cellulose whiskers nanocomposites, *Compos. Interfaces* 14 (7–9) (2007) 617–630.
- [17] N. Bitinis, R. Verdejo, J. Bras, E. Fortunati, J.M. Kenny, L. Torre, M.A. López-Manchado, Poly(lactic acid)/natural rubber/cellulose nanocrystal bionanocomposites part I. processing and morphology, *Carbohydr. Polym.* 96 (2) (2013) 611–620.
- [18] M. Jonoobi, J. Harun, A.P. Mathew, K. Oksman, Mechanical properties of cellulose nanofiber (CNF) reinforced polylactic acid (PLA) prepared by twin screw extrusion, *Compos. Sci. Technol.* 70 (12) (2010) 1742–1747.
- [19] A. Arias, M.-C. Heuzey, M.A. Huneault, G. Ausias, A. Bendahou, Enhanced dispersion of cellulose nanocrystals in melt-processed polylactide-based nanocomposites, *Cellulose* 22 (1) (2015) 483–498.
- [20] T.C. Nguyen, C. Ruksakulpiwat, Y. Ruksakulpiwat, The study on the grafting of glycidyl methacrylate onto poly(lactic acid) in an internal mixer, *Walaialak J. Sci. Technol. (WJST)* 13 (12) (2016) 1037–1046.
- [21] T. Xu, Z. Tang, J. Zhu, Synthesis of polylactide-graft-glycidyl methacrylate graft copolymer and its application as a coupling agent in polylactide/bamboo flour biocomposites, *J. Appl. Polym. Sci.* 125 (S2) (2012) E622–E627.
- [22] Z.-G. Wang, X. Wang, B.S. Hsiao, S. Andjelic, D. Jamiolkowski, J. McDwitt, J. Fischer, J. Zhou, C.C. Han, Time-resolved isothermal crystallization of absorbable PGA-co-PLA copolymer by synchrotron small-angle X-ray scattering and wide-angle X-ray diffraction, *Polymer* 42 (21) (2001) 8965–8973.
- [23] J. Cho, S. Baratian, J. Kim, F. Yeh, B.S. Hsiao, J. Runt, Crystallization and structure formation of poly(l-lactide-co-meso-lactide) random copolymers: a time-resolved wide- and small-angle X-ray scattering study, *Polymer* 44 (3) (2003) 711–717.
- [24] S. Soontaranon, S. Rugmai, Small angle X-ray scattering at Siam photon laboratory, *Chin. J. Phys.* 50 (2) (2012) 204–210.
- [25] C.G. Vonk, G. Kortleve, X-ray small-angle scattering of bulk polyethylene, *Kolloid-Z. U. Z. Polym.* 220 (1) (1967) 19–24.
- [26] O. Glatter, O. Kratky, *Small Angle X-ray Scattering*, Academic Press, London, 1982.
- [27] J. Luo, Y. Liang, J. Yang, H. Niu, J.-Y. Dong, C.C. Han, Mechanisms of nucleation and crystal growth in a nascent isotactic polypropylene/poly(ethylene-co-octene) in-reactor alloy investigated by temperature-resolved synchrotron SAXS and DSC methods, *Polymer* 52 (20) (2011) 4590–4599.
- [28] B. Lee, T.J. Shin, S.W. Lee, J. Yoon, J. Kim, M. Ree, Secondary crystallization behavior of poly(ethylene isophthalate-co-terephthalate): time-resolved small-angle X-ray scattering and calorimetry studies, *Macromolecules* 37 (11) (2004) 4174–4184.
- [29] R. Verma, H. Marand, B. Hsiao, Morphological changes during secondary crystallization and subsequent melting in poly(ether ether ketone) as studied by real time small angle X-ray scattering, *Macromolecules* 29 (24) (1996) 7767–7775.
- [30] J.T. Koberstein, R.S. Stein, Small-angle x-ray scattering measurements of diffuse phase-boundary thicknesses in segmented polyurethane elastomers, *J. Polym. Sci. Polym. Phys. Ed.* 21 (10) (1983) 2181–2200.
- [31] D.A. Ivanov, R. Legras, A.M. Jonas, Interdependencies between the evolution of amorphous and crystalline regions during isothermal cold crystallization of poly(ether-ether-ketone), *Macromolecules* 32 (5) (1999) 1582–1592.
- [32] D.A. Ivanov, Z. Amalou, S.N. Magonov, Real-time evolution of the lamellar organization of poly(ethylene terephthalate) during crystallization from the melt: high-temperature atomic force microscopy study, *Macromolecules* 34 (26) (2001) 8944–8952.
- [33] H. Zhou, G. Wilkes, Comparison of lamellar thickness and its distribution determined from dsc, SAXS, TEM and AFM for high-density polyethylene films having a stacked lamellar morphology, *Polymer* 38 (23) (1997) 5735–5747.
- [34] B.S. Hsiao, R.K. Verma, A novel approach to extract morphological variables in crystalline polymers from time-resolved synchrotron SAXS data, *J. Synchrotron Radiat.* 5 (1) (1998) 23–29.
- [35] Z. Xia, H.-J. Sue, Z. Wang, C.A. Avila-Orta, B.S. Hsiao, Determination of crystalline lamellar thickness in poly(ethylene terephthalate) using small-angle X-ray scattering and transmission electron microscopy, *J. Macromol. Sci. Part B* 40 (5) (2001) 625–638.
- [36] Z.-G. Wang, B. Hsiao, B. Fu, L. Liu, F. Yeh, B. Sauer, H. Chang, J. Schultz, Correct determination of crystal lamellar thickness in semicrystalline poly(ethylene terephthalate) by small-angle X-ray scattering, *Polymer* 41 (5) (2000) 1791–1797.
- [37] A.J. Ryan, W. Bras, G.R. Mant, G.E. Derbyshire, A direct method to determine the degree of crystallinity and lamellar thickness of polymers: application to

- polyethylene, *Polymer* 35 (21) (1994) 4537–4544.
- [38] A. Jonas, T. Russell, D. Yoon, Time-resolved SAXS studies of morphological changes in cold crystallized poly (ethylene terephthalate) during annealing and heating, *Colloid Polym. Sci.* 272 (11) (1994) 1344–1351.
- [39] P. Dismore, W. Statton, *Small-angle Scattering from Fibrous and Partially Oriented Systems*, Interscience, New York, 1966.
- [40] B. Crist, Small-angle x-ray scattering of semicrystalline polymers. I. Review of existing models, *J. Polym. Sci. Polym. Phys. Ed.* 11 (4) (1973) 635–661.
- [41] B.K. Vainshtein, *Diffraction of X-rays by Chain Molecules*, Elsevier Publishing Company, New York, 1966.
- [42] S. Rastogi, J.G.P. Goossens, P.J. Lemstra, An in situ SAXS/WAXS/Raman spectroscopy study on the phase behavior of syndiotactic polystyrene (sPS)/solvent systems: compound formation and solvent (dis)ordering, *Macromolecules* 31 (9) (1998) 2983–2998.
- [43] B. Lee, T.J. Shin, S.W. Lee, J. Yoon, J. Kim, H.S. Youn, M. Ree, Time-resolved X-ray scattering and calorimetric studies on the crystallization behaviors of poly(ethylene terephthalate) (PET) and its copolymers containing isophthalate units, *Polymer* 44 (8) (2003) 2509–2518.
- [44] Z.-G. Wang, B. Hsiao, B. Sauer, W. Kampert, The nature of secondary crystallization in poly (ethylene terephthalate), *Polymer* 40 (16) (1999) 4615–4627.



The Study on the Grafting of Glycidyl Methacrylate onto Poly(lactic acid) in an Internal Mixer

Thanh Chi NGUYEN¹, Chaiwat RUKSAKULPIWAT² and Yupaporn RUKSAKULPIWAT^{1*}

¹*School of Polymer Engineering, Institute of Engineering, Suranaree University of Technology, Nakhon Ratchasima 30000, Thailand*

²*Department of Chemistry, Faculty of Science, Khon Kaen University, Khon Kaen 40002, Thailand*

(*Corresponding author's e-mail: yupa@sut.ac.th)

Presented at 41st Congress on Science and Technology of Thailand: November 6th - 8th 2015
Full paper accepted: 2 March 2016

Abstract

Glycidyl methacrylate (GMA) was grafted onto poly(lactic acid) (PLA) by melt mixing in an internal mixer using dicumyl peroxide (DCP) as an initiator. The results from nuclear magnetic resonance (¹H-NMR) and Fourier transform infrared (FTIR) spectroscopy indicated that the grafting reaction of GMA onto PLA took place successfully. After grafting, the brittle behaviour of PLA was changed to ductile behaviour of glycidyl methacrylate grafted poly(lactic acid) (PLA-g-GMA). The elongation at break and impact strength of PLA-g-GMA were significantly higher than those of pure PLA. In order to obtain the optimal mixing conditions, the mixing time was varied from 7, 10 to 14 min. PLA-g-GMA prepared by mixing for 10 and 14 min showed melt crystallization upon cooling. This was different from PLA and PLA-g-GMA prepared by mixing for 7 min, which did not undergo crystallization upon cooling from the melt. A mixing time of 10 min was found to give the optimum grafting yield, elongation at break and impact strength of PLA-g-GMA. With the significantly improved mechanical properties compared to those of pure PLA, the new, biodegradable PLA-g-GMA obtained from this study can be used to replace pristine PLA which has many drawbacks in many industrial applications.

Keywords: Poly(lactic acid), PLA, bioplastic, grafting, mechanical properties, GMA

Introduction

Due to environmental issues related to non-degradable plastic wastes, research and development of biodegradable polymers has recently received considerable attention. Poly(lactic acid) (PLA), a synthetic aliphatic polyester derived from biomasses, is an environmentally friendly polymer and has emerged as an alternative to conventional petroleum-based polymeric materials because of its renewability, biodegradability and greenhouse gas neutrality. Moreover, PLA also possesses good mechanical properties and can be easily processed [1]. However, PLA is still more expensive than many petroleum-derived commodity plastics. It has some poor physical properties such as slow crystallization rate, high brittleness, which hinder PLA to be used for various end-use applications.

Free radical grafting of PLA with monomers containing reactive groups has been considered to be a potential approach to modify the basic properties of pristine PLA. In addition, it is an effective method to produce compatibilizing agent for PLA-based polymer blends. So far, in addition to solution copolymerization, a melt grafting process by using an internal mixer has been extensively used in order to prepare many functionalized reactive polymers because of the relative simplicity and cost efficiency of this method. This grafting method can be applied for industrial scale production. The reactive grafting of glycidyl methacrylate (GMA) onto non-polar polyolefins such as polypropylene (PP) backbones via

reactive extrusion was carried out successfully [2,3]. Cho *et al.* investigated the melt grafting of GMA onto high-density polyethylene (HDPE) in the presence of free radical initiators in the batch mixer [4]. The results showed that the grafting reaction was significantly influenced by reaction time. It is one of the important variables for the preparation of functional polymers.

Recently, GMA has been increasingly used as a grafting monomer because of its dual functionality, which consists of epoxy and acrylic groups. It is believed that the epoxy group of GMA can react with many other groups, such as hydroxyl and carboxyl groups. Meanwhile, acrylic groups show the capability of free-radical grafting of GMA onto the polymer chain [5]. Even the radical grafting of GMA onto polyolefin in the melt mixing process has been investigated extensively, there have been very few studies focusing on the grafting of GMA onto PLA and the effect of reaction time on the physical properties of prepared PLA-g-GMA. Therefore, in this study, we report the grafting of GMA onto PLA with different mixing times using dicumyl peroxide (DCP) as an initiator in the internal mixer.

PLA-g-GMA obtained from this study can be used as a potentially biodegradable material used in various applications such as packaging materials, textile materials, environmental technology including wastewater treatment and bioremediation. Moreover, with the chemical structure containing hydrophilic and oleophilic chains, the obtained PLA-g-GMA can be used as a potential compatibilizer in natural fibers reinforced PLA-based biocomposites.

Materials and methods

Materials

Commercial PLA (PLA 4043D) was purchased from NatureWorks LLC. Dicumyl peroxide (DCP, 99 %), glycidyl methacrylate (GMA, 99 %), dichlorobenzene (DCB), chloroform (HPLC grade) and methanol were supplied from Sigma-Aldrich®. Before being used for grafting, GMA was purified by basic alumina pack column to remove inhibitor and stored in the refrigerator at about 5 °C.

Preparation of glycidyl methacrylate grafted poly (lactic acid)

The grafting of GMA onto the PLA chain was carried out by an internal mixer (Hakke Rheomix, 3000p). Before being used, PLA pellets were dried at 70 °C for 2 h. The grafting reaction was carried out under constant temperature at 170 °C. The mixing speed was held at 60 rpm. A GMA content of 10 wt% of PLA was used. The mixing time was varied from 7, 10 to 14 min. The obtained grafted samples were labeled as PLA-g-GMA7min, PLA-g-GMA10min and PLA-g-GMA14min, respectively with the number indicating the mixing time used. Before being used for grafting, GMA was stored in the refrigerator at 5 °C. The concentration of DCP used was 0.2 wt% of PLA. The grafting procedure is described as follows:

First, appropriate amounts of PLA and DCP were premixed by hand in a small plastic bag before being charged into the mixing chamber. After 2 min of mixing, GMA was added into the chamber. After the addition of GMA, the mixing chamber was closed immediately in order to minimize the loss of GMA due to vaporization.

Purification of glycidyl methacrylate grafted poly (lactic acid)

In order to remove unreacted GMA and possible homopolymer of GMA, which can be generated during the grafting reaction, after completion of mixing, the obtained samples were dissolved in DCB (5 wt% solution) at 120 °C. After that, the solution was poured into a large excess of methanol to precipitate PLA-g-GMA. The obtained white PLA-g-GMA precipitate was washed several times with methanol to completely remove the residual GMA and homopolymer of GMA. After the purification process, the pure white PLA-g-GMA was dried in a vacuum oven at 70 °C for 24 h.

Characterization of glycidyl methacrylate grafted poly (lactic acid)

Nuclear Magnetic Resonance (NMR): The percentage of GMA grafted onto PLA was determined by ¹H-NMR analysis. It was determined by calculating the relative area of the characteristic peaks of PLA and GMA. Its value was examined by Eq. (1) [9]. The ¹H-NMR spectra of PLA, PLA-g-GMA and GMA

monomer were recorded on a Varian model Inova 300 NMR spectrometer at 25 °C using CDCl₃ as a solvent and tetramethylsilane (TMS) as an internal standard.

$$\% \text{grafting} = \frac{\text{relative area of characteristic peak of GMA}}{\text{relative area of characteristic peak of PLA}} \times 100 \quad (1)$$

Fourier Transform Infrared (FTIR) Spectroscopy: The measurements of structural characterization of PLA and PLA-g-GMA were recorded on a Bruker Tensor 27 spectrometer using attenuated total reflectance (ATR) equipped with a platinum diamond crystal (TYPE A225/QL). Spectra were obtained at 4 cm⁻¹ resolution and 32 scans in the wavenumber range from 4000 to 400 cm⁻¹. All samples were dried in a vacuum oven at 60 °C for 24 h before testing.

Mechanical properties: In order to prepare the test specimens for mechanical properties testing, samples were compression molded at 170 °C for 10 min. PLA-g-GMA was dried in an oven at 70 °C for 2 h to eliminate moisture before being compressed. Tensile properties of all compression molded samples were obtained according to ASTM D638 using an Instron Universal Testing Machine (UTM 5565) with a load cell of 5 kN. The unnotched Izod impact strengths of pure PLA and PLA-g-GMA were obtained by using an Instron CEAST 9050 Pendulum Impact System according to ASTM D256.

Thermal properties: The nonisothermal crystallization behavior of pure PLA and PLA-g-GMA was investigated using differential scanning calorimetry (DSC) (model: DSC204F1 Phoenix). The samples were first heated to 200 °C with the rate of 5 °C/min and kept at 200 °C for 5 min (First heating scan). After that, they were cooled to 40 °C with the rate of 5 °C/min (Cooling scan). Then they were heated again to 200 °C with the rate of 5 °C/min (Second heating scan). Enthalpy of crystallization (ΔH_c) was determined from the area under the peak of the thermograms from the cooling scan. Enthalpy of cold crystallization (ΔH_{cc}) was obtained from the area under the recrystallization peak of the thermograms from the second heating scan. Enthalpy of melting (ΔH_m) was determined from the area under the melting peak of the thermograms from the second heating scan. The degree of crystallinity ($\%X_c$) of pure PLA and PLA-g-GMA was determined by Eq. (2) [6]:

$$\%X_c = \frac{\Delta H_m}{\Delta H_{m0}} \times 100 \quad (2)$$

where, ΔH_m is the measured melting enthalpy (in J/g) from the second heating scan and ΔH_{m0} is the theoretical melting enthalpy of completely crystalline PLA (93.7 J/g) [7].

Results and discussion

The FTIR spectra of pure PLA and PLA-g-GMA are shown in **Figure 1**. The spectrum of pure PLA showed peaks at 3000 - 2940 cm⁻¹, 1761 cm⁻¹ and 1190 - 1090 cm⁻¹, which are associated with CH₃ stretching, C=O stretching and the O-C=O stretching, respectively [8]. The peaks at 910, 1150, 1761 and 3000 cm⁻¹ were observed in the spectrum of PLA-g-GMA. Compared to the spectrum of pure PLA, the spectrum of PLA-g-GMA presented a small new peak appeared at 910 cm⁻¹, which is attributed to the asymmetric stretching of the epoxy group. This evidence demonstrates that the GMA was successfully grafted onto the PLA chain.

The NMR analysis also confirmed the result above. As seen in **Figure 2**, the ¹H-NMR spectra of PLA and PLA-g-GMA showed 2 peaks at 5.2 and 1.6 ppm, which represent the methylene and methyl protons of the PLA chain, respectively. However, compared to the spectrum of pure PLA, the spectrum of PLA-g-GMA exhibited the new and weak peaks at 0.9 - 4.3 ppm. These peaks represent the protons 1 - 7 in the chemical structure of GMA as shown in **Figure 3**. Moreover, from the ¹H-NMR spectrum of GMA, it can be observed that the chemical shifts of all peaks, which are associated with the GMA constitutional unit of proton CH, CH₂ and CH₃, are different from those in the spectrum of PLA-g-GMA. This observation demonstrates that the new multiplet belongs to GMA grafted onto the PLA chain (not

unreacted GMA). These results again confirmed that the GMA was successfully grafted onto the PLA chain. Similar results were also reported in another study [9].

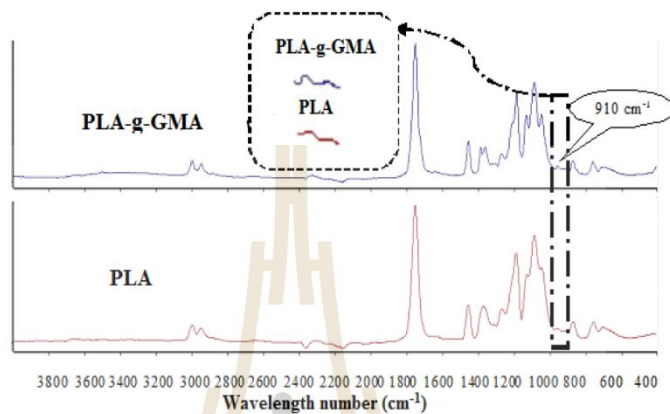


Figure 1 FTIR spectra of pure PLA and PLA-g-GMA with mixing time of 10 min.

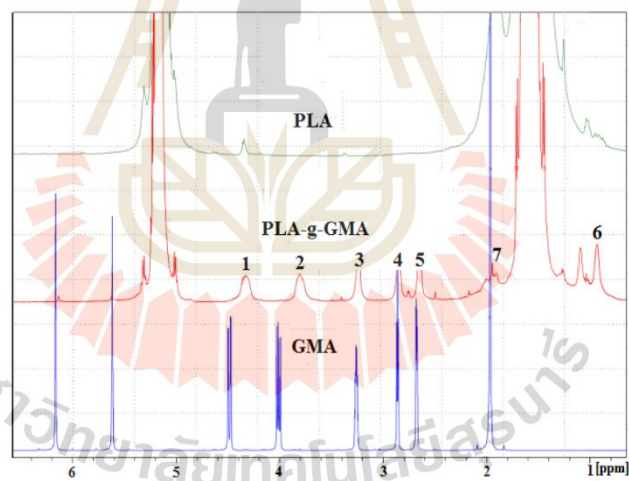


Figure 2 $^1\text{H-NMR}$ spectra of pure PLA, GMA and PLA-g-GMA at a mixing time of 10 min.

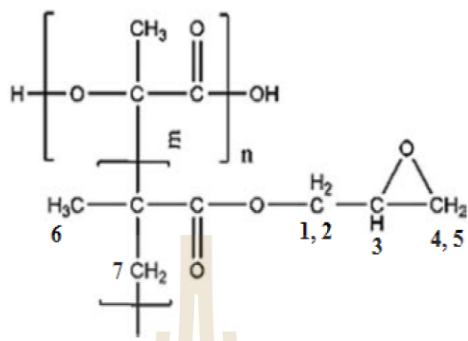


Figure 3 The probable structure of PLA-g-GMA.

The effect of mixing time on grafting yield was determined by calculating the relative area of the characteristic peaks of GMA and PLA from the $^1\text{H-NMR}$ spectra. Calculated results are shown in **Table 1** and **Figure 4**. It indicates that the percentage of GMA grafted onto PLA chain increased from 1.123 to 1.379 % as the mixing time increased from 7 to 10 min. However, further increases in the mixing time to 14 min, led to a decrease from 1.379 to 1.128 %. The reason for this decrease may be attributed to depolymerization of GMA which takes place if the mixing time is too long.

Table 1 The relative area of characteristic peaks of GMA and PLA calculated from $^1\text{H-NMR}$ spectra of PLA-g-GMA at different mixing times.

Samples	Relative area	
	Characteristic peak of PLA	Characteristic peak of GMA
PLA-g-GMA7min	4.275	0.048
PLA-g-GMA10min	4.279	0.059
PLA-g-GMA14min	4.345	0.049

The effect of mixing time on the mechanical properties of PLA-g-GMA is shown in **Figure 5** and **Figure 6**. From **Figure 5**, PLA-g-GMA showed ductile fracture with necking and cold drawing in the stress-strain curve. In contrast, brittle fracture of pure PLA was demonstrated. The elongation at break of PLA-g-GMA was considerably higher than that of PLA. From this result, it can be thought that a re-orientation of the molecular chain of PLA-g-GMA can occur under tensile force. This phenomenon did not occur in the case of pure PLA, which indicates a difference in crystallization behavior between pure PLA and PLA-g-GMA under applied tensile force. However, the tensile strength at break of PLA-g-GMA decreased significantly compared to that of pure PLA. This decrease is attributed to the decrease of crystallinity of PLA after grafting. Moreover, **Figure 5** also shows that elongation at break of PLA-g-GMA increased slightly with an increase in mixing time from 7 to 10 min. This is due to the increase of GMA grafting yield as the mixing time increases from 7 to 10 min as observed in **Figure 4**. On the other hand, it decreased significantly when the mixing time reached 14 min. It has been known that PLA is highly sensitive to heat, therefore, if the mixing time was too long, degradation of the PLA chain can

occur easily. Furthermore, the GMA grafting yield had a tendency to drop at certain mixing time as observed in **Figure 4** and where GMA was grafted onto HDPE [4].

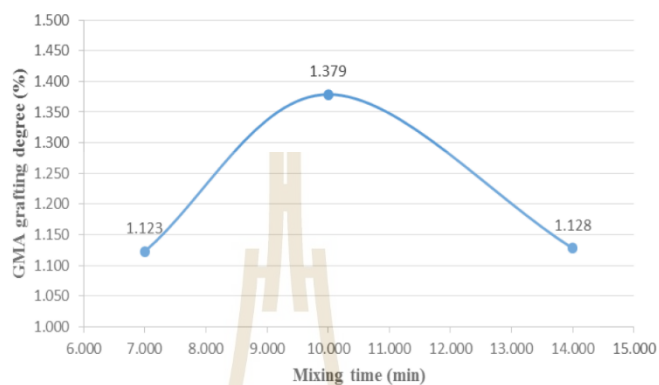


Figure 4 Effect of mixing time on GMA grafting yield.

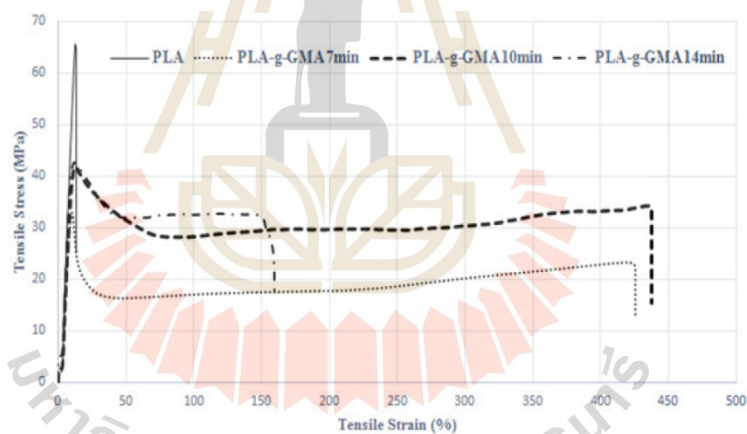


Figure 5 Stress-strain curves of pure PLA and PLA-g-GMA at different mixing times.

Figure 6 demonstrates that the impact strength of PLA-g-GMA was considerably higher than that of pure PLA. However, it was not significantly influenced by the mixing time. The impact strength of PLA-g-GMA increased slightly as mixing time increased from 7 to 10 min. Conversely, it decreased as mixing time increased from 10 to 14 min. This decrease is due to the decrease of GMA grafting yield and

degradation of the PLA chain as the mixing time became too long. The results above indicate that a mixing time of 10 min was optimal for the elongation at break and impact strength of PLA-g-GMA.

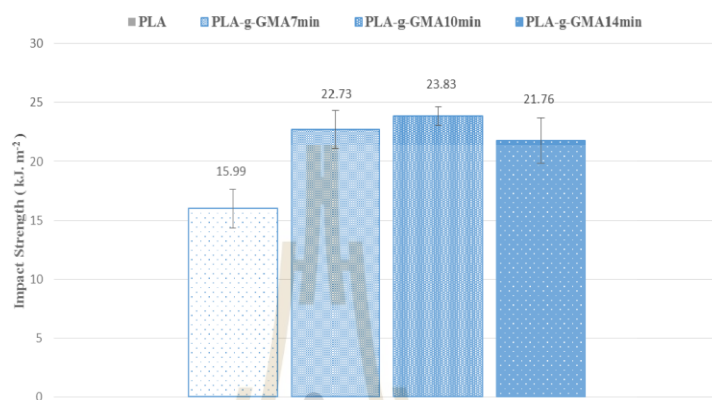


Figure 6 Effect of mixing time on impact strength of PLA-g-GMA.

DSC thermograms during cooling and heating of PLA and PLA-g-GMA with different mixing times are shown in **Figure 7** and **Figure 8**, respectively. As observed from the cooling scan (**Figure 7**) pure PLA and PLA-g-GMA7min did not show crystallization from melt upon cooling. PLA-g-GMA10min and PLA-g-GMA14min samples, however, underwent melt crystallization upon cooling. This indicates a difference in crystallization behavior between pure PLA and PLA-g-GMA as the mixing time was long enough so that the grafting reaction could take place effectively.

As seen in the heating scan (**Figure 8**) pure PLA and PLA-g-GMA7min present strong cold crystallization peaks upon heating. Meanwhile, PLA-g-GMA10min and PLA-g-GMA14min showed very weak cold crystallization peaks. The reason for this difference is due to the fact that PLA and PLA-g-GMA7min did not undergo melt crystallization under cooling (**Figure 7**). Therefore, the reorientation of their chain can occur easily upon heating. Conversely, the packed crystals of PLA-g-GMA10min and PLA-g-GMA14min, which were generated under cooling could not rearrange upon heating. As a result, very weak cold crystallization peaks were observed with respect to PLA-g-GMA10min and PLA-g-GMA14min samples.

Moreover, the double melting peak located at lower and higher temperature was observed in **Figure 8** for pure PLA, which related to less organized crystals and well-organized crystals, respectively [10]. The lower temperature peak (T_{m1}) is attributed to melting of the primary crystals formed upon cooling from the melt, and the higher one (T_{m2}) which corresponds to the melting of the crystals generated from recrystallization upon heating [11]. Besides that, **Figure 8** also shows that the melting temperature of PLA-g-GMA was lower than that of pure PLA. This implied that the crystals formed upon cooling from the melt of PLA-g-GMA are thermally less stable than those of pure PLA, which were almost formed from recrystallization upon heating [12]. In addition, as can be seen clearly from **Figure 8** the melting temperature of PLA-g-GMA did not change considerably with respect to the increase of mixing time from 7 to 14 min. The values of enthalpy of crystallization (ΔH_c), enthalpy of cold crystallization (ΔH_{cc}), enthalpy of melting (ΔH_m), crystallization temperature (T_c), cold crystallization temperature (T_{cc}), melting temperatures (T_{m1} and T_{m2}) and degree of crystallinity ($\%X_c$) of pure PLA and PLA-g-GMA at various

mixing times are shown in **Table 2**. The degree of crystallinity of PLA-g-GMA did not change significantly with respect to mixing time.

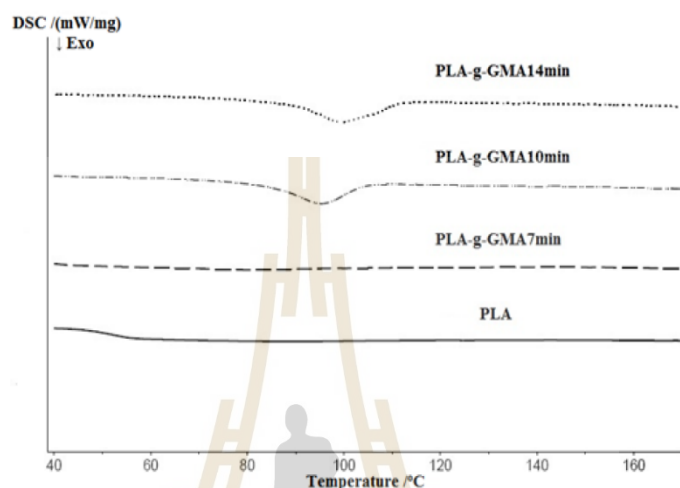


Figure 7 DSC thermograms of PLA and PLA-g-GMA at various mixing times (cooling scan).

Table 2 Thermal properties of PLA and PLA-g-GMA at different mixing times.

Samples	Thermal properties							
	T_c (°C)	T_{cc} (°C)	T_{m1} (°C)	T_{m2} (°C)	ΔH_c (J/g)	ΔH_{cc} (J/g)	ΔH_m (J/g)	% X_c (%)
PLA	-	100.2	145.3	155.5	0.00	29.80	31.23	33.33
PLA-g-GMA7min	-	86.3	135.2	148.2	0.00	21.50	24.52	26.17
PLA-g-GMA10min	95.3	87.3	139.4	148.3	13.26	7.34	22.96	24.50
PLA-g-GMA14min	99.5	84.9	139.6	147.9	14.38	5.38	23.88	25.49

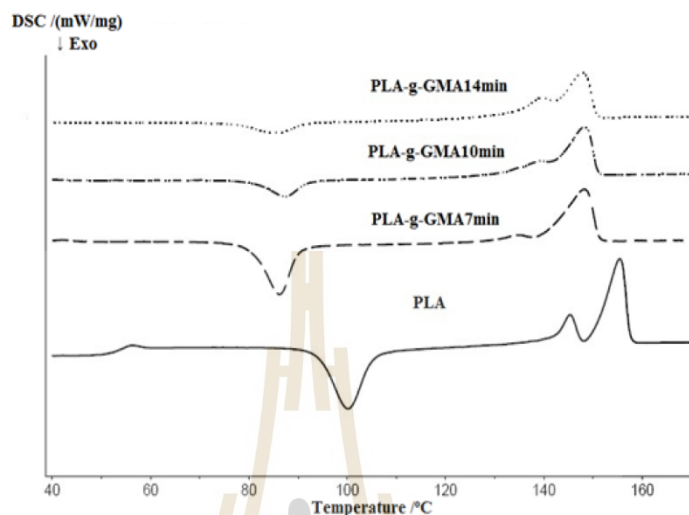


Figure 8 DSC thermograms of PLA and PLA-g-GMA at various mixing times (second heating scan).

Conclusions

FTIR and $^1\text{H-NMR}$ analyses demonstrate that glycidyl methacrylate can be successfully grafted onto poly(lactic acid) in an internal mixer using dicumyl peroxide as an initiator. The mechanical properties and thermal properties of PLA-g-GMA were found to be considerably different from those of pure PLA. It changed from brittle PLA to ductile PLA-g-GMA. The elongation at break and impact strength of PLA-g-GMA were significantly higher than those of pure PLA. Moreover, it was also found that GMA grafting yield, mechanical properties and crystallization behavior of PLA-g-GMA were affected by melt mixing time. The optimal grafting yield, elongation at break and impact strength of PLA-g-GMA was achieved at a mixing time of 10 min.

Acknowledgements

The authors would like to express gratitude to the SUT-PhD Scholarship for Asian Countries Program of Suranaree University of Technology, Thailand for financial support and analytical instruments.

References

- [1] D Garlotta, W Doane, R Shogren, J Lawton and JL Willett. Mechanical and thermal properties of starch-filled poly(D,L-lactic acid)/poly(hydroxy ester ether) biodegradable blends. *J. Appl. Polym. Sci.* 2003; **88**, 1775-86.
- [2] SS Pesetskii and OA Makarenko. Grafting of glycidyl methacrylate to polypropylene in an extruder, initiated with organic peroxides. *Russ. J. Appl. Chem.* 2002; **75**, 629-35.
- [3] EL Burton, M Woodhead, P Coates and T Gough. Reactive grafting of glycidyl methacrylate onto polypropylene. *J. Appl. Polym. Sci.* 2010; **117**, 2707-14.

- [4] KY Cho, JY Eom, CH Kim and JK Park. Grafting of glycidyl methacrylate onto high-density polyethylene with reaction time in the batch mixer. *J. Appl. Polym. Sci.* 2008; **108**, 1093-9.
- [5] T Xu, Z Tang and J Zhu. Synthesis of polylactide-graft-glycidyl methacrylate graft copolymer and its application as a coupling agent in polylactide/bamboo flour biocomposites. *J. Appl. Polym. Sci.* 2012; **125**, E622-E627.
- [6] J Huang, MS Lisowski, J Runt, ES Hall, RT Kean, N Buehler and J Lin. Crystallization and microstructure of poly (l-lactide-co-meso-lactide) copolymers. *Macromolecules* 1998; **31**, 2593-9.
- [7] EW Fischer, H Sterzel and G Wegner. Investigation of the structure of solution grown crystals of lactide copolymers by means of chemical reactions. *Kolloid-ZZ Polym.* 1973; **251**, 980-90.
- [8] VH Orozco, W Brostow, W Chonkaew and BL Lopez. Preparation and characterization of poly (Lactic acid)-g-maleic anhydride + starch blends. *Macromol. Symp.* 2009; **277**, 69-80.
- [9] J Liu, H Jiang and L Chen. Grafting of glycidyl methacrylate onto poly (lactide) and properties of PLA/starch blends compatibilized by the grafted copolymer. *J. Polym. Environ.* 2012; **20**, 810-6.
- [10] RY Chen, W Zou, CR Wu, SK Jia, Z Huang, GZ Zhang, ZT Yang and JP Qu. Poly(lactic acid)/poly(butylene succinate)/calcium sulfate whiskers biodegradable blends prepared by vane extruder: Analysis of mechanical properties, morphology, and crystallization behavior. *Polym. Test.* 2014; **34**, 1-9.
- [11] M Yasuniwa, S Tsubakihara, Y Sugimoto and C Nakafuku. Thermal analysis of the double-melting behavior of poly (L-lactic acid). *J. Polym. Sci. B Polym. Phys.* 2004; **42**, 25-32.
- [12] H Zhou, TB Green and YL Joo. The thermal effects on electrospinning of polylactic acid melts. *Polym.* 2006; **47**, 7497-505.



Effect of Acid/Fiber Ratio on Physical Properties of Cellulose Nanofibers Extracted from Cassava Pulp

THANH Chi Nguyen^{1, a}, CHAIWAT Ruksakulpiwat^{1, b}
 and YUPAPORN Ruksakulpiwat^{1, c}

¹School of Polymer Engineering, Institute of Engineering, Suranaree University of Technology,
 Nakhon Ratchasima 30000 Thailand

^ancthanh27@gmail.com, ^bcharuk@sut.ac.th, ^cyupa@sut.ac.th

Keywords: Cellulose nanofibers, Cassava pulp, Acid hydrolysis, Crystallinity, Thermal stability.

Abstract. Cellulose nanofibers (CeNF) were extracted successfully from cassava pulp (CP) by submitting to alkali, bleaching and acid hydrolysis treatments. The raw CP was mercerized with NaOH solution and then followed by bleaching treatment using a solution made up of equal parts (v:v) of acetate buffer and aqueous chlorite. In order to obtain cellulose nanofibers, the acid hydrolysis treatment of bleached fibers was performed using a mixture of HCl/H₂SO₄ (1:2 v/v). In this acid treatment reaction, the effects of acid/fiber ratio (ml/g) on physical properties of obtained cellulose nanofibers were investigated. Nanofibers were morphologically characterized by transmission electron microscopy (TEM) revealing the nanofibers with diameter in the range of 12-24 nm and immeasurable length were obtained. An increase in crystallinity of fibers after treatments was revealed by X-ray diffraction (XRD). Due to the introduction of sulfate groups at the outer surfaces of fibers during the hydrolysis, thermal stability of nanofibers, characterized by thermogravimetric analysis (TGA), was lower than that of raw CP. The acid/fiber ratio of 150ml/2g was found to be a proper ratio for thermal stability of obtained nanofibers. The crystallinity of nanofibers increased with the increase of acid/fiber ratio.

Introduction

Cassava pulp is the solid waste produced as a consequence of starch production. This pulp contains high starch content (50-60% dry basis) [1]. In Thailand, cassava starch is a large and growing industry with about 10 million tons of fresh cassava roots used for the production of starch, generating at least 1 million tons of pulp annually. The main application for the large quantities of waste material produced each year, after drying, is as a low value animal feed or fertilizer [2]. In addition to residual starch, cassava pulp contains 15-50 % cellulose fibers (dry weight basis) [3]. These characteristics suggest the possibility of using the CP as a source for the extraction of cellulose nanofibers.

Cellulose nanofibers can be obtained by mechanical and chemical paths. By chemical path, so far, acid hydrolysis treatment has proven its efficiency in isolating cellulose nanofibers from various kinds of cellulosic materials. H.A. Silvério et al. investigated the preparation of cellulose nanofibers from corncobs by sulfuric acid hydrolysis treatment [4]. Pre-treatment steps including alkali and bleaching treatments were carried out to remove non-cellulosic materials such as hemicellulose and lignin prior to submitting to acid treatment. The results of AFM indicated that the needle-like cellulose nanofibers were obtained. XRD analysis also showed that after acid treatment, the crystallinity of samples increased significantly and structure of cellulose was maintained. The 7-8 nm in diameter and 100-200 nm in lengths cellulose nanofibers were extracted successfully from cotton fibers by using hydrobromic acid as a hydrolyzing agent [5]. This indicated that besides sulfuric acid, hydrobromic acid was also an effective hydrolyzing agent for the preparation of cellulose nanofibers. N. Johar et al., studied on extraction of cellulose nanofibers from rice husk using H₂SO₄ as hydrolyzing agent [6]. The XRD and TGA results showed that after treatment, the crystallinity of obtained nanofibers was higher than that of raw material. However, a significant decrease in the thermal stability of nanofibers compared to that of raw rice husk was observed.

In case of cassava pulp, the remaining starch particles can be eliminated by this acid treatment. During this treatment, amorphous and paracrystalline regions of cellulose are preferentially hydrolyzed, whereas crystalline regions that have a higher resistance to acid attack remain intact [7, 8]. The overall efficiency of the acid hydrolysis treatment and physical properties of obtained cellulose nanofibers are affected by several factors such as acid type, acid concentration, hydrolysis temperature, hydrolysis time, and acid/fiber ratio.

In this work, cassava pulp was the lignocellulosic material used as the cellulose source to obtain nanofibers. Prior to being submitted to acid treatment, cassava pulp was treated by alkali and bleaching treatments to remove hemicellulose and lignin. The main objective is to produce cellulose nanofibers from cassava pulp via acid hydrolysis method as well as study on the effects of acid/fiber ratio on physical properties of obtained cellulose nanofibers.

Materials and Methods

Materials. Cassava pulp was supplied by Ratchasima Boonpa Co., Ltd. Sulfuric acid (95.0–98.0wt%), hydrochloric acid (37 wt%), sodium hydroxide, and glacial acetic acid were purchased from Carlo. Sodium chlorite (NaClO_2 , technical grade, 80%), and cellulose membrane (D9402) were supplied from Sigma–Aldrich.

Preparation of Cellulose Nanofibers. Cassava pulp (CP) was dried in an oven at 130 °C for 25 h to remove excess moisture. About 10 g of CP was dispersed in 200 ml of alkali solution (4 wt% NaOH). The mixture was transferred into a beaker and treatment was performed at 70 °C under vigorously mechanical stirring for 3 h in a water bath. The solid was then filtered and washed many times by distilled water until the pH reached 6–7. Following alkali treatment, the bleaching treatment was carried out by a solution made up of equal parts (v/v) of acetate buffer (NaOH and glacial acetic acid) and aqueous chlorite (NaClO_2 in water). This bleaching treatment was performed at 80 °C for 10h. The bleached fibers were washed repeatedly in distilled water until the pH of the fibers became neutral and subsequently dried using a freeze dryer. After bleaching treatment, the acid hydrolysis treatment was performed by using a mixture of $\text{HCl}/\text{H}_2\text{SO}_4$ (1:2 v/v). The used reaction time and acid concentration were 60 min and 6.5 M, respectively. Three acid/fiber ratios of 100ml/2g, 150ml/2g, and 200ml/2g were used in this treatment step. All reactions were carried out at 60 °C under mechanical stirring. The excess of acid was removed from the ensuing suspension by centrifugation at 9,000 rpm for 10 min. After that, the suspension was submitted to dialysis against distilled water using a cellulose membrane until the pH reached 6–7. Finally, the ultrasonic treatment of fiber suspension was carried out for 10 min to destroy aggregates and the fiber suspension was dried using a freeze dryer.

Characterization

Transmission electron microscopy (TEM). TEM (Phillips model Tecnai G2 F30 S/TEM S-Twin) was used to determine the dimensions of the cellulose nanofibers obtained from the cassava pulp. A drop of a diluted suspension (1 wt%) was deposited on the surface of a clean copper grid and coated with a thin carbon film. The sample was dried at ambient temperature before TEM analysis was carried out.

X-ray diffraction (XRD). Crystallinity index of cassava pulp and obtained cellulose nanofibers was determined by a D8 advanced Bruker AXS diffractometer with a $\text{CuK}\alpha$ radiation source ($\lambda = 0.1542$ nm) in the range between 5° and 40° (2θ angle) with a scan rate of 2° min^{-1} at 40 kV and 40 mA. All samples were analyzed in transmission mode. The crystallinity index (CI) was evaluated by using empirical method [9] as follows:

$$\text{CI}\% = \frac{(I_{002} - I_{am})}{I_{002}} \times 100. \quad (1)$$

where I_{002} is the maximum intensity of diffraction of the (0 0 2) lattice peak at a 2θ angle between 21° and 23° . I_{am} is the minimum intensity of diffraction taken at a 2θ angle between 18° and 20° [10].

Thermogravimetric analysis (TGA). Thermal stability of all samples was determined by TGA using a Mettler Toledo STARe System (TGA/DSC1 Modulae) by heating the samples from 30°C to 800°C at a heating rate of $10^\circ\text{C}/\text{min}$ under a nitrogen atmosphere with a gas flow of $100\text{ ml}/\text{min}$. The sample with a weight between 5 and 10 mg was used for each run.

Results and Discussion

Morphology of Cellulose Nanofibers. Fig. 1a shows the TEM image of obtained CeNF. It can be seen from Fig. 1a that the CeNF with the immeasurable length were obtained. The diameter distribution of 100 samples of CeNF extracted from cassava pulp is shown in Fig. 1b. As observed from Fig. 1b, most cellulose nanofibers displayed a diameter in the range of 12-24 nm. This result indicated that the cellulose nanofibers were successfully prepared from cassava pulp by using acid hydrolysis method. The alkali and bleaching treatments helped eliminate hemicellulose and lignin [6], which leads to the separation of cellulose fibers down to the nanometer scale during acid treatment step. The acid treatment resulted into defibrillation of the cellulose nanofibers and released the individual nanofibers.

X-ray Diffraction Analysis. The change of crystalline structure and crystallinity of CeNF after being treated at different acid/fiber ratios was investigated using XRD technique. Fig. 2 shows the XRD patterns of CP and obtained CeNF at different acid/fiber ratios. These patterns are typical of semicrystalline materials with an amorphous broad hump and crystalline peaks. As can be observed from Fig. 2, after acid treatment, the crystalline peak became narrower and sharper, especially for CeNF treated using the acid/fiber ratio of $200\text{ml}/2\text{g}$. The higher acid/fiber ratio, the sharper crystalline peak. It is attributed to the higher crystallinity of obtained CeNF. From the XRD patterns, the crystallinity index of CP and CeNF can be determined by using Eq. 1. Table 1 shows the crystallinity index of CP and obtained CeNF at different acid/fiber ratios. As shown in Table 1, the crystallinity index of obtained CeNF was significantly higher than that of raw CP. It is due to the fact that the amorphous regions of cellulose were hydrolyzed and the paracrystalline domains were partially removed during acid treatment [4]. In addition to that, the -OH groups on the surface of cellulose could form new hydrogen bonds as amorphous components were removed. The CI of CeNF monotonically increased with acid/fiber ratio. This is ascribed to more extensive hydrolysis of the amorphous regions of cellulose under strongly acidic reaction condition.

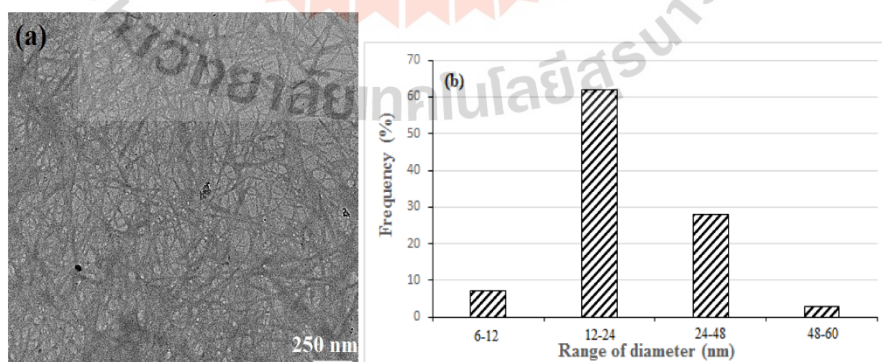


Fig. 1 (a) TEM image of CeNF, (b) diameter distribution of cellulose nanofibers extracted from cassava pulp.

Table 1 Intensity and crystallinity index of CP and CeNF at different acid/fiber ratios.

Sample	2 theta (degree)		Intensity (a.u)		Crystallinity Index (%)
	I_{am}	I_{002}	I_{am}	I_{002}	
Cassava pulp	19.412	22.963	2498	3186	21.59
CeNF 100ml/2g	18.432	22.132	42.0	144	70.83
CeNF 150ml/2g	19.107	22.030	67.5	265	74.53
CeNF 200ml/2g	18.225	22.214	54.9	239	77.03

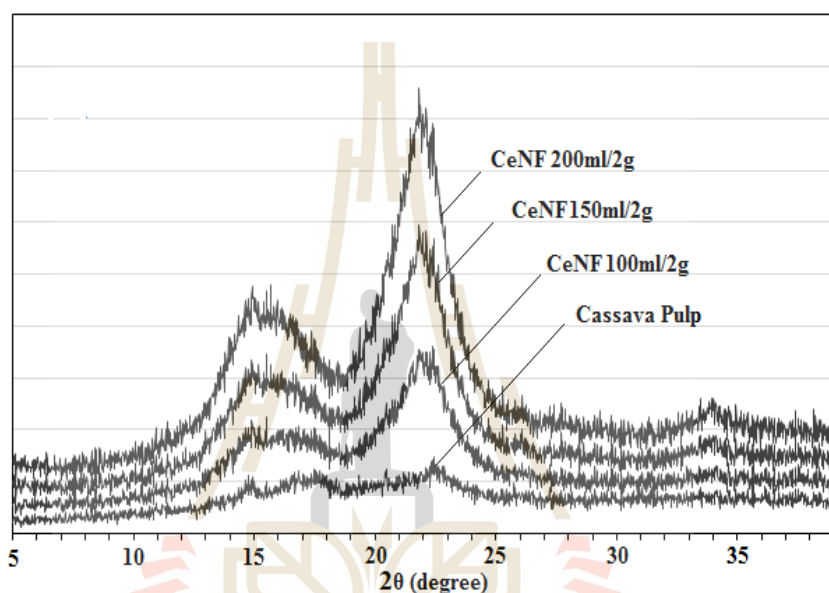


Fig. 2 XRD patterns of CP and CeNF at different acid/fiber ratios.

Thermal Stability. Fig. 3 shows the TGA and derivative thermogravimetric (DTG) curves of CP and CeNF at different acid/fiber ratios. As can be observed from Fig. 3, the thermal stability of CeNF was lower than that of raw CP. It is noted that the acid hydrolysis was carried out using a mixture of $\text{HCl}/\text{H}_2\text{SO}_4$ (1:2 v/v). Therefore, during the hydrolysis, the sulfate groups could be introduced at the outer surface of cellulose. These groups caused the dehydration reaction to take place, which leads to lowering the thermal stability of obtained CeNF [11]. Furthermore, as shown in Fig. 3, the thermal stability of CeNF increased with the increase of acid/fiber ratio from 100ml/2g to 150ml/2g. It is attributed to the increase of crystallinity of CeNF with increased acid/fiber ratio (Table 1). However, with further increase of acid/fiber ratio from 150ml/2g to 200ml/2g, the thermal stability of CeNF lowered significantly. It is due to the fact that the higher acid/fiber ratio, the higher amount of sulfate groups introduced at the outer surfaces of cellulose during the hydrolysis. Thus, as acid/fiber ratio was relatively high (200ml/2g), the negative effect caused by sulfate groups on the thermal stability of CeNF dominated the positive effect caused by the increased crystallinity. As a result, the thermal stability of CeNF lowered.

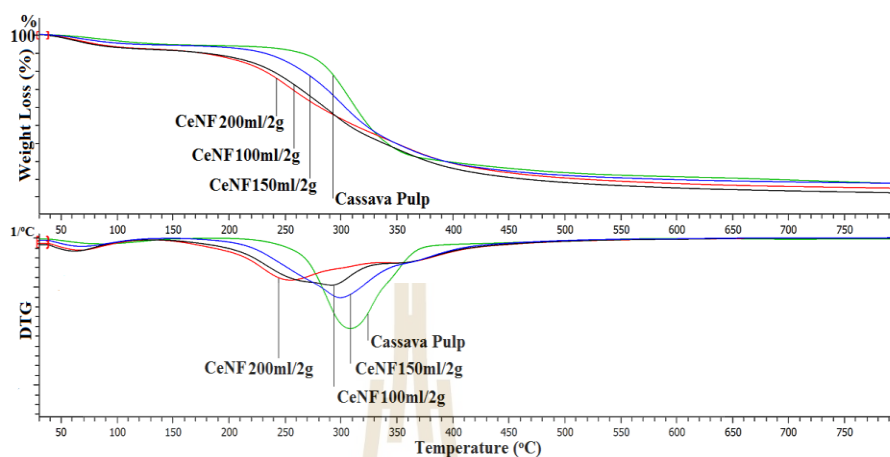


Fig. 3 TGA and DTG curves of raw CP and CeNF at different acid/fiber ratios.

Summary

Cellulose nanofibers with diameter in the range of 12-24 nm and immeasurable length were extracted successfully from cassava pulp by submitting the fibers to alkali and bleaching pre-treatments and acid hydrolysis treatment under different conditions. Acid/fiber ratio was found to have influence on crystallinity and thermal stability of obtained CeNF. Increasing acid/fiber ratio resulted in the increase of crystallinity of CeNF. However, with a relatively high acid/fiber ratio, the thermal stability of CeNF lowered considerably.

References

- [1] K. Siroth, R. Chollakup, S. Chotineeranat, K. Piyachomkwan and C.G. Oates: *Bioresource Technol.* Vol. 71 (2000), p. 63-69.
- [2] K. Siroth, V. Santisopasri, C. Petchalanuwat, K. Kurotjanawong, K. Piyachomkwan and C.G. Oates: *Carbohyd. Polym.* Vol. 38 (1999), p. 161-170.
- [3] Ed.M. Teixeira, A.A.S. Curvelo, A.C. Corrêa, J.M. Marconcini, G.M. Glenn and L.H.C. Mattoso: *Ind. Crop. Prod.* Vol. 37 (2012), p. 61-68.
- [4] H.A. Silverio, W.P.F. Neto, N.O. Dantas and D. Pasquini: *Ind. Crop. Prod.* Vol. 44 (2013), p. 427-436.
- [5] H. Sadeghifar, I. Filpponen, S.P. Clarke, D.F. Brougham and D.S. Argyropoulos: *J. Mater. Sci.* Vol. 46 (2011), p. 7344-7355.
- [6] N. Johar, I. Ahmad and A. Dufresne: *Ind. Crop. Prod.* Vol. 37 (2012), p. 93-99.
- [7] M.N. Angles and A. Dufresne: *Macromolecules.* Vol. 34 (2001), p. 2921-2931.
- [8] Y. Habibi, L.A. Lucia and O.J. Rojas: *Chem. Rev.* Vol. 110 (2010), p. 3479-3500.
- [9] L. Segal, J. Creely, A. Martin and C. Conrad: *Text. Res. J.* Vol. 29 (1959), p. 786-794.
- [10] D. Dai, M. Fan and P. Collins: *Ind. Crop. Prod.* Vol. 44 (2013), p. 192-199.
- [11] A.C. Corrêa, E.M. Teixeira, L.A. Pessan and L.H.C. Mattoso: *Cellulose.* Vol. 17 (2010), p. 1183-1192.

BIOGRAPHY

Thanh Chi Nguyen was born on July 2, 1985 in Phu Yen, Vietnam. He completed his Bachelor degree in Material Science from Vietnam National University - University of Science Ho Chi Minh City in 2008. Then, he got the SUT-PhD Scholarship for Asian Countries Program of Suranaree University of Technology for his graduate study in Polymer Engineering at School of Polymer Engineering, Institute of Engineering, Suranaree University of Technology. During his study, he published six papers in international journal as shown in Appendix B. Also, he presented one poster at the 2014 IUPAC World Polymer Congress (MACRO 2014), Chiang Mai, Thailand and five oral presentations at the 41st Congress on Science and Technology of Thailand (STT41), Nakhon Ratchasima, Thailand; 2016 International Conference on Materials Engineering and Nanotechnology (ICMEN 2016), Taipei, Taiwan; 2016 International Conference on Material Science and Engineering (ICMSE 2016), Guangzhou, China; 2016 5th International Conference on Material Science and Engineering Technology (ICMSET 2016), Tokyo, Japan; and 2017 International Symposium on Advanced Material Research (ISAMR 2017), Seoul, Republic of Korea.